THEORETICAL CHARACTERIZATION OF THE CHARGE-TRANSPORT AND ELECTROLUMINESCENCE PROPERTIES OF PI-CONJUGATED ORGANIC MATERIALS

A Thesis
Presented to
The Academic Faculty

by

Seyhan Salman

In Partial Fulfillment
of the Requirements for the Degree
Doctor of Philosophy in the
School of Chemistry and Biochemistry

Georgia Institute of Technology
August 2009

THEORETICAL CHARACTERIZATION OF THE CHARGE-TRANSPORT AND ELECTROLUMINESCENCE PROPERTIES OF PI-CONJUGATED ORGANIC MATERIALS

Approved by:

Dr. Jean-Luc Brédas, Advisor
School of Chemistry and Biochemistry
Georgia Institute of Technology

Dr. Seth R. Marder
School of Chemistry and Biochemistry
Georgia Institute of Technology

Dr. Rigoberto Hernandez
School of Chemistry and Biochemistry
Georgia Institute of Technology

Dr. Joseph W. Perry
School of Chemistry and Biochemistry
Georgia Institute of Technology

Dr. Bernard Kippelen
School of Electrical and Computer Engineering
Georgia Institute of Technology

Date Approved: June 12, 2009

This thesis is dedicated to my parents and sister.

ACKNOWLEDGEMENTS

I would first like to express my deep gratitude to my graduate advisor Dr. Jean-Luc Brédas for his continuous guidance throughout this work and his constant generosity in taking time to review this document and make helpful comments. His valuable collaboration, constructive criticisms and persistence to help me accomplish my goals mean a lot to me. Apart from his scientific guidance, I also wish to thank him for his kindness and understanding, especially at personal times when I needed to visit my family. Secondly, I would like to thank Dr. Veaceslav Coropceanu, Dr. Demétrio A. da Silva Filho, and Dr. Karin Schmidt for their valuable suggestions, assistance and contributions throughout my work. Next, I would like to thank Dr. Mari Carmen Ruiz Delgado for her endless encouragement, positive attitude and valuable friendship which means a lot to me. She was always there to meet, share ideas and develop vision. Additionally, I wish to acknowledge the former and current members of the Brédas group for their support and friendship over the last five years. I would also like to thank the Brédateurs at Materia Nova who made my stay in Mons so enjoyable. I acknowledge my committee members, Dr. Rigoberto Hernandez, Dr. Bernard Kippelen, Dr. Seth R. Marder and Dr. Joseph W. Perry, for their helpful advice. Last but not the least, special thanks to my parents and sister for their continuous trust and encouragement to pursue my interests throughout my life as well as the spiritual support they showed me at critical and opportune times.

TABLE OF CONTENTS

LIST OF TABLES

LIST OF FIGURES

LIST OF SYMBOLS

Å	Angstrom
a_m	Annihilation Operator
W	Bandwidth
a_m^+	Creation Operator
D	Debye
ΔE_{12}	Dimer Energy Splitting
M	Dipole Moment
R	Distance
ε^{eff}	Effective Site Energy
t^{eff}	Effective Transfer Integral
F	Electric Field
eV	Electron Volt
E	Electronic Charge
V_{RP}	Electronic Coupling
ΔE_{ST}	Exchange Energy
λ_s	External Reorganization Energy
ΔG°	Gibbs Free Energy of Reaction
H	Hamiltonian
S	Huang-Rhys Factor
λ_i	Internal Reorganization Energy
Q	Mulliken Atomic Charge
V_{OC}	Open-Circuit Voltage

E_g^{Op}	Optical Band Gap
F	Oscillator Strength
S	Overlap Matrix
τ_p^r	Phosphorescence Radiative Lifetime
Φ	Quantum Yield
λ	Reorganization Energy
ε	Site Energy
E	Total Energy
t	Transfer Integral
ψ	Wavefunction

LIST OF ABBREVIATIONS

6T	Sexithienyl
ADF	Amsterdam Density Functional
ADT	Acenedithiophenes
AEA	Adiabatic Electron Affinity
AIP	Adiabatic Ionization Potential
Alq_3	Tris(8-hydroxy-quinoline) aluminum
AM	Active Matrix
a-Si	Amorphous Silicon
BLA	Bond Length Alternation
B3LYP	Becke-three-parameter-Lee-Yang-Parr
BP	Becke-Perdew
CB	Conduction Band
CIS	Configuration Interaction Singles
CIS(D)	Configuration Interaction Singles and Doubles
CT	Charge Transfer
DFT	Density Functional Theory
DZ	Double-Zeta
DTP	Dithieno[3,2-*b*:2',3'-*d*]pyrrole
DTT	Dithieno[3,2-*b*:2',3'-*d*]thiophene
EA	Electron Affinity
ESD	Energy-Splitting-in-Dimer
ET	Electron Transfer

ET/HB	Electron-Transporting/Hole-Blocking
Fc	Ferrocenyl
FET	Field-Effect Transistor
FF	Finite Field
FIrpic	Iridium(III)bis[4,6-difluorophenyl]pyridinato-*N*,$C^{2'}$]picolinate
GGA	Generalized Gradient Approximation
GMH	Generalized Mulliken-Hush
HF	Hartree-Fock
HOMO	Highest-Occupied Molecular Orbital
HT	Hole Transfer
INDO	Intermediate Neglect of Differential Overlap
IP	Ionization Potential
$Ir(ppy)_3$	Tris(2-phenylpyridine)iridium
ITO	Indium Tin Oxide
IQE	Internal Quantum Efficiency
ISC	Intersystem Crossing
KT	Koopmans' Theorem
LANL2DZ	Los-Alamos National Laboratory Double-Zeta
LC	Ligand-Centered
LCD	Liquid Crystal Display
LLCT	Ligand-to-Ligand Charge Transfer
LUMO	Lowest-Unoccupied Molecular Orbital
mCP	N,N'-dicarbazolyl-3,5-benzene
MC	Metal-Centered
MDMO-PPV	2-methoxy-5-(3',7'-dimethyloctyloxy)-1,4-phenylene-vinylene

MLCT	Metal-to-Ligand Charge Transfer
OLED	Organic Light-Emitting Diode
OTFT	Organic Thin Film Field-Effect Transistor
OXD	1,3,4-Oxadiazole
OXD7	1,3-bis(tert-butylphenyl)-1,3,4-oxadiazole
PBD	2-(4-biphenylyl)-5-(4-tertbutylphenyl)-1,3,4-oxadiazole
PCBM	[6,6]-phenyl-C_{61} butyric acid methyl ester
PCM	Polarized Continuum Model
PDPDP	2,5-bis[2-(4-*tert*-butylphenyl)-1,3,4-oxadiazol-5-yl]phenylene
PF	Polyfluorene
PHOLED	Phosphorescent Organic Light-Emitting Diode
Pic	Picolinate
PLED	Polymer Organic Light-Emitting Diode
Pmb	1-Phenyl-3-methylbenzimidazole
PO	Phosphine-Oxide
PPP	Polyparaphenylene
PPV	Polyparaphenylenevinylene
Ppy	2-Phenylpyridine
Ppz	1-Phenylpyrazole
PT	Polythiophene
PTCDA	3,4,9,10-perylene-tetracarboxylic-dianhydride
PTCDI	3,4,9,10-perylene-tetracarboxylic-diimide
PV	Photovoltaic
PW91	Perdew Wang 1991
QM	Quantum Mechanics

QR	Quadratic Response
Q-TTF-Q	Tetrathiafulvalene-diquinone
Rc	Ruthenocenyl
SCF	Self-Consistent Field
SDD-ECP	Stuttgart-Dresden Double-Zeta Effective Core Potential
SDS	3-dicyanomethylidene-2,3-dihydrobenzothiophene-1,1-dioxide
SMOLED	Small Molecule Organic Light-Emitting Diode
SOC	Spin Orbit Coupling
TB	1,3-diethyl-2-thiobarbituric acid
TD-DFT	Time-Dependent Density Functional Theory
TES-pentacene	6,13-bis(triethylsilylethynyl)pentacene
TIPS-pentacene	6,13-bis(triisopropylsilylethynyl)pentacene
TPD	4,4'-bis(*N*-*m*-tolyl-*N*-phenylamino)biphenyl
TTF	Tetrathiafulvalene
TZP	Triple-Zeta plus Polarization
UB3LYP	Unrestricted Becke-three-parameter-Lee-Yang-Parr
UV/vis/NIR	Ultraviolet/Visible/Near Infrared
VB	Valence Band
VEA	Vertical Electron Affinity
VIP	Vertical Ionization Potential
VWN	Vosko-Wilk-Nussair
xc	Exchange-Correlation
ZORA	Zero-Order-Relativistic-Approximation

SUMMARY

Conjugated organic materials are currently the object of much interest because of the intrinsic scientific challenges they present and the technological potential they offer, including light-emitting diodes, solar cells, and field-effect transistors. The charge-transport mechanisms in organic conductive materials are still subject to considerable uncertainty and vary substantially as a function of the nature of the materials. However, around room temperature, conjugated oligomers and polymers usually transport charge via a thermally activated hopping-type mechanism, which depends on the relative orientations and solid-state packing of the species involved. The key parameters in hopping transport are the reorganization energies accompanying the geometric relaxations associated with electron transfer and the effective electronic coupling matrix elements between neighboring species, dictated largely by orbital overlap. A first contribution described in this thesis has been to underline that there is another but often ignored parameter affecting charge transport that results from the polarization of the localized electronic states by intermolecular interactions. We demonstrate that this contribution can be significant and, as in the case of the electronic coupling, is also very sensitive to the details of the system environment. Application of our methodology to a number of organic semiconductors is described.

In order to reach high performance in organic light-emitting diodes, efficient light emission from excited state(s) is critical. Iridium (III) organometallic complexes are of great interest because they can harvest both singlet and triplet states from electrically generated excitons; as a result, theoretical efficiencies of up to 100% can be achieved, whereas fluorescent molecules can only exploit singlet excitons and thus have a maximum theoretical efficiency of 25%. Of special interest for Ir(III) complexes is the color tunability of the emission from red to green and, in particular, to blue. Tuning of

emission over the entire visible spectrum could be achieved by judicious modification of the coordinated ligands; however, the relation between the structure of the ligands and the emission characteristics of such complexes is still not well understood. Part of our work has thus focused on the description of the ground- and excited-state characteristics of Ir(III) complexes, to better understand the interactions between these states and help establish the relationships between the ligand structure and the photophysical properties.

A careful choice of the host material for organometallic phosphors is also very important for optimizing emission properties. It is desirable that the host has a large enough bandgap for effective energy transfer to the guest, good carrier transport properties for a balanced carrier recombination in the emitting layer, and energy-level matching with electrodes for effective charge injection. Because these conditions are difficult to meet simultaneously, host materials for blue triplet emitters are relatively scarce. Part of this thesis, therefore, has described the ground- and excited-state properties of several classes of host materials including carbazoles, phosphine oxides, oxadiazoles and organosilicon compounds with the aim to understand their structure-property relationships and thus develop guidelines for the design of effective host materials for blue phosphorescence emitters.

CHAPTER 1

INTRODUCTION

Organic Electronics

Organic electronics has emerged as an exciting field of research and development encompassing a wide variety of scientific disciplines including chemistry, physics, materials science and device engineering. The field became a focus of deep investigation following the seminal work of Alan J. Heeger, Alan G. MacDiarmid, and Hideki Shirakawa, rewarded by the 2000 Nobel Prize in Chemistry;[1] this work demonstrated that organic conjugated polymers can present metallic-like electrical conductivity upon chemical doping (oxidation or reduction).[2] After this discovery, conjugated organic π-electron materials have attracted much attention in both academia and industry due to the opportunity of combining the electrical properties of (semi)conductors with the properties of plastics such as low cost, versatility of chemical synthesis, easy solution-based processability, and mechanical flexibility. Although the performance of organic semiconductors is still far from matching silicon-based technologies, their properties make them ideal candidates as active components in light-emitting diodes (LEDs),[3] photovoltaics,[4] field-effect transistors (FETs),[5] lasers and (bio)sensors.[6]

The OLED technology originated in 1963 when Pope and co-workers[7] discovered electroluminescence in organic crystals. However, since electroluminescence was associated with a very large voltage, the discovery did not make a big impact on the community at that time. The major breakthrough in the area came in 1987 when Tang and VanSlyke[8] at Kodak reported an efficient, low-voltage electroluminescent device based on a π-conjugated material, tris(8-hydroxy-quinoline) aluminum (Alq_3). Shortly afterwards, Friend and co-workers[9] at the University of Cambridge constructed a similar device using a conjugated polymer, poly(*para*-phenylenevinylene) (PPV), as the organic emitter. Rapid developments in organic materials lead to a new generation of thinner,

lighter, and high-resolution displays for computers, televisions and small hand-devices. Many OLED based consumer products are now commercially available in the market. For instance, Pioneer launched the first monochrome OLED car stereo in 1998.[10] Five years later, Kodak introduced a full-color active-matrix display for digital camera.[11] Today, a variety of small hand devices such as cellular phones and MP3 players with OLED panels have reached the market. Unlike liquid-crystal displays (LCDs), OLEDs do not require backlighting for screen illumination which makes these devices thin and light-weight. Furthermore, lower power requirements, faster response times, wider viewing angles, higher contrast and brightness are other advantage of OLEDs *vs*. LCDs. In 2005, Samsung Electronics announced the world's first 40-inch active matrix (AM) amorphous silicon (a-Si)-based OLED for emissive flat panel TV applications.[12] The new OLED prototype made from solution-processed polymers has a brightness of 600 cd/m^2 and a resolution of 1280x800 pixels which combines all of the traditional features of emissive OLED technology, including wide viewing angles, thin package size, and no color filter or backlight, with the enormous production infrastructure advantages of standard a-Si techniques. Following Samsung, Sony also managed to make large OLED screens that can function as TVs (see Figure 1.1). As such, Sony announced the availability of the industry's first OLED television in the United States in 2008.[13] Toshiba announced the Toshiba Vision Times Square full-color LED display that supports over one billion colors and high definition resolution in the same year.[14] Recently, Polymer Vision launched the world's first mobile phone with a rollable display.[15] While smaller than a typical mobile phone, the new device features a display which extends up to 5-inches and which can be folded away after use due to the flexibility of the polymer-based display material (see Figure 1.2). Plastic Logic, one of the leading companies in plastic electronics, creates products enabling information access. Their first product, focusing on reading digital content, will enter the market in 2009.

Figure 1.1 Large 27-inch OLED panel, along with other small OLED screens by Sony. Picture downloaded from *http://news.cnet.com*.[13]

Moreover, OLEDs bring new vistas for architects, designers and consumers. For instance, researchers at Philips have been working to develop OLEDs as a new light source for homes, offices, public areas, and even cars and planes that will enhance the look of the interior as well as be environmentally friendly. Philips has developed plain white and "warm white" panels, while "color-variable" OLEDs, capable of producing light of almost any color are likely to appear in the next 3 to 5 years (see Figure 1.3). Another research focus is on the development of transparent OLEDs; this means that OLED panels can function as ordinary windows during the day and provide light after dark, either mimicking the natural light, or providing attractive interior lighting.

Figure 1.2 World's first mobile phone with a rollable display developed by Polymer Vision. Picture downloaded from *http://www.polymervision.com*.[15]

In addition, scientists at Philips Research are looking for ways to make plastic substrates that will open the way for flexible and moldable OLED lighting panels, so that in the future almost any surface area, flat or curved, could become a light source. We could witness the development of luminous walls, curtains, ceilings and even furniture. Flexible OLED panels are likely to become available within 5 to 8 years.

Figure 1.3 OLED lighting demonstrated by Philips. Pictures downloaded from *http:// www.research.philips.com*.[16]

A typical OLED architecture, see Figure 1.4, consists of an anode, such as indium tin oxide (ITO), deposited onto a transparent substrate. The emissive organic layer is sandwiched between two conducting layers, the hole injection layer and the electron

transport layer. At the top, there is a reflective metal cathode. When a voltage is applied across the electrodes, holes are injected from the anode and electrons from the cathode. The holes migrate through the hole injection layer, while the electrons migrate through the organic electron transport layer. The holes and electrons meet in the organic emitter layer where they recombine to form an exciton. Relaxation from the excited state to the ground state gives rise to light emission. In summary, there are 5 main steps for light generation: (i) charge injection; (ii) charge-transport; (iii) charge recombination – exciton formation; (iv) exciton decay; and (v) light outcoupling. The organic emissive layer is made of a π-conjugated material that can be either a small molecule (small molecule OLEDs or SMOLEDs) or a polymer (polymer OLEDs or PLEDs). The color of the emitted light depends on the precise composition of the organic material. For instance, red, green, and blue emissive materials can be used together to produce the full color spectrum.

Recently, by dispersing a phosphorescent "guest" material into a light-emitting polymer "host", improvements in POLED efficiency have been achieved.[17,18] This is due to the use of all excited states, singlet and triplet for light emission provided that the triplet energy gap of the host is higher than that of the guest. Phosphorescent organic molecules incorporate a heavy metal surrounded by organic ligands. The strong spin-orbit coupling (SOC) of the heavy metal allows a very fast intersystem crossing (ISC) between the singlet and triplet excited states and allows the excitation to be stored in the lowest long-lived triplet state. Participation of the triplet excitons in the emission leads to OLEDs with 100% internal quantum efficiency (IQE). To date, heavy metals such as Os^{II}, Ru^{II}, Re^{I}, Ir^{III}, and Pt^{II} complexes are among the most studied phosphorescent metal complexes. It is now very well established that the tuning of the phosphorescence wavelength from blue to red is possible through modifications of the ligand structure.

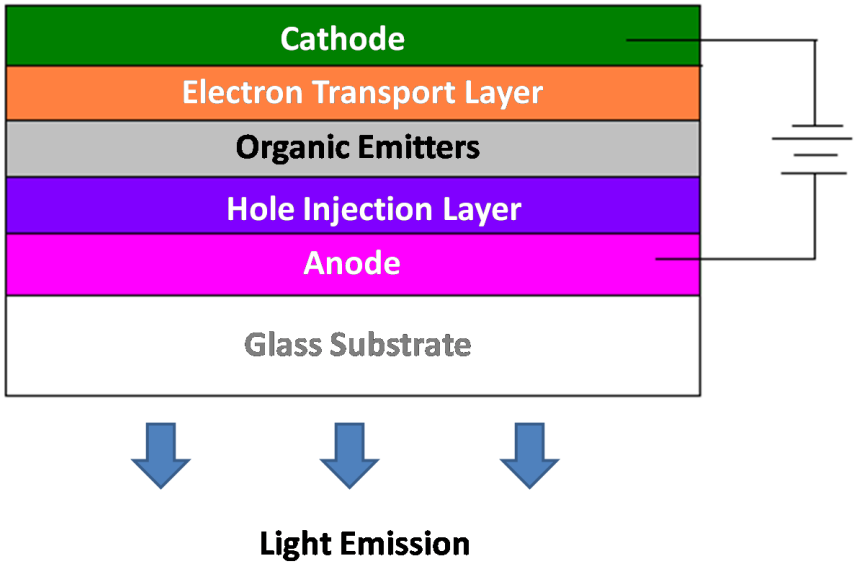

Figure 1.4 Illustration of a multilayered OLED structure.

Recent advances in solar power conversion efficiencies open up the ways to organic-based photovoltaics as a low-cost power generation technique.[19] Harvesting energy directly from sunlight using photovoltaics, or solar cells, is an essential component of future global energy production. The photovoltaic effect was discovered by 19-year old French physicist Alexandre-Edmond Becquerel in 1839.[20] Commercialization, however, started only after 1954, when the first crystalline Si photovoltaic (PV) device was developed at Bell Laboratories.[21] PV devices have an architecture similar to that of LEDs; the active organic layers are generally made of two components and sandwiched between two electrodes of a different nature (Figure 1.5). However, organic solar cells operate in a reverse way with respect to OLEDs (Figure 1.6).[22] The light is absorbed in the organic layers and excitons are generated. Next, excitons migrate toward the interfacial region between the organic components, where they dissociate as a result of photoinduced electron-transfer (ET) from a donor (D) component to an acceptor (A) component.[4] The separated charges are then accelerated by the electric field toward the electrodes. The charges reach the electrodes and leave the

device in order to drive the external circuit. Consequently, there are 4 main steps that might limit the power conversion efficiency in PV devices:[23] (i) light absorption; (ii) charge-carrier generation; (iii) charge transport; and (iv) charge collection at the electrodes. To date, efficiencies exceeding 5-6% have been reached in thin-film organic solar cells.[24]

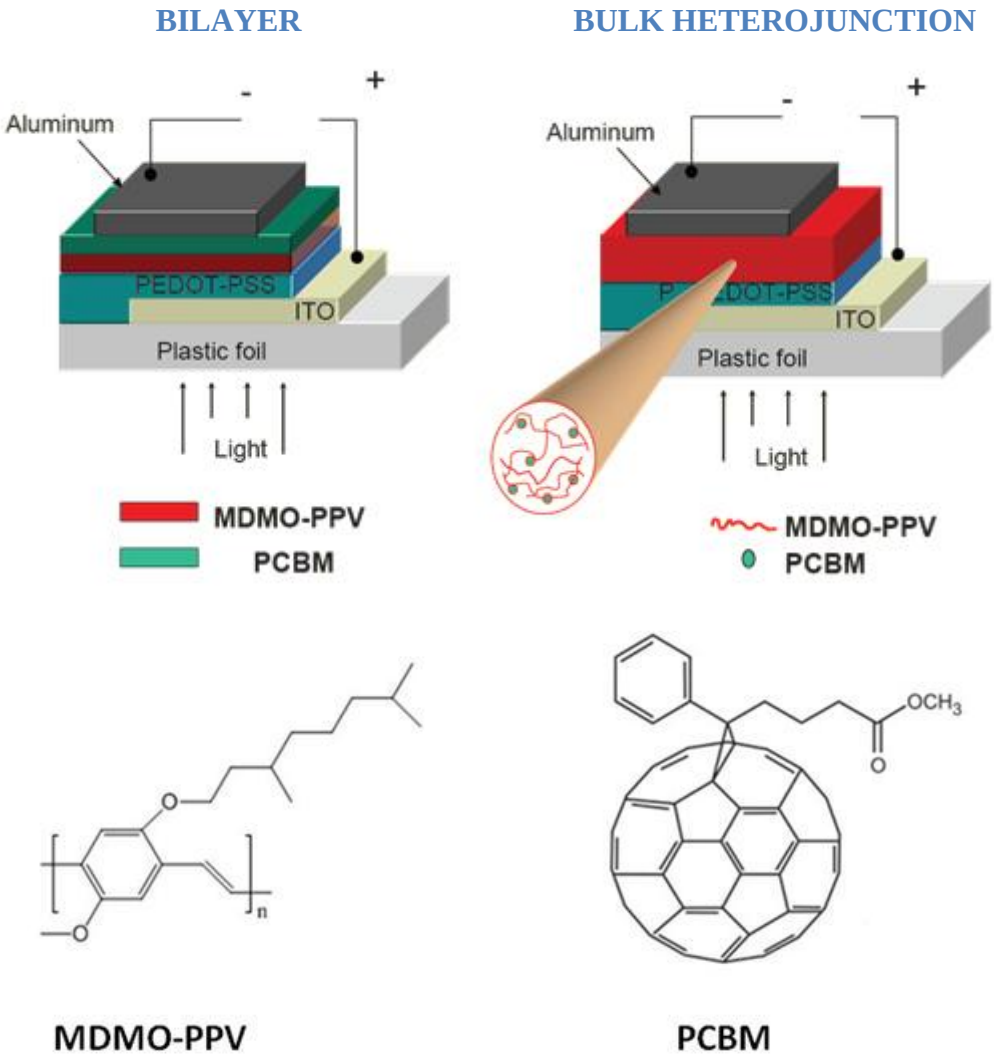

Figure 1.5 Schematic of photovoltaic device architectures as well as the chemical structures of typical donors and acceptors in the active layer: poly(2-methoxy-5-(3',7'-dimethyloctyloxy)-1,4-phenylene-vinylene) (MDMO-PPV); [6,6]-phenyl-C_{61} butyric acid methyl ester (PCBM).[25]

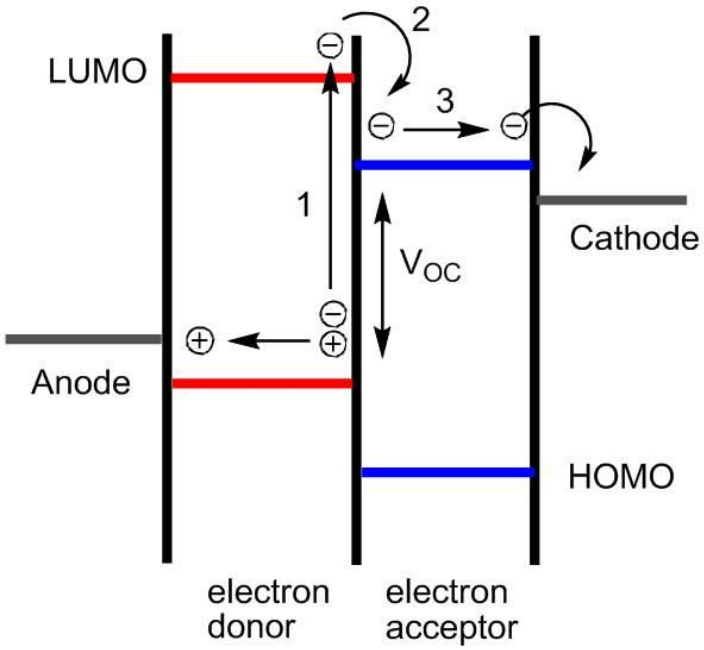

Figure 1.6 Heterojunction energy diagram of an organic photovoltaic cell, illustrating (1) light absorption and promotion of an electron to the LUMO of an electron-donor semiconductor and formation of an exciton; (2) electron transfer and formation of a charge-transfer state; (3) subsequent charge separation and transport to the electrodes. Note: V_{OC} is the open-circuit voltage.

Organic thin film field-effect transistors (OTFTs) are particularly interesting as their fabrication processes are much less complex compared to conventional Si technology. In general, low-temperature deposition and solution processing are the preferred methods of fabrication. Since the report of the first organic field-effect transistor in 1986,[26] there has been great progress in both materials performance and development of new fabrication techniques. An OTFT is similar to its inorganic counterpart in basic design and function (see Figure 1.7). It is a three-terminal device, in which a voltage applied to a gate electrode controls current flow between a source and drain electrode under an imposed bias. The control of source-drain current in FETs via a third terminal has resulted in their widespread use as switches. The mobility, μ, describes how easily charge carriers can move within the active layer under the influence of an electric field and is, therefore, directly related to the switching speed of the device.

Typical values range from 0.1-1 cm^2/Vs for a-Si devices, while organic semiconductors can reach mobilities of 0.1-20 cm^2/Vs range.[27,28] In an OFET, the keys steps of operation can be summarized as follows:[22] (i) formation of a conducting channel within the organic semiconductor as a result of an applied gate voltage; (ii) charge injection from the source electrode into the organic semiconductor and charge-transport across the organic layer; and (iii) charge collection at the drain electrode.

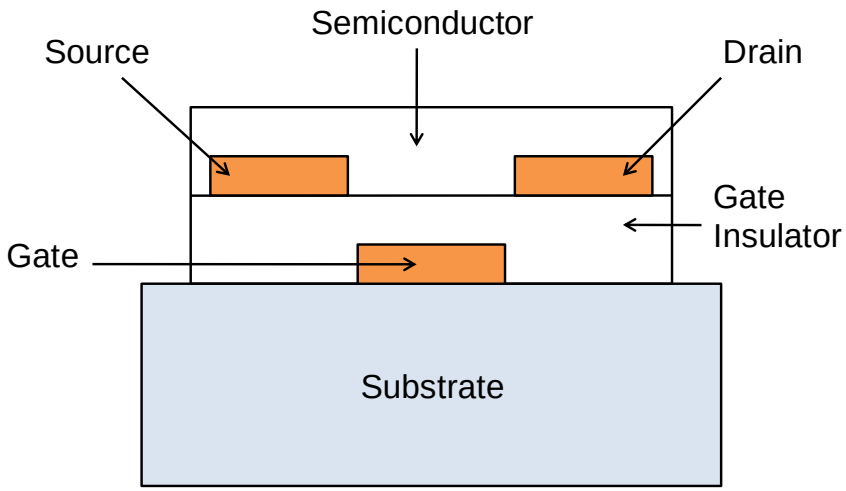

Figure 1.7 Basic schematic of a field-effect transistor.

This brief description of the operation principles in organic (opto)electronic devices highlights the importance of charge-transfer and energy-transfer processes in π-conjugated organic materials. Some of the most studied organic *molecular* semiconductors are shown in Figure 1.8. Among them, oligoacenes have been widely studied for several decades and at present provide the best performance in the field of organic electronics. Especially, tetracene and pentacene have been the focus of many studies due to their well-defined crystal structures combined with improved purification and film deposition techniques.[29-32] Hole mobilities of 1.3 and 2.2 cm^2/Vs have been measured for tetracene and pentacene single crystals, respectively.[33,34] Rubrene is also extensively studied both theoretically[35] and experimentally[36] as an excellent hole-

transporting material. It is now a material of choice for essential studies of charge-transport in organic crystals due to its high mobility, stability, and ease of growth. At room temperature hole mobility of up to 20 cm^2/Vs has been measured on rubrene single crystals.[37] Oligothiophenes represent another commonly investigated class of organic semiconductors. The interest in these materials started after the first report of an organic transistor fabricated from the well-known p-type semiconductor sexithienyl (6T).[38] Triphenylene,[39] hexabenzocoronene,[40] perylenedimide,[41] and metal phthalocyanines[42] are disc-shaped (discotic) liquid crystals with rigid aromatic cores and flexible alkyl side chains that show fast electronic conduction. High mobility photoconduction in the columnar mesophases of discotic liquid crystals was discovered in 1994.[43] Over the past years, they emerged as particularly interesting materials due to their efficient charge and energy transport along the self-organized columnar stacks.[44-46] Charge carrier mobilities in the discotic phases of liquid crystals are comparable to those in amorphous-Si (~0.1 cm^2/Vs).[47] Triphenylamines, such as the prominent 4,4'-bis(*N*-*m*-tolyl-*N*-phenylamino) biphenyl (TPD), have been recognized as hole-transporting materials in OLEDs.[48] 3,4,9,10-perylene-tetracarboxylic-dianhydride (PTCDA) and 3,4,9,10-perylene-tetracarboxylic-diimide (PTCDI) are two derivatives of the family of perylenes that exhibit good n-type properties.[41] Tetrathiafulvalene (TTF) compounds are important components of charge-transfer complexes, and they have been integrated in devices with high mobilities.[49] Fullerene (C_{60}) derivatives are prominent among electron-acceptor components in photoinduced ET reactions.[4,24] In molecular PV devices as well as bulk heterojunction polymer solar cells, a π-conjugated polymer acting as a p-type material and a C_{60} derivative as an n-type material constitute the photoactive layer. High efficiency thin-film organic solar cells based on pentacene and C_{60} heterojunctions have been fabricated with a power conversion efficiency of 2.7 ± 0.4%.[50] In addition, high mobility electron transporting (n-channel) organic transistors and circuits based on C_{60} have been reported.[51,52]

Charge-transport in *molecular* semiconductors is attractive since a number of conjugated molecules can be grown as single crystals from the vapor phase. These crystals allow the investigation of fundamental parameters affecting charge carrier mobilities. However, their industrial application is limited by their slow growth and lack of processability; one prefers solution-processable materials that are easy to fabricate and cost-efficient. Therefore, there has been enormous research activity to come up with soluble, stable, high-performance organic semiconductors.[53,54] A common strategy for rendering semiconductors soluble is the introduction of alkyl or bulky side chains. For instance, John Anthony and co-workers[53-56] synthesized soluble and oxidatively stable pentacene derivatives through functionalization with bulky triisopropylsilylethynyl and triethylsilylethynyl groups at the 6,13-positions of pentacene. Functionalized pentacene derivatives, 6,13-bis(triisopropylsilylethynyl)pentacene (TIPS-pentacene) and 6,13-bis(triethylsilylethynyl)pentacene (TES-pentacene) show considerable promise for applications as organic semiconducting materials due to their solubility, stability, and ease of processability. Following soluble and stable pentacene derivatives, the same group was able to functionalize higher acenes such as hexacene and heptacene by applying the silylethynylation method.[57] Likewise, silylethynyl functionalized fused acenedithiophenes (ADT) (see Figure 1.9) show increased solubility and stability.[58] Recently, fluorinated ADTs showing enhanced stability were reported.[59] These functional groups not only imparted solubility and stability to acenes but also enhanced the cofacial interactions in the solid. For instance, TIPS-pentacene showed improved solid-state ordering, yielding FET devices with a hole mobility of 0.4 cm^2/Vs.[54] Similarly, the tetramethylpentacene (Me_4PENT) synthesized by Wudl and co-workers showed promising charge transport mobility in devices.[60] Lately, Swager *et al.*[61] reported soluble tetracene derivatives by addition of long alkyl and alkoxy chains to tetracene backbone.

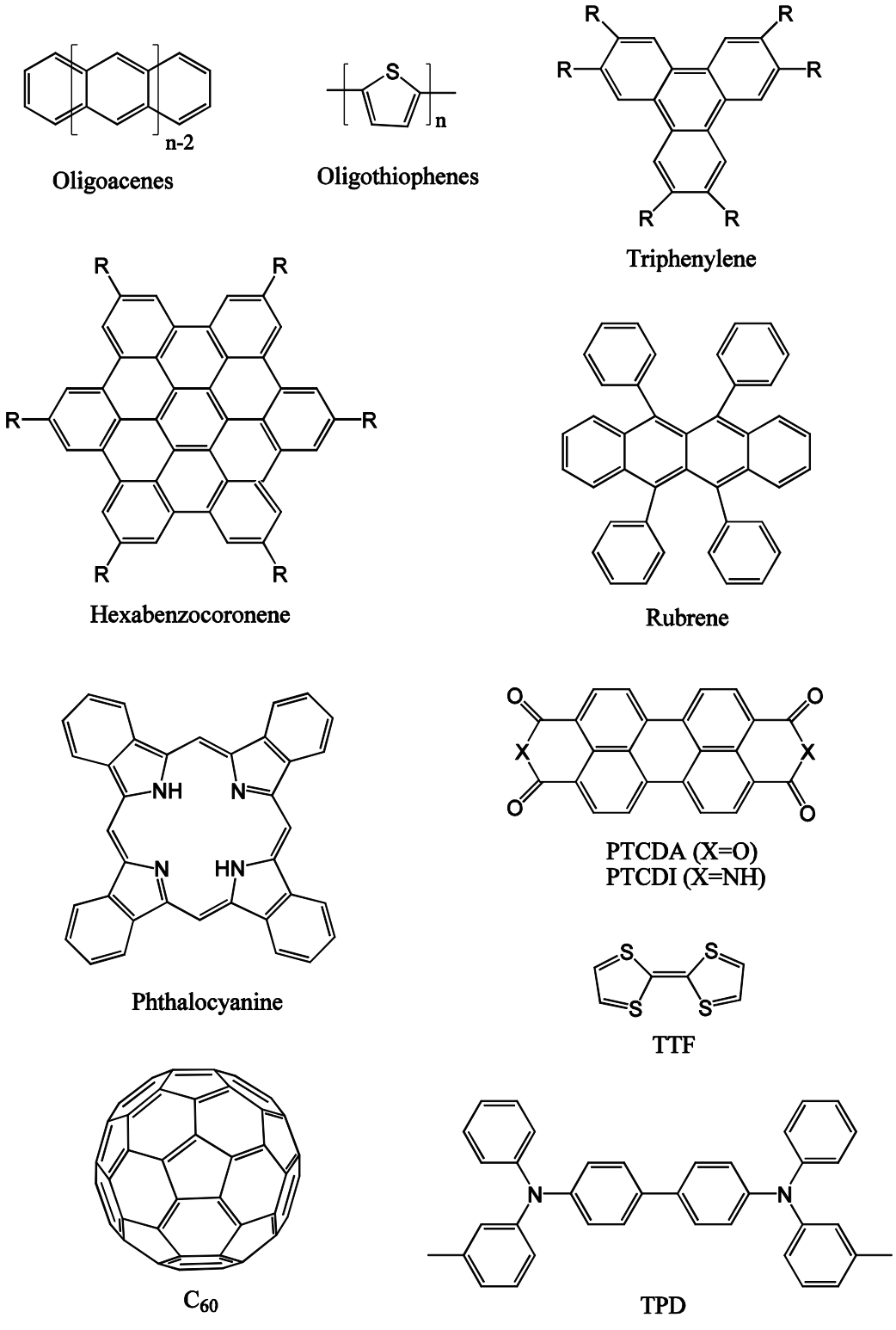

Figure 1.8 Prominent organic *molecular* semiconductors.[62]

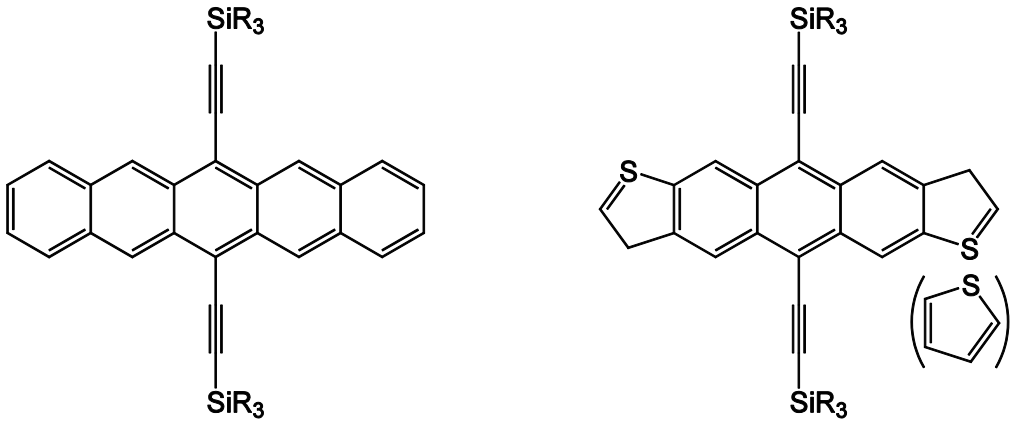

Figure 1.9 Examples of functionalized pentacene and anthradithiophene (ADT) derivatives. R can be methyl, ethyl, *i*-propyl, or *t*-butyl groups.[53,58]

Charge transport in conjugated *polymeric* semiconductors (for chemical structures, see Figure 1.10) is also widely investigated for opto(electronic) applications. For instance, polythiophene (PT) and its derivatives[26] are among the most studied polymer families due to their good solubility and processability. Head-to-tail regioregularity in alkyl-substituted polythiophenes decreases band gaps, improves micro-crystallinity in the solid state, and considerably improves field-effect mobilities.[5,63] Additionally, fused thiophenes appear as remarkable systems for OFET applications.[64-66] Another family of solution-processable polymers for OFETs is based on polyfluorene (PF) and some of its copolymers.[67] Polyparaphenylene (PPP)[68] and polyparaphenylenevinylene (PPV)[69,70] derivatives are also extensively investigated due to their electroluminescence properties for light-emitting applications.

π-Conjugated polymers are generally exploited as p-type (hole) charge-transport materials. However, n-type (electron) charge-transport materials are essential for the further development of efficient organic electroluminescent devices. Thus, incorporating electron-withdrawing groups such as fluorine and perfluoroalkyl substituents into p-type semiconductors has been a part of ongoing research efforts to lower the LUMO energies and facilitate electron injection, changing the semiconductor from a hole to an electron conductor.[71] For example, perfluorohexyl-,[72] perfluoroarene-,[73] carbonyl-,[74] and

dicyanomethyl-[75] substituted oligothiophenes have been reported to be good n-type semiconductors. More recently, tricyanovinyl-capped oligothiophenes have been reported as n-channel organic semiconductors.[76] Selected examples of electron-deficient thiophene oligomers as n-channel organic semiconductors are shown in Figure 1.11.

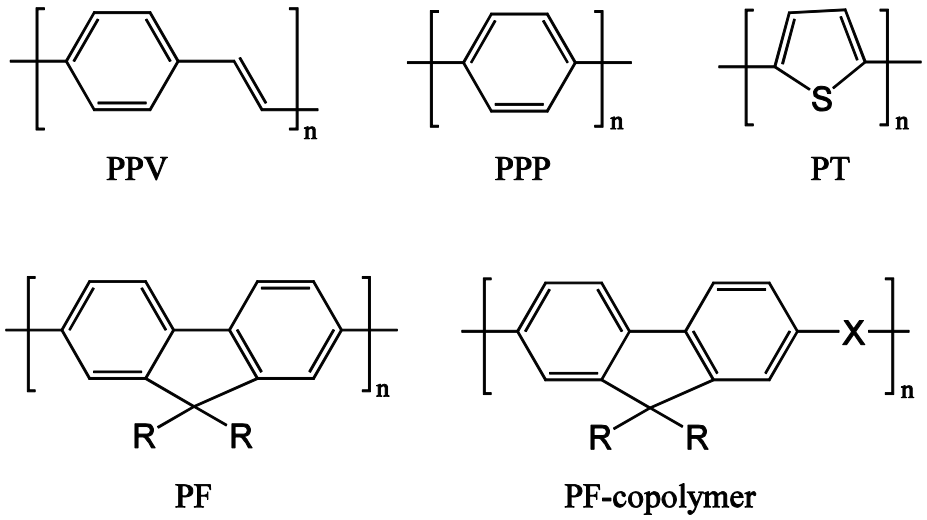

Figure 1.10 Prominent organic *polymeric* semiconductors - polyparaphenylenevinylene (PPV), polyparaphenylene (PPP), polythiophene (PT), and polyfluorene (PF).[62]

In addition, oxadiazole,[77,78] triazole, thiadiazole[79] (see Figure 1.12 for their chemical structures), and silole[80] derivatives are widely reported as efficient electron-transport (ET) materials for OLEDs. For instance, 2-*tert*-butylphenyl-5 biphenyl-1,3,4-oxadiazole (PBD) was the first small organic material used as an ET layer in OLEDs.[81] It is one of the most efficient ET materials due to its high electron affinity and wide band gap.[82]

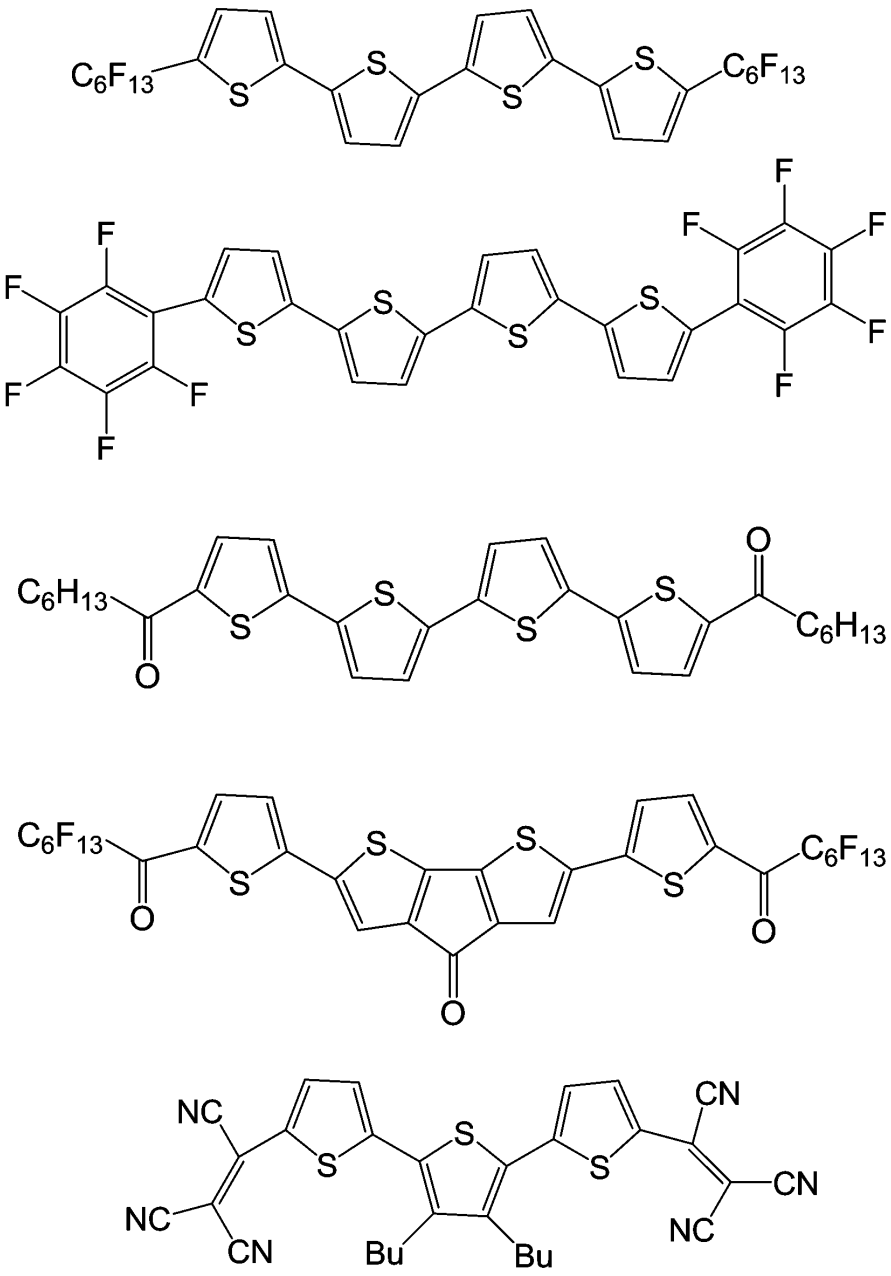

Figure 1.11 Selected examples of electron-deficient thiophene oligomers as n-channel organic semiconductors.[72-75]

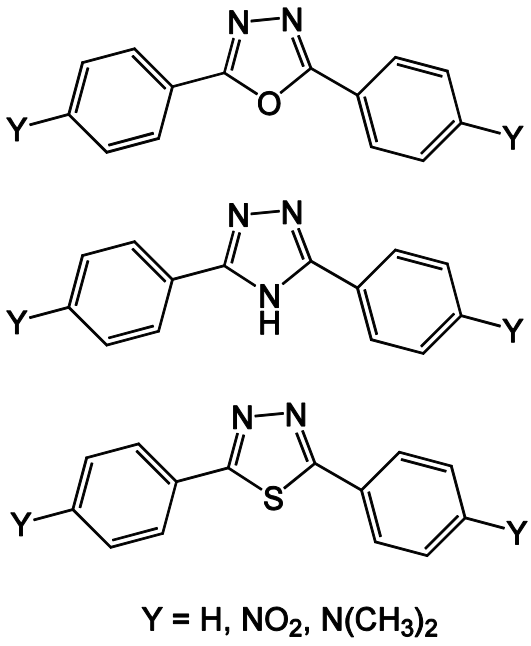

Figure 1.12 Structures of the 2,5-aryl-oxadiazole (top), 2,5-aryl-triazole (middle) and 2,5-aryl-thiadiazole (bottom) systems as ET materials.[79]

Furthermore, in many organic semiconductors the electron and hole mobilities are comparable, leading to ambipolar charge transport possessing both n- and p-type behavior.[83] For example, fluoroarene-oligothiophene semiconductors are reported to function as ambipolar charge-transport materials under appropriate macroscopic conditions.[84]

It should be noted that for efficient charge transport, the charges have to move from molecule to molecule and should not be trapped or scattered by numerous types of structural defects. This implies that charge carrier mobility is influenced by several factors such as crystal packing, disorder, material purity, temperature, pressure, electric field, charge-carrier density, size and molecular weight. The highest carrier mobilities reported to date have been obtained in single crystals of oligomers with a herringbone-type of solid-state packing. In the herringbone motif, organic molecules are packed edge-to-face in 2D layers, which limits the π-overlap between adjacent molecules. On the other hand, face-to-face π-stacks result in enhanced intermolecular interactions, facilitating

charge transport.[85] One of the common strategies to overcome herringbone packing and improve the charge-transport properties of oligomers is based on the introduction of functional groups on the polymer backbone.[57,59,61] As was already mentioned, Anthony and co-workers[86] have applied this technique to pentacene by substitution via TIPS and TES groups. In addition to imparting solubility to pentacene, these functional groups enhanced packing by introducing π-stacking into the crystal structure and, therefore, optimized the charge-transport properties. Another strategy receiving considerable attention is exploitation of the interactions between extended π-electron systems as a driving force to generate supramolecular structures with a noncovalent π-π stacking motif.[87]

Charge-Transport Mechanism in Organic Materials

The nature of how charges propagate through molecular materials is at the heart of organic electronics. Therefore, a better understanding of the charge-transport mechanism in organic semiconductors is necessary to optimize the performance of organic electronic devices.

The charge-transport mechanism varies as a function of temperature.[88] At very low temperatures, the charge carriers can be delocalized in perfectly ordered materials and charge transport then corresponds to a coherent band-like motion. In this case, the charge mobility is primarily determined by the bandwidth of the valence (hole transport) and conduction (electron transport) bands. When temperature increases, lattice vibrations lead to charge scattering and effectively reduce the total bandwidths and thus the charge mobilities. The band regime can be considered within a simple tight-binding approximation in which the total valence (conduction) bandwidth (W) results from the interaction of the HOMO (LUMO) levels of each molecule. For example, in the case of an infinite one-dimensional stack, the total bandwidth W is equal to $4t$, where t is the transfer integral between adjacent molecules. In a dimer involving two interacting

molecules, the splitting of the HOMO (LUMO) energy levels of each molecule is equal to $2t$. This result often provides a simple and reliable way to estimate the transfer integrals. However, when the interacting molecules are not symmetrically equivalent, this approximation (often referred to as "energy splitting in dimer" method) becomes insufficient due to the polarization-induced differences in site energy.

At higher temperatures, the charge carriers are localized due to the interaction with molecular vibrations. In this case, which is also the situation in disordered materials, the charge transport becomes a sequential electron hopping process between adjacent molecules. Most conjugated oligomers and polymers are assumed to transport charge at room temperature via a thermally activated hopping mechanism. Viewing each hopping event as a nonadiabatic electron-transfer reaction, the rate of charge motion between neighboring molecules can be described by Marcus theory.[89] In the semiclassical limit of Marcus theory, the rate of the electron-transfer process is expressed as:

$$k_{ET} = \frac{4\pi^2}{h} V_{RP}^2 \frac{1}{(4\pi\lambda k_B T)^{1/2}} \exp\left(-\frac{(\Delta G^\circ + \lambda)^2}{4\lambda k_B T}\right) \tag{1.1}$$

Here, ΔG° represents the Gibbs free energy of the electron-transfer reaction, V_{RP} is the electronic coupling between the initial and final states, and λ is the reorganization energy. The latter includes two contributions: (i) the internal part λ_i, which describes the changes in the geometry of the molecules upon charge transfer and (ii) the external part λ_s, related to the change in electronic and nuclear polarizations of the surrounding medium. When ΔG° is negative, the square dependence in $(\Delta G^\circ + \lambda)$ of the exponential term implies that the transfer rate displays a peak profile as a function of λ (which has a positive value) and reaches a maximum when $|\Delta G^\circ|$ is equal to λ. The rate is smaller when $|\Delta G^\circ| < \lambda$ (known as the normal region) and when $|\Delta G^\circ| > \lambda$ (the so-called inverted region).

It is worthwhile to note that the semiclassical Marcus formalism is based on the assumption that the system has to reach the transition state for the transfer to occur; it neglects tunneling effects that can assist the transfer, especially at low temperatures. More advanced vibronic theories have been developed, in particular by Jortner and Bixon,[90] that take into account the effect of specific vibrational modes on the charge-transfer rate:

$$k_{ET} = \frac{4\pi^2}{h} V_{RP}^2 \frac{1}{(4\pi\lambda_s k_B T)^{1/2}} \sum_{\nu} \exp(-S) \frac{S^{\nu}}{\nu!} \exp\left[-\frac{(\Delta G^{\circ} + \lambda_s + \nu\hbar\langle\omega\rangle)^2}{4\lambda_s k_B T}\right] \quad (1.2)$$

In Equation 1.2, the Huang-Rhys factor S is directly related to the internal reorganization energy by $S = \lambda_i/\hbar\omega$, and the summation runs over the vibrational levels in the final state.

Finally, in the absence of any external potential, the mobility values can be approximated from the calculated transfer rates using the Einstein-Smoluchowski equation for diffusive motion:[91]

$$D = \frac{k_{ET}\,\langle X^2\rangle}{n} \quad (1.3)$$

In this equation, D is the diffusion coefficient, $\langle X^2\rangle$ is the mean-square displacement of the charges, and n is an integer number equal to 2, 4, or 6 for one-, two-, and three-dimensional (1D, 2D, and 3D) systems, respectively. D is related to the charge mobility μ by the Einstein relation:[91]

$$\mu = \frac{eD}{k_B T} \quad (1.4)$$

where e is the electronic charge.

The application of an external electric field induces a drift of the charge carriers; the mobility can then be alternatively defined as the ratio between the velocity, v, of the charges and the amplitude of the applied electric field, F:

$$\mu = v/F \tag{1.5}$$

The conventional unit of carrier mobility is cm^2/Vs (since it corresponds to velocity over electric field).

Thesis Objectives and Outline

The primary objective of this thesis is to characterize the structural, electronic, and optical properties of organic π-conjugated polymer, oligomer, or molecular materials of interest for applications in organic electronics. For this purpose, quantum-chemical techniques ranging from Density Functional Theory to Hartree-Fock ab initio and semi-empirical methods are used to evaluate the charge transport, charge transfer and electroluminescence properties of organic semiconducting materials.

Chapter 2 provides a brief introduction to the electronic-structure theory methods that are used throughout the thesis. The computational techniques used to obtain the ground-state and excited-state properties of the systems are summarized.

In Chapter 3, the main emphasis is on the evaluation of reliable charge-transport parameters in organic semiconductors. The application of the symmetric orthogonalization method to obtain effective transport parameters such as transfer integrals and site energies is discussed. Emphasis is given to the effect of electronic polarization on the charge-transport parameters of organic materials. These parameters, that are extensively used for theoretical modeling, are evaluated as a function of molecular properties such as twist angles and intermolecular distances. The charge-

transport characteristics of the heterocyclic oligomers are calculated in an orthonormal basis; it is shown that the neglect of site energy differences in perpendicular configurations can lead to erroneous interpretations. The electronic coupling elements of selected dimers of crystalline oligoacenes and derivatives are investigated with the methodology we contributed to develop.

In Chapter 4, the charge-transport parameters of π-stacking fluorine- and alkyl/alkoxy-substituted tetracene crystals are investigated in the framework of the approach introduced in Chapter 3. In addition, the charge-transport parameters of fused heterocyclic oligomers as potential p-type materials in OFET applications are considered; their charge-transport characteristics are compared to those of commonly studied oligoacenes.

In Chapter 5, we turn to molecular organic materials presenting intramolecular charge transfer. The systems under investigation are metallocene-based donor-acceptor compounds that contain ferrocene, octamethylferrocene, and ruthenocene as donors and strong π-acceptors; the focus is on the effect of acceptor strength, metal identity, and metallocene methylation on the geometric, electronic, and spectroscopic properties of the chromophores.

Chapter 6 focuses on new charge transporting hosts for use in phosphorescent blue OLEDs. Small building blocks such as biphenyl, carbazole, dibenzofuran, fluorene, and their derivatives are analyzed as potential host materials for efficient blue electrophosphorescence. The ground-state electronic structure as well as the singlet and triplet excited states of several classes of host materials including carbazole trimers, phosphine oxides, oxadiazoles, and organosilicon compounds are addressed by means of a range of quantum-chemical techniques.

Finally, in Chapter 7, we investigate the emission properties of iridium(III) complexes used as triplet emitters in phosphorescent OLEDs. Benchmark calculations are

performed for facial and meridional isomers of homoleptic Ir compounds and the results are compared to the available experimental data in order to develop an understanding of the influence of ligand chemical structure and orientation (facial *vs*. meridional) on emission characteristics. The impact of electroactive substituents attached to cyclometalated and ancillary ligands of the heteroleptic Ir complexes are examined in detail to understand the role of ligand modification on emission properties such as emission maximum, quantum efficiency, and shape of spectrum. The effect of solvent on absorption and emission is also considered.

CHAPTER 2

QUANTUM-CHEMICAL METHODOLOGIES

The charge-transport parameters (site energies and transfer integrals) investigated in our work have generally been calculated at the Density Functional Theory (DFT) level using the generalized gradient approximation (GGA) and Perdew-Wang functional (PW91)[92] in combination with the triple-ζ plus polarization (TZP) basis set, as implemented in the *Amsterdam Density Functional* (*ADF*) program package.[93] This method has proven to give reliable transfer integrals for oligoacenes, and therefore can serve as a basis for our charge-transport calculations on these and related compounds.[94] Calculations have also been carried out with the semiempirical Intermediate Neglect of Differential Overlap (INDO) technique developed by Zerner and co-workers;[95] the focus there was to consider the energetic splitting of the HOMO and LUMO levels in systems consisting of two adjacent molecules. It is important to note that several earlier theoretical works have shown that INDO appropriately describes the intermolecular charge-transfer integrals.[30,35]

The geometries of the neutral, cationic, and anionic states of the molecules under study have been optimized at the DFT level by using the Becke-three-parameter-Lee-Yang-Parr (B3LYP)[96] hybrid density functional along with the 6-31G(d,p) basis set as implemented in the *Gaussian 98* and *Gaussian 03* program packages.[97,98] It was shown that the B3LYP functional gives the best description of geometries upon ionization in oligoacenes.[99,100] The spin-unrestricted formalism was used for the ionic states. Harmonic frequencies were computed at the same level of theory in order to identify the stationary points as minima (with all real frequencies). Single-point calculations were performed at the optimized neutral and ionic geometries using the same functional and basis set.

The ionization energies were calculated from the ΔSCF procedure where the first ionization potential (IP) is obtained from the energy difference between the neutral molecule and its cation both in the ground-state geometry of the neutral species (vertical ionization potential, VIP), or as the energy difference between the neutral and cation in their most stable geometries (adiabatic ionization potential, AIP).[101] The electron affinity (EA) was calculated according to the same ΔSCF procedure where VEA is defined as the energy difference between the neutral molecule and its anion both in the optimized ground state of the neutral species, and AEA is defined as the energy difference between the anion and neutral molecule in their respective most stable geometries.[84]

The intramolecular reorganization energy, λ, for a self-exchange ET reaction consists of two terms related to the geometry relaxation energies upon going from the neutral state to the charged molecular state and vice versa; it is given by:[62]

$$\lambda = \lambda_{\text{rel}}^{(1)} + \lambda_{\text{rel}}^{(2)} \tag{2.1}$$

The geometry relaxation energies, $\lambda_{\text{rel}}^{(1)}$ and $\lambda_{\text{rel}}^{(2)}$, were calculated directly from the adiabatic potential energy surfaces (PESs) illustrated in Figure 2.1 for the neutral and charged states as:

$$\lambda_{\text{rel}}^{(1)} = E^{(1)}(M) - E^{(0)}(M) \tag{2.2}$$

$$\lambda_{\text{rel}}^{(2)} = E^{(1)}(M^{\bullet}) - E^{(0)}(M^{\bullet}) \tag{2.3}$$

In Equations 2.2 and 2.3, $E^{(0)}(M)$ and $E^{(0)}(M^{\bullet})$ are the ground-state energy of the neutral state and the energy of the charged molecular state, respectively. $E^{(1)}(M)$ is the

energy of the neutral molecule at the optimized ion geometry, and $E^{(1)}(M^{\bullet})$ is the energy of the ionic state at the optimized neutral geometry.

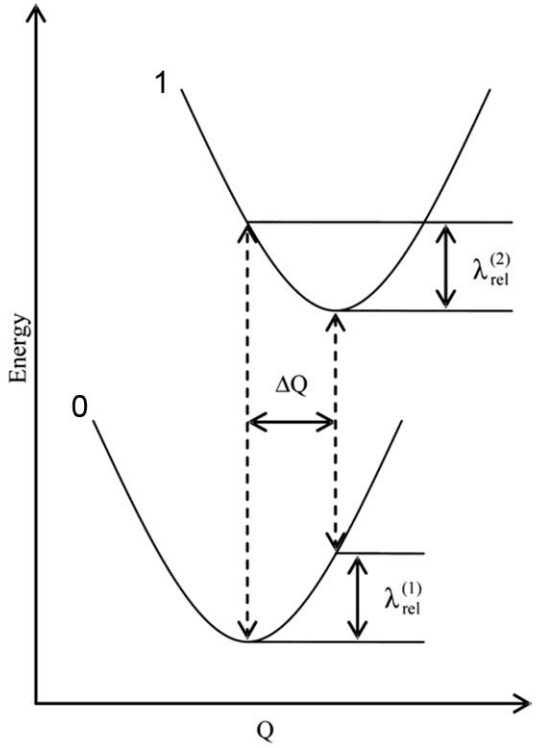

Figure 2.1 Schematics of the potential energy surfaces (PESs) for the neutral state 0 and charged state 1, showing the vertical transitions (dashed lines), the normal mode displacement ΔQ, and the relaxation energies $\lambda_{rel}^{(1)}$ and $\lambda_{rel}^{(2)}$.

The DFT calculations of the metallocene-based systems were performed with the B3LYP functional and the Los-Alamos National Laboratory double-ζ (LANL2DZ)[102] basis set for ruthenium and the 6-31G* basis set for all other atoms by using the *Gaussian 98* program.[97] The excitation energies are calculated using the Becke-Perdew (BP)[103,104] functional along with the double-ζ (DZ) basis set as implemented in the *ADF* program package.[93] The relativistic scalar Zero-Order-Relativistic-Approximation (ZORA)[105-109] is used for ruthenium.

The calculations on the lowest-lying excited singlet and triplet state calculations were done at various levels of theory, including INDO,[95] time-dependent (TD)-DFT,[110]

and Hartree-Fock (HF) with Configuration Interaction Singles (CIS)[111] and CI Singles and Doubles (CIS(D)).[112,113] HF/CIS and CIS(D) calculations were carried out with the *Q-Chem* package.[114]

Calculations on the singlet ground state and excited triplet state of the iridium complexes were achieved at the DFT/B3LYP level with the 6-31G basis set for the ligands and LANL2DZ basis set for iridium using the *Gaussian 98* program package.[97] For triplet state optimizations, the unrestricted (UB3LYP) formalism was used, whereas optimizations in the ground state were performed at the spin-restricted level. On the basis of the optimized geometry structures in the ground and excited states, the emission properties were calculated with the TD-DFT method.

In addition, the influence of the solvent (ethanol) on the lowest triplet states of the iridium complexes was evaluated using Onsager solvent model.[115] The solvent dependence of the absorption and emission spectra was studied by performing TD-DFT calculations on the optimized ground and excited states in combination with the polarized continuum model (PCM).[116,117] This combination of TD-DFT and PCM was used earlier by Liu *et al.* to predict the absorption and emission spectra of iridium complexes.[118]

The dipole moments (μ) of the lowest lying excited triplet states of the iridium complexes were obtained by applying the finite-field (FF) method through TD-DFT calculations on the optimized ground states in the presence of a uniform finite electric field.[119] According to the finite-field method, the individual components of μ were calculated by using the following equation:

$$\mu_i = -[45\{E(F_i) - E(-F_i)\} - 9\{E(2F_i) - E(-2F_i)\} + \{E(3F_i) - E(-3F_i)\}]/60F_i \qquad (2.4)$$

where E is the total energy and F is the applied electric field (i = x, y, z); the minimum electric field value F_i is set to 0.001 atomic units (5.15 x 10^6 V/cm).

The phosphorescence matrix elements between the excited triplets and singlet ground state of the iridium complexes were calculated from the residues of the quadratic response (QR) functions, as implemented in the *DALTON* program.[120] The phosphorescence radiative lifetime (τ^{r}_{p}) from the three sublevels of the lowest triplet state (corresponding to three spin projections, m_s = 0, ±1) was evaluated at the S_0 and T_1 optimized geometries. The radiative lifetime of the triplet state in the high-temperature limit, *i.e.*, when spin relaxation equalizes sublevel population before emission, was obtained by averaging over the three sublevels according to:

$$\frac{1}{\tau} = \frac{1}{3}\sum_{k=1}^{3}\frac{1}{\tau_k} \tag{2.5}$$

CHAPTER 3

EFFECT OF ELECTRONIC POLARIZATION ON CHARGE-TRANSPORT PARAMETERS IN MOLECULAR ORGANIC SEMICONDUCTORS

Introduction

A detailed understanding of the charge-transport processes in molecular organic semiconductors is a key element in the development of new generations of (opto)electronic devices, since charge transport is a critical component of device performance. The challenge for theory is to explain how chemical composition, geometric structure, and molecular packing influence the transport properties. Although there is now some understanding of how some of these parameters affect charge-transport rates in organic thin films or crystal, there still remain fundamental questions concerning the impact of structural factors important in charge-transport processes, and their dependence on supramolecular architecture.

The relationship between the charge-transport properties and geometric structure can be understood by starting from the electronic Hamiltonian in a simple tight binding approximation:

$$H = \sum_{m} \varepsilon_m a_m^{+} a_m + \sum_{m \neq n} t_{mn} a_m^{+} a_n \tag{3.1}$$

where a_m^{+} and a_m are the creation and annihilation operators, respectively. For an electron on molecular site m, ε_m is the electron site energy, and t_{mn} is the transfer integral (electronic coupling to site n). Whether a band-like or hopping transport mechanism is operative, the charge-transport properties depend on both parameters. These are simply obtained from the following equations:

$$\varepsilon_m = \langle \psi_m(r - R_m) | H | \psi_m(r - R_m) \rangle \quad (3.2)$$

$$t_{mn} = \langle \psi_m(r - R_m) | H | \psi_n(r - R_n) \rangle \quad (3.3)$$

where vector $R_{m(n)}$ indicates the position of site *m* (*n*). In equations 3.1 to 3.3, a single localized molecular orbital ψ has been considered on each site and corresponds to the HOMO or LUMO for hole and electron transport, respectively. It is important to emphasize that orbitals $\psi_{m(n)}$ in the above equations are assumed to be orthogonal; however, this is usually not the case for HOMOs or LUMOs located on adjacent sites (or molecules). We will show in the next section how ε_m and t_{mn} transform when going from a nonorthogonal to an orthogonal basis. Rigorously, ψ_m and ψ_n correspond to the wavefunctions of two charge-localized states (diabatic states), *i.e.*, the states obtained in the hypothetical absence of any coupling between the molecular units. The determination of the diabatic states is in general very challenging; as a result, it is customary to rely on a transformation to an adiabatic basis, ψ_1 and ψ_2, that can be directly assessed by means of quantum-chemical calculations

The transfer integral is determined by the intermolecular overlap of the electronic wavefunctions and depends in a subtle way on the intermolecular distance and orientation. As a result, the transfer integrals can be strongly modulated by lattice phonons (vibrations), a phenomenon referred to as *nonlocal* coupling; the nonlocal electron-phonon coupling is the major interaction taken into account in Peierls-type models.[121] On the other hand, the site energy is affected by the polarization of the environment and by (intramolecular) vibrations. The electron–vibration coupling that leads to overall modulations of the site energy is known as *local* coupling, which is the key interaction considered in Holstein's molecular polaron model.[122,123] In organic

molecular crystals, both local and nonlocal electron-phonon interactions impact the carrier mobilities.

A number of computational methods have been proposed and applied to obtain estimates of the transfer integrals. The most simple approach, which has been widely used,[30,35,45,124-126] relies on the consideration of the energy splittings obtained in a system composed of two molecules (two monomers), a method usually referred to as the "energy-splitting in dimer" (ESD) model. It is based on the realization that, at the transition point, where the excess charge is equally delocalized over both sites (symmetric dimer), the energy difference $E_2 - E_1$ between the adiabatic states ψ_1 and ψ_2 corresponds to $2t_{mn}$ (see Figure 3.1); as a result $t_{mn} = (E_2 - E_1)/2$. Strictly, the method requires the use of the geometry at the transition state (*i.e.*, at the avoided crossing point) of the charged dimer. In practice, the calculations are simplified by either considering the geometry of the neutral dimer or the geometry obtained as the average over the neutral and ionic nuclear coordinates of the monomers.

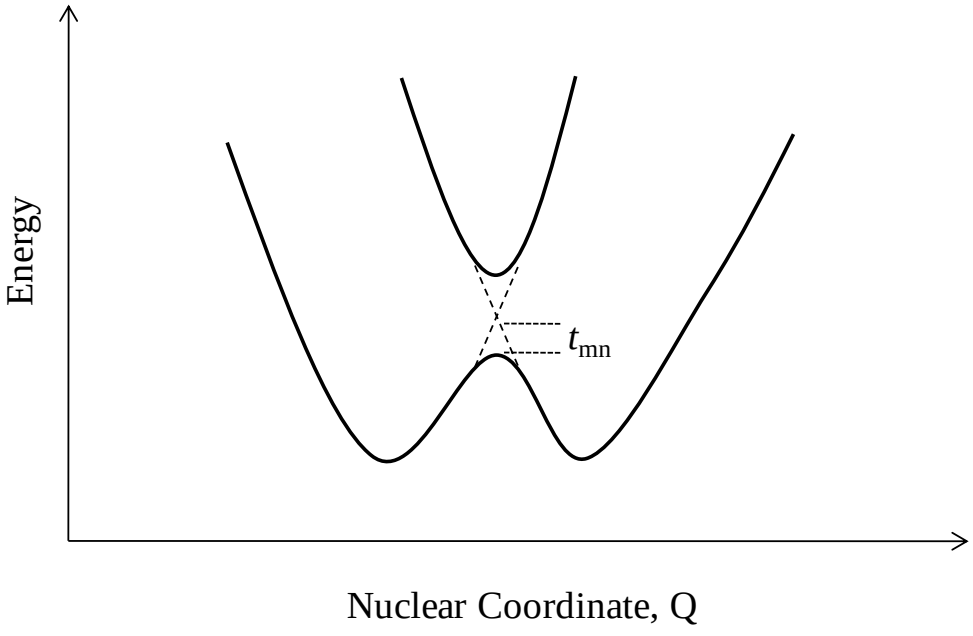

Figure 3.1 Schematics of the adiabatic potential energy curves for a symmetric electron transfer reaction.

Another approximation is to consider the one-electron orbitals instead of the total adiabatic electronic wavefunctions, in the context of Koopmans' theorem (KT).[127] According to KT, the transfer integrals are estimated as half the splitting of the HOMO levels (for holes) and LUMO levels (for electrons) induced by the interaction of monomer orbitals (HOMOs and LUMOs) in a dimer. It is given as:

$$t = \frac{\epsilon_{\mathrm{L}+1[\mathrm{H}]} - \epsilon_{\mathrm{L}[\mathrm{H}-1]}}{2} \tag{3.4}$$

where $\epsilon_{\mathrm{L}\,[\mathrm{H}]}$ and $\epsilon_{\mathrm{L}+1\,[\mathrm{H}-1]}$ are the energies of the LUMO and LUMO+1 [HOMO and HOMO-1] levels taken from the closed-shell configuration of the neutral dimer. Because of its simplicity, the KT-ESD approach is currently the most frequently used method for the estimation of the transfer integrals in organic semiconductors.

The electronic coupling matrix element between excited state and charge-transfer state can also be calculated from the energy and intensity of the appropriate charge-transfer transition. An expression to estimate the transfer integrals in this way is based on the two-state generalized Mulliken-Hush (GMH) model, where t_{mn} is obtained as:

$$t_{mn} = \frac{M_{ab}\,\Delta E_{ab}}{\sqrt{(\Delta\mu_{ab})^2 + 4(M_{ab})^2}} \tag{3.5}$$

Here, $\Delta\mu_{ab}$ and M_{ab} are the change in permanent dipole moment and the transition dipole moment, respectively, between the adiabatic states associated with the considered diabatic states; ΔE_{ab} is the free energy difference between these adiabatic states.

Another method of calculating the electron transfer coupling elements is based on the use of the constrained DFT method.[128] The basic idea of constrained DFT is to find an effective external potential [the constraining potential $V_c w_c(r)$] to add to the Hamiltonian

so that the resulting ground-state density satisfies some specific density constraint, *i.e.*, $\int w_c(r)\rho_c(r)dr = N_c$, where $w_c(r)$ is the operator that defines the property of interest. The constraint can be a local charge or spin configuration, for instance, a charge-separated state D^+A^- or a broken-symmetry singlet $B(\uparrow) - B(\downarrow)$. In order to study ET reactions by constrained DFT, different states with the electron localized on either the donor or the acceptor are explicitly constructed with appropriate constraints (*e.g.*, D^+A^- or DA), and those constrained states can be regarded as the diabatic states. It then calculates adiabatic quantities based on the diabatic states. The electronic coupling matrix element is calculated from the energy differences between diabatic states of constrained DFT and the adiabatic ground state of unconstrained DFT. If the diabatic states are assumed to be orthogonal, the electronic coupling matrix element is given by:

$$|t_{mn}| = \sqrt{(E - E_D)(E - E_A)} \tag{3.6}$$

where E_D and E_A are the constrained DFT energies.

As an example, the diabatic and adiabatic energy curves along the reaction pathway for intervalence ET in the tetrathiafulvalene-diquinone (Q-TTF-Q, Figure 3.2) anion are shown in Figure 3.3. While the unconstrained DFT curve has no reaction barrier (which disagrees with experimental results), the generated adiabatic ground-state curve constructed from the diabatic curves and constrained DFT H_{ab} values shows a barrier between the reactant and product states, successfully predicting Q-TTF-Q anion to be a class II mixed-valence compound.

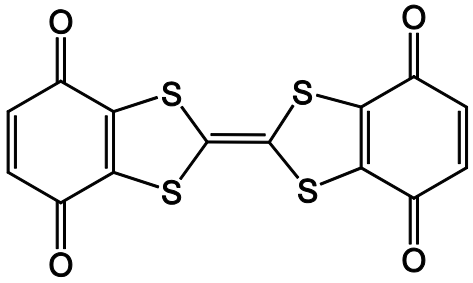

Figure 3.2 Chemical structure of the tetrathiafulvalene diquinone (Q-TTF-Q).

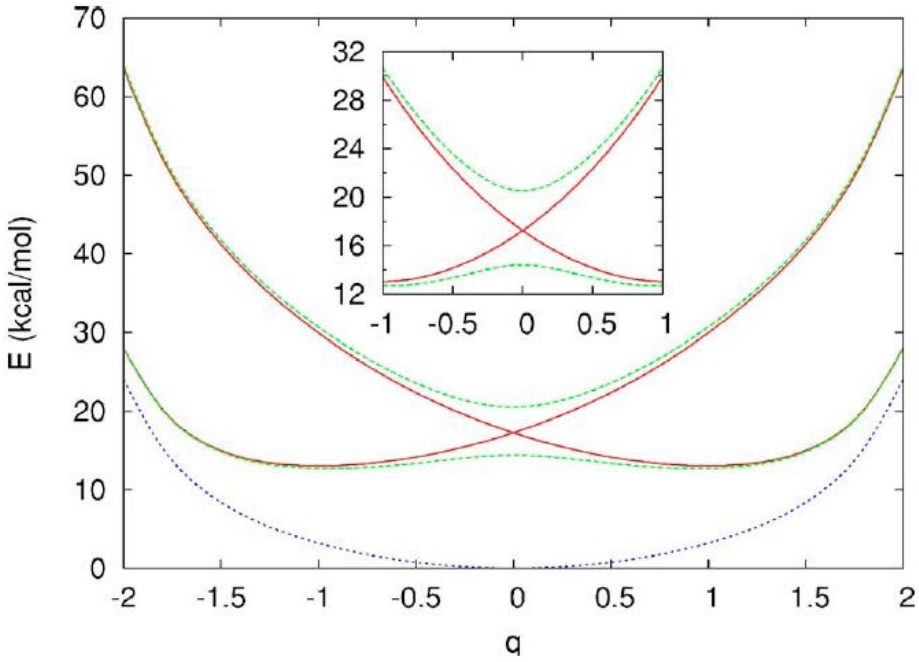

Figure 3.3 Potential energy curves of the Q-TTF-Q anion. Red solid lines: diabatic energies from constrained DFT. Green dashed lines: adiabatic energies from constrained DFT. Blue dotted line: unconstrained DFT energies. The inset has the diabatic and adiabatic curves at a different scale. Figure adapted from Ref. 128.

In our work, we have developed a generalized methodology in which we considered the entire dimer Hamiltonian in combination with a basis orthogonalization procedure to evaluate the electronic coupling. Unlike the "energy splitting in dimer" method, such a methodology is applicable to asymmetric situations, *i.e.*, when the interacting molecules are not equivalent by symmetry.

Basis Orthogonalization Method

As we mentioned above, the ESD method provides a simple and often reliable way to estimate the transfer integrals. However, the application of this simple approach can sometimes fail, even in molecular crystals with weak van der Waals intermolecular interactions, due to the considerable (but often ignored) impact of polarization effects, mainly on the site energies. For instance, the authors of Ref. 126 examined the evolution of the orbital splitting as a function of tilt angle (where one molecule is tilted about the longitudinal molecular axis relative to the other) for a series of oligomers and found that at 90°, where the two molecules are perpendicular, the MO splitting reaches a maximum. However, this is not a correct way of estimating the transfer integrals. It is commonly understood that cofacial configurations (0° tilt angle) lead to the largest electronic splitting because of the maximum atomic orbital overlap at this orientation.[85] The issue in Ref. 126 is due to the neglect of the site energy difference between the molecules, especially at the face-to-edge configuration. The transfer integrals should be estimated as half of ΔE_{12} only when the site energies are equal. Although the fact that ΔE_{12} can be affected by site energies has been previously discussed in the literature, this dependence was solely attributed to the chemical or geometric differences between the two molecules.[30,124] We show here that there is another contribution to the site energy difference that results from the polarization of the localized electronic states by intermolecular interactions.

Organic molecules in the solid state, due to weak van der Waals interactions, maintain their molecular identities to a large extent. This often leads to localization of excess charge carriers on individual molecules. The energy of a localized charge carrier in a molecular crystal differs from that of the free molecular ion by the apparent polarization energy. Historically, the situation has been simplified and polarization energy for non-polar aromatic organic molecular crystals is practically determined only by charge-induced dipole interactions. Nonpolar organic molecules like polyacenes have

no permanent dipole moment but due to the planar structure of the molecules, they have a permanent quadrupole moment which increases rapidly with increasing number of aromatic rings in the molecule. These inherent quadrupoles cause static classical polarization energy as a result of the charge-permanent quadrupole interaction in organic solids. In addition to electronic polarization energy terms, there is also a nuclear (vibronic) polarization term. At this stage, we emphasize that the polarization in this chapter refers to the static polarization term caused by the charge-quadrupole interaction of the nonpolar species.

Following Siebbeles and co-workers,[129] we define one-electron dimer states in terms of localized monomer orbitals. Assuming that the splitting between the HOMO (LUMO) levels of the dimer results only from the interaction of the monomer HOMOs (LUMOs), the orbital energies of the dimer can be described by the following generalized matrix eigenvalue equation:

$$HC - ESC = 0 \tag{3.7}$$

where H and S are the system Hamiltonian and overlap matrices in the basis of nonorthogonal monomer orbitals:

$$H = \begin{pmatrix} \varepsilon_1 & t_{12} \\ t_{12} & \varepsilon_2 \end{pmatrix} \tag{3.8}$$

$$S = \begin{pmatrix} 1 & S_{12} \\ S_{12} & 1 \end{pmatrix} \tag{3.9}$$

where the matrix elements are defined as:

$$\varepsilon_{1(2)} = \left\langle \psi_{1(2)} \middle| H \middle| \psi_{1(2)} \right\rangle \tag{3.10}$$

$$t_{12} = \langle \psi_1 | H | \psi_2 \rangle \tag{3.11}$$

$$S_{12} = \langle \psi_1 | \psi_2 \rangle \tag{3.12}$$

In these equations, the monomer orbitals $\psi_{1(2)}$ are nonorthogonal. However, Equation 3.1 is valid in an orthogonal basis. An orthonormal basis set that maintains as much as possible the initial local character of the monomer orbitals can be obtained from $\psi_{1(2)}$ by means of Löwdin's symmetric transformation.[130] If the basis $\psi_{1(2)}$ is orthonormalized:

$$S_{12} = \langle \psi_1 | \psi_2 \rangle = \delta_{12} \tag{3.13}$$

one gets a "standard" matrix eigenvalue equation:

$$H^{eff}\, C = EC \tag{3.14}$$

with the Hamiltonian defined as:

$$H^{eff} = \begin{pmatrix} \varepsilon_1^{eff} & t_{12}^{eff} \\ t_{12}^{eff} & \varepsilon_2^{eff} \end{pmatrix} \tag{3.15}$$

In this case, the matrix elements have the form:

$$\varepsilon_{1(2)}^{eff} = \frac{1}{2} \frac{(\varepsilon_1 + \varepsilon_2) - 2t_{12}S_{12} \mp (\varepsilon_1 - \varepsilon_2)\sqrt{1 - S_{12}^2}}{1 - S_{12}^2} \tag{3.16}$$

$$t_{12}^{eff} = \frac{t_{12} - \frac{1}{2}(\varepsilon_1 + \varepsilon_2)S_{12}}{1 - S_{12}^2} \tag{3.17}$$

In this way, $\varepsilon_{1(2)}^{eff}$ and t_{12}^{eff} become identical to ε_m and t_{mn} (in Equation 3.1). At this point, it is important to emphasize that neglecting to apply the orthogonalization procedure[39] leads to t_{12} values that can differ from the t_{12}^{eff} values by as much as a factor of 2.

As a result, the energetic splitting between the HOMO (LUMO) levels of the dimer is given by:

$$|\Delta E_{12}| = \sqrt{\left(\varepsilon_1^{eff} - \varepsilon_2^{eff}\right)^2 + \left(2t_{12}^{eff}\right)^2} \tag{3.18}$$

Equation 3.18 indicates that the transfer integral can be estimated as one-half of ΔE_{12} when the site energies are equal and the HOMO (LUMO) and HOMO-1 (LUMO+1) orbitals of the dimer contain contributions that come exclusively from the monomer HOMOs (LUMOs). We also note that when the transfer integral is derived from ΔE_{12}, it is explicitly assumed that an orthogonal localized (diabatic) basis set is used and the derived transfer integral should be interpreted as an effective quantity that accounts for both t_{12} and S_{12}.

The fact that ΔE_{12} can be affected by site energies was largely overlooked in the literature, especially when dealing with systems formed from identical monomers. The common assumption that the site energies of identical monomers are the same is incorrect when the monomers are not equivalent. This can be easily understood based on symmetry considerations: the energy difference $\varepsilon_1 - \varepsilon_2$ $\left(\varepsilon_1^{eff} - \varepsilon_2^{eff}\right)$ vanishes only if the matrix elements H_{11} and H_{22}, which define the site energies, can be obtained from one another

by a symmetry transformation; *i.e.*, the dimer is symmetric. Otherwise, when the molecules are not equivalent by symmetry, the molecules polarize each other differently and $\Delta\varepsilon_{12}^{eff}$ is no longer zero. In this case, as we show in the following examples, the energy splitting approach can drastically overestimate the transfer integral.

Results and Discussion

As a first example of how t_{12}^{eff} and $\Delta\varepsilon_{12}^{eff}$ depend on the intermolecular parameters, we consider a π-stacked ethylene dimer with a fixed 5.0 Å center-to-center distance and in which one monomer is tilted around its longitudinal molecular axis. Figure 3.4 illustrates the evolution of t_{12}^{eff} and $\Delta\varepsilon_{12}^{eff}$ as a function of the tilt angle. As seen from Figure 3.4, ΔE_{12} varies only slightly with the angle and is maximized at the face-to-edge configuration. The transfer integral gradually decreases with the tilt angle from its maximum value at the cofacial orientation to exactly zero when the system reaches the face-to-edge configuration. On the contrary, $\Delta\varepsilon_{12}^{eff}$ reveals the opposite trend. As a consequence, in the face-to-edge configuration, $\Delta\varepsilon_{12}^{eff}$ is the only contribution to the energy splitting, ΔE_{12}. The same qualitative behaviors are observed when considering a π-stacked pentacene dimer with a fixed 5.0 Å center-to-center distance and in which one monomer is tilted around its longitudinal molecular axis. Evolution of the transfer integral and site energy difference as a function of the tilt angle in the pentacene dimer is shown in Figure 3.5. As can be seen from Figure 3.5, the transfer integral is nearly zero at all orientations. In contrast, $\Delta\varepsilon_{12}^{eff}$ increases with the tilt angle reaching its maximum value at the face-to-edge configuration. As a result, $\Delta\varepsilon_{12}^{eff}$ dictates the evolution of the energy splitting, ΔE_{12}. We note that the largest transfer integral at 90° is presumably due to the fact that the edge H and face C atoms are becoming too close (<3.5 Å) at this configuration.

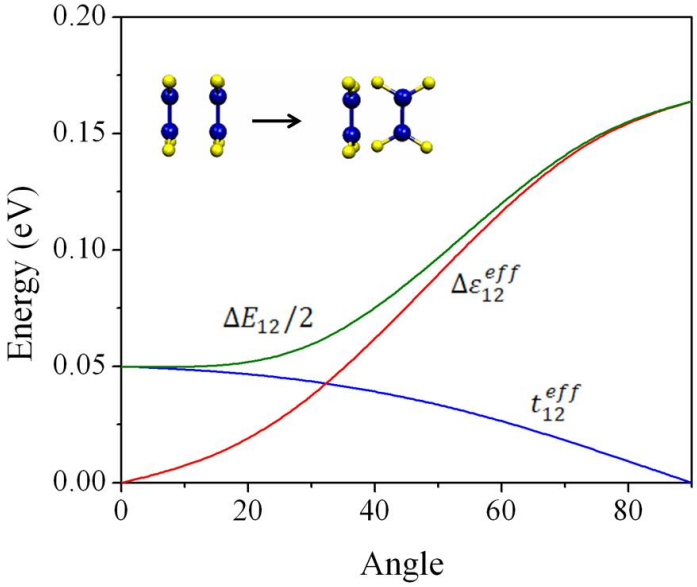

Figure 3.4 Evolution of the transfer integral and site energy difference as a function of the tilt angle in the ethylene dimer at an intermolecular separation of 5.0 Å.

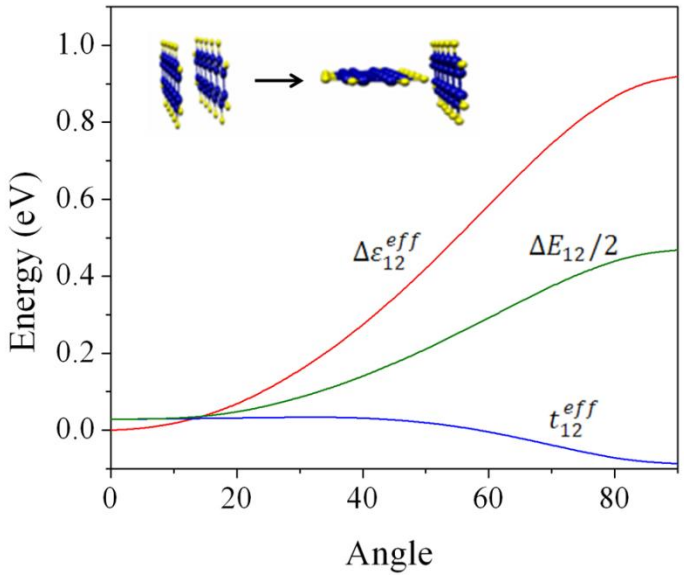

Figure 3.5 Evolution of the transfer integral and site energy difference as a function of the the tilt angle in the pentacene dimer at an intermolecular separation of 5.0 Å.

The significant polarization-induced energetic splitting (which results from site energy difference) between the HOMO levels in the face-to-edge dimers of these nonpolar species should not be surprising. A simple rationalization is that the positively charged hydrogens of the edge molecule lower the energy of the mainly π-type HOMO of the face molecule. This hypothesis was tested through calculations of orbital energies of each ethylene in the dimer where the other molecule was represented by point charges derived from the monomer calculation.[131] The site energies estimated in this way along with those derived from the quantum-mechanical (QM) calculations (using Equation 3.16) of the dimer are compared in Figure 3.6. The site energy of the face molecule decreases with the tilt, while the site energy of the edge molecule remains mostly constant. Although the values of the site energies computed with the two methods differ to some extent, the qualitative behaviors are similar. The good agreement between QM and QM/electrostatic results underscores the mainly classical origin of site energy difference.

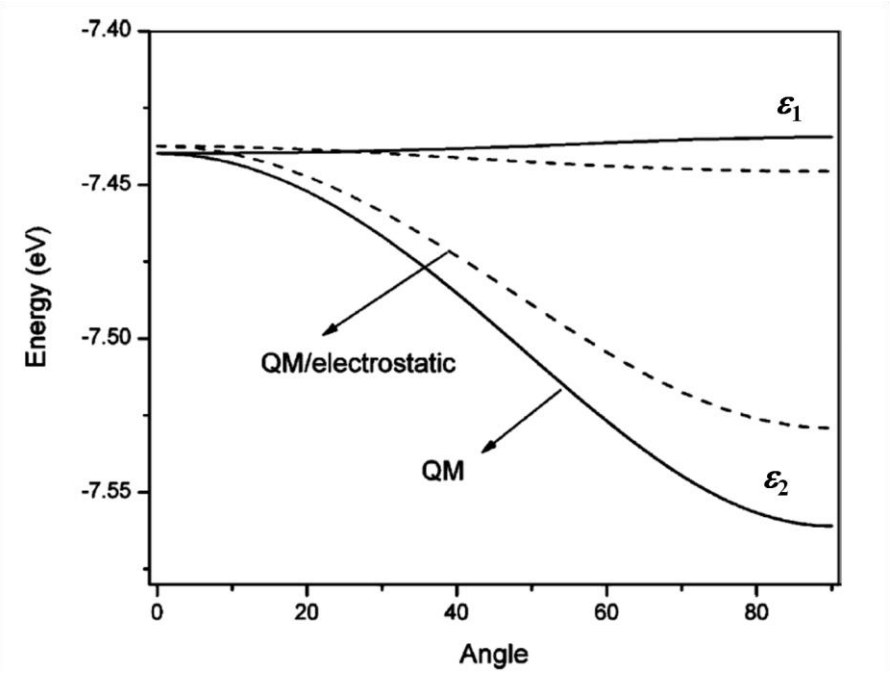

Figure 3.6 Comparison of site energies in the ethylene dimer derived from quantum-mechanical (QM) and mixed QM/electrostatic calculations.

The site energy difference decreases exponentially as the intermolecular separation (R) between the two molecules in the dimer increases. For instance, Figure 3.7 shows the dependence of the site energy difference to R in the ethylene perpendicular (face-to-edge) dimer, where the site energy difference vanishes as the two molecules are pulled apart as a result of the weak electrostatic interactions at large intermolecular distances.

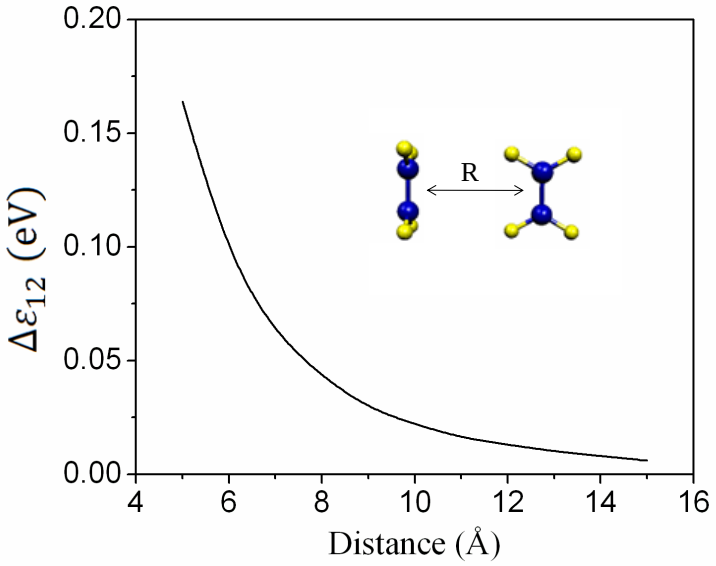

Figure 3.7 Evolution of the site energy difference as a function of the intermolecular separation (R) in the ethylene perpendicular dimer.

Additionally, INDO- and DFT-calculated transfer integrals as a function of the tilt angle in the ethylene dimer with a fixed intermolecular separation of 5.0 Å are compared in Figure 3.8. INDO predicts an evolution of the transfer integrals with the tilt angle, similar to the DFT evolution. The transfer integral gradually decreases from its maximum value at the cofacial orientation to exactly zero at the face-to-edge configuration. However, as Figure 3.8 suggests, INDO underestimates the transfer integrals as compared to the DFT values.

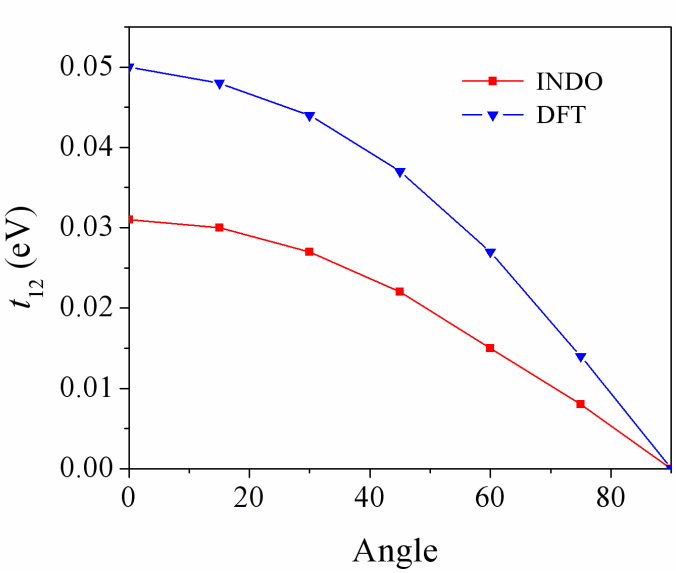

Figure 3.8 Comparison of the INDO- and DFT-calculated transfer integrals (without taking into account the sign) as a function of the tilt angle in the ethylene dimer.

In our next example, we have studied the dependence of t_{12}^{eff} as a function of the center-to-center distance, R. Figure 3.9 compares the charge transfer parameters of the pentacene cofacial dimer with that of the tilted dimer as encountered in the pentacene crystal. As is evident from Figure 3.9, for all considered distances, the electronic coupling derived for a cofacial dimer is larger than that in the tilted dimer. In both cases, t_{12}^{eff} exhibits the same exponential dependence on intermolecular distance. This result is not surprising since the electronic coupling is driven by the orbital overlap, which decays exponentially with distance regardless of the monomer-monomer orientation. For the cofacial dimer, the estimates of t_{12}^{eff} based on Equation 3.17 and on the energy splitting method are identical. In contrast, in the case of the tilted dimer, the energy splitting method overestimates the coupling. In addition, the energy splitting approach in general would predict a qualitatively incorrect dependence of t_{12}^{eff} on R. This failure is due to the fact that for R larger than 5-6 Å, the dimer level energy splitting term is dominated by site energy difference; due to its electrostatic nature, this contribution decays with R much more slowly than the overlap and, consequently, the transfer integral.

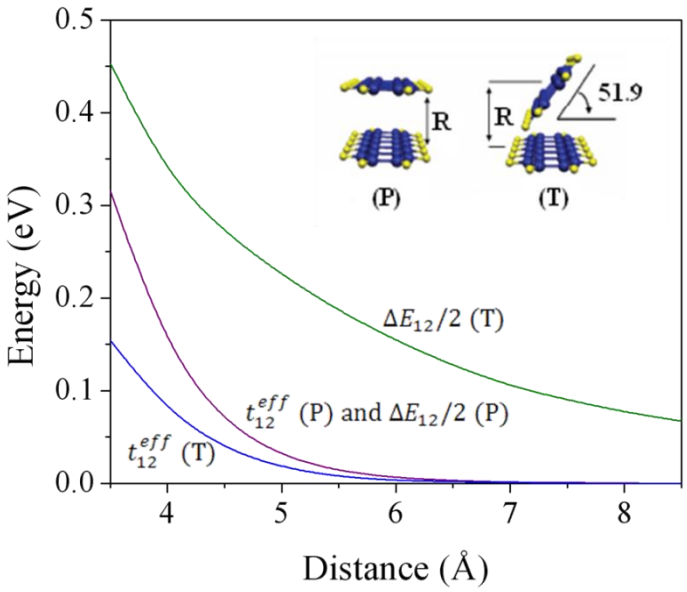

Figure 3.9 Evolution of the effective transfer integral as a function of the intermolecular center-to-center distance (R) of the cofacial (P) and tilted (T) dimers computed by means of Equation 3.17 and dimer energy splitting approach ($\Delta E_{12}/2$). The two approaches are equivalent for the cofacial dimer, but differ qualitatively for the tilted dimer.

The evolution of the transfer integral as a function of intermolecular distance in pentacene cofacial and tilted dimers was also investigated at the INDO level and similar trends have been observed. Transfer integrals decay exponentially with distance, and for all considered distances the transfer integral of the cofacial dimer is larger than that of the tilted dimer in accordance with the DFT results.

As mentioned earlier, a recent study of charge transport in a series of oligoheterocycle-based molecular systems[126] presents a significant enhancement of dimer energy splitting upon going from the cofacial to the perpendicular orientation. The enhancement in the energy splitting upon increase in the tilt angle was explained by the increase in overlap (and thus transfer integral) resulting from the reduction of the nearest-contact intermolecular distance. However, as we show in our next example, the enhancement of ΔE_{12} is due to an increase in the polarization-driven site energy splitting and has little to do with the transfer integral. Figure 3.11 shows the evolution of the

transfer integral and site energy difference as a function of the tilt angle in oligoheterocycles (chemical structures are shown in Figure 3.10) at a fixed intermolecular distance of 5.0 Å. As Figure 3.11 suggests, the transfer integral is nearly zero at all configurations. On the contrary, the site energy difference gradually increases with the tilt angle from its minumum value at the cofacial orientation to its maximum value (~0.6 eV) when the system reaches the face-to-edge configuration. Therefore, $\Delta\varepsilon_{12}^{eff}$ is the only contribution to the energy splitting, ΔE_{12}. Furthermore, the evolution of the charge transfer parameters in oligoheterocycles has been analyzed as a function of the tilt angle at fixed intermolecular distances of 6.5 and 8.0 Å. Figure 3.12 shows the evolution of the transfer integral and site energy difference for the terthiophene dimer as a function of the tilt angle at fixed intermolecular distances of 6.5 and 8.0 Å. At these large intermolecular separations, the transfer integral is zero in all orientations. In contrast, $\Delta\varepsilon_{12}^{eff}$ increases with the tilt angle, reaching its maximum value (~0.3/0.2 eV at 6.5/8.0 Å) at the face-to-edge configuration. As a result, $\Delta\varepsilon_{12}^{eff}$ is the one and only contribution to ΔE_{12}. We note again that the site energy difference decreases at increased intermolecular separations of 6.5 and 8.0 Å due to the decrease in electrostatic interactions at large distances.

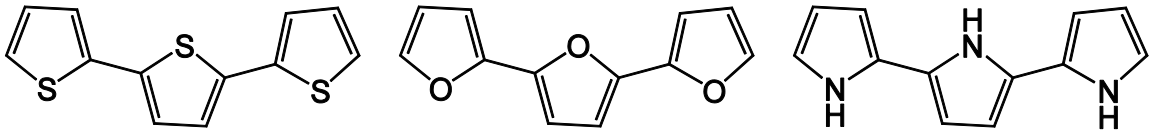

(a) **(b)** **(c)**

Figure 3.10 Chemical structures of the oligoheterocycles: (a) terthiophene, (b) terfuran, and (c) terpyrrole.

The intermolecular separations considered here yield almost identical trends for the computed charge-transport parameters as a function of the heteroatom identity and oligomer length. For instance, the same general trends are also observed for the

homologues tetraheterocycles. The similarity in charge-transport parameters as a function of the heteroatom identity is consistent with the HOMO composition which does not include appreciable heteroatom population in these systems. On the other hand, the similarity of charge-transport parameters for extended dimensions of oligomers is contrary to the known effect of chain length on the intermolecular interactions. At smaller separations (3.5-4.0 Å), the intermolecular interactions are found to decrease with increasing chain length.[85] However, the intermolecular separations considered here (>5 Å) might be too large to capture the dependence of the charge-transport parameters on the oligomer length.

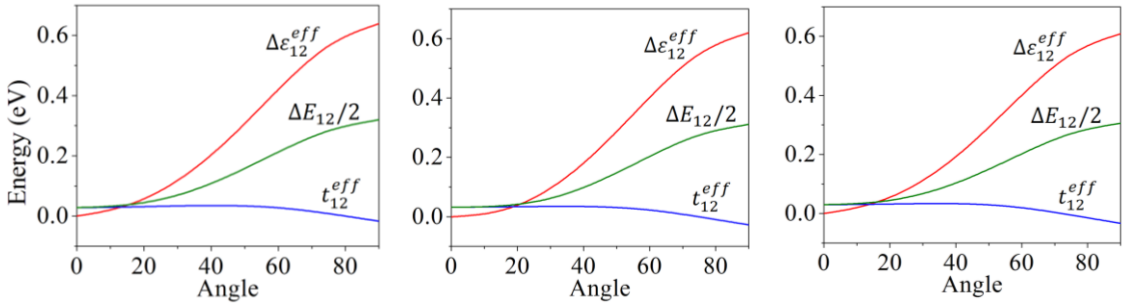

Figure 3.11 Evolution of the transfer integral and site energy difference as a function of the tilt angle for (a) terthiophene, (b) terpyrrole, and (c) terfuran dimers at a fixed intermolecular distance of 5.0 Å.

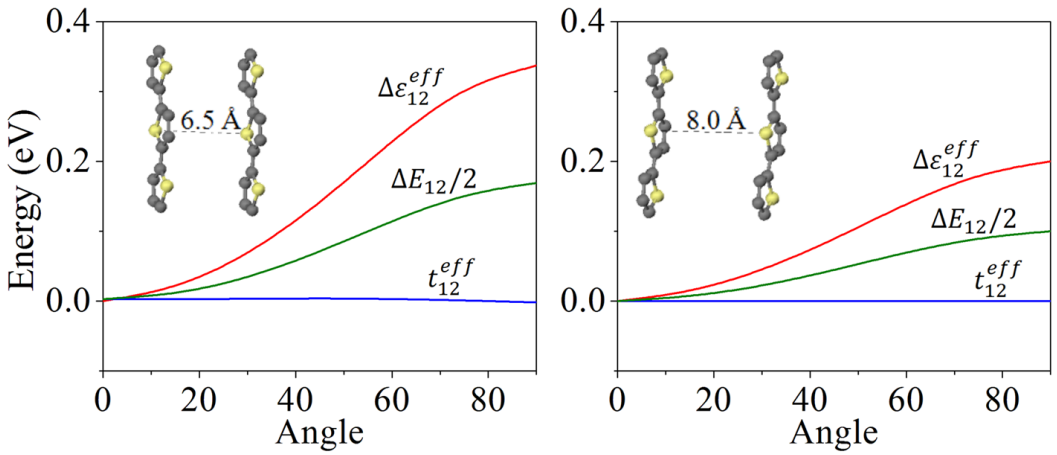

Figure 3.12 Evolution of the transfer integral and site energy difference as a function of the tilt angle for terthiophene dimer at a fixed intermolecular distance of 6.5 (left) and 8.0 Å (right).

Fused Thiophenes

We now turn our attention to real crystal structures to further illustrate the effect of electronic polarization and thus site-energy splitting on the charge-transport parameters of organic semiconductors. The systems of interest consist of oligothiophenes presenting striking differences in their solid-state properties. Oligothiophenes generally pack in the herringbone motif in the solid state, an arrangement that does not optimize π-π overlap between adjacent molecules. However, it was recently found that moving from single-bonded thiophene units toward fully fused thienoacenes changes the packing from herringbone to face-to-face π-stacking.[132] For instance, β-linked oligothiophene containing fused thiophene units – thieno[3,2-*b*]thiophene – showed marked differences in its solid state packing.[133] It reveals a nearly planar molecular conformation with a packing arrangement consisting of edge-to-face π-stacked dimers (sandwich-herringbone packing shown in Figure 3.13). Due to the significant π-π interactions present in the solid state of this fused thiophene compound, it is an attractive system to illustrate the important effect of polarization-induced site-energy splitting on the charge-transport parameters of organic crystals.

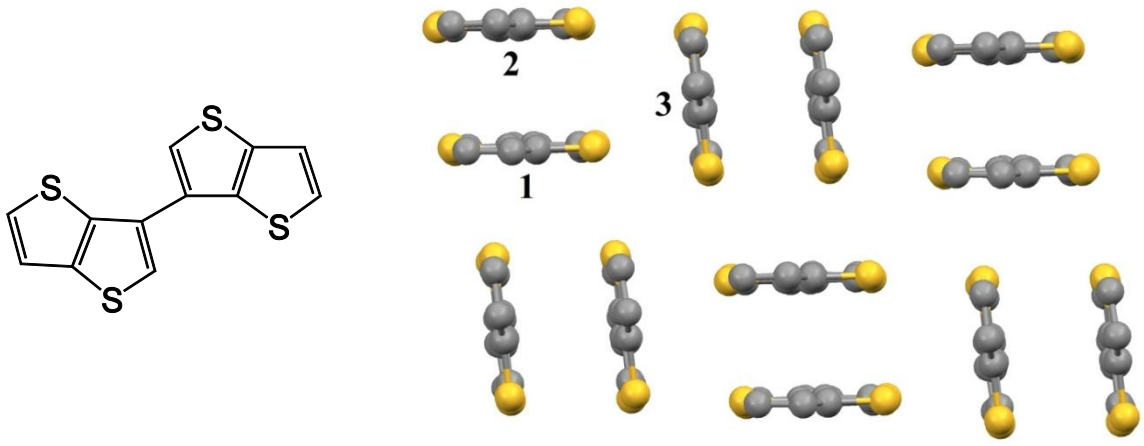

Figure 3.13 Chemical structure (left) and crystal packing (right) of thieno[3,2-*b*]thiophene molecule. Note the parallel (dimer 1-2), herringbone (dimer 2-3), and T-shaped (dimer 1-3) arrangements of the molecules in the crystal (H's are not shown for clarity purposes).

Table 3.1 gathers the charge-transport parameters for the cofacial and face-to-edge dimers of the thieno[3,2-*b*]thiophene extracted from its crystal structure. As it is seen from Table 3.1, $\Delta\varepsilon_{12}^{eff}$ is zero for the symmetric parallel dimer 1-2, and therefore the transfer integral is equal to the half of the energy splitting, ΔE_{12}. In the case of the herringbone and T-shaped dimers (2-3 and 1-3, respectively), the monomers are no longer equivalent by symmetry and polarize each other differently, resulting in a significant site-energy difference. In this case, using the energy splitting in dimer approach will give incorrect estimates of transfer integrals due to the neglect of this large site energy difference between the molecules. For the herringbone dimer 2-3, the transfer integral calculated using Equation 3.17 is very small (9/7 meV for holes/electrons). This is due to the weak intermolecular π-π interactions, which are critical factors in the determination of the transfer integrals. On the other hand, in this face-to-edge configuration, the electronic polarization caused by the edge molecule on the face molecule causes a very large site energy difference. This large site energy difference is the major contribution to the dimer level energy splitting at this configuration. In the case of T-shaped dimer 1-3, the transfer integral is several times larger than that of the

herringbone dimer 2-3 due to an increase in π-orbital overlap and interaction between the two molecules. For instance, the closest intermolecular S-S distance of 4.5 Å in the herringbone dimer decreases to 3.7 Å in the T-shaped dimer causing enhanced intermolecular interactions. Furthermore, the effect of electronic polarization is more pronounced in the T-shaped dimer 1-3 as compared to the herringbone dimer 2-3 as a result of the increased electrostatic interactions in this configuration. This gives rise to a very large site-energy difference and thus very large dimer energy splitting for the T-shaped dimer. As a conclusion, this example illustrates the importance of the site-energy difference on the dimer level energy splitting. The enhancement of ΔE_{ij} in the face-to-edge (herringbone) configuration is due to the polarization-driven site energy difference, and has little to do with the transfer integral.

Table 3.1 DFT/PW91 calculated charge transfer integrals and energy splitting (in meV) in thieno[3,2-*b*]thiophene dimers extracted from the crystal structure.

Dimers[a]	t_{ij}^{eff}	$\Delta\varepsilon_{ij}^{eff}$	ΔE_{ij}
	Holes		
1-2	-85	0	170
2-3	9	333	334
1-3	53	482	493
	Electrons		
1-2	-92	0	184
2-3	-7	349	349
1-3	-67	471	490

[a]Refer to Figure 3.13 for the labeling of the molecules.

Oligoacenes and Derivatives

In this section, we examine the electronic coupling between the nearest neighbor molecular pairs of the four crystalline oligoacenes (naphthalene, anthracene, tetracene, and pentacene) and rubrene (a tetraphenyl derivative of tetracene) in the framework of

the methodology discussed above. Oligoacenes, in particular tetracene, pentacene and derivatives, are currently of high interest due to their large intrinsic mobilities[134-136] and have been used in the field of organic semiconductors as test systems for charge-transport theories. They generally present the herringbone motif in the solid state. For instance, Figure 3.14 illustrates the herringbone packing of crystalline pentacene and rubrene within the *ab* layer. In the case of pentacene (and tetracene), there are two inequivalent molecules within the layers (labeled as **1** and **3** in Figure 3.14), which have slightly different geometries. This leads to a significant site energy difference between the two molecules.

Table 3.2 Crytallographic parameters for the unit cells of oligoacenes[3,137-139] and rubrene.[37]

Molecule	a[a]	b	C	α[b]	β	γ
Naphthalene	8.10	5.95	8.65	90.00	124.40	90.00
Anthracene	8.41	5.99	11.10	90.00	125.29	90.00
Tetracene	6.06	7.84	13.01	77.13	72.12	85.79
Pentacene	6.28	7.71	14.44	76.75	88.01	84.52
Rubrene	7.18	14.43	26.90	90.00	90.00	90.00

[a] Units in Å. [b] Units in deg.

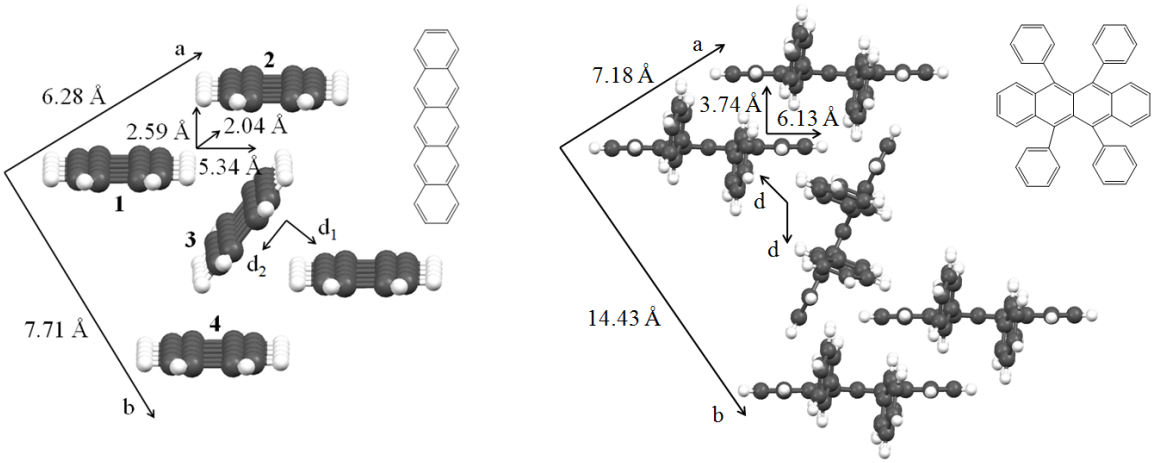

Figure 3.14 Illustration of the crystal packing of pentacene (left) and rubrene (right) within the *ab* layer. The short-axis and long-axis displacements along the π-stacks in the *a*- direction are also indicated. The labeling of the molecules used in the calculations of the transfer integrals is shown on the left.

Here, we have computed the transfer integrals for holes and electrons for dimers extracted from the crystal structure along various crystallographic axes (Table 3.2). The results are summarized in Table 3.3 (we note that the INDO results are generally similar to the DFT values). As seen from Table 3.3, significant intermolecular interactions occur along the diagonal directions within the *ab*-plane (dimers 1-3 and 2-3, in Figure 3.14) and short crystal axis (for naphthalene and anthracene along the *b*-direction; for tetracene, pentacene and rubrene along the *a*-direction). There is simply no interaction between the molecules located in adjacent layers (*i.e.*, along the *c*-axis). These results are in agreement with previous calculations for oligoacene crystals[30,124] and mobility measurements, suggesting two-dimensional transport in oligoacene crystals.[140,141] Furthermore, the evolution of the extent of transfer integrals with respect to the size of oligoacenes, from two rings in naphthalene to five rings in pentacene, indicates that the size of the conjugated π-system and the structure of the crystal are both important factors in determining the strength of the interactions. For example, as Table 3.3 indicates, the intermolecular interactions increase as the chain size of the molecule increases such that

the largest hole transfer integrals of 83 and 85 meV are obtained along the *a*-direction of rubrene and the diagonal direction of pentacene, respectively.

Table 3.3 DFT/PW91 calculated charge transfer integrals (in meV) in oligoacenes.[a]

Dimers	Naphthalene	Anthracene	Tetracene	Pentacene	Rubrene
	Holes				
1-2 (*a*-axis)[b]	0	0	-4/16	37/34	83
1-4 (*b*-axis)	-35	-44	0	0	0
1-3 (*ab*-plane)[c]	-8	-23	-23	-51	15
2-3 (*ab*-plane)[c]	-8	-23	70	85	15
c-axis[d]	0	-1	0	0	0
	Electrons				
1-2 (*a*-axis)[b]	0	1	-13/-32	-45/-43	-41
1-4 (*b*-axis)	14	33	-1	-1	0
1-3 (*ab*-plane)[c]	-38	-61	-65	-82	-7
2-3 (*ab*-plane)[c]	-38	-61	64	81	-7
c-axis[d]	1	-4	0	0	0

[a]The crystal direction along which the coupling takes place is also indicated between parentheses.
[b]Due to the presence of two geometrically inequivalent molecules in the unit cell of tetracene and pentacene, two different electronic coupling values are obtained along the *a*-axis.
[c]The coupling here corresponds to the diagonal directions within the *ab*-plane.
[d]Nearest-neighbor pair along the *c*-direction.

The transfer integrals tabulated in Table 3.3 are calculated according to the basis orthogonalization procedure (Equation 3.17) by taking into account the spatial overlap and site energy difference of the molecules forming the dimer system. It is important to note that the application of the energy splitting in dimer approach to estimate the transfer integrals along the diagonal directions within the *ab*-plane would result in significant errors. For instance, in the case of pentacene, the hole transfer integrals estimated from the energy splitting in the dimer are 310 and 339 meV for dimers 1-3 and 2-3 (along the

diagonal directions), respectively. These values are several times larger than the ones calculated according to Equation 3.17 (51 and 85 meV). The difference is due to the neglect of the spatial overlap and site energy difference between the molecules forming the dimers. Similar consequences of this phenomenon are also observed in recent pentacene calculations where the bandwidth obtained with the overlap neglected is *ca*. 1.5 times larger than that obtained with the overlap and site energy taken into account.[142]

Compared to pentacene (or tetracene), rubrene has bulky side groups resulting in a larger offset and greater separation of the molecular units (see Figure 3.14). The long molecular axes all come out of the *ab*-plane in pentacene (or tetracene) while, in rubrene, they are embedded in that plane due to these bulky side groups. As a consequence, the long molecular axes of adjacent molecules along the diagonal (herringbone) directions are parallel in pentacene, while they are almost perpendicular in rubrene. This explains the smaller transfer integrals along the diagonal directions in rubrene. The largest transfer integrals of rubrene are calculated along the crystal *a*-direction, where the molecules are found to form π-stacks with an intermolecular separation of 3.74 Å. While this distance is larger than the typical π-stacking distances (recall that electronic coupling depends exponentially on the intermolecular distance, as illustrated in Figure 3.9), a striking feature is that there are no short-axis displacements along the *a*-direction in rubrene. On the other hand, the bulky phenyl side groups cause a very large sliding of 6.13 Å along the long molecular axis. Such long-axis displacements are known to reduce the electronic coupling between adjacent molecules. However, in the case of rubrene, this large long-axis sliding coincides with extrema in the evolution of the transfer integrals upon sliding. This trend is illustrated in Figure 3.15 where the calculated transfer integral reaches a near-maximum for holes at a displacement of 6.13 Å observed in the rubrene single crystal. Such subtleties suggest that lateral displacements are key considerations in determining the transfer integrals when two molecules are in cofacial or near-cofacial configurations.

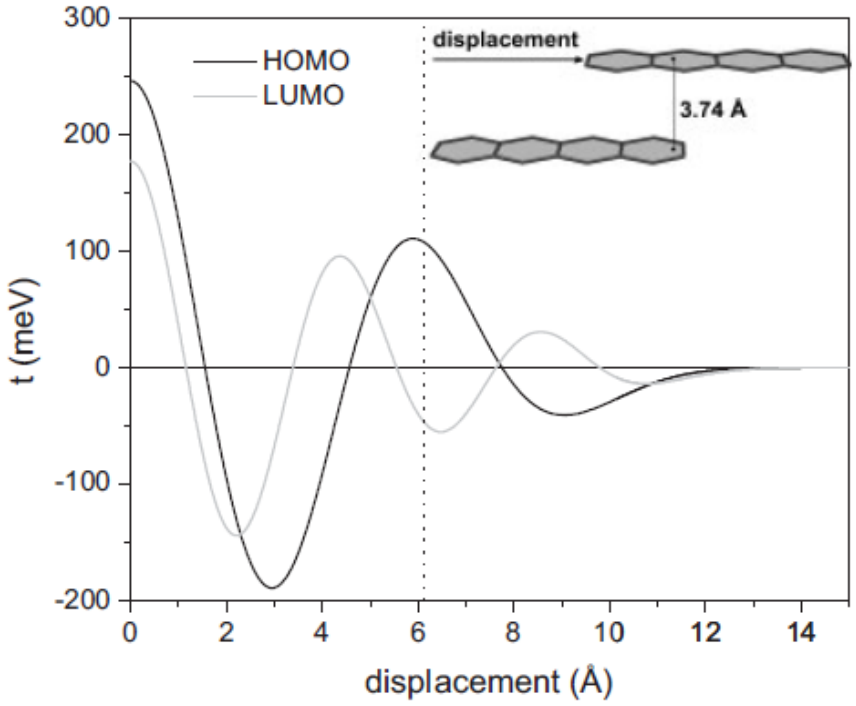

Figure 3.15 Evolution of the transfer integral as a function of the displacement for the core tetracene units of rubrene at the intermolecular spacing seen in the crystal arrangement.[37] Figure adapted from Ref. 35.

Lastly, the case of rubrene illustrates how the careful study of materials with similar functionality, but different molecular packing characteristics, reveals variations of electronic interactions in the crystal. For instance, as shown in Figure 3.14, the orientation of rubrene molecules is quite different along each crystal axis, suggesting anisotropic electronic behavior. This is indeed seen in the anisotropy of the calculated transfer integrals for holes and electrons such that smaller transfer integrals are found along the diagonal direction rather than the *a*-direction, in agreement with the experimental findings that show a strong anisotropy of the mobility within the herringbone planes of rubrene.[28]

Pentacene Polymorphs

As we have mentioned earlier, the carrier mobility is affected by various factors, including structural properties such as solid-state packing and thin-film morphology. For instance, it was shown that pentacene, one of the most studied and promising organic semiconductors, crystallizes in different phases depending on growth conditions and film thickness.[139,143,144] At least four pentacene crystalline polymorphs have been reported in the literature.[143] Recent studies on pentacene monolayers[145] indicate that this variety is even larger. The electronic, optical, and transport properties of different morphologies, despite similar geometric parameters, vary significantly.[142,146]

Table 3.4 Crytallographic parameters for the unit cells of pentacene polymorphs.[139,143,147]

Polymorph	a[a]	B	c	α[b]	β	γ
I	6.28	7.71	14.44	76.75	88.01	84.52
II	6.26	7.79	14.51	76.65	87.50	84.61
III	6.27	7.78	14.53	76.47	87.68	84.68
IV	6.24	7.64	14.33	76.98	88.14	84.42

[a] Units in Å. [b] Units in deg.

As a result, we considered interesting to perform a structure-property study on the four pentacene polymorphs to illustrate the impact of morphology on the transport parameters. The pentacene polymorphs investigated here all pack in a herringbone fashion within the *ab*-plane. We calculated the charge transfer integrals for the nearest neighbor molecular pairs extracted from the crystal structure (Table 3.4). As can be seen from Table 3.5, the transfer integrals practically coincide for all polymorphs suggesting similar charge mobility behavior.

Table 3.5 DFT/PW91 calculated charge transfer integrals (in meV) in pentacene polymorphs I-IV.

Dimers[a]	I	II	III	IV
	Holes			
1-2 (*a*-axis)	34	34	31	36
1-4 (*b*-axis)	0	0	0	0
1-3 (*ab*-plane)[b]	-51	-45	-46	-54
2-3 (*ab*-plane)[b]	85	77	79	91
	Electrons			
1-2 (*a*-axis)	-43	-46	-39	-45
1-4 (*b*-axis)	-1	-1	-1	-1
1-3 (*ab*-plane)[b]	-82	-75	-78	-88
2-3 (*ab*-plane)[b]	81	77	-76	86

[a]The labeling of the molecules is shown in Figure 3.14.
[b]The coupling here corresponds to the diagonal directions within the *ab*-plane.

Cluster Approach *vs*. Dimer Approach

It is clear that the parameters obtained from dimer calculations might be of limited usefulness for explaining charge transfer in larger systems, such as thin films or crystals, because the polarization in the dimer might not reflect the polarization in the larger structure. The straightforward way to describe larger structures is to use the Hamiltonian of the full (infinite) system. Such a Hamiltonian, however, can only be computed for a periodic system. We thus approximate the full system by a small subset M. In this case, Equations 3.10 and 3.11 become:

$$\varepsilon_{1(2)} = \left\langle \psi_{1(2)} \middle| H_M \middle| \psi_{1(2)} \right\rangle \tag{3.19}$$

$$t_{12} = \left\langle \psi_1 \middle| H_M \middle| \psi_2 \right\rangle \tag{3.20}$$

For a reliable description of the local electrostatic fields when computing the site energies and the transfer integral between two given sites (1 and 2), the subset M must include the sites of interest as well as at least all nearest neighbors.

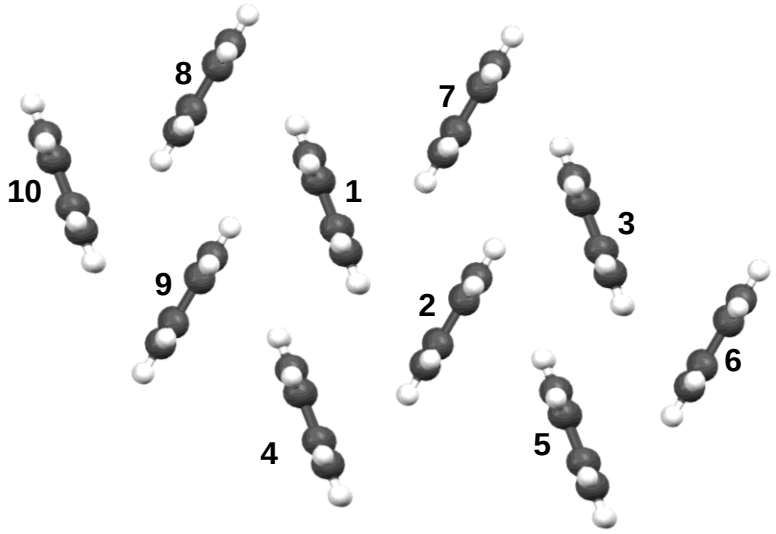

Figure 3.16 The 10-monomer fragment of a pentacene crystal used to mimic the actual crystal environment of molecules **1** and **2**.

As an illustration, we examined polarization effects in a two-dimensional layer found in the pentacene crystal.[139] This structure contains two molecules per "unit cell", labeled **1** and **2**. Polarization-driven site energy splitting is therefore expected. The 10-monomer fragment, shown in Figure 3.16, was chosen as a suitable approximation to the full crystal environment of molecules **1** and **2**. The target molecules **1** and **2** in this cluster have four nearest neighbors, thus each of them experiences four face-to-edge interactions. These interactions should result in a significant site-energy splitting in dimers. For all four interactions, the dimer splittings ($\Delta\varepsilon_{12}^{eff}$) are 0.385 eV, within 1 meV of each other. The important consequence of this is a near complete cancellation of the polarization effects of the four face-to-edge interactions giving a net result of $\Delta\varepsilon_{12}^{eff}$ = 0.034 eV between molecules **1** and **2**, which is an order of magnitude smaller than that in the isolated dimer of **1** and **2**. The main conclusion is that the site energies of the two types of

molecules are nearly identical in the pentacene crystal. The transfer integrals calculated for the isolated and embedded dimers practically coincide.

Our results suggest that, depending on the exact topology, the site-energy difference obtained for an isolated dimer can build up or cancel in the crystal. Thus, any deformation of the crystal could significantly affect both the transfer integral and site-energy difference. This aspect should be properly taken into account in any modeling of the charge-transport properties.

Basis Set Effects

In this section, we investigate the dependence of the charge-transport parameters (site energies and transfer integrals) on the level of theory (such as INDO and DFT) and various basis sets. The motivation has come from the search of a starting point to theoretically evaluate the transport properties of organic molecular materials.

To start with, we compare the performance of INDO with that of DFT in estimating charge transfer integrals. We have already shown that both methods predict similar variations of intermolecular charge-transfer integrals as a function of the tilt angle (see Figure 3.8). Here, we further illustrate these variations with the example of a pentacene cofacial dimer where the transfer integrals are evaluated as a function of intermolecular center-to-center distance. As seen from Figure 3.17, INDO and DFT predict similar trends for the evolution of the transfer integrals as a function of the intermolecular center-to-center distance. The exponential dependence of the transfer integrals on intermolecular separation is verified by both methods. However, it is important to emphasize that although INDO predicts similar variations of transfer integrals with molecular parameters such as twist angles or molecular separations, the values obtained from INDO do not match those obtained from DFT.

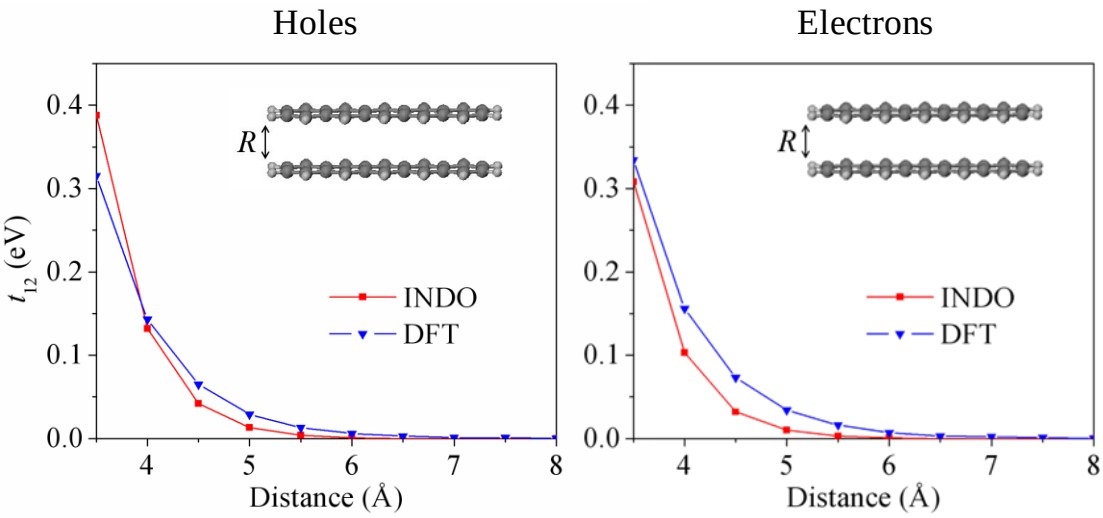

Figure 3.17 Evolution of the INDO- and DFT-calculated transfer integrals for hole (left) and electron (right) transport in the pentacene cofacial dimer as a function of the intermolecular center-to-center distance (R).

Furthermore, we investigated the basis set dependence of the charge-transport parameters in ethylene and pentacene cofacial and perpendicular dimers. The perpendicular dimers are good model systems to illustrate the dependence of the site energy on the basis set choice. Table 3.6 summarizes the charge-transport parameters calculated at various level of theory for a perpendicular pentacene dimer with a fixed intermolecular separation of 5.0 Å. One striking result is that the orbital energy splitting and site energy difference depend significantly on the computational method used. The energy values can vary by as much as a factor of 2 with different basis sets. However, importantly, regardless of these variations in site energies or dimer orbital splittings, transfer integrals do not show any considerable variation with the method used. Transfer integrals calculated by using small basis sets, *e.g.*, TZP, or very large basis sets, *e.g.*, ET-pVQZ, turned out to be similar. At this point, it is important to stress that these results validate the use of TZP basis set throughout this work.

Table 3.6 DFT calculated charge-transport parameters[a] (in meV) in pentacene perpendicular model dimer at various levels of theory.

Level of theory	$E^{HOMO} - E^{HOMO-1}$	$\Delta\varepsilon_{12}^{eff}$	Δt_{12}^{eff}
PW91/DZ	622	600	-82
PW91/DZP	635	610	-85
PW91/TZP	937	919	-87
PW91/TZ2P	867	847	-87
BLYP/TZP	930	912	-89
BLYP/ET-pVQZ	576	546	-88

[a]Charge-transport parameters of holes only are shown.

It is interesting to note that a previous basis set dependence study of intermolecular charge transfer integrals has suggested that the transfer integrals are sensitive to the basis sets used. In addition, the dependence of transfer integrals on the level of theory (such as as INDO, DFT, HF, or post-HF) was found to be very significant.[94] Actually, these conclusions come from the application of the dimer approach where the transfer integrals are estimated from the splitting of the dimer orbital energy levels. As we have shown above, the dimer energy splitting is very sensitive to the level of theory. Therefore, it is not surprising to find significant basis set dependence of transfer integrals upon application of the dimer approach.

Conclusions

Our key finding is that failure to account for polarization effects can impact the computed charge-transport parameters of even nonpolar materials, *e.g.*, pentacene, in a dramatic fashion. Since the polarization effect in these systems is largely electrostatic in nature, it can change dramatically upon transition from a dimer to an extended system. In ethylene and pentacene dimers, polarization is the greatest contributor to the site-energy splitting in the "face-to-edge" structures. Such face-to-edge interactions are present in the

herringbone-type motifs commonly found in organic materials of interest such as oligoacenes or oligothiophenes. To describe the electronic structure of such materials, the effective one-particle Hamiltonian must explicitly take into account the polarization effects. We here presented a straightforward method to include these effects in a tight-binding Hamiltonian. Similar examples of significant polarization effects on site energies are likely to occur in other materials.[129]

Our results also indicate that the energy splitting between the dimer HOMO and HOMO-1 levels could contain a significant contribution from the polarization-induced site-energy difference, even in the case of chemically identical (but symmetry-distinct) monomers (*e.g.*, a tilted dimer). In this case, as we have shown for ethylene and pentacene dimers, the dimer energy splitting approach significantly overestimates the transfer integral. We have also shown that the problems arising from the energy splitting approach can be avoided by computing the transfer integrals directly in terms of the properly orthogonalized monomer orbitals (Equation 3.17). Our calculations indicate that the transfer integrals calculated in this way for isolated dimers and for dimers embedded in a crystal environment practically coincide. In contrast to the evolution of the site energy difference, the polarization effects have little impact on the transfer integrals.

Finally, as we illustrated with several examples, the magnitude of the transfer integrals depend strongly on the intermolecular overlap of electronic wavefunctions, which is extremely sensitive to the intermolecular packing geometry and intermolecular distance in the crystal. The exponential distance dependence of the transfer integrals is verified by both semiempirical INDO and DFT methods. The calculated effective transfer integrals are found to be largely insensitive to the functional and basis set used.

CHAPTER 4

CHARGE-TRANSPORT PARAMETERS OF TETRACENE DERIVATIVES AND FUSED HETEROCYCLIC OLIGOMERS

In this chapter, we discuss the charge-transport properties of two classes of molecules for OFET applications. The first set of molecules includes alkyl or alkoxy-substituted partially fluorinated tetracene derivatives that show significant π-stacking motifs in their crystal lattices. The second set consists of extended versions of fused thiophene-pyrrole oligomers. In contrast to tetracene derivatives, the crystal structures of these fused thiophene-pyrrole systems are not available. However, as we showed in the previous chapter, there is evidence from the crystal structures of fused thiophene compounds that fused-ring oligomers tend to form π-stacking arrangements.

Charge-Transport Parameters of Functionalized Tetracenes

As we mentioned earlier, oligoacenes such as tetracene and pentacene derivatives are appealing as active components in (opto)electronic devices due to their high mobilities.[28,145,148] For instance, the hole mobility in pentacene is consistently measured to be higher than 1 cm^2/Vs.[33,148] Unfortunately, pentacene lacks oxidative stability and solubility.[149] In addition, its herringbone packing in the solid state limits molecular orbital overlap between adjacent molecules, limiting charge transport. Therefore, many attempts have been made to improve the solubility and stability of pentacene as well as to design oligoacene derivatives with enhanced carrier mobilities by avoiding the herringbone motif in the solid state. For instance, Anthony and co-workers synthesized soluble and oxidatively stable pentacene derivatives through functionalization with bulky triisopropylsilylethynyl groups (TIPS pentacene).[56] In addition to soluble and stable functionalized pentacenes, they functionalized higher acenes such as hexacene and heptacene by applying the silylethynylation method and achieved control over crystal

packing and thus the electronic properties of the crystals.[57] Similarly, silylethynyl-functionalized fused acenedithiophenes showed increased solubility and stability as well as improved solid-state ordering.[58] Janzen *et al*. avoided the herringbone motif in oligothiophenes by substitution via quinodimethane and introduced π-stacking in oligothiophenes to get high carrier mobility in devices.[150] More recently, Swager *et al*. synthesized soluble and π-stacking tetracene derivatives.[61] They introduced long alkyl/alkoxy chains to tetracene in order to impart solubility and applied partial fluorination to overcome the herringbone packing in the solid state. It is also known that introduction of long alkyl/alkoxy side chains affects the field-effect carrier mobility.[151]

On the other hand, fluorine has been extensively used to tune the structural and electronic properties of organic semiconductors.[59,61,73,152-157] For instance, it was shown that partial fluorination enhances crystallization and stability of soluble anthradithiophene semiconductors.[59] It was also demonstrated that partial fluorination eliminates herringbone packing in tetracyclic aromatic compounds and leads to enhanced face-to-face π-stacking in an alternating manner.[155] The reason for enhanced π-overlap in partially fluorinated compounds is that they tend to stack face-to-face with the electron-deficient rings facing the electron-rich rings in a head-to-tail fashion. This arene-perfluoroarene interaction arises from electrostatic attraction between adjacent molecules and is seen in a broad range of chemical and biological systems.[158,159] Partial fluorination is also known to affect the interplanar spacing between adjacent molecules in the π-stack. For instance, it is well established that silylethynyl-functionalized fluorinated pentacenes adopt two-dimensional π-stacked arrangements similar to that of their nonfluorinated analogue; in addition, they have smaller intermolecular separation between molecules due to the strong interaction between the π-surfaces of the fluorinated and non-fluorinated rings.[154] Furthermore, field-effect mobility in the fluorinated pentacenes scales with the intermolecular separation which is in turn controlled by the degree of fluorination.[154] It

was theoretically shown that the electronic coupling and thus the charge-carrier mobility strongly depend on the spacing between the aromatic faces of the interacting units.[85]

The incorporation of both donor and acceptor substituents into the main chain of π-stacking tetracene derivatives also induces a strong dipole moment.[61] Strong dipole-dipole interactions between neighboring molecules afford π-stacking with short intermolecular distances and self-assembly in thin-film transistors.[160] For instance, end-functionalization of pentacene with the 1,4-quinone moiety on one side imparts a static dipole moment to pentacene and leads to antiparallel cofacial π-stacks with aromatic planes that are very closely spaced (<3.25 Å). We note that this π-π separation is even closer than the π-π distance in graphite sheets (3.35 Å).[160]

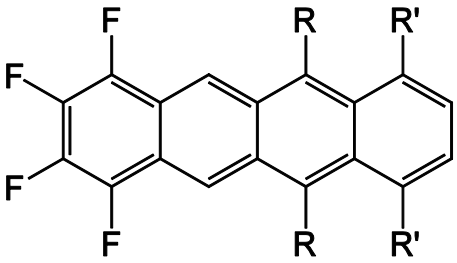

FTETa: R = H, R' = OC_6H_{13}
FTETb: R = OC_6H_{13}, R' = H
FTETc: R = H, R' = C_8H_{17}
FTETd: R = C_8H_{17}, R' = H

TET

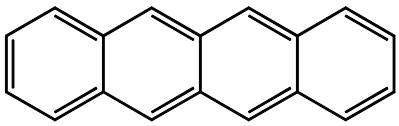

FTET

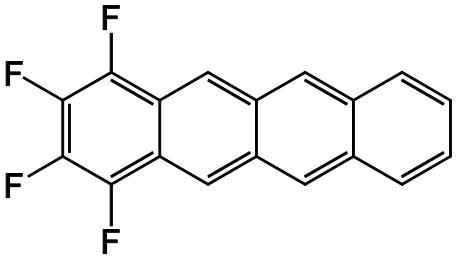

Figure 4.1 General chemical structures of the tetracenes examined in this study with the notation used throughout the text: fluorine- and alkyl/alkoxy-functionalized tetracene derivatives (**FTETa-d**), tetracene (**TET**), and partially fluorinated tetracene (**FTET**).

In our work, we investigated the effect of crystal packing on the charge-transport parameters of the fluorine- and alkyl/alkoxy-functionalized π-stacking tetracene derivatives **FTETa-d** shown in Figure 4.1. In order to gain a better understanding of the

role of partial fluorination and alkyl/alkoxy functionalization, the results of the donor/acceptor substituted tetracenes **FTETa-d** were compared with those of unsubstituted tetracene (**TET**) and partially fluorinated tetracene (**FTET**). The substituents on tetracene affect the solid-state packing and thus the charge carrier mobility in these systems. The functionalized molecules stack in a slipped cofacial manner. Molecules **FTETa**, **FTETb**, and **FTETd** form antiparallel π-stacks with the electron-rich ring (alkyl/alkoxy-substituted ring) facing the electron-poor ring (fluorinated ring), highlighting the arene-perfluoroarene interactions in the crystal. Furthermore, they pack in an alternating way with two π-stacking distances. On the other hand, **FTETc** forms parallel π-stacks in its crystal with a single π-stacking distance. Alternating π-stacking distances and antiparallel cofacial arrangements are also observed in quinodimethane oligothiophene crystals.[150]

Geometric Structure

The geometry optimizations are carried out by replacing the long alkyl/alkoxy groups of tetracene derivatives with methyl/methoxy groups in order to save computational time. Selected bond-lengths for the optimized geometries of the isolated **FTETa-d** molecules in their neutral, radical-anion and radical-cation states are collected in Tables 4.1-4.6. A good agreement is found between the DFT/B3LYP computed bond lengths for the neutral states of **FTETa-d** and their experimental crystal data.[61]

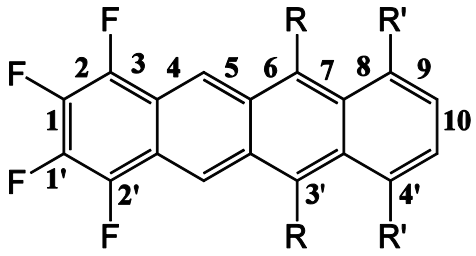

Table 4.1 DFT/B3LYP calculated bond lengths (in Å) in neutral and ionic states of **FTETa**.

Bond	Neutral	Cation	Anion
1	1.427	1.418	1.404
2	1.364	1.377	1.381
3	1.429	1.418	1.415
4	1.391	1.401	1.408
5	1.409	1.402	1.412
6	1.411	1.413	1.408
7	1.389	1.393	1.408
8	1.445	1.437	1.432
9	1.369	1.399	1.380
10	1.431	1.399	1.421
1’	1.339	1.325	1.356
2’	1.345	1.334	1.361
3’	1.084	1.084	1.085
4’	1.366	1.336	1.385

Table 4.2 DFT/B3LYP calculated bond lengths (in Å) in neutral and ionic states of **FTETb**.

Bond	Neutral	Cation	Anion
1	1.428	1.415	1.406
2	1.364	1.381	1.380
3	1.429	1.416	1.415
4	1.390	1.403	1.407
5	1.410	1.401	1.412
6	1.416	1.421	1.410
7	1.399	1.421	1.412
8	1.433	1.417	1.421
9	1.367	1.382	1.384
10	1.429	1.412	1.412
1’	1.338	1.323	1.354
2’	1.345	1.332	1.360
3’	1.380	1.351	1.399
4’	1.084	1.083	1.085

Table 4.3 DFT/B3LYP calculated bond lengths (in Å) in neutral and ionic states of **FTETc**.

Bond	Neutral	Cation	Anion
1	1.428	1.413	1.406
2	1.364	1.383	1.380
3	1.429	1.416	1.415
4	1.391	1.404	1.407
5	1.409	1.403	1.412
6	1.411	1.409	1.408
7	1.393	1.403	1.411
8	1.447	1.433	1.433
9	1.369	1.389	1.385
10	1.426	1.406	1.409
1’	1.338	1.323	1.355
2’	1.345	1.331	1.361
3’	1.085	1.085	1.086
4’	1.508	1.506	1.509

Table 4.4 DFT/B3LYP calculated bond lengths (in Å) in neutral and ionic states of **FTETd**.

Bond	Neutral	Cation	Anion
1	1.428	1.415	1.407
2	1.364	1.382	1.380
3	1.428	1.415	1.415
4	1.390	1.401	1.406
5	1.413	1.407	1.416
6	1.424	1.424	1.418
7	1.405	1.425	1.422
8	1.439	1.421	1.426
9	1.365	1.381	1.383
10	1.424	1.408	1.407
1’	1.339	1.323	1.355
2’	1.346	1.332	1.360
3’	1.513	1.507	1.512
4’	1.082	1.082	1.085

Table 4.5 DFT/B3LYP calculated bond lengths (in Å) in neutral and ionic states of **TET**.

Bond	Neutral	Cation	Anion
1	1.430	1.414	1.412
2	1.367	1.382	1.385
3	1.433	1.419	1.422
4	1.393	1.407	1.409
5	1.410	1.406	1.410
6	1.410	1.406	1.410
7	1.393	1.407	1.409
8	1.433	1.419	1.422
9	1.367	1.382	1.385
10	1.430	1.414	1.412
1’	1.086	1.085	1.088
2’	1.087	1.086	1.089
3’	1.088	1.087	1.089
4’	1.087	1.086	1.089

Table 4.6 DFT/B3LYP calculated bond lengths (in Å) in neutral and ionic states of **FTET**.

Bond	Neutral	Cation	Anion
1	1.428	1.412	1.406
2	1.364	1.385	1.380
3	1.429	1.415	1.416
4	1.390	1.403	1.407
5	1.410	1.405	1.412
6	1.410	1.407	1.407
7	1.393	1.406	1.410
8	1.434	1.419	1.422
9	1.367	1.382	1.384
10	1.430	1.415	1.412
1’	1.338	1.322	1.355
2’	1.345	1.330	1.361
3’	1.087	1.087	1.089
4’	1.087	1.086	1.089

The geometry modifications occurring upon oxidation and reduction in the substituted tetracenes and the parent **TET** and **FTET** molecules are listed in Tables 4.7 and 4.8, respectively. The calculations show that, while most of the geometrical changes upon oxidation/reduction of **TET** take place within the C-C bonds along the whole

molecular periphery, in the case of **FTETa-d** the main geometrical modifications occur on the substituted benzene rings. These results parallel the asymmetry in charge distribution along the tetracene backbone (and resulting molecular dipole moments, see Table 4.9) induced by the incorporation of both electron donating and withdrawing substituents onto the parent molecule. **FTETa** presents the biggest dipole moment in the series (about 6.2 D) and also undergoes the most significant structural changes upon going from the neutral to the cationic state; the largest C-C bond length evolution is around 0.032 Å in **FTETa** and decreases to 0.029 Å for **FTETb** and 0.020 Å for **FTETc** and **FTETd**.

Upon oxidation, the largest geometrical modifications in **FTETa** and **FTETb** occur in the C-O bonds (bonds 4' and 3' for **FTETa** and **FTETb**, respectively). On the other hand, reduction of **FTETa-d** brings the largest C-C bond length changes along the fluorinated ring; significant geometrical evolution of the C-O bonds (0.019 Å) are also observed in the alkoxy side chains of **FTETa** and **FTETb**, although less pronounced than those observed upon oxidation. The C-F bonds present similar geometric relaxations (bonds 1' and 2') upon oxidation and reduction within the **FTETa-d** series and in **FTET**.

Table 4.7 DFT/B3LYP calculated bond length changes (in Å) upon oxidation (going from the neutral to the cation state) in functionalized tetracenes **FTETa-d**, **TET**, and **FTET**.

Bonds	**FTETa**	**FTET b**	**FTETc**	**FTETd**	**TET**	**FTET**
1	-0.009	-0.013	-0.015	-0.013	-0.016	-0.016
2	0.013	0.017	0.019	0.018	0.015	0.021
3	-0.011	-0.013	-0.013	-0.013	-0.014	-0.014
4	0.010	0.013	0.013	0.011	0.014	0.013
5	-0.007	-0.009	-0.006	-0.006	-0.004	-0.005
6	0.002	0.005	-0.002	0.000	-0.004	-0.003
7	0.004	0.022	0.010	0.020	0.014	0.013
8	-0.008	-0.016	-0.014	-0.018	-0.014	-0.015
9	0.030	0.015	0.020	0.016	0.015	0.015
10	-0.032	-0.017	-0.020	-0.016	-0.016	-0.015
1’	-0.014	-0.015	-0.015	-0.016	-0.001	-0.016
2’	-0.011	-0.013	-0.014	-0.014	-0.001	-0.015
3’	0.000	-0.029	0.000	-0.006	-0.001	0.000
4’	-0.030	-0.001	-0.002	0.000	-0.001	-0.001

Table 4.8 DFT/B3LYP calculated bond length changes (in Å) upon reduction (going from the neutral to the anion state) in functionalized tetracenes **FTETa-d**, **TET**, and **FTET**.

Bonds	**FTETa**	**FTETb**	**FTETc**	**FTETd**	**TET**	**FTET**
1	-0.023	-0.022	-0.022	-0.021	-0.018	-0.022
2	0.017	0.016	0.016	0.016	0.018	0.016
3	-0.014	-0.014	-0.014	-0.013	-0.011	-0.013
4	0.017	0.017	0.016	0.016	0.016	0.017
5	0.003	0.002	0.003	0.003	0.000	0.002
6	-0.003	-0.006	-0.003	-0.006	0.000	-0.003
7	0.019	0.013	0.018	0.017	0.016	0.017
8	-0.013	-0.012	-0.014	-0.013	-0.011	-0.012
9	0.011	0.017	0.016	0.018	0.018	0.017
10	-0.010	-0.017	-0.017	-0.017	-0.018	-0.018
1’	0.017	0.016	0.017	0.016	0.002	0.017
2’	0.016	0.015	0.016	0.014	0.002	0.016
3’	0.001	0.019	0.001	-0.001	0.001	0.002
4’	0.019	0.001	0.001	0.003	0.002	0.002

Table 4.9 B3LYP/6-31G(d,p) dipole moments in functionalized tetracenes **FTETa-d** and **FTET**.

Compound	Dipole moment, μ (Debye)
FTETa	6.19
FTETb	3.68
FTETc	3.89
FTETd	3.66
FTET	3.69

Energetics of Ionization

The reorganization energy, λ, measures the strength of the so-called local electron-phonon coupling;[62] the smaller λ, the larger the expected charge mobility. It consists of both intra- and intermolecular contributions; the former reflects the changes in the geometry of individual molecules and the latter in the polarization of the surrounding molecules upon going from the neutral to the charged state and vice versa. Here, we focus on the intramolecular contribution to λ as the nuclear polarization contribution is expected to be significantly smaller.[161] The DFT reorganization energies are collected in Table 4.10. In **FTETa-d**, λ is in the range of 160-270 meV and 200-240 meV for hole-transfer (HT) and electron-transfer (ET) processes, respectively. These values are significantly larger than those for unsubstituted tetracene, **TET** (108 meV for HT and 157 meV for ET). Among the series, the largest reorganization energies are found for the alkoxy-substituted system **FTETa** (267 meV for holes and 242 meV for electrons), which is consistent with the large geometric modifications upon ionization discussed above; **FTETc** has the smallest λ for both HT (159 meV) and ET (208 meV) with values essentially identical to those calculated for **FTET**. The DFT calculations show that the λ values for alkoxy-substituted compounds **FTETa-b** are larger than for alkyl-substituted systems **FTETc-d**; this is consistent with the observed significant geometrical changes in the C-O bonds of the alkoxy side chains upon ionization of **FTETa-b**.

It is interesting to note that, on a relative basis, the substitutions considered here impact the reorganization energy for electron transfer to a much smaller extent than for hole transfer (the increase from **TET** to **FTETa-b** is on the order of 50% in the former case and about 250% in the latter); λ (ET) even becomes slightly smaller than λ (HT) in **FTETa-b**.

Table 4.10 B3LYP/6-31G(d,p) estimates of the reorganization energy λ (in meV) for hole-transfer (HT) and electron-transfer (ET) processes for **FTETa-d**, **TET**, and **FTET**.

Compound	λ (HT)	λ (ET)
FTETa	267	242
FTETb	264	239
FTETc	159	208
FTETd	195	208
TET	108	157
FTET	160	205

Vertical and adiabatic ionization potentials and electron affinities derived from ΔSCF calculations are given in Table 4.11. Upon going from **TET** to **FTET**, the ionization potentials increase by 0.3-0.4 eV. However, further inclusion of alkyl or alkoxy side-chains into **FTET** decreases the ionization potentials by 0.1-0.5 eV with the alkoxy groups having expectedly a larger impact than the alkyl groups; as a result, **FTETc-d** have relatively higher ionization potentials than **FTETa-b**, which is consistent with the electrochemical measurements (the oxidation potentials of **FTETc** and **FTETd** are 0.56 and 0.48 V with respect to a Pt electrode, whereas those for **FTETa** and **FTETb** are 0.31 and 0.44 V, respectively).[61] The electron affinities become more exothermic upon partial fluorination (the **FTET** electron affinity is about 0.4 eV more exothermic than in **TET**) and are reduced with the introduction of the alkyl/alkoxy substituents (except for **FTETb**). Overall, fluorination has a greater impact than alkyl/alkoxy substitution, and tetracenes **FTETa-d** have more exothermic EAs than **TET**. The DFT

results are supported by the electrochemical measurements which show that **FTETa-d** present reduction potentials between -1.84 and -1.92 V with respect to a Pt electrode compared to -2.05 V in **TET**.[61] Thus, in comparison to tetracene, our results suggest that partially fluorinated, alkyl/alkoxy-substituted tetracenes are expected to reduce the electron injection barrier from low work-function electrodes in organic electronic devices.

Table 4.11 B3LYP/6-31G(d,p) calculated first ionization potentials (IPs) and electron affinities (EAs) for **FTETa-d**, **TET**, and **FTET**, as obtained from ΔSCF calculations.

Compound	IP (eV)		EA (eV)	
	Vertical	Adiabatic	Vertical	Adiabatic
FTETa	6.28	6.15	-0.79	-0.91
FTETb	6.47	6.34	-1.01	-1.13
FTETc	6.57	6.49	-0.96	-1.06
FTETd	6.49	6.39	-0.98	-1.09
TET	6.34	6.28	-0.63	-0.71
FTET	6.69	6.61	-1.00	-1.11

The energies of the frontier orbitals are collected in Table 4.12. Partial fluorination stabilizes both the HOMO and LUMO (in a similar way) due to the strong inductive electron withdrawing effect of fluorine. On the other hand, the introduction of alkyl and alkoxy groups to **FTET** results in the destabilization of the frontier molecular orbitals due to the electron donating ability of these side chains. The combination of these effects leads to HOMO and LUMO energies in **FTETa-d** that lie in between those of **TET** and **FTET**. Both the calculated HOMO-LUMO gaps and the TD-DFT energies of the vertical $S_0 \rightarrow S_1$ electronic transitions (which essentially correspond to HOMO-LUMO single excitations) reproduce the decrease in experimental optical transition energy upon donor/acceptor substitution of **TET**. Within the **FTETa-d** series, the TD-

DFT $S_0 \rightarrow S_1$ transition energies provide an excellent agreement with the experimental optical transitions measured from the onset of the UV absorbance spectra; for instance, TD-DFT yields the largest [smallest] optical transition for **FTETc** [**FTETa**] with a value of 2.46 [2.30] eV, which is fully consistent with the experimental value observed at 2.47 [2.25] eV.[61]

Table 4.12 B3LYP/6-31G(d,p) HOMO and LUMO energies along with the experimental optical transition (E_{op}) and computed TD-DFT energies ($E_{TD\text{-}DFT}$) of the $S_0 \rightarrow S_1$ transitions, for **FTETa-d**, **TET**, and **FTET**. All values are given in eV.

Compound	HOMO	LUMO	Δ(HOMO-LUMO)	$E_{TD\text{-}DFT}$[a]	E_{op}[b]
FTETa	-4.89	-2.22	2.67	2.30	2.25
FTETb	-5.06	-2.42	2.64	2.34	2.34
FTETc	-5.16	-2.39	2.77	2.46	2.47
FTETd	-5.07	-2.40	2.67	2.38	2.40
TET	-4.87	-2.09	2.78	2.49	2.57
FTET	-5.23	-2.47	2.76	2.47	-

[a]TD-DFT/B3LYP/6-31G(d,p) vertical $S_0 \rightarrow S_1$ electronic transitions dominated by promotion of an electron from HOMO to LUMO.
[b]Calculated from the onset of UV absorbance spectra measured in CH_2Cl_2 solution (Ref. 61)

Electronic Structure of the Crystals

All fluorinated tetracenes **FTETa-d** crystallize in the triclinic (P-1) space group with the lattice parameters given in Table 4.13. Interestingly, the molecules in all four structures are arranged in π-stacks in a slipped cofacial manner; this is in marked contrast to the herringbone packing motif of the parent tetracene crystal.[162]

The unit cells of **FTETa** and **FTETb** contain two translationally inequivalent molecules and present two alternating intermolecular distances between adjacent molecules along the π-stacks; the two related dimers are labeled in Figure 4.2 as a- and b-type. The intermolecular distances in **FTETa** and **FTETb** are 3.22 and 3.44 Å in the a-dimer, and 3.24 and 3.53 Å in the b-dimer, respectively.[61] It is also interesting to note that in the case of **FTETa** the alkoxy groups appear in a "cis-like" configuration in the a-

dimer (*i.e*., facing each other) and in an "anti" configuration in the b-dimer. As seen from Figure 4.2, **FTETa** and **FTETb** form antiparallel π-stacks in the crystal with the electron-rich ring (alkyl/alkoxy-substituted ring) facing the electron-poor ring (fluorinated ring), which is indicative of arene-perfluoroarene interactions. As a consequence of the different relative intermolecular orientations in the a- and b-type dimers, the corresponding intermolecular wavefunction overlap integrals and the electronic couplings are also markedly different (see Figure 4.2); for instance, in the case of holes for **FTETa**, t_H = 110 meV in a-dimers and 6 meV in b-dimers (note that the electronic-coupling calculations are perfomed with the dimer structures extracted from the crystal structure, *i.e*., with the full alkyl or alkoxy groups).

Table 4.13 Crystallographic parameters for the unit cells of the fluorinated tetracenes **FTETa-d**.[61]

	a[a]	b	c	α[b]	β	γ
FTETa	7.1616	13.2625	13.4547	94.215	100.102	96.192
FTETb	7.547	11.965	14.843	79.330	82.968	79.947
FTETc	4.9461	9.748	28.705	92.905	93.547	92.621
FTETd	7.9507	16.883	22.692	107.104	99.040	102.780

[a]in Å. [b]in deg.

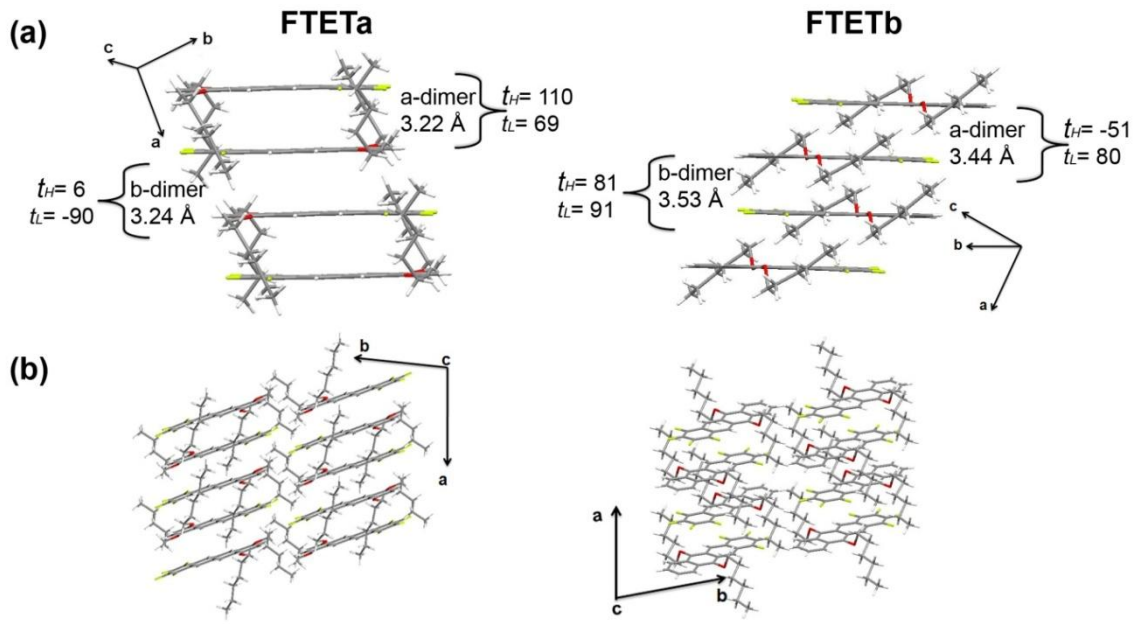

Figure 4.2 (a) Crystal packing (view along the short axis) of **FTETa** (left) and **FTETb** (right) showing the intermolecular distances within the a- and b-type dimers as given in Ref. 61. The DFT-estimates of the transfer integrals (in meV) for holes (t_H) and electrons (t_L) for these molecular pairs are also shown. (b) Crystal structure of **FTETa** (left) and **FTETb** (right) viewed along the *c* direction of the crystal lattice.

FTETc contains two translationally inequivalent molecules per unit cell that give rise to two translationally inequivalent π-stacks. In contrast to **FTETa** and **FTETb** , only one type of dimer is distinguished in the crystal structure with an intermolecular separation of 3.35 Å, see Figure 4.3. We do not observe arene-perfluoroarene interactions since molecules stack in a parallel cofacial fashion; however, we do notice C-F$\cdots\pi_F$ interactions between the electronegative fluorine atoms and the electropositive center of a perfluorinated ring as observed in other perfluorinated aromatic compounds.[159,163] We found larger electronic couplings for holes than for electrons between π-stacked dimers (-106 *vs*. 59 meV), whereas moderate electronic couplings for electrons (32 meV) occur for dimers in adjacent π-stacks along the *b*- direction, see Figure 4.3; thus, charge transport might present more of a two dimensional character in the **FTETc** crystal. Band-structure calculations also imply similar outcomes.[164] The conduction band shows two moderate

dispersions: one along the π-stacking direction (*a*-axis) and the other one across neighboring π-stacks (*b*-axis) (see Figure 4.5).

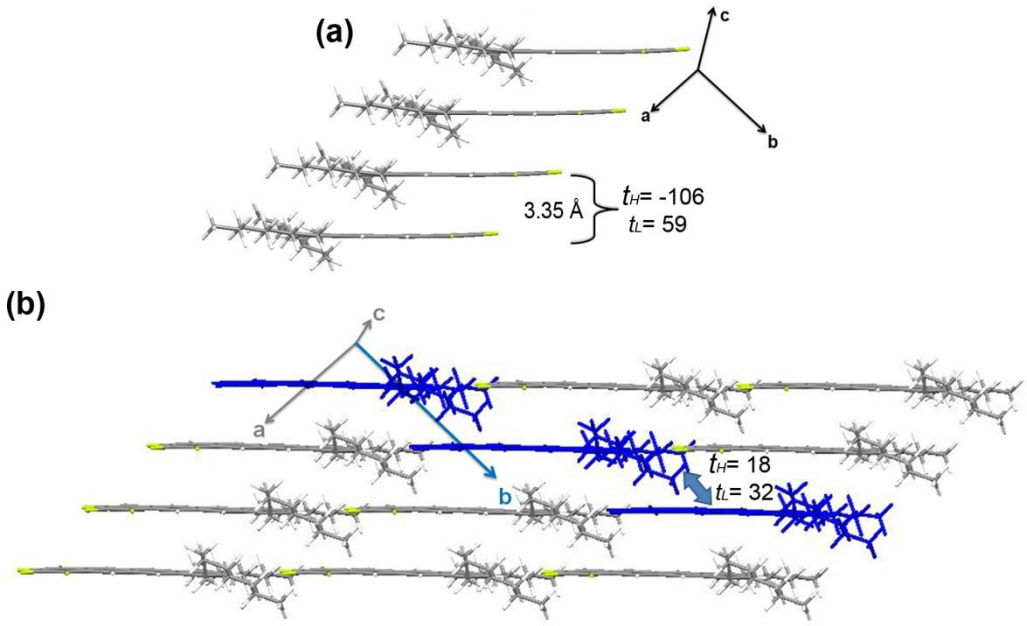

Figure 4.3 (a) Crystal packing (view along the short axis) of **FTETc** showing the interplanar separation distances between the π–stacked cofacial dimers.[61] (b) Crystal structure of **FTETc** showing the π-stacking along the *b*-direction of the crystal lattice. The DFT-estimates of the transfer integrals (in meV) for holes (t_H) and electrons (t_L) for these molecular pairs are also shown.

We finally examined the electronic properties of the **FTETd** crystal. Its unit cell presents four translationally inequivalent molecules where two are geometrically inequivalent giving rise to two geometrically inequivalent π-stacks with two different patterns for the interaction between neighboring molecules along the π-stacks, namely, a1- and b1-type dimers for stack 1, and a2- and b2-type dimers for stack 2 (see Figure 4.4). As found in **FTETa** and **FTETb** crystals, **FTETd** stacks in an antiparallel cofacial way, indicating arene-perfluoroarene interactions. Significant electronic coupling elements between translationally inequivalent molecules are found, which vary along the

two different π-stacks (*i.e.*, t_H=-86 meV for a1-dimers versus 52 meV for a2-dimers, see Figure 4.4).

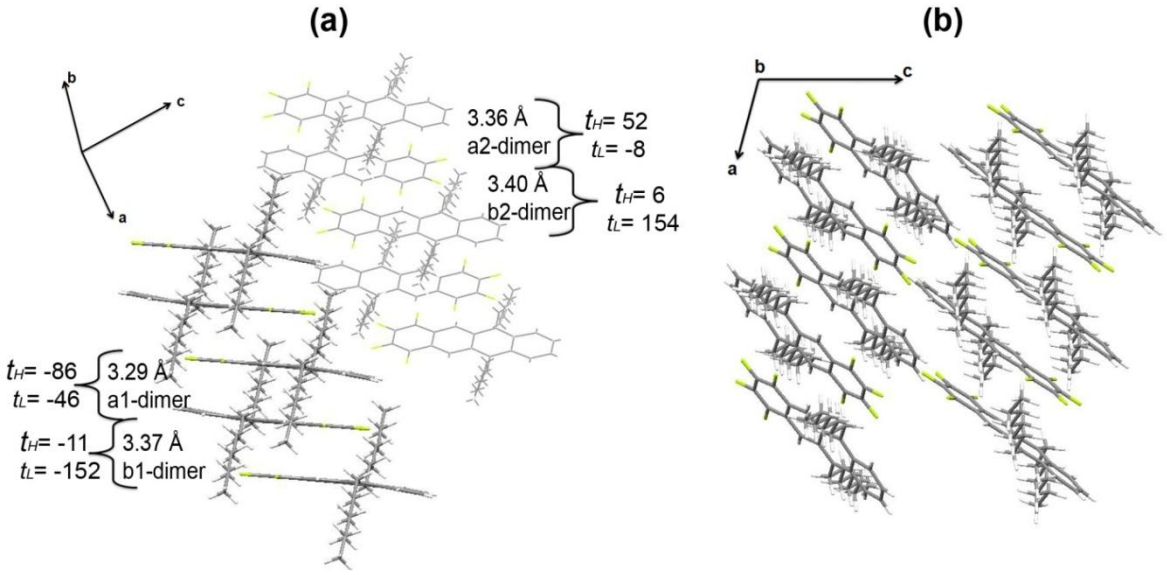

Figure 4.4 (a) Crystal packing (view along the short axis) of **FTETd** showing the interplanar separation distances between the a- and b-type dimers for the two geometrically different π-stacks 1 (capped sticks) and 2 (wireframe). The DFT-estimates of the transfer integrals (in meV) for holes (t_H) and electrons (t_L) for these molecular pairs are also shown. (b) Crystal structure of **FTETd** along the *b*-direction of the crystal lattice.

Finally, it is important to note that the tetracenes under investigation show strong orientational anisotropy of the band dispersions in the crystal as depicted by electronic band-structure calculations shown in Figure 4.5.[164] The largest valence and conduction band dispersions occur along the π-stack direction which involves the alternating a- and b-dimers. Among the series, **FTETc** exhibits the largest bandwidths for both conduction and valence bands, which is consistent with the large transfer integrals.

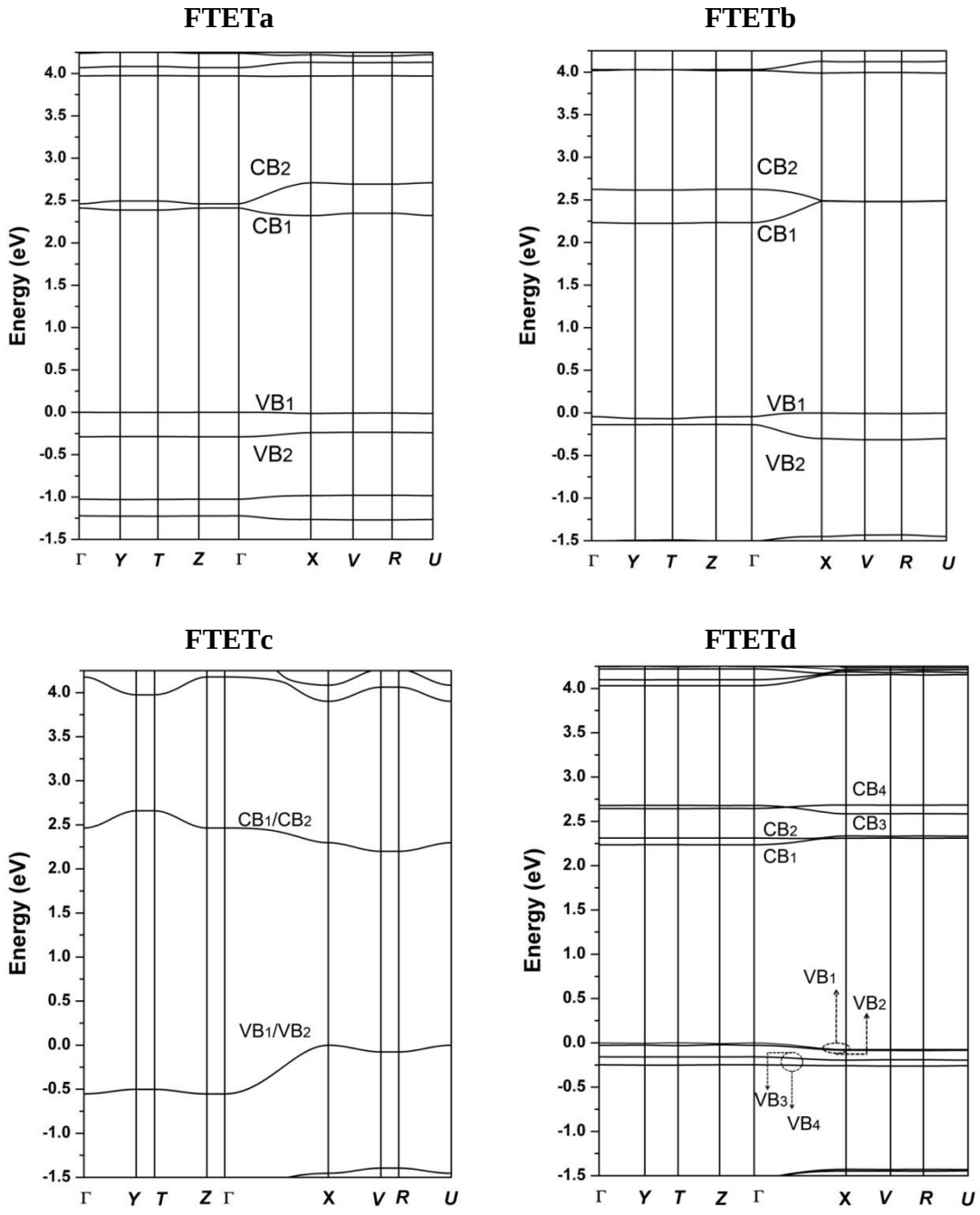

Figure 4.5 DFT-B3LYP/6-21G electronic band structures of **FTETa-d** crystals. Points of high symmetry in the first Brillouin zone are labeled as follows: Γ=(0,0,0), *Y*=(0,0.5,0), *T*=(0,0.5,0.5), *Z*=(0,0,0.5), *X*=(0.5,0,0), *V*=(0.5,0.5,0), *R*=(0.5,0.5,0.5) and *U*=(0.5,0,0.5), all in reciprocal space coordinates.

Conclusions

We have investigated the electronic structure and charge-transport parameters in four partially fluorinated tetracenes substituted with alkyl or alkoxy side-chains. The results indicate that the incorporation of both donor and acceptor substituents leads, in comparison to tetracene, to a substantial increase in the geometry modifications upon both oxidation and reduction. As a result, the reorganization energies for hole transport in **FTETa-d** are in the range of 160-270 meV, which are two to three times larger than in tetracene. The reorganization energies for electron transport in **FTETa-d** are also larger by 30-60% than in **TET**. The alkoxy-substituted tetracenes (**FTETa** and **FTETb**) have higher reorganization energies than the alkyl-substituted compounds (**FTETc** and **FTETd**), which is consistent with the large geometry relaxations observed within the C-O bonds of these compounds. Among the series, **FTETc** presents the smallest reorganization energies for holes and electrons with values nearly identical to those calculated for the partially fluorinated compounds, **FTET**; the reorganization energies in **FTETc** are smaller than those found in a good electron-transport material such as perfluoropentacene.[163] The calculated electron affinities suggest that the electron injection barrier from a low work-function electrode is smaller than in tetracene.

The crystal structures exhibit a single π-stacking distance with parallel cofacial stacking (**FTETc**) or with alternating distances and antiparallel cofacial stacking (**FTETa**, **FTETb**, and **FTETd**). **FTETa** and **FETb** reveal dimer motifs with two π-stacking distances (a and b dimers). In the case of **FTETd**, there are two geometrically inequivalent alternating π-stacks (stacks 1 and 2) giving rise to dimer structures with four distinct intermolecular distances (a1, b1, a2, b2 dimers). DFT calculations of transfer integrals indicate significant interactions along the π-stacking directions with notably different relations for a- and b-type dimers. **FTETc** shows considerable transfer integrals in two different directions, suggesting two-dimensional charge transport behavior

whereas **FTETa**, **FTETb**, and **FTETd** display one-dimensional charge transport character (along the π-stack).

Overall, among the series investigated in this work, the **FTETc** crystal appears as the most promising with regard to charge-transport properties: it presents the smallest local electron-phonon couplings for both holes and electrons, and electron transport has a 2-D character. At this point in time, however, we are unaware of any measurements of charge mobilities in these crystals. We hope that the present results can stimulate work in these directions.

Charge-Transport Properties of Fused Heterocyclic Oligomers

In this second part of Chapter 4, we investigate fused heterocyclic oligomers as potential p-type materials for OFET applications. The systems of interest consist of fused thiophene-pyrrole rings with tunable structures and properties. A brief introduction on fused-ring conjugated π-systems follows.

Fused-ring oligomers are an attractive class of conjugated materials as they combine the rigid planarity of acenes, *e.g.*, pentacene, with the chemical stability of heterocycles, *e.g.*, oligothiophenes.[132,165] For instance, Katz and co-workers[166,167] have recently shown that anthradithiophene (ADT) displays improved solubility and stability toward oxidation and exhibits a mobility of 0.15 cm^2/Vs approaching that of amorphous silicon. Lately, it was demonstrated that in solution oligothiophenes with the same number of double bonds but varying extents of sulfur-bridging ring fusion display similar absorbance maxima but differ dramatically in fluorescence behavior. Such molecular properties can be perturbed significantly in the solid state and the structural similarity of the planar oligothiophenes offers the ability to systematically explore the role of solid-state packing in altering electronic properties, a critical issue in determining the device performance. Furthermore, there is evidence from crystal structures of the dimer of dithieno[3,2-*b*:2',3'-*d*]thiophene (DTT)[66] and pentathienoacene[165] that fused thiophene

rings may promote π-stacking. This mode of crystal packing is predicted to facilitate charge transport leading to potentially higher field-effect mobility in OTFT devices when compared to herringbone motifs. Far less investigated are the dithieno[3,2-*b*:2',3'-*d*]pyrroles (DTPs, Figure 4.6),[168-171] which are emerging as useful fused-ring precursors for the production of conjugated polymers. N-functionalization of DTPs with electron-withdrawing groups is intriguing with regard to the development of reduced band gap materials given the fact that these derivatives possess lower oxidation potentials than DTTs.

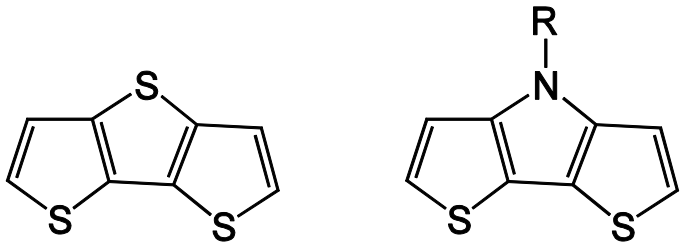

Figure 4.6 Structures of the dithieno[3,2-*b*:2',3'-*d*]thiophene, DTT (left) and dithieno[3,2-*b*:2',3'-*d*]pyrroles, DTP (right).

The motivation here is to understand some of the transport parameters of fused heterocyclic oligomers with extended conjugation. The oligomers under study (Figure 4.7) consist of dithieno[3,2-*b*:2',3'-*d*]pyrroles as building blocks, which allow the incorporation of solubilizing side chains via the N atom without causing much steric interactions and thus maintaining the planarity. In the absence of crystal structure data, we have focused our attention on the structural reorganization processes in extended thiophene-pyrroles containing from 3 to 7 fused rings and compared our results with other fully fused systems, such as oligoacenes and oligothiophenes.

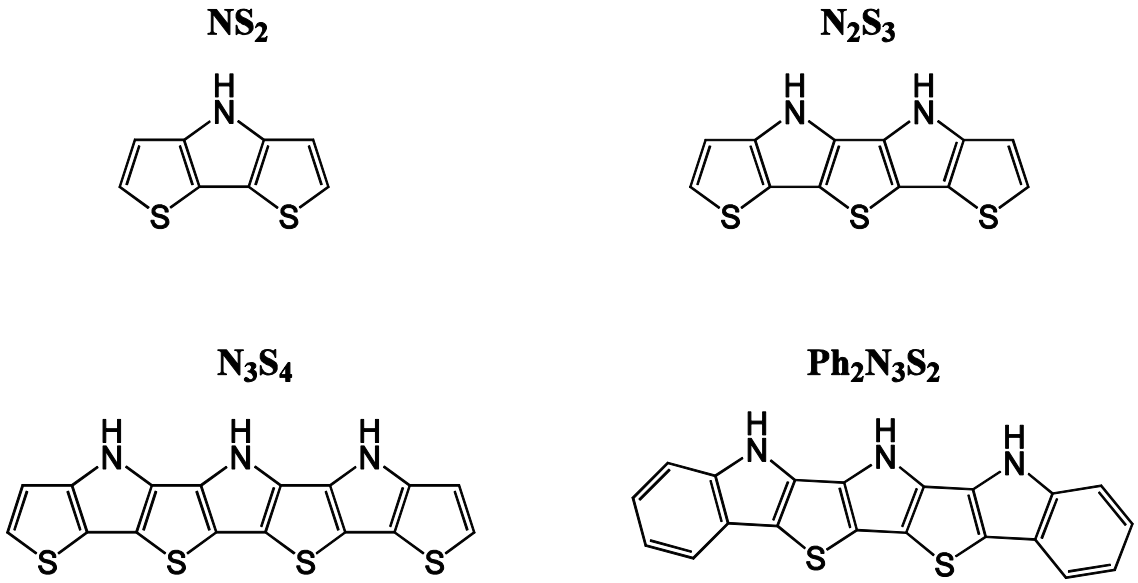

Figure 4.7 Chemical structures of the fused thiophene-pyrrole oligomers investigated in this work along with the abbreviations used throughout the text.

Geometric Structure

The analysis of the geometries in the neutral and ionic states of fused thiophene-pyrrole oligomers are collected in Tables 4.14 - 4.17. The calculated bond lengths are in very good agreement with the experimental geometrical parameters of the N-substituted DTPs.[171] However, upon comparison of the bond lengths of the fused systems with the calculated bond lengths of thiophene and pyrrole, it can be seen that the annulation of the rings results in small deviations in both the pyrrole and thiophene portions of the thiophene-pyrrole oligomers. The C-S bond lengths in the neutral state alternate between 1.74 and 1.76 Å, and show some slight elongation in comparison to the C-S distances in the parent thiophene (1.736 Å). The C-N bond lengths are 1.38-1.39 Å, in accordance with the C-N distances in pyrrole (1.375 Å). The shared C=C bonds between the two heterocyclic rings are 1.39-1.40 Å and are slightly lengthened as compared to the C=C bond length of the parent pyrrole ring (1.378 Å). Since the analogues thiophene C=C bond is shorter in comparison to the pyrrole (1.367 *vs.* 1.378 Å), it is inferred that this shared bond is primarily pyrrole in character. The C-C bonds show very good agreement

with that of thiophene (1.429 Å) and pyrrole (1.425 Å) for the exterior rings but exhibit shortening in the interior rings in comparison to the parent. Interestingly, in the case of **$Ph_2N_3S_2$**, the C=C and C-C bond lengths of the pyrroles close to the exterior (for instance, bonds 6 and 8 in Table 4.17) are identical (1.43 Å).

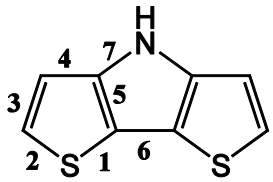

Table 4.14 DFT/B3LYP calculated bond lengths (in Å) in neutral and ionic states of **NS_2**.

Bond	Neutral	Cation	Anion
1	1.741	1.747	1.761
2	1.756	1.745	1.797
3	1.368	1.389	1.406
4	1.424	1.397	1.395
5	1.402	1.442	1.421
6	1.417	1.379	1.398
7	1.384	1.377	1.420

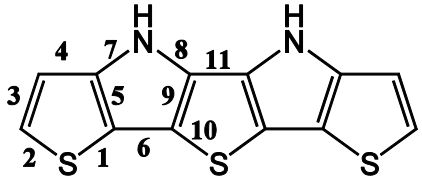

Table 4.15 DFT/B3LYP calculated bond lengths (in Å) in neutral and ionic states of **N_2S_3**.

Bond	Neutral	Cation	Anion
1	1.741	1.744	1.755
2	1.757	1.748	1.780
3	1.369	1.379	1.390
4	1.422	1.408	1.403
5	1.402	1.426	1.415
6	1.415	1.387	1.399
7	1.386	1.379	1.419
8	1.384	1.381	1.415
9	1.404	1.438	1.422
10	1.760	1.760	1.775
11	1.420	1.388	1.392

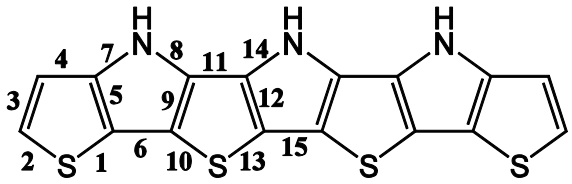

Table 4.16 DFT/B3LYP calculated bond lengths (in Å) in neutral and ionic states of **N_3S_4**.

Bond	Neutral	Cation	Anion
1	1.741	1.742	1.751
2	1.757	1.750	1.774
3	1.369	1.374	1.384
4	1.422	1.413	1.408
5	1.402	1.418	1.412
6	1.415	1.395	1.402
7	1.387	1.380	1.406
8	1.384	1.383	1.401
9	1.404	1.429	1.420
10	1.761	1.759	1.772
11	1.419	1.393	1.396
12	1.404	1.433	1.420
13	1.760	1.760	1.772
14	1.386	1.383	1.419
15	1.413	1.385	1.397

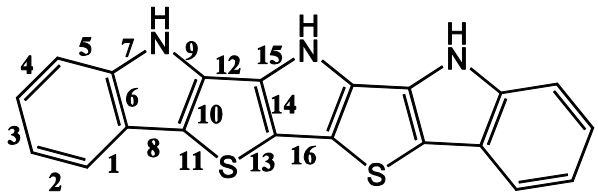

Table 4.17 DFT/B3LYP calculated bond lengths (in Å) in neutral and ionic states of **$Ph_2N_3S_2$**.

Bond	Neutral	Cation	Anion
1	1.404	1.412	1.414
2	1.390	1.383	1.397
3	1.407	1.413	1.401
4	1.392	1.393	1.410
5	1.395	1.393	1.386
6	1.431	1.435	1.442
7	1.390	1.391	1.402
8	1.430	1.414	1.414
9	1.384	1.376	1.400
10	1.394	1.420	1.411
11	1.761	1.756	1.776
12	1.418	1.394	1.393
13	1.757	1.760	1.771
14	1.405	1.433	1.423
15	1.386	1.382	1.420
16	1.414	1.384	1.395

The degree of geometry relaxation upon oxidation and reduction has been evaluated in the fused thiophene-pyrrole oligomers. Figure 4.8 shows the C-S and C-N bond length changes when going from the neutral to the cation (oxidation) or anion (reduction) states. The C-S and C-N bond relaxations occur predominantly upon reduction (as we will see below in Figure 4.10, the wavefunctions of the HOMO have nodes on the S and N atoms). For the C-S bond, the geometric relaxations are more pronounced toward the molecular periphery. **NS_2** shows the largest C-S and C-N bond relaxations upon reduction (~0.04 Å). Furthermore, Figure 4.9 summarizes the C-C and C=C bond length changes upon oxidation and reduction. The C-C and C=C bonds undergo geometric changes to a greater extent in the cationic state than in the anionic

state; these bond relaxations are more pronounced toward the molecular center. The largest C-C and C=C bond length changes are observed in the case of short oligomers such as **NS_2**. In addition, the bond length changes decrease with the increase in oligomer length. As we will see below, these geometry relaxations correlate well with the extent of the reorganization energies.

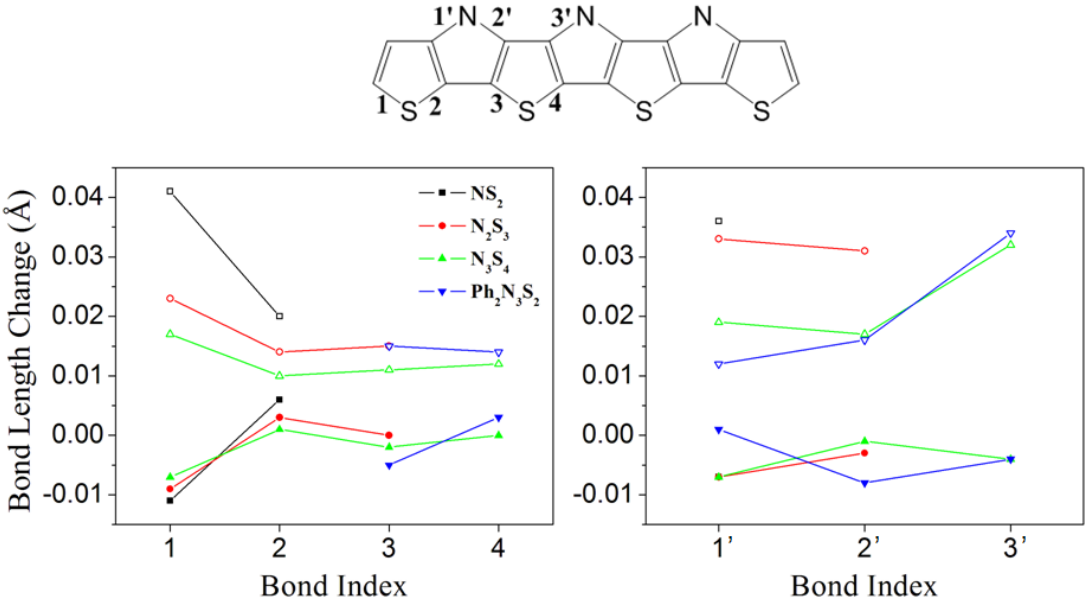

Figure 4.8 Variations in the C-S (on the left) and C-N (on the right) bond lengths upon oxidation (filled symbols) and reduction (open symbols) in fused thiophene-pyrrole oligomers.

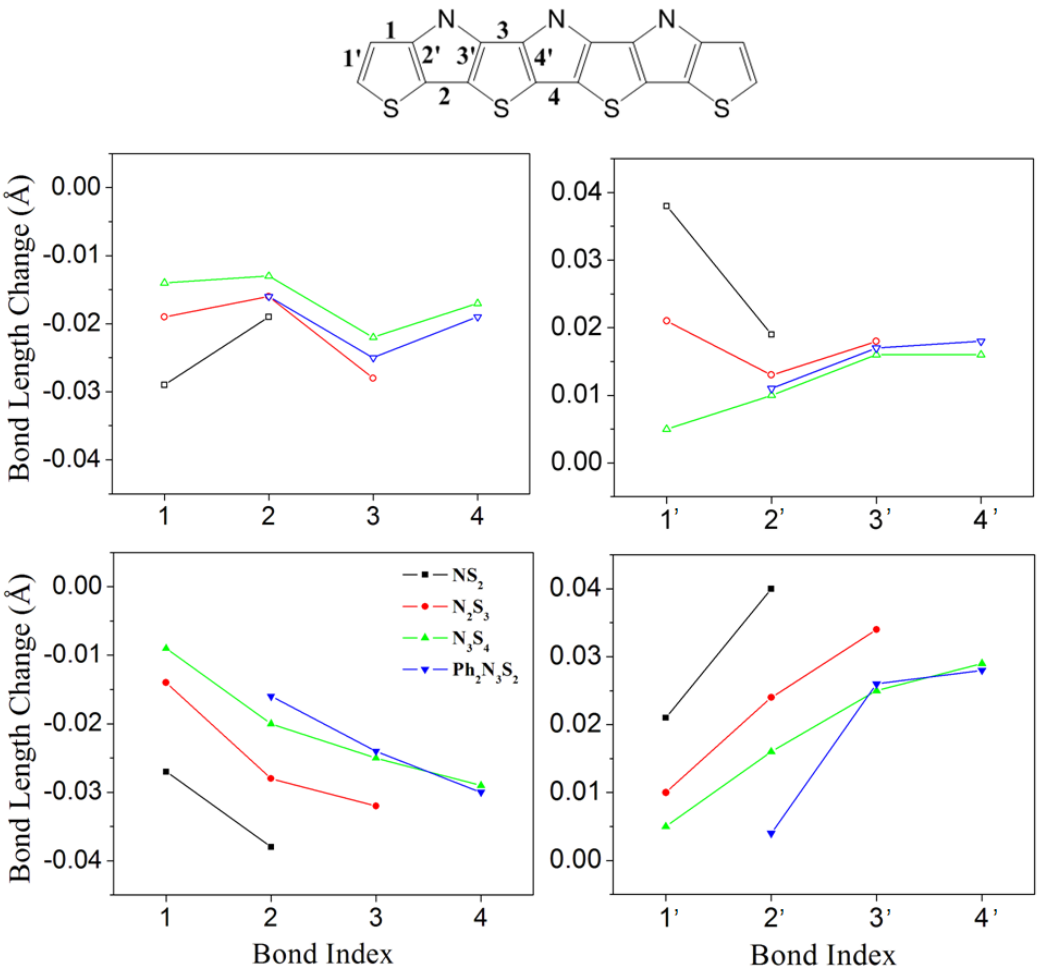

Figure 4.9 Variations in the C-C (on the left) and C=C (on the right) bond lengths upon oxidation (filled symbols) and reduction (open symbols) in fused thiophene-pyrrole oligomers.

The variations in bond lengths upon oxidation or reduction can be understood from the analysis of the shape of the frontier molecular orbitals. As Figure 4.10 suggests, the HOMO level localizes on the carbon backbone with nodes on the C-C bonds. The S and N atoms do not contribute to the HOMO in all four molecules. This is consistent with the negligible geometrical changes in C-S and C-N bonds upon oxidation. On the contrary, the LUMO level has nodes on the C=C bonds. There is also considerable electron density on the S and N atoms, which is consistent with the larger variations of C-S and C-N bond lengths upon reduction. We note that the HOMO and LUMO surfaces of

the fused thiophene-pyrrole oligomers studied here are representative of the motifs for all oligoheterocycles.[172,173]

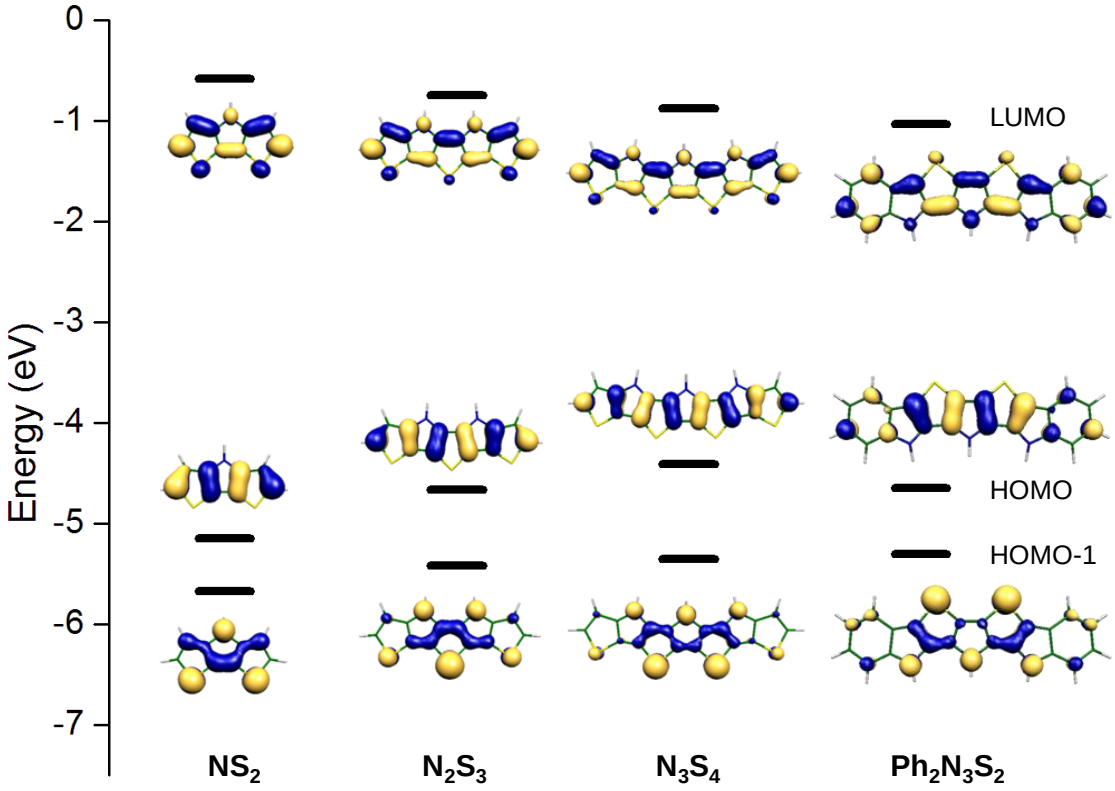

Figure 4.10 DFT/B3LYP calculated energies and wavefunctions of the frontier molecular orbitals in fused thiophene-pyrrole oligomers.

Energetics of Ionization

The reorganization and ionization energies of the fused oligomers are calculated according to the procedure outlined in Chapter 2. Table 4.18 collects the DFT estimates of the reorganization energies λ associated with hole- and electron-transfer processes in fused thiophene-pyrrole oligomers. First of all, λ (HT) in fused thiophene-pyrrole oligomers is much smaller than λ (ET), as in the case of oligoacenes and acenedithiophenes (see Table 4.19 for other fully fused systems). The shortest oligomer, **NS_2**, has the largest reorganization energy in the series. The reorganization energy decreases with the increase in the oligomer length in agreement with the calculated

geometry relaxations. We note that the variation of the reorganization energy with oligomer length follows the well-established approximate "1/*N*" relationship, where *N* is the number of monomer units.[172] The molecule containing benzene rings at the periphery, **$Ph_2N_3S_2$**, has the lowest reorganization energy in the series. The reorganization energy of **$Ph_2N_3S_2$** is lower than that of **N_3S_4**, which contains the same number of monomers. This suggests that introducing acene character into the oligomer may enhance charge carrier mobilities of fused thiophene-pyrrole oligomers.

Table 4.18 B3LYP/6-31G(d,p) estimates of the reorganization energies, λ (in meV) related to hole-transfer (HT) and electron-transfer (ET) in fused thiophene-pyrrole oligomers.

Compound	λ (HT)	λ (ET)
NS_2	320	615
N_2S_3	286	473
N_3S_4	269	430
$Ph_2N_3S_2$	237	385

Furthermore, we have compared the reorganization energies of the fused thiophene-pyrrole oligomers with other fully fused systems such as oligoacenes and oligothienoacenes (see Table 4.19). It turns out that fused thiophene-pyrrole systems have two to four times larger reorganization energies than their oligoacene analogues. For instance, the estimated reorganization energy for holes in **N_2S_3** is three times larger than in pentacene. In addition, the reorganization energies of the fused thiophene-pyrrole compounds are three times as large as that of acenedithiophenes containing the same number of monomer units.[100] Due to their large reorganization values, fused thiophene-pyrrole oligomers are expected to have lower charge-transfer rates than those of oligoacenes and acenedithiophenes. On the other hand, the fused oligomers under study have slightly lower hole reorganization energies than their oligothienoacene counterparts.[173]

Table 4.19 B3LYP/6-31G(d,p) estimates of the reorganization energies, λ (in meV) related to hole-transfer (HT) and electron-transfer (ET) in other fully fused systems.

# fused rings	λ (HT)	λ (ET)
Oligoacenes[a]		
3	138	198
5	94	132
7	67	93
Oligothienoacenes[b]		
3	352	324
5	306	270
7	279	237
Acenedithiophenes[c]		
3	107	256
5	94	159

[a]This work.
[b]The data is taken from Ref. 173.
[c]The data (for *syn* isomer) is taken from Ref. 100.

Lastly, vertical and adiabatic ionization potentials and electron affinities are given in Table 4.20. Our data show that the first ionization energy of fused thiophene-pyrrole oligomers decreases with increasing oligomer length as in oligoacenes (see Table 4.21) and in agreement with the experimentally observed oligomer length dependence of the ionization energy.[174] We note that ionization energies obtained from the application of the Koopmans' Theorem (negative of the HOMO energy, see Figure 4.10) and ΔSCF calculations predict similar trends. Furthermore, the ionization energies are comparable to those of corresponding oligoacenes. Positive electron affinities suggest that the anions of the fused thiophene-pyrrole oligomers are unstable, which would restrict the use of these compounds as p-type materials.

Table 4.20 B3LYP/6-31G(d,p) calculated first ionization potentials (IPs) and electron affinities (EAs) for fused thiophene-pyrrole oligomers as obtained from ΔSCF calculations.

Compound	IP (eV)		EA (eV)	
	Vertical	Adiabatic	Vertical	Adiabatic
NS_2	6.96	6.80	1.16	0.94
N_2S_3	6.17	6.03	0.69	0.46
N_3S_4	5.73	5.59	0.38	0.17
$Ph_2N_3S_2$	5.94	5.82	0.22	0.02

Table 4.21 B3LYP/6-31G(d,p) calculated first ionization potentials (IPs) and electron affinities (EAs) for oligoacenes as obtained from ΔSCF calculations.

# fused rings	IP (eV)		EA (eV)	
	Vertical	Adiabatic	Vertical	Adiabatic
3	6.89	6.82	-0.02	-0.12
5	5.95	5.90	-1.07	-1.14
7	5.43	5.39	-1.65	-1.70

Conclusions

We have investigated both hole- and electron-transfer processes in fused thiophene-pyrrole compounds **NS_2**, **N_2S_3**, **N_3S_4**, and **$Ph_2N_3S_2$**. DFT calculations indicate that the intramolecular reorganization energy decreases with increasing oligomer length as in oligoacenes. Furthermore, the reorganization energies for holes are much smaller than those for electrons, suggesting charge transport to be more efficient for holes than electrons. Positive electron affinities imply that the anions of the fused thiophene-pyrrole oligomers are unstable, confirming the use of these compounds rather as hole transporters. The reorganization energies for holes in fused thiophene-pyrrole oligomers (237-320 meV) are two to four times larger than in corresponding oligoacenes (67-138 meV) and acenedithiophenes (94-107 meV). In contrast, the fused oligomers under study have slightly lower hole reorganization energies than their oligothiophene counterparts

(279-352 meV), indicating that hole mobilities along fused thiophene-pyrroles might be similar to those found in fused oligothiophene systems. The lack of crystal structures prevents us from considering the electronic coupling terms (*i.e.*, transfer integrals) for a full understanding of the charge-transport characteristics of these materials.

CHAPTER 5

CHARGE-TRANSFER PROCESSES IN METALLOCENE-BASED DONOR-ACCEPTOR COMPOUNDS

Group 8 metallocenes are among the most extensively investigated organometallic donors in donor-π-acceptor chromophores.[175] A few studies have involved ruthenocenyl, Rc, or extensively methylated ferrocenyl donors such as 2,3,4,5,1',2',3',4'-octamethylferrocen-1-yl, Fc", or nonamethylferrocenyl, Fc*; however, most have employed the unsubstituted ferrocenyl group, Fc.[176] Ionization potentials for the relevant parent metallocenes indicate that the electron-transfer donor strength of these metallocenyl units, *i.e.* the strength of these species as donors in electron-transfer reactions or electron-transfer-type optical transitions, decreases in the order Fc" (or Fc*) > Fc > Rc.[177,178] For chromophores with a given π-bridging group and acceptor, the energies of the lowest-energy vis-NIR transitions follow the trend Fc" < Fc < Rc, consistent with the assignment of this band as a metal-to-acceptor charge transfer.[179]

However, the relative π-donor strengths of these different metallocenyl units are less straightforward to assess. The π-donor strength can be thought of as the ability to couple to an attached π-system and can be gauged by the extent to which zwitterionic resonance structures of the type shown in Figure 5.1a contribute to the ground-state structure. Some insight into the importance of the zwitterionic resonance form may potentially be gained from crystal structures of metallocenyl-polyene-acceptor chromophores with strong π-acceptor groups. Increased π-donation from donor to acceptor should be manifested in a decrease of the bond-length alternation (BLA) between formally double and single CH–CH bonds in the polyene bridge, by bond-length changes in the acceptor group, and by geometric changes in the metallocenyl group. In the case of metallocenyl donors where the acceptor is a directly attached carbocation,

contributions can be anticipated from the [(η^6-fulvene)(η^5-cyclopentadienyl)metal(II)]$^+$ limiting structure with the [(η^1alkyl)bis(η^5-cyclopentadienyl)metal(IV)]$^+$ limiting structure also being a possible contributor (Figure 5.1b, ii and iii, respectively). In the case of cationic systems where ferrocenyl and ruthenocenyl groups compete to stabilize a full positive charge – the [Fc(CH)Rc]$^+$ ion,[180] related species derived from mixed-metal metallocenophanes,[180,181] and the [Fc(CH)$_3$Rc]$^+$ ion[182] – crystallographic data indicate the presence of "normal" ferrocenes and [(η^6-fulvene)CpRu]$^+$ groups suggesting that, at least in these types of system, ruthenocenyl acts as a stronger π-donor than ferrocenyl. In the crystal structure of [Fc"(CH)$_3$Fc]$^+$[BF$_4$]$^-$ both metallocenyl groups are somewhat distorted towards [(η^6-fulvene)CpM]$^+$ but with the metallocenyl distortions and bond lengths in the allylium bridge indicating more stabilization of charge by the octamethylferrocenyl group.[182] However, the extent to which these observations can be extended to chromophores in which neutral, but potent, acceptors are attached through π-conjugated bridges to a metallocenyl unit is unclear. It is our goal in this Chapter to contribute to this assessment.

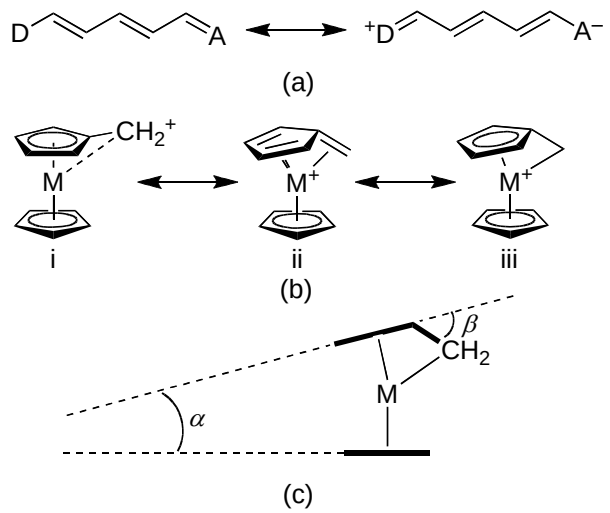

Figure 5.1 (a) Neutral and zwitterionic resonance structures for a donor-conjugated bridge-acceptor polyene; (b) resonance structures contributing to the stabilization of metallocenyl carbocations; and (c) definition of angles quantifying structural distortions in metallocenyl carbocations.

In order to do so, we have investigated the geometric and electronic structure of six organometallic compounds (Figure 5.2) in which ferrocenyl, octamethylferrocenyl, or ruthenocenyl donors are linked through a polyene bridge to strong non-aromatic 1,3-diethyl-2-thiobarbituric acid (TB) or 3-dicyanomethylidene-2,3-dihydrobenzothiophene-1,1-dioxide (SDS) acceptors. The compounds under investigation are the first in which one can directly compare the structures of analogues metallocenyl-polyene-acceptor chromophores with three different metallocenyl donors: ferrocenyl, heavily methylated ferrocenyl, and ruthenocenyl, while previous comparisons between even two types of donors are very limited.[183-185] In addition, a detailed analysis of molecular orbitals and optical properties is provided in order to understand the molecular origin of electronic transitions observed in the UV-vis-NIR spectra of these chromophores. Our results should thus be helpful to develop guidelines for the design of metallocene-based donor-acceptor compounds.

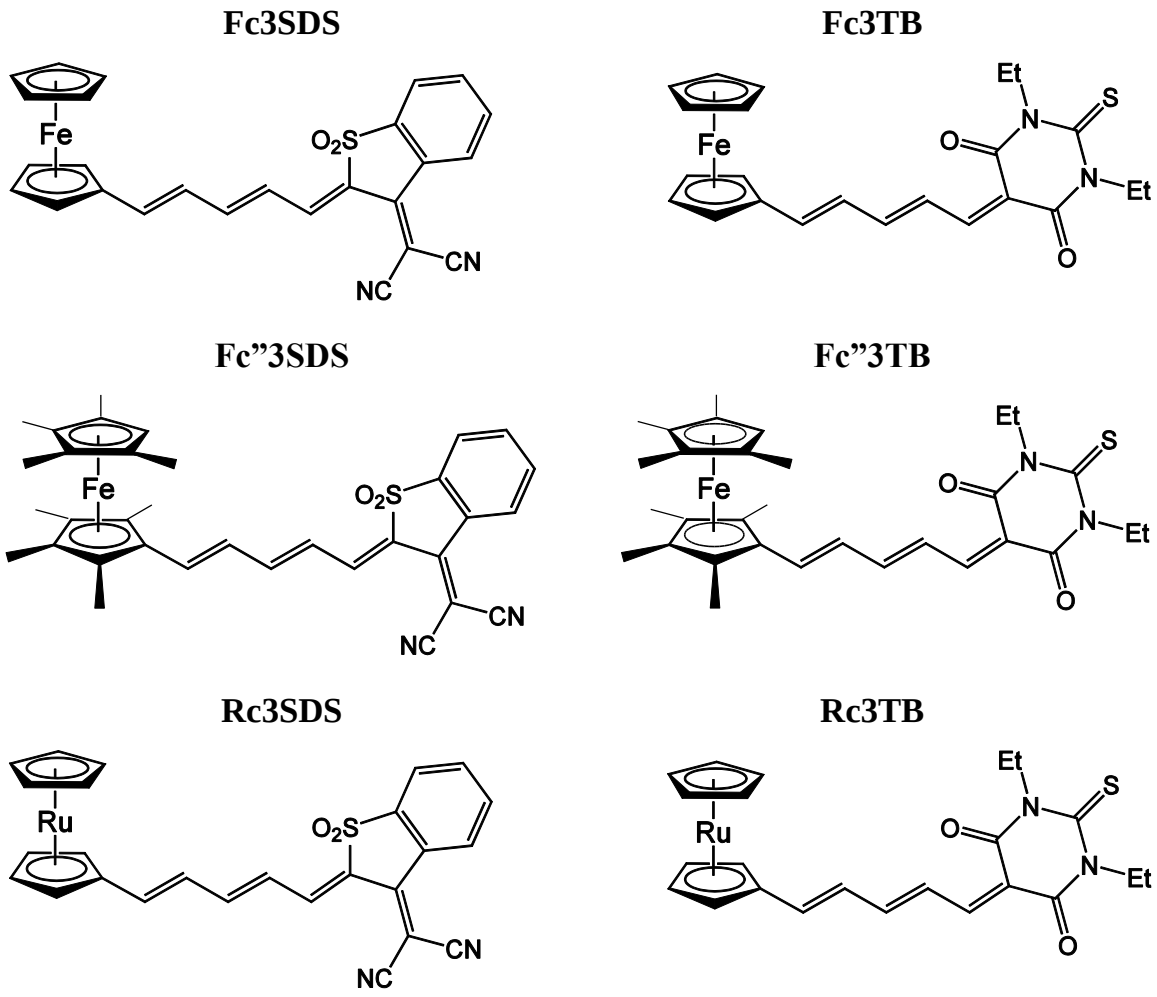

Figure 5.2 Chemical structures of the metallocene donor-acceptor compounds.

Molecular Geometries

In all the structures, the π-systems are approximately planar from the substituted cyclopentadienyl ring of the donor to the plane of the acceptor heterocycle. The formally double C_ε–C_A bonds (see Table 5.1 for definitions) of all three SDS chromophores have a Z configuration, *i.e.*, with the donor–acceptor conjugation path running in a trans fashion. The two cyclopentadienyl rings of the π-donors are almost parallel to each other. The DFT-calculated ring tilt angles (*i.e.*, angle between the planes of two cyclopentadienyl rings) are negligible.

The contribution of the zwitterionic resonance form to the ground-state structure of a donor-acceptor polyene can be gauged by the BLA, defined here as the difference between the average lengths of the bonds of the polyene chain which are formally single in the neutral resonance form and those which are formally double. The DFT-calculated lengths of selected bonds in the metallocene compounds are summarized in Table 5.1 along with the crystallographic data for comparison. The BLA values calculated using all the C-C bonds between the metallocenyl group and the heterocycle of the acceptor fall in the range 0.054-0.063 Å in remarkably good agreement with the crystallographic data (Table 5.1). In addition, the experimentally observed decreases in BLA from the donor to the acceptor end of the polyene chain are well reproduced in our calculations. The average BLA parameters for metallocenes indicate significant contribution from zwitteronic resonance forms in metallocenyl chromophores of this type with very strong non-aromatic π-acceptors (TB and SDS). In polyenes without significant donor/acceptor π-interaction,[186-191] including ferrocenyl-terminated examples,[192] typical bond-length alternations are 0.10-0.12 Å. Indeed, ferrocenyl-polyene-acceptor chromophores incorporating the aromatic *p*-nitrophenyl π-acceptor, which although a strong acceptor is considerably weaker than TB and SDS, also exhibit crystallographic BLAs of over 0.1 Å,[193] while $Fc(CH=CH)_3CHO$ shows a BLA of 0.09 Å.[194] Differences in the DFT bond lengths and BLAs between different molecules (which are too small to be reliably detected in the crystallographic data) show distinct trends, suggesting that the degree of ground-state charge-transfer increases in the order Fc < Rc << Fc" and TB < SDS.

The BLAs for metallocenes can also be compared to all-organic chromophores incorporating the same acceptor moieties. For the TB-based chromophore **I** (Figure 5.3), the BLA is close to zero (–0.01 Å), indicating that charge-separated and neutral resonance structures make approximately equal contributions to the ground-state structure;[195] this also underlines that dialkyl amines directly attached to the polyene chain are much stronger π-donors than metallocenes. SDS-based chromophore **II** (Figure 5.3)

exhibits greater BLA (ca. 0.04 Å)[196] than **I** due to the aromaticity of the phenylene ring resisting contributions from the zwitterionic form. The experimental BLA in **II** is slightly lower than in the analogous metallocenyl chromophores **Fc3SDS, Fc"3SDS,** and **Rc3SDS**, suggesting that *p*-aminophenyl groups act as stronger π-donors than metallocenyl groups with this type of acceptor; however, the DFT geometries tend to indicate that *p*-$^{n}Bu_2NC_6H_4$ exhibits a very similar π-donor strength to Fc" (calculated BLA of 0.055 Å).

Table 5.1 DFT/B3LYP calculated bond lengths and bond-length alternation parameters (in Å) for metallocenes, with values from crystal structures[197] (in italics) included for comparison.

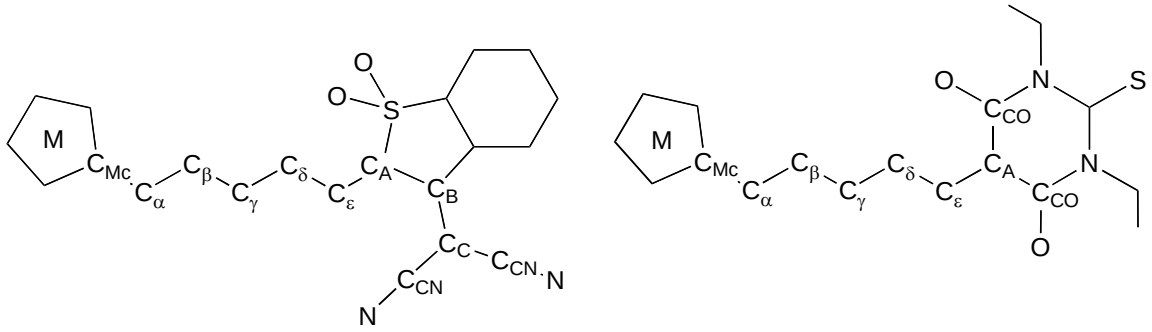

	Fc3TB	**Fc"3TB**[a]	**Rc3TB**	**Fc3SDS**	**Fc"3SDS**	**Rc3SDS**
C_{Mc}-C_α	1.447	1.444	1.446	1.445	1.440	1.444
	1.448	*1.440/1.427*	*1.447*	*1.444*	*1.419*	*1.446*
C_α-C_β	1.361	1.366	1.362	1.363	1.369	1.364
	1.354	*1.357/1.361*	*1.353*	*1.360*	*1.355*	*1.349*
C_β-C_γ	1.429	1.428	1.429	1.426	1.424	1.426
	1.426	*1.437/1.417*	*1.429*	*1.425*	*1.418*	*1.422*
C_γ-C_δ	1.370	1.372	1.371	1.371	1.374	1.372
	1.367	*1.369/1.358*	*1.363*	*1.363*	*1.357*	*1.361*
C_δ-C_ε	1.422	1.419	1.421	1.422	1.418	1.421
	1.420	*1.433/1.404*	*1.421*	*1.409*	*1.412*	*1.416*
C_ε-C_A	1.377	1.379	1.378	1.373	1.376	1.374
	1.372	*1.366/1.357*	*1.367*	*1.364*	*1.372*	*1.373*
BLA	0.063	0.058	0.062	0.062	0.054	0.060
	0.067	*0.073/0.057*	*0.071*	*0.064*	*0.054*	*0.067*
M-C_α	3.152	3.150	3.285	3.144	3.149	3.273
	3.106	*3.076/3.056*	*3.194*	*3.070*	*3.098*	*3.162*

[a]In the case of **Fc"3TB**, there are two inequivalent molecules in the asymmetric unit in the crystal.

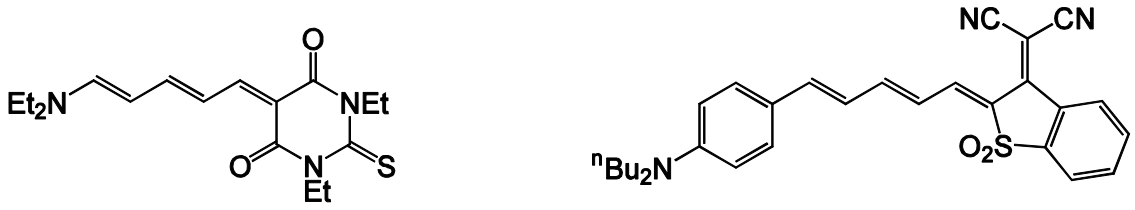

Figure 5.3 Chemical structures of the organic chromophores discussed in the text.

Although, as discussed above, the BLAs in the polyene bridges of the metallocenes indicate significant contributions from zwitterionic resonance forms, this contribution is accompanied by small distortions of the metallocenyl donors towards the $[(\eta^6\text{-fulvene})CpM]^+$ extreme (Figure 5.1b-ii) as suggested by experimental and calculated structures. The geometric parameters defined in Figure 5.1c all fall within the ranges found for the appropriate "undistorted" metallocenes. For example, unmethylated $[(\eta^6\text{-fulvene})CpRu]^+$ derivatives exhibit values of the Ru-C_α bond lengths in the range 2.251-2.604 Å,[182] whereas the corresponding values for **Rc3TB** (3.285 Å) and **Rc3SDS** (3.273 Å) are typical for "normal" ruthenocenes. There is also evidence from other ferrocenyl-based chromophores with strong π-acceptors that the extent to which the $[(\eta^6\text{-fulvene})CpM]^+$ resonance form contributes to the ground-state structure depends on the polyene chain length in addition to the identity of the acceptor.[198] This observation, along with the decreased BLA seen towards the acceptor end of the polyene and the calculated partial charges (see below), indicates that the polyene bridging group, as well as the metallocene itself, can act as a donor towards the heterocyclic acceptor. Moreover, the lowest-lying empty orbitals of the compounds investigated here, as in those of *p*-nitrostyryl derivatives,[199] are located towards the acceptor end of the polyene chains, precluding direct overlap with a filled metal orbital.

Charge Densities

DFT calculations were also performed to obtain information regarding the charge distribution in the chromophores; in Table 5.2, the atomic (Mulliken) charges are summed over the donor, π-bridge, and acceptor portions of each chromophore. The charge distribution plots are shown in Figure 5.4. Inspection of the total atomic charges for the donor portion is clearly consistent with a π-donor order of *p*-$^{n}Bu_2NC_6H_4$ > Fc" > Rc > Fc and a π-acceptor order of SDS > TB. The total acceptor charges indicate similar conclusions, although, surprisingly, the TB acceptor of **Fc"3TB** and **Rc3TB** bear essentially the same charge. In all the chromophores examined, the polyene bridge bears a net positive charge implying that the bridge acts as a net donor in these particular systems. The magnitude of the bridge charge does not vary in a particularly straightforward way with the donor, although consistently more donation from the bridge is observed in SDS chromophores than in their TB analogues; this is apparently at variance with ^{13}C NMR chemical shift data for the polyene atoms of the bridge, which suggest the bridges of the TB chromophores to be more electron-poor than those of the SDS chromophores.[197]

Table 5.2 Sum of Mulliken charges on donor, bridge, and acceptor portions of metallocenes and all-organic chromophore **II**.

	Fc3TB	**Fc"3TB**	**Rc3TB**	**Fc3SDS**	**Fc"3SDS**	**Rc3SDS**	**II**
Donor	0.090	0.191	0.128	0.126	0.251	0.154	0.335
Bridge	0.159	0.085	0.148	0.204	0.164	0.225	0.085
Acceptor	–0.249	–0.276	–0.276	–0.330	–0.415	–0.378	–0.420

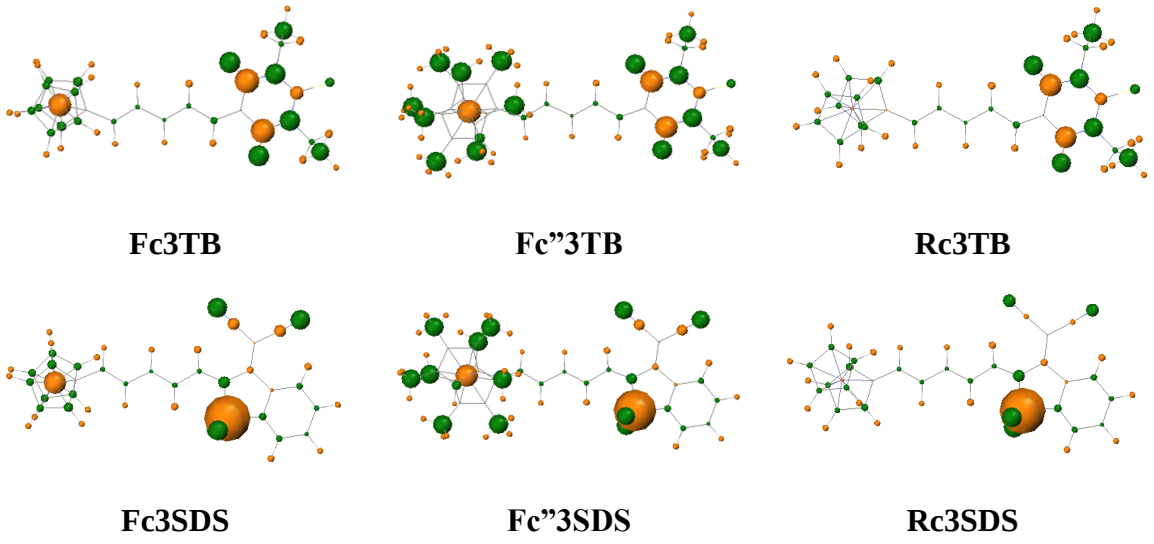

Figure 5.4 Charge (Mulliken) distribution plots of metallocene compounds.

Optical Properties

In this part we aim to describe the optical transitions observed in the UV-vis-NIR spectra of the metallocene-based donor-acceptor compounds by means of DFT calculations. There is evidence from experiment that these compounds exhibit two absorption bands: (i) a less intense lower-energy band (assigned as metal-to-acceptor charge-transfer transition); and (ii) a sharper and more intense higher-energy band (assigned as π-π^* charge-transfer transition).[179,200] The challenge for theory is to find a method that can properly describe these transitions. For instance, as we show in Table 5.3, the energy of the lowest-lying singlet state in **Fc3SDS** shows a significant variation as a function of the theoretical approach. There is nearly a 1 eV energy difference between two of the methods used (such as TD-DFT/B3LYP/6-31G* *vs*. TD-DFT/VWN/DZ).

Table 5.3 Energy of the lowest-lying singlet state (S_1) of **Fc3SDS** calculated at various levels of theory.

Method	*E* (eV)
TD-DFT/B3LYP/6-31G*	1.81
TD-DFT/BLYP/6-31G*	1.05
TD-DFT/BP/DZ	0.91
TD-DFT/VWN/DZ	0.88
HF/CIS/VDZ	1.18
HF/CIS/6-31G*	1.31

Note: Oscillator strength f is zero for S_1 state.

Today, several quantum chemical approaches for the calculation of excited states are available that yield energies and oscillator strengths of several excited states in one single calculation. For instance, time-dependent DFT is a very fast and reliable method developed about 25 years ago[110] that has become one of the most prominent and widely used approaches for the calculation of excited-state properties (*e.g.*, excitation energies and oscillator strengths) of medium to large molecular systems. In TD-DFT, standard time-independent exchange-correlation (xc) functionals derived for ground-state DFT, *i.e.*, local functionals such as Slater-Vosko-Wilk-Nussair (SVWN),[201] gradient-corrected ones (GGAs) such as Becke-Lee-Yang-Parr (BLYP),[103,202] Perdew-Burke-Enzerhof (PBE),[203,204] or Becke-Perdew 1986 (BP86),[103,104] and hybrid functionals such as Becke3-Lee-Yang- Parr (B3LYP),[96] are used. Moreover, the development of improved exchange-correlation functionals is still a very active field of research. In many cases, results obtained with TD-DFT are quite sensitive to the choice of the xc functional, in particular when local or GGA functionals are compared with hybrid functionals. Therefore, the reliability of TD-DFT calculations should be checked by comparison with experimental data or wavefunction-based methods.

Although TD-DFT reaches the accuracy of the high-level quantum chemical methods (*e.g.*, EOM-CCSD or CASPT2) with a very favorable computational cost for valence-excited states (the excitation energies of which lie well below the ionization potential), it is now well-established that TD-DFT has severe problems with the correct description of charge-transfer (CT) excited states when current standard xc functionals are used.[205-207] TD-DFT employing standard xc functionals leads to an incorrect long-range behavior of the potential energy curves due to the self-interaction error arising through the electron transfer in the CT state.[206] Improved density functionals such as the Minnesota M05 and M06 series have been developed to treat the interactions dominated by medium- or long-range correlation energy;[208-210] however, TD-DFT applications with these functionals have not yet been feasible with the available programs. Therefore, here, we provide an assessment of the widely used density functionals, *i.e.*, B3LYP, BLYP, BP, and VWN, for calculating the excitation energies of the metallocene compounds. Since TD-DFT encounters problems in the description of charge-transfer excited states, the excitation energies are also calculated by means of a wavefunction-based method, CIS. Configuration interaction singles is the simplest wavefunction-based *ab initio* method for the calculation of electronic excitation energies.[111] The impact of using various basis sets such as 6-31G*, DZ, and VDZ at the DFT and HF levels is also assessed.

Table 5.4 collects the energies and assignments of the strong singlet transition in **Fc3SDS**. Comparison of calculated energies with the experimental value of 2.40 eV[200] shows that the CIS method significantly overestimates the energy of this transition. Indeed, the excitation energies computed with the CIS approach are usually found to be too large (about 0.5-2 eV) in comparison to the experimental values[211-213]; this is due to the calculation of the energies of the virtual orbitals for the (N+1)-electron system instead of for the N-electron system within HF theory.[214] On the other hand, while TD-DFT employed with B3LYP provides energies that are comparable with the experimental

value, values at the BLYP and BP levels are in very good agreement with experiment. At this point, we emphasize that experimental measurements are strongly affected by environmental effects (such as solvent) and these effects are not taken into account in our calculations. Thus, TD-DFT calculations for the isolated molecule may result in fortuitous agreement with experimental optical transition data. However, as we demonstrate below, TD-DFT employed with the BP functional also gives orbital picture for metallocene donors that are in line with experimentally observed spectral trends.[179] Therefore, in the next sections, we discuss the optical transitions of metallocene compounds based on the calculations of excitations at the DFT level by using the BP functional as implemented in the *ADF* program package.[93]

Table 5.4 Energy and nature of the strong singlet transition in **Fc3SDS** as a function of level of theory.

Method	*E* (eV)	*f*	Nature
TD-DFT/B3LYP/6-31G*	2.60	0.533	H-2 → L
TD-DFT/BLYP/6-31G*	2.30	0.843	H-3 → L
TD-DFT/BP/DZ	2.26	0.831	H-3 → L
TD-DFT/VWN/DZ	2.25	0.872	H-3 → L
HF/CIS/VDZ	3.45	1.870	N/A
HF/CIS/6-31G*	3.42	1.831	H → L

The strong high-energy (HE) transitions calculated at the DFT/BP level are shown in Table 5.5. The calculations were able to give the energies of the HE transitions for Fc compounds within 0.2 eV of the experimental data.[200] The strong transitions are red-shifted by 0.3-0.5 eV with the stronger acceptor SDS. Similarly, metallocene methylation results in red-shift of this transition (shifts of 0.3 and 0.5 eV for **Fc"3SDS** and **Fc"3TB**, respectively). According to our calculations, Rc compounds are red-shifted by less than

0.1 eV as compared to Fc compounds, suggesting that changing the metal Fe for Ru has almost no effect on the energetics of the strong transition.

Furthermore, our calculations indicate that the strong HE transitions in metallocenes are characterized by HOMO-5 [HOMO-3] to LUMO transitions for the TB [SDS] chromophores. From the topology of the molecular orbitals shown in Figures 5.5 and 5.6, we see that HOMO-5 [HOMO-3] of TB [SDS] has a delocalized π structure mainly on the acceptor and polyene chain. The metal contribution to these orbitals is very small (less than 8% in all compounds except **Rc3SDS**, which has 20% metal contribution in HOMO-3). Similarly, the LUMO is delocalized over the polyene and acceptor moieties, with negligible metal contribution (2-8%). As a result, our calculations at the DFT/BP level confirm that the strong HE transitions in metallocenes are characterized by π-π* charge-transfer transitions.

Table 5.5 DFT/BP calculated strong HE transitions in metallocenes along with the experimental data.[200]

Compound	$E^{exp.}$ (eV)	$E^{calc.}$ (eV)	f	Nature
Fc3TB	2.71[a]	2.76	0.987	H-5 → L
Fc"3TB	2.40[b]	2.31	0.694	H-5 → L
Rc3TB		2.69	0.902	H-5 → L
Fc3SDS	2.40[a]	2.26	0.831	H-3 → L
Fc"3SDS	2.19[b]	2.00	0.448	H-3 → L
Rc3SDS		2.19	0.758	H-3 → L

[a]Data obtained from Ref. 200. Measured in dichloromethane.
[b]Data obtained from personal communications with Dr. Stephen Barlow. Measured in dichloromethane.

Table 5.6 summarizes the weak low-energy (LE) transitions in metallocene D-A compounds. In a way similar to the strong HE transitions, these transitions are red-shifted (by 0.3 eV) with the stronger acceptor SDS, which is also observed in experiment.[200] Metallocene methylation also leads to a red-shift of the LE transition (Fc" compounds are

red-shifted by 0.2 eV as compared to Fc compounds). In contrast to the HE transition, changing Fe for Ru results in a blue-shift of the LE transition by 0.2 eV. At the same time, the oscillator strength in Rc compounds slightly increases relative to Fc analogues suggesting that the LE transition gains in intensity upon exchanging Fe for Ru. On the other hand, the HE transition loses its intensity as evidenced by the slight decrease in oscillator strength when Fe is exchanged for Ru (see Table 5.5). These variations in oscillator strength are consistent with the experimental finding of an increase in intensity of the LE transition at the expense of the HE transition, which is attributed to the LE transition borrowing intensity from the HE transition.[179]

Table 5.6 DFT/BP calculated weak LE transitions in metallocenes along with the experimental data.[200]

Compound	$E^{exp.}$ (eV)	$E^{calc.}$ (eV)	f	Nature
Fc3TB	1.96[a]	1.64	0.137	H-3 → L
Fc"3TB	1.61[b]	1.40	0.065	H-2 → L
Rc3TB	2.34[a]	1.87	0.217	H-1 → L
Fc3SDS	1.66[a]	1.31	0.125	H-2 → L
Fc"3SDS	1.41[b]	1.14	0.091	H-2 → L
Rc3SDS	1.99[a]	1.51	0.171	H → L

[a]Data obtained from Ref. 200. Measured in dichloromethane.
[b]Data obtained from personal communications with Dr. Stephen Barlow. Measured in dichloromethane.

To understand the nature of the LE transition, one can examine the molecular orbital distributions shown in Figures 5.5 and 5.6. In **Fc3TB**, the HOMO is localized on the metal, as are the HOMO-1 and HOMO-3. In the case of **Fc"3TB**, the HOMO, HOMO-1 and HOMO-2 are localized on the metal, whereas the HOMO-1, HOMO-2, and HOMO-3 are largely metallic in character for **Rc3TB**. In SDS chromophores, the HOMO, HOMO-1, and HOMO-2 are confined on the metal. On the other hand, the

LUMOs, as was mentioned before, are delocalized over the polyene chain and acceptor with a small amount of metal contribution. One of the common features of the weak LE transitions is that they can all be described by a metal-to-acceptor type of charge-transfer transition. This explains the dependence of this transition on the metal identity.

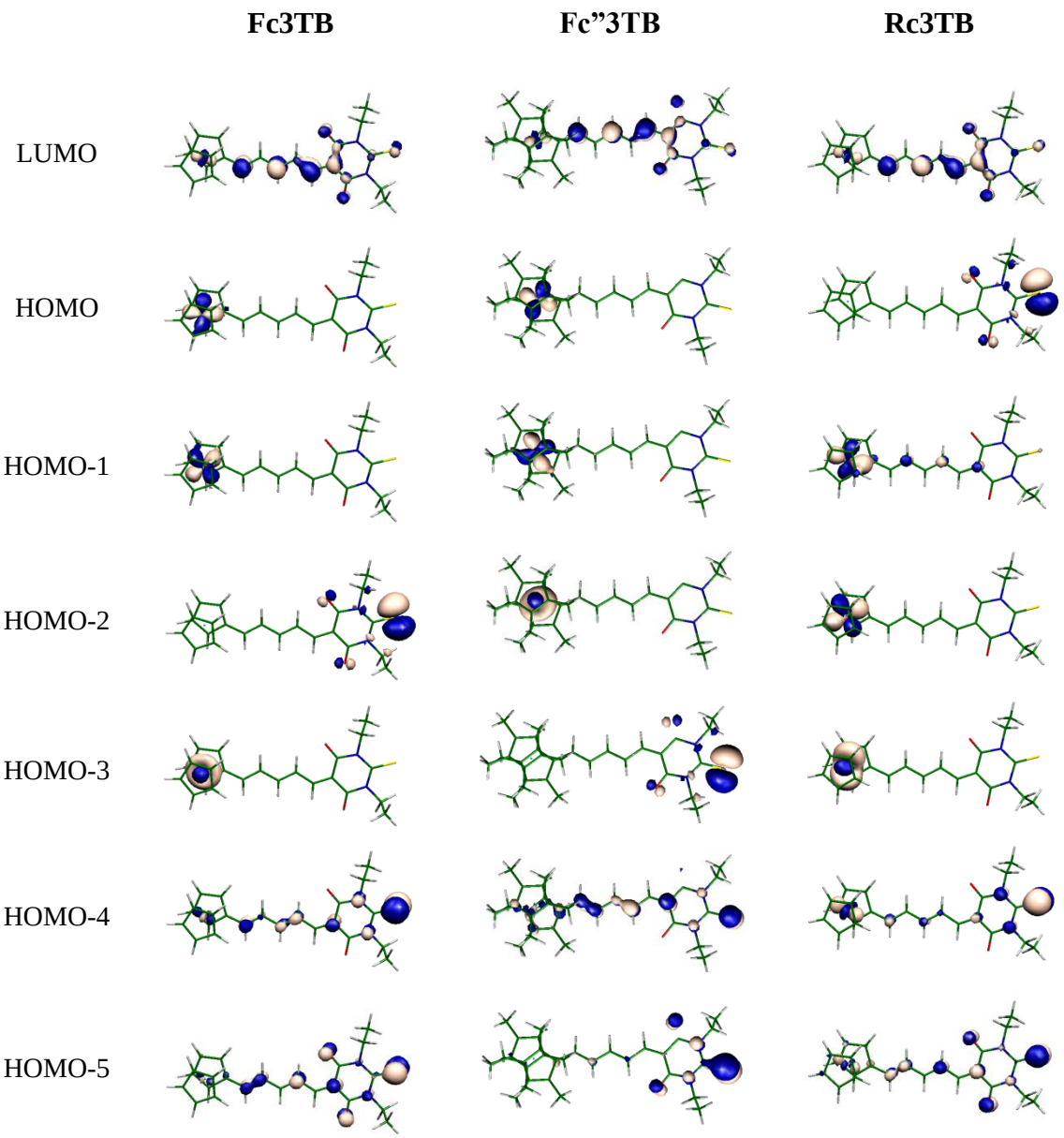

Figure 5.5 Wavefunctions of the DFT/BP calculated molecular orbitals for TB chromophores.

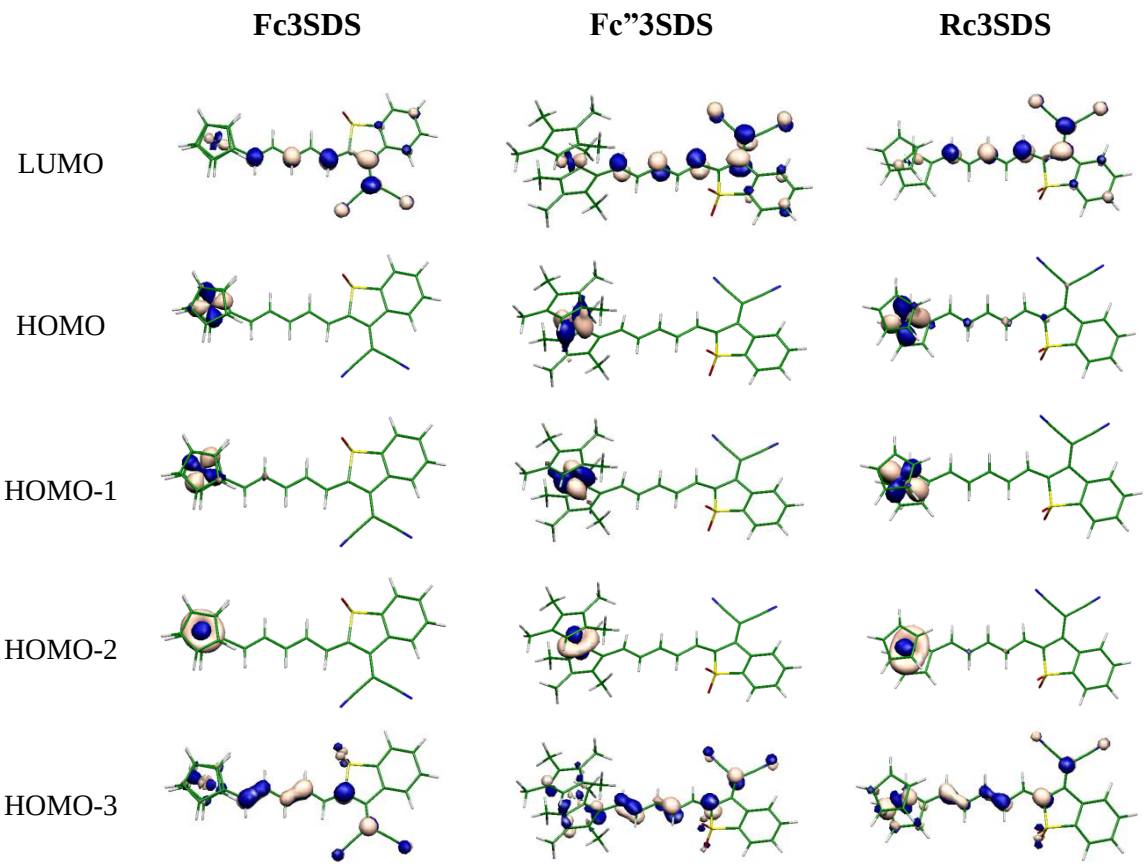

Figure 5.6 Wavefunctions of the DFT/BP calculated molecular orbitals for SDS chromophores.

Conclusions

The bond-length alternations between the formally double and single bonds of the polyene bridges are reduced in metallocenes compared to simple polyenes, indicating significant contribution from charge-separated resonance structures, although the metallocenes are not significantly distorted towards the [(η^6-fulvene)(η^5-cyclopentadienyl)metal(II)]$^+$ extreme. DFT geometries are in excellent agreement with those determined crystallographically; while the π-donor [π-acceptor] strengths between Fc, Fc”, and Rc [TB and SDS] are insufficient to result in crystallographically detectable variation in the BLA between the different chromophores, the DFT geometries as well as DFT-calculations of partial charges for atoms suggest that Fc" is a considerably stronger

π-donor than Fc or Rc and is similar in π-donor strength to a *p*-(dialkylamino)phenyl group. In this series of chromophores, our calculations indicate Rc is a slightly stronger donor than Fc, with experimental data indicating Fc and Rc are very similar in π-donor strength. The superior π-donor strength of Fc" parallels the known effect of methylation on the electron-transfer strength (ease of ionization) of ferrocenes (the gas-phase ionization potential of $FeCp^*_2$ is ca. 1.0 eV lower than that of $FeCp_2$;[177] numerous electrochemical studies[215-217] indicate methylated ferrocenes are more readily oxidized than $FeCp_2$). However, the similarity in π-donor strength for Fc and Rc can be contrasted to the very different electron-transfer donor strengths indicated by the gas-phase vertical ionization potentials of the parent metallocenes ($FeCp_2$ is ca. 0.6 eV more easily ionized than $RuCp_2$).[177,178] To understand this discrepancy, it should be realized that the highest occupied orbitals of metallocenes are essentially metal-based d-orbitals which can couple only weakly to an attached π-system, at least in the case of weakly accepting π-systems. However, the energies of the highest ligand-based orbitals, which are known to couple strongly to attached π-systems in π-nitrostyryl derivatives,[179] are sensitive to methylation, but relatively insensitive to the identity of the metal; values of 8.7, 7.3, and 8.5 eV have been assigned to the first ligand-based ionizations of $FeCp_2$, $FeCp^*_2$ and $RuCp_2$, respectively,[177,178] this pattern being consistent with the order of π donor strengths observed in the present series of $Mc(CH=CH)_2CH=A$ chromophores with strong neutral heterocyclic acceptors, *i.e*, Fc" >> Rc ≥ Fc.

DFT/BP molecular orbital analyses of the electronic transitions in metallocenes reproduced the experimentally observed trends in the UV-vis-NIR spectra of these compounds. Calculations and experimental evidence concur to indicate that the strong HE transitions are π-π* charge transfer, whereas the weak LE transitions are of metal-to-acceptor charge-transfer type. Both transitions are red-shifted with the stronger acceptor (SDS) and metallocene methylation. HE transitions are insensitive to the identity of the metal due to the negligible metal contribution in these transitions. On the other hand, LE

transitions are blue-shifted with Ru as compared to Fe, presumably due to the higher oxidation state of Ru than Fe. As a result, it is possible to modify the optical transition energies of metallocenes by subtle changes in their molecular structure without affecting the nature of the electronic transitions.

CHAPTER 6

INVESTIGATION OF NEW HOST MATERIALS FOR EFFICIENT BLUE ELECTROPHOSPHORESCENCE

Introduction

Phosphorescent organic light-emitting diodes (PHOLEDs) have attracted considerable attention recently because of their high quantum efficiency achieved by harvesting both singlet and triplet excitons due to efficient intersystem crossing.[18,218,219] In phosphorescent devices, to reduce the quenching associated with relatively long excited-state lifetimes of triplet emitters and triplet-triplet annihilation, the phosphorescent emitters of heavy-metal complexes are usually doped into a suitable host material. Thus, the development of host materials is as important as that of dopants for the formation of efficient PHOLEDs. It is critical that the triplet energy of the organic host be larger than that of the phosphorescent guest;[220,221] this facilitates an exothermic energy transfer from host to guest and prevents back energy transfer from guest to host (which could lead to phosphorescence quenching). In addition to high triplet energy, an effective host material should also have favorable ionization energy (approximated here by the energy of the HOMO level) and electron affinity (energy of the LUMO level) to facilitate charge injection from neighboring layers.

Although highly efficient and long-lived red and green emitting phosphorescent OLEDs have been demonstrated,[18,222] the realization of an effective blue organic phosphor remains a challenge. This is partly because of the difficulty in finding organic charge-transporting host materials with high triplet energies (~3.0 eV). To obtain materials with large energy gaps (HOMO-LUMO energy), the extent of conjugation in the molecule must be confined, which in turn would usually impose constraints in molecular size. On the other hand, for the molecules to form morphologically stable and uniform amorphous thin films with typical processing techniques, it usually requires the

molecules to be bulky and steric. As such, there has been a limited number of effective host materials for blue electrophosphorescent devices. Among them, carbazole-based materials (with triplet energies ~2.9 eV or less) have received special attention.[223-227] For instance, N,N'-dicarbazolyl-3,5-benzene (mCP) is commonly used along with the phosphorescent iridium complex iridium(III)bis[4,6-difluorophenyl]pyridinato-*N*,$C^{2'}$]picolinate (FIrpic) to fabricate blue phosphorescent devices of high quantum efficiency.[220] In addition, high triplet energy hosts are obtained when carbazole is functionalized with phenylsilanes[226] or phosphine oxide moieties[228] where silicon and phosphine oxide act as points of saturation. Lately, it has been shown that triscarbazole derivatives with 3(6),9'-linked topology (see Figure 6.3) result in host materials with both large triplet energies and good morphological stability. Devices based on this type of molecular architecture yield maximum quantum efficiencies of up to 15% (31 cd/A) and maximum power efficiencies of 28 lm/W.[225]

1,3,4-Oxadiazoles (OXDs), which are commonly used as electron-transporting (ET) and hole-blocking (HB) materials in OLEDs, are becoming attractive as electron-transporting host materials in phosphorescent OLEDs.[229-231] The use of electron deficient heterocyclic small molecules or polymers as a blend with the emissive material has proven to be useful in improving balanced injection and recombination in OLEDs. As is the case for carbazole derivatives, molecular topology and substitution pattern significantly affect the electronic properties of the oxadiazole-containing compounds.[232]

Hybrid oxadiazole/carbazole compounds have recently aroused considerable interest as bipolar hosts in PHOLEDs because they can balance the charge recombination and simplify the device structure.[233,234] However, a compromise is required between the bipolar transporting property and the band gap of the material since electron-donating and electron-withdrawing moieties in bipolar molecules are susceptible to lower the band gap of the material via intramolecular charge transfer.

An added complication of deep-blue phosphors is that they possess low-lying HOMO levels which typically fall near or below the HOMO levels of the carbazole-based host materials. Having host triplet energies that are close to the phosphor energy and similar host-dopant HOMO levels leads to both energy and electron transfer quenching pathways, which ultimately limit device performance. Therefore, design strategies that overcome the limitations of current host materials are crucial. We have thus analyzed the ground-state electronic structure and excited-state properties of several classes of host materials containing carbazoles, phosphine oxides, oxadiazoles, and organosilicon compounds with the aim of understanding their structure-property relationships. Such an understanding would help in providing design guidelines to achieve effective electrophosphorescence from blue phosphors.

This Chapter is structured as follows: First, the ground-state electronic structure of small building blocks such as carbazole, dibenzofuran, dibenzothiophene, fluorene, and their derivatives is presented. After that, the assessment of a range of quantum-chemical techniques to calculate the excitation energies of these molecules is given. Following small molecules, the ground-state molecular orbitals and excited-state properties (*i.e.*, the singlet and triplet levels) of five classes of host materials, namely: triscarbazoles, phosphine oxides, oxadiazole-containing molecules, hybrid oxadiazole/carbazole, and organosilicon compounds, are examined in detail. Finally, some important conclusions on the structure-property relations of these hosts are given.

Small Building Blocks (Monomers)

Previous quantum-chemical calculations of a series of host molecules including carbazole derivatives have shown that the system energetics can be significantly affected by molecular topology modifications and substitutions at specific positions.[235,236] For instance, it is shown that the HOMO level of carbazole compounds can be tuned by substitution at the 3, 6, and/or 9 positions (see Figure 6.1 for the numbering of the ring

system) while maintaining a high triplet energy.[223] In order to understand the structure-property relations of host molecules, we first investigated the electronic structure of small building blocks such as carbazole and related compounds shown in Figure 6.1 with variations in their X groups. We have applied DFT to describe the electronic structure in the S_0 ground state. The singlet (S_1) and triplet (T_1) excited states are examined by means of both semiempirical and ab initio methods (see below).

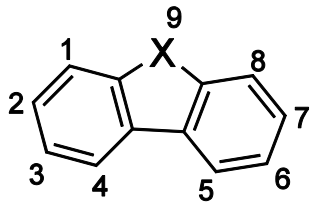

Figure 6.1 Chemical structure of carbazole and related compounds with X= NH, O, S, CH_2, $C(CH_3)_2$, $C(CH_3)(CF_3)$, and $C(CF_3)_2$. The site numbering in carbazole is also shown.

Electronic Structure of Monomers

The energies of the frontier molecular orbitals in carbazole and related compounds with varying X groups are shown in Table 6.1. Carbazole (X=NH) exhibits the highest HOMO and LUMO energies in the series. The substitution of X=NH with O, S, CH_2, $C(CH_3)_2$, $C(CH_3)(CF_3)$, and $C(CF_3)_2$ stabilizes the energy of the HOMO level by 0.3-0.8 eV and the LUMO by 0.1-0.6 eV. However, the HOMO-LUMO energy gap is less affected by these substitutions and remains in the range of 4.9±0.1 eV within the series. The frontier molecular orbitals of all investigated compounds are depicted in Figure 6.2. The spatial distributions of the LUMOs with nodes in the *meta* positions (3, 6 positions in Figure 6.1) show similar trends within the series. On the other hand, the HOMOs show slight variations within the series. On the one hand, they are the same for five compounds with X = O, CH_2, $C(CH_3)_2$, $C(CH_3)(CF_3)$, and $C(CF_3)_2$ with large coefficients in the *meta* and *para* positions and a nodal plane between the two phenyl

rings on both sides (note that *meta* and *para* positions are defined with respect to the bridging C-C bond of the carbazole, see Figure 6.1); in addition, the contributions of the X groups to the MOs are negligible. On the other hand, for the other two compounds with X=NH and S, the HOMO and HOMO-1 characteristics are exchanged. In this case, the HOMOs have nodes in the *para* positions and large MO coefficients on the X atoms; the HOMO-1 has large coefficients in the *meta* and *para* positions and a nodal plane between the two phenyl rings.

Table 6.1 B3LYP/6-31G* energies (in eV) of the frontier molecular orbitals in monomers.

X	HOMO	LUMO	Δ(HOMO-LUMO)
NH	-5.44	-0.64	4.80
O	-6.01	-0.92	5.09
S	-5.82	-0.95	4.87
CH_2	-5.75	-0.71	5.04
$C(CH_3)_2$	-5.73	-0.74	4.99
$C(CH_3)(CF_3)$	-6.00	-0.99	5.01
$C(CF_3)_2$	-6.25	-1.25	5.00

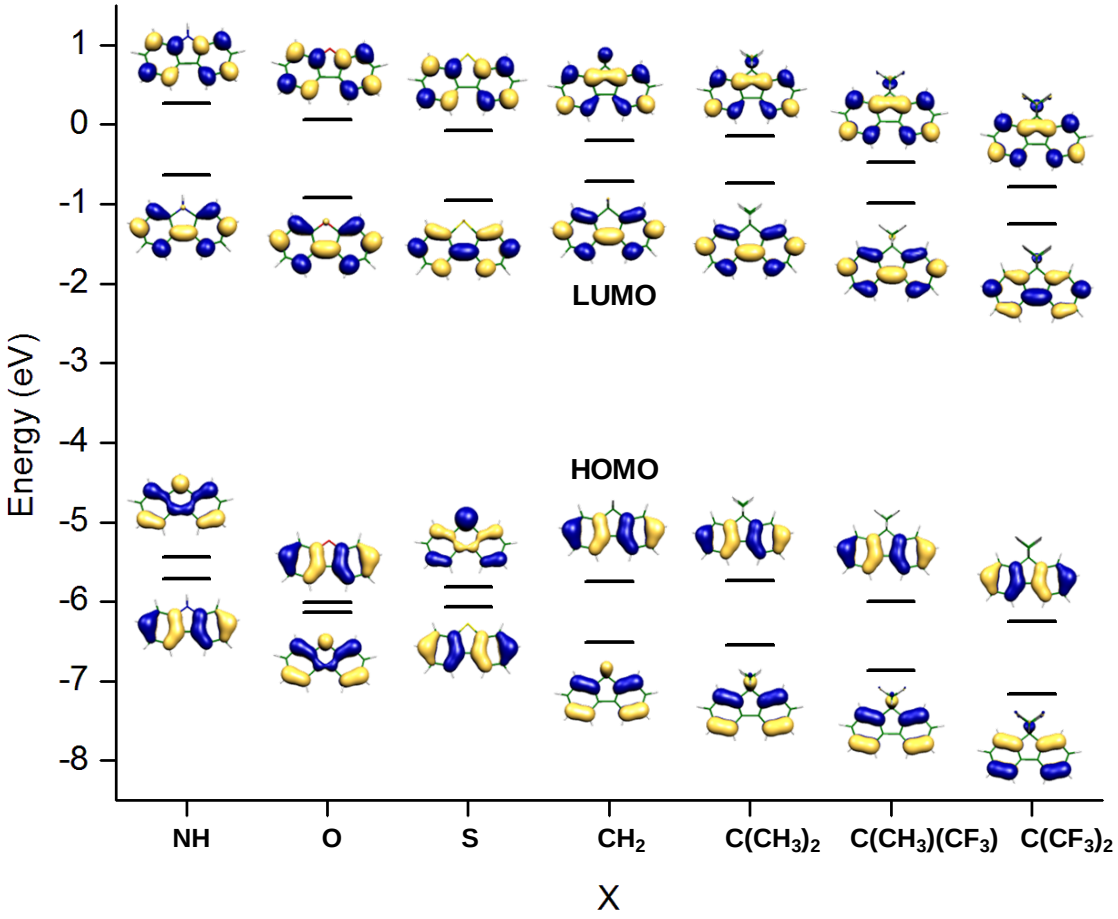

Figure 6.2 B3LYP/6-31G* derived energies and wavefunctions of the frontier MOs in monomers with varying X group. Note the interchange in the electronic distribution of the HOMO and HOMO-1 in the case of X = NH and S.

Singlet and Triplet Excited States of Monomers

First, we would like to address the accuracy of a range of quantum-chemical techniques to compute the singlet and triplet excitation energies in these organic conjugated molecules. Ground-state calculations were performed at the DFT level using B3LYP functional and 6-31G* basis set. The excited states are calculated by both semiempirical and ab initio methods using Zerner's Intermediate Neglect of Differential Overlap (INDO),[95] time-dependent (TD)-DFT,[110] and Hartree-Fock (HF) with Configuration Interaction Singles (CIS)[111] and CI Singles and Doubles (CIS(D))[112,113]

techniques. TD-DFT calculations were done with the B3LYP functional and the 6-31G* basis set.

The calculated S_1 and T_1 energies along with the available experimental data are shown in Tables 6.2 and 6.3. Although INDO calculations predict the S_1 energies well, they largely underestimate the T_1 energies; the mean absolute and maximum errors amount to 0.99 and 1.12 eV, respectively. At the ab initio level, while CIS significantly overestimates the S_1 energies (the mean absolute and maximum errors correspond to 1.55 and 1.80 eV), it leads to the best prediction of the T_1 energies. Calculations at the CIS(D) level considerably overestimate the S_1 and T_1 energies (mean absolute and maximum errors of 1.31 [0.90] and 1.88 [0.92] eV for S_1 [T_1] energies, respectively). TD-DFT/B3LYP calculations, on the other hand, reproduce T_1 energies that are in very good agreement with experiment and S_1 energies that are comparable with experiment; the mean absolute and maximum errors correspond to 0.50 and 0.63 eV, respectively. We have therefore adapted the TD-DFT/B3LYP methodology to discuss the singlet and triplet excited states.

Table 6.2 Energies (in eV) of the S_1 state in monomers calculated at various level of theory along with the available experimental data.

X	INDO/CI	HF/CIS	HF/CIS(D)	TD-DFT[a]	Exp.	Ref.
NH	3.91	5.33	4.46	4.15	3.53	225
O	4.17	5.43	5.78	4.53	3.90	237
S	4.23	5.37	4.47	4.20	3.78	238
CH_2	4.30	5.34	5.83	4.40	4.08	239
$C(CH_3)_2$	4.29	5.29	5.72	4.39		
$C(CH_3)(CF_3)$	4.30	5.30	5.78	4.41		
$C(CF_3)_2$	4.32	5.29	5.78	4.42		

[a]TD-DFT is applied with B3LYP functional and 6-31G* basis set.

Table 6.3 Energies (in eV) of the T_1 state in monomers calculated at various level of theory along with the available experimental data.

X	INDO/CI	HF/CIS	HF/CIS(D)	TD-DFT[a]	Exp.	Ref.
NH	2.03	3.03	3.96	3.19	3.05	240
O	2.00	3.01	3.99	3.21	3.12	237
S	2.06	2.93	3.91	3.16	3.01	241
CH_2	1.94	2.88	3.86	3.09	2.94	242
$C(CH_3)_2$	2.04	2.87	3.84	3.06	2.92	242
$C(CH_3)(CF_3)$	2.02	2.85	3.82	3.05		
$C(CF_3)_2$	2.02	2.85	3.80	3.03		

[a]TD-DFT is applied with B3LYP functional and 6-31G* basis set.

The TD-DFT/B3LYP calculated energies of the singlet and triplet excited states in monomers with various X groups are summarized in Table 6.4. Moving away from the carbazole leads to an increase in the singlet energy. For instance, substitution of the N atom with O or CH_2 increases the singlet energy by 0.38 and 0.25 eV, respectively. On the other hand, the triplet energy depends less on the choice of the X group; for instance, the triplet energy decreases by 0.1 eV upon replacing the N atom with the CH_2 group. Substitution of CH_2 with $C(CH_3)_2$, $C(CH_3)(CF_3)$, and $C(CF_3)_2$, however, do not influence either the singlet or the triplet energy. The exchange energy, estimated here as the singlet-triplet energy difference ΔE_{ST}, is found to be in the range of 1 to 1.4 eV, which is slightly larger than the exchange energy of many small molecules (0.7 to 1 eV).[243]

Table 6.4 TD-DFT/B3LYP calculated energies E (in eV) of the singlet (S_1) and triplet (T_1) excited states along with the singlet-triplet energy difference (ΔE_{ST}) of monomers.

X	E (S_1)	E (T_1)	ΔE_{ST}
NH	4.15	3.19	0.96
O	4.53	3.21	1.32
S	4.20	3.16	1.04
CH_2	4.40	3.09	1.31
$C(CH_3)_2$	4.39	3.06	1.33
$C(CH_3)(CF_3)$	4.39	3.05	1.34
$C(CF_3)_2$	4.41	3.03	1.38

Triscarbazole Derivatives

As we have mentioned, for carbazole-based molecules to acquire enough morphological stability when they are deposited as thin films, extension of the molecular dimensions beyond single carbazole units is necessary. A starighforward approach to achieve this is to directly link carbazoles to form oligocarbazoles. The direct oligomeric approach, in principle, should afford morphologically stable, medium-molecular weight molecules without the need for additional linkages (such as silicon and phosphine oxide). Directly linking large energy gap monomeric moieties to form oligomers, however, does not always produce host materials with large triplet energies suitable for blue electrophosphorescence.[223,236] This difficulty is mainly associated with challenges in blocking the electronic coupling between monomeric units, thus avoiding a significant reduction in triplet energy. In this sense, 3(6),9'-linked oligomers (triscarbazoles) result in a small reduction in triplet energies in directly-linked oligocarbazoles, giving a family of host materials with both large triplet energies and excellent morphological stability suitable for blue electrophosphorescence.[225]

Here, we have analyzed the electronic structure of triscarbazoles with 3(6),9'-linked topology as a function of the X group where X = NH, O, S, CH_2, $C(CH_3)_2$, $C(CH_3)(CF_3)$, and $C(CF_3)_2$, shown in Figure 6.3 (note that the middle carbazole in the triscarbazole architecture will be referred to as the "central" unit and the end carbazoles as the "side" units throughout the text).

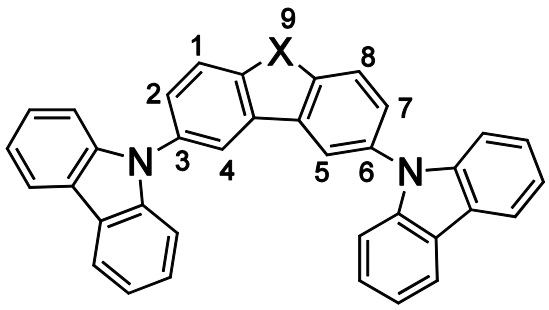

Figure 6.3 Chemical structure of the triscarbazole and related compounds with X=NH, O, S, CH_2, $C(CH_3)_2$, $C(CH_3)(CF_3)$, and $C(CF_3)_2$. The numbering of the central ring is also shown.

Electronic Structure of Triscarbazoles

The DFT/B3LYP calculated energies and wavefunctions of the frontier molecular orbitals in triscarbazole derivatives are shown in Table 6.5 and Figure 6.4, respectively. As seen from Figure 6.4, the LUMO is mostly localized on the central unit while the HOMO is delocalized on the side carbazoles. The DFT/B3LYP calculations show a significant stabilization (~0.4-0.6 eV) of the LUMO and destabilization (~0.2-0.7 eV) of the HOMO levels of triscarbazoles in comparison to the monomers. In order to examine the impact of the side carbazoles, a natural population analysis was conducted where the electron density distribution of triscarbazole derivatives is calculated based on the orthonormal natural atomic orbitals. The results show that the side carbazoles act as electron acceptors such that the total charges on both side units are consistently found to be negative (0.40-0.43e). Thus, the stabilization of the LUMO with respect to monomers can be attributed to the inductive electron-withdrawing effect of side carbazoles. On the other hand, the increase in the HOMO levels of triscarbazoles can be explained from a

combination of destabilizing MO interactions and stabilizing inductive effects. In the carbazole molecule, the HOMO has significant contributions from the *meta* carbons and the nitrogen; thus, in the triscarbazole, given the molecular topology, the interaction between the HOMOs of the central and side carbazoles are expected to be significant (note that MO interactions do not affect the LUMO because the carbazole LUMO has nodes on the *meta* carbons and nitrogen). Similarly, Marsal and co-workers observed stabilization in the LUMO of triphenylamine (TPA) when substituted with carbazole side groups (see molecule abbreviated as TCB in Ref. 235). The authors attributed the lowering of the LUMO level (with respect to TPA) to the inductive electron-accepting ability of the side carbazoles; on the other hand, the constant HOMO energies is explained by the cancellation between inductive acceptor and mesomeric donor effects.[235] Consequently, we note that the HOMO-LUMO energy gap of the triscarbazole derivatives, in line with previous calculations,[236] decreases by approximately 1.0 eV when compared to that of the monomers (4.9±0.1 eV).

Table 6.5 B3LYP/6-31G* energies (in eV) of the frontier molecular orbitals in triscarbazole derivatives.

X	HOMO	LUMO	Δ(HOMO-LUMO)
NH	-5.20	-1.23	3.97
O	-5.38	-1.44	3.94
S	-5.36	-1.43	3.93
CH_2	-5.33	-1.23	4.10
$C(CH_3)_2$	-5.32	-1.25	4.07
$C(CH_3)(CF_3)$	-5.43	-1.45	3.98
$C(CF_3)_2$	-5.52	-1.64	3.88

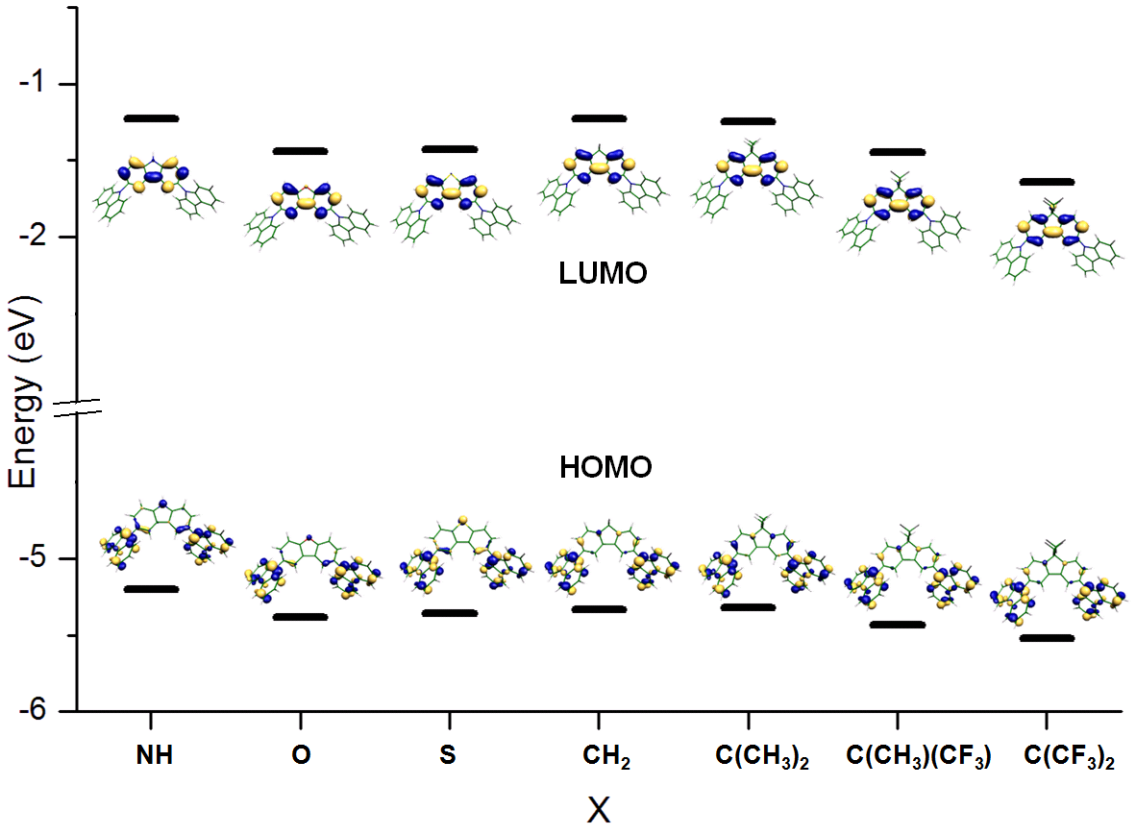

Figure 6.4 B3LYP/6-31G* energies and wavefunctions of the molecular orbitals in triscarbazole derivatives with varying X groups. The HOMOs are delocalized on the side carbazoles and the LUMOs are localized on the central units.

Singlet and Triplet Excited States of Triscarbazoles

The singlet and triplet excited state energies of the triscarbazole derivatives with varying X groups are given in Table 6.6. Upon going from monomers to triscarbazoles, we found that the singlet energies decrease by about 1 eV; however, the triplet energies remain almost constant (compare Tables 6.4 and 6.6). These results give rise to interesting conclusions. The singlet excited states of the triscarbazole derivatives dominated by a HOMO → LUMO transition have a strong intramolecular charge transfer (CT) character as indicated by the different localization patterns of the HOMO and LUMO. The HOMOs are delocalized on the side carbazoles and the LUMOs are localized on the central units (see Figure 6.4). These CT excitations can explain the

lowering of the singlet energy upon going from monomers to triscarbazoles. On the other hand, the maintenance of the high triplet energy in triscarbazole derivatives suggests a monomer-like triplet state. To test this hypothesis, we have analyzed the structural changes in the triscarbazole derivatives upon relaxation into the T_1 state. We found that the largest geometrical changes upon $S_0 \rightarrow T_1$ transition take place on the central units; this implies that the triplet states of triscarbazoles are very similar to that of the monomers. In addition, the wavefunctions of the molecular orbitals contributing the most to the triplet excited states show that the triplet excitons in these molecules are confined on the central units (Figure 6.5). These findings explain the almost constant triplet energies upon going from monomers to trimers. Furthermore, this distinct property, *i.e.*, confinement of the triplet excitons on a short conjugation segment, results in materials with high triplet energies.[223] Consequently, the triscarbazole derivatives studied here are a class of materials for which the HOMO/LUMO levels can be adjusted to a significant extent without much influencing the triplet energy.

Table 6.6 TD-DFT/B3LYP calculated energies E (in eV) of the singlet (S_1) and triplet (T_1) excited states along with the singlet-triplet energy difference (ΔE_{ST}) of triscarbazole derivatives.

X	E (S_1)	E (T_1)	ΔE_{ST}
NH	3.34	3.08	0.26
O	3.34	3.13	0.21
S	3.35	3.08	0.27
CH_2	3.56	3.00	0.56
$C(CH_3)_2$	3.41	2.97	0.44
$C(CH_3)(CF_3)$	3.41	2.94	0.47
$C(CF_3)_2$	3.35	2.89	0.46

We note that, as opposed to the rest of the molecules in the series, the lowest triplet state of the triscarbazole (X=NH) is characterized by a charge-transfer type of transition. However, careful analysis of the higher-lying triplet states reveals that the next triplet state (T_2) of the triscarbazole is very close in energy to the T_1 state ($\Delta\varepsilon$ = 0.05 eV) and is governed by localized excitations on the central unit similar to the rest of the compounds in the series. As a result, for X=NH, we found that the T_1 and T_2 states have interchanged their characteristics. This points to the importance of analyzing all of the lowest-lying triplet excited states in these molecules since substituents may affect the nature and ordering of these states.

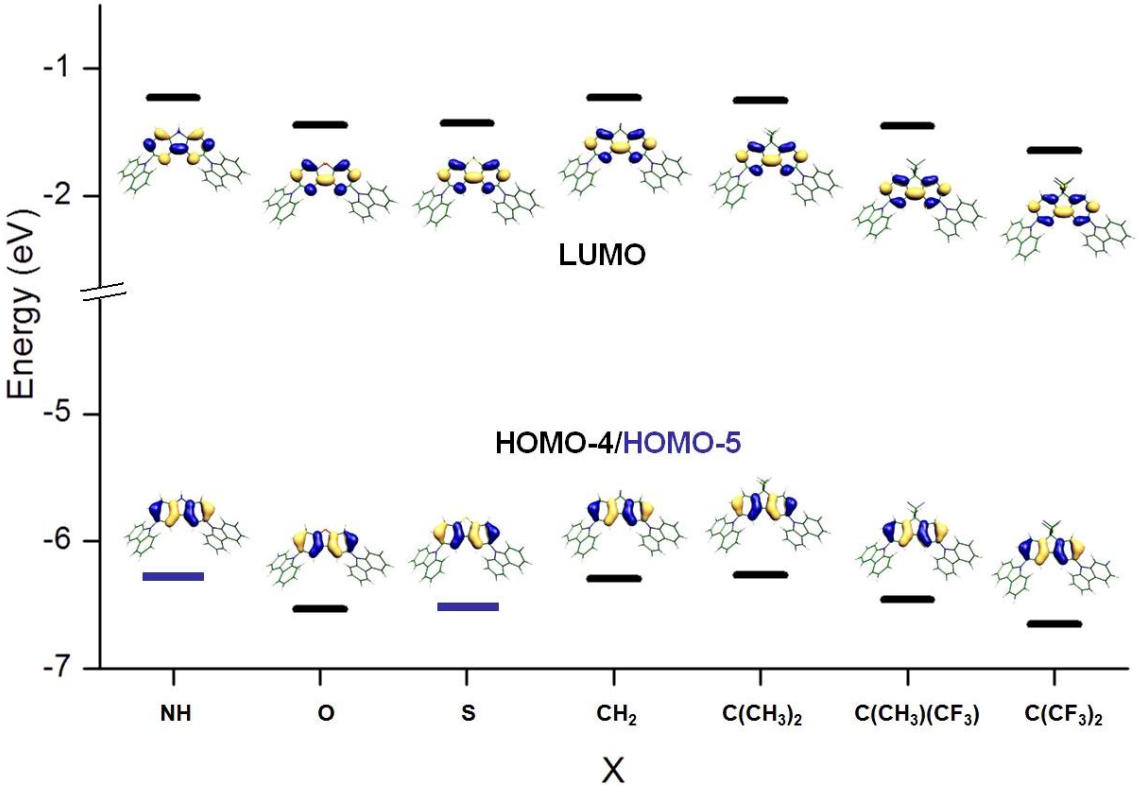

Figure 6.5 DFT/B3LYP wavefunctions of the MOs showing the localized triplet excitations (HOMO-4/HOMO-5 to LUMO transitions) in triscarbazole derivatives (HOMO-4/HOMO-5 and LUMOs are localized on the central units).

Phosphine Oxides

As mentioned before, organic charge-transporting host materials should have high triplet energies, high enough to prevent quenching of the dopant emission. Such high triplet energies require a molecule with a short conjugation length which can be formed by introduction of saturated centers into the molecule.[244] Recently, diphenylphoshine oxide ($Ph_2P=O$) substituted biphenyl,[245] carbazole,[246] dibenzofuran,[237] dibenzothiophene,[246] and fluorene[242] have been shown to function as effective electron-transporting host materials for blue OLEDs; in these molecules, phosphine oxide (P=O) is used as a point of saturation between the active chromophore center and outer phenyl groups, resulting in materials with triplet energies characteristic of the active centers. External quantum efficiencies as high as 9.8% at low drive voltages are reported for OLEDs using phosphine oxide hosts doped with the sky blue phosphor, FIrpic.[242,245,246]

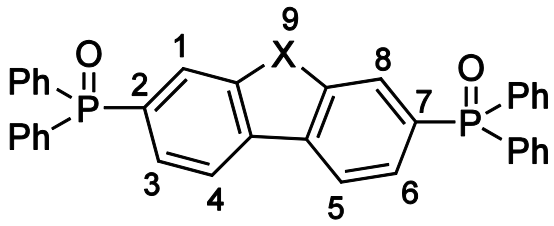

Figure 6.6 Chemical structure of the 2,7-diphenylphosphine oxide substituted biphenyl derivatives. The central units are biphenyl (X=2H), carbazole (X=NH), fluorene ($X=CH_2$), and dibenzofuran (X=O).

In this part, we have investigated 2,7-bis(diphenylphosphine oxide) biphenyl derivatives with variations in their X group (see Figure 6.6) as charge-transporting host materials for blue electrophosphorescent OLEDs (note that phosphine oxide is substituted at the *para* positions with respect to the bridging C-C bond in the central ring). The ground-state electronic structure and singlet and triplet excited states of these molecules are described by means of quantum-chemical calculations. Different substitution patterns such as 3,6-substitution (*meta*) of small molecules with phosphine oxides are also

considered to examine the effect of interconnection position on the energetics of this family of host compounds.

Electronic Structure of Phosphine Oxides

Since the P=O group acts as a point of saturation and prevents π-electron communication between the center rings and the outer phenyl groups, the electronic structures of phosphine oxides are expected to be representative of the central monomer units (*i.e.*, biphenyl, carbazole, fluorene, and dibenzofuran). However, as seen in Table 6.7, the strong inductive electron-withdrawing effect of the P=O moiety lowers both the HOMO and LUMO energies by 0.4 and 0.8 eV, respectively, relative to the monomers (see Table 6.1). As shown by other groups, substitution with electron-withdrawing groups (*e.g.*, bromine) lowers both the HOMO and LUMO energies, but in some cases the energy stabilization caused by the inductive effect can be counteracted by mesomeric effects; in this case, the HOMO level can be raised enabling hole injection.[235,242] For instance, such counteracting effects were observed in the molecular orbital levels of the triscarbazole derivatives discussed in the previous section where the HOMOs [LUMOs] were raised [lowered] with respect to monomers. In the case of phosphine oxides, both MOs are lowered upon PO substitution of small molecules.

Table 6.7 B3LYP/6-31G* energies (in eV) of the frontier molecular orbitals in phosphine oxides (POs).

	HOMO	LUMO	Δ(HOMO-LUMO)
Biphenyl PO	-6.42	-1.42	5.00
Carbazole PO	-5.87	-1.45	4.42
Fluorene PO	-6.19	-1.54	4.65
Dibenzofuran PO	-6.37	-1.61	4.76

The wavefunctions of the MOs in the phosphine oxides are depicted in Figure 6.7; it is seen that both HOMOs and LUMOs are predominantly localized on the central units. The HOMO energy is higher for the carbazole-based PO because of the involvement of the nitrogen atom of the carbazole ring in the HOMO. The HOMOs of biphenyl, fluorene and dibenzofuran POs are stabilized by 0.3-0.6 eV relative to that of the carbazole PO.

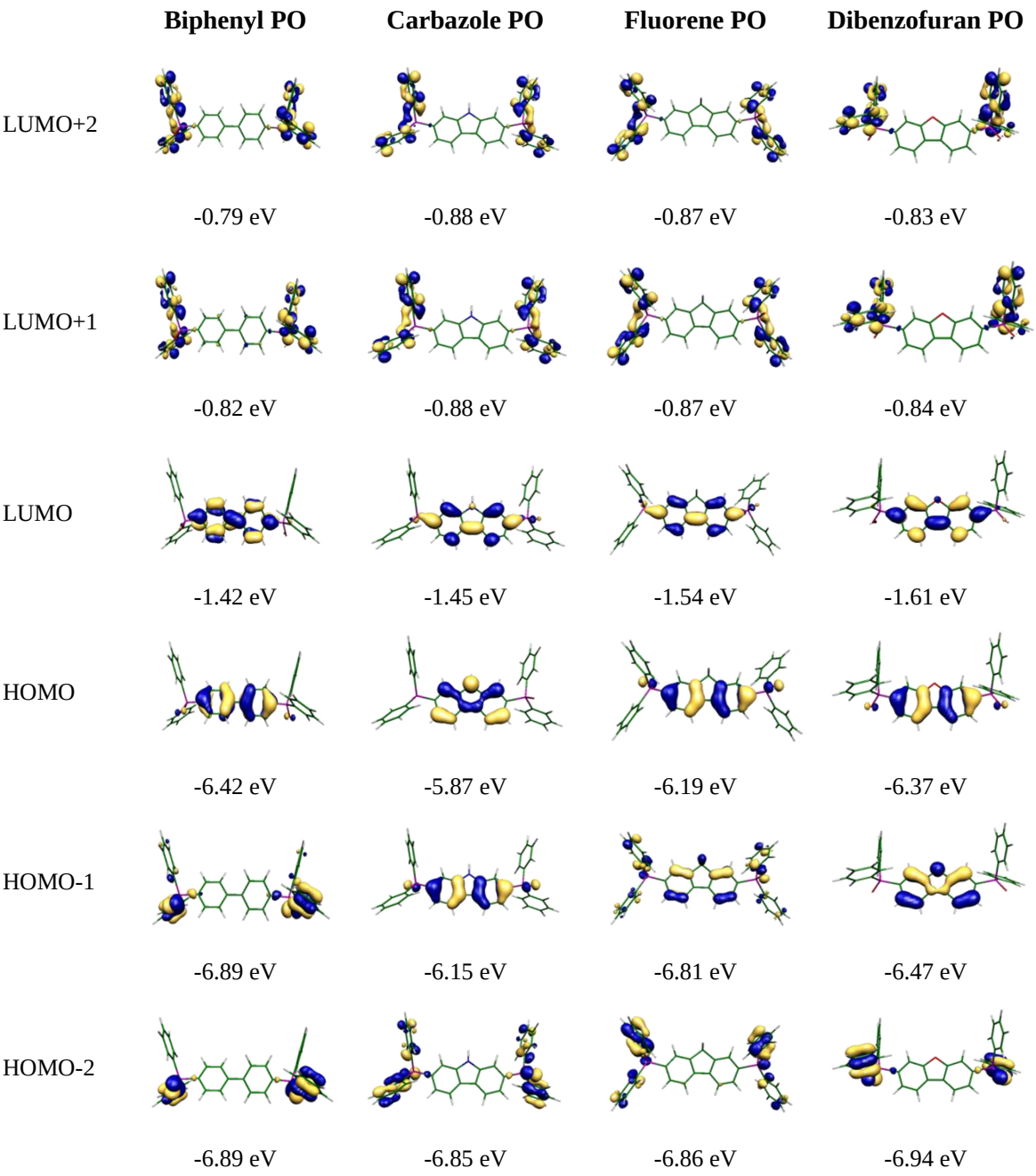

Figure 6.7 B3LYP/6-31G* energies and wavefunctions of the molecular orbitals in phosphine oxides.

Singlet and Triplet Excited States of Phosphine Oxides

Table 6.8 summarizes the energies of the lowest-lying singlet and triplet excited states of the phosphine oxides investigated here. Our calculations indicate that $Ph_2P{=}O$ substitution of biphenyl, carbazole, fluorene, and dibenzofuran at the 2,7-positions does

not significantly change the T_1 energy but lowers the S_1 level by 0.4-0.6 eV. This is consistent with the experimental absorption spectra where the absorption maximum of the diphenylphosphine oxides are slightly red shifted from the absorption of the monomers due to the inductive influence of the P=O moieties.[237,242] The weak influence on the triplet energy, however, indicates that the phosphine oxide substitution of small molecules does not alter the electron delocalization length of the active chromophore. All four PO compounds show triplet states characterized by localized excitations on the central units; as a result, triplet exciton energies calculated for POs turn out to be similar to the corresponding monomers *i.e*., biphenyl, carbazole, fluorene, and dibenzofuran.

Table 6.8 TD-DFT/B3LYP calculated energies *E* (in eV) of the singlet (S_1) and triplet (T_1) excited states along with the singlet-triplet energy difference (ΔE_{ST}) of phosphine oxides.

	E (S_1)	E (T_1)	ΔE_{ST}
Biphenyl PO	3.84	3.18	0.66
Carbazole PO	3.72	3.05	0.67
Fluorene PO	3.72	2.93	0.79
Dibenzofuran PO	4.06	3.07	0.99

Effect of Interconnection Position

DFT/B3LYP calculations show that Ph_2P=O substitution of small building blocks at the 2,7- or 3,6-positions (*para vs*. *meta*, see Figure 6.6) lowers both the HOMO and LUMO levels due to the inductive effect of phosphine oxide. However, as illustrated in Figure 6.8, the extent of stabilization of the MOs shows some discrepancies depending on the interconnection position of the PO groups. Substitution at 2,7- or 3,6-positions is expected to affect the frontier orbitals in a different way due to the dissimilar electron density at these points. As an example, we found that substitution of carbazole with POs

at the 2,7- or 3,6-positions lowers the HOMO levels by approximately the same amount (around 0.4 eV); however, the decrease in the LUMO differs as a function of the interconnection position (see Figure 6.8). The LUMO of the 2,7-substituted compound is further stabilized by 0.3 eV as compared to the LUMO of the 3,6-substituted compound. This difference in the LUMOs can be explained from the topology of the molecular orbitals shown in Figure 6.8. The 2,7-substitution of carbazole with POs leads to a further stabilization of the LUMO due to the contribution of the P=O to this level (note the extension of the π-conjugation towards the P=O group in Figure 6.8 on the left). On the other hand, substitution of carbazole with POs at 3,6-positions leaves the LUMO unaffected. Due to the larger extent of stabilization in the LUMO (caused by the combined inductive and MO effects), the triplet state of the 2,7-bis(diphenylphosphine oxide)carbazole is slightly red-shifted with respect to the T_1 of the 3,6-bis(diphenylphosphine oxide)carbazole.[247]

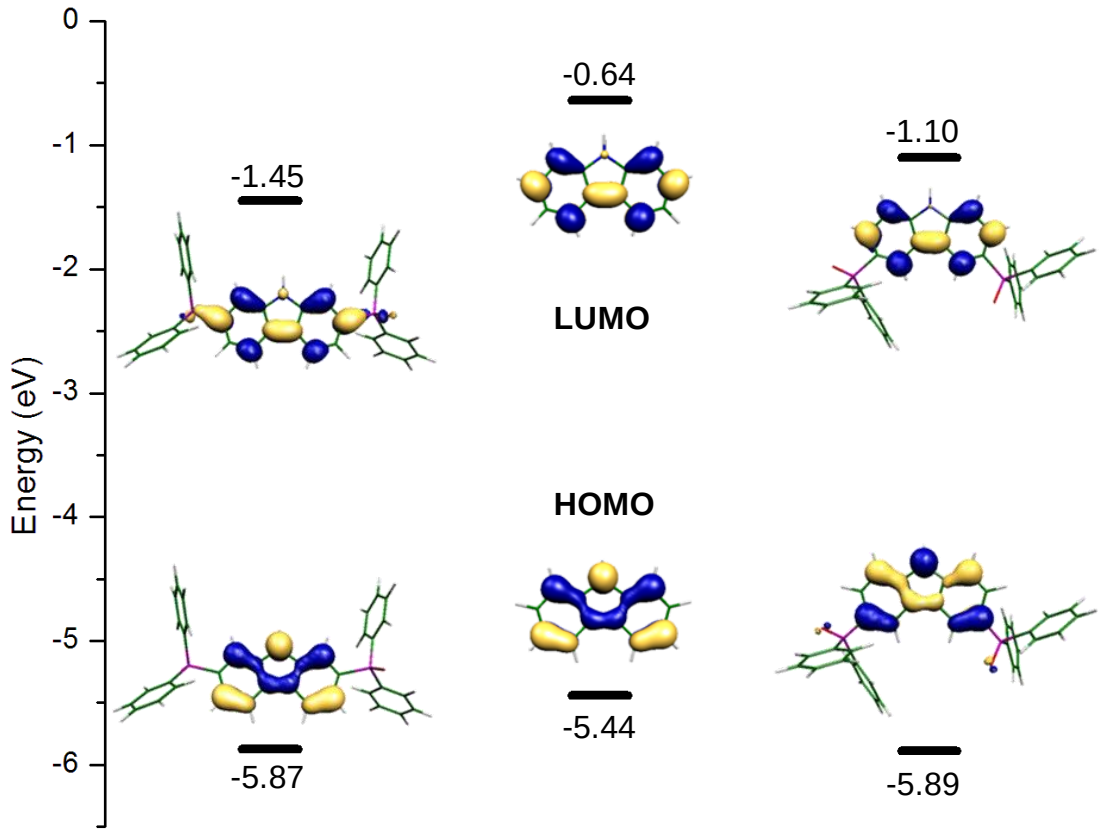

Figure 6.8 B3LYP/6-31G* energies and wavefunctions of the frontier molecular orbitals of 2,7-bis(diphenylphosphine oxide)carbazole (left) and 3,6-bis(diphenylphosphine oxide)carbazole (right) illustrating the effect of interconnection position on the electronic properties of phosphine oxides.

Oxadiazole-Containing Molecules

Most of the current materials used as emissive materials in OLEDs are good p-type (hole-transporting) materials. They, however, have generally small electron affinities and poor electron-transporting properties. Compared with organic hole-transporting materials, electron-transporting materials with low electron injection barriers and high electron mobilities are also required for improving the performance of the devices. The use of electron-deficient heterocyclic small molecules or polymers as a separate electron-transporting layer or as a blend component in conjunction with the emissive material has proved very useful in improving balanced injection and recombination in OLEDs.[248-251]

1,3,4-Oxadiazoles (OXDs) are electron-transporting and hole-blocking compounds that have been widely used in OLEDs due to their electron deficient nature and high chemical stability.[77,232,248] For example, 2-(4-biphenylyl)-5-(4-tertbutylphenyl)-1,3,4-oxadiazole (PBD) and 1,3-bis[4-tert-butylphenyl)-1,3,4 oxadiazolyl]phenylene (OXD7)[248] have often been incorporated in OLEDs as electron-transport materials. The use of OXDs as hosts for PHOLEDs is however more rare.[230,231] In addition to their electron-transporting ability, oxadiazoles can present a wide band gap if one restricts the extensions of π-conjugation. As such, large band gap host materials based on oxadiazoles have been reported for blue electrophosphorescent devices.[231]

In this part, we assess oxadiazole derivatives **1**-**6** shown in Figure 6.9 as potential molecules for electron-transport materials and hosts for blue-green emission. The effect of different side chains and their attachment position are examined to foresee structure property relations that can guide further development of new materials. To the best of our knowledge, there has not been any comprehensive theoretical study on the electronic and photophysical properties of hosts adopting an oxadiazole moiety.

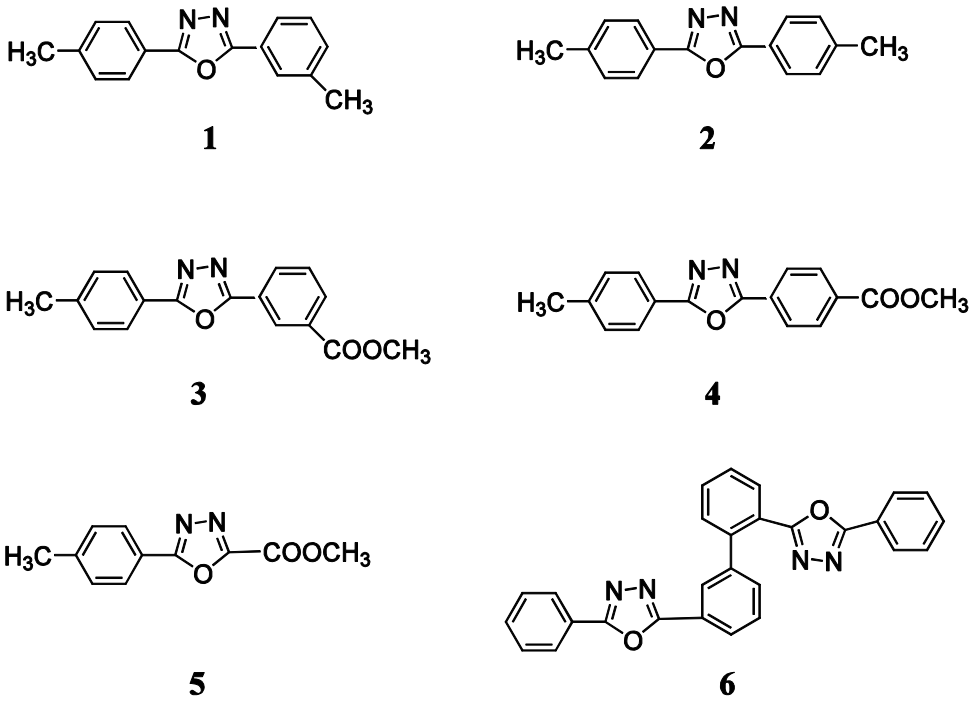

Figure 6.9 Chemical structures of the oxadiazole derivatives **1**-**6** investigated here.

Electronic Structure of Oxadiazoles

Table 6.9 summarizes the energies of the frontier molecular orbitals in oxadiazole derivatives **1**-**6**. They all have low LUMO levels as compared to previously discussed triscarbazoles and phosphine oxides making them better candidates as ET materials. Compounds **1** and **2** have relatively high-energy HOMOs with respect to the rest of the molecules which may result in a better hole injection ability. Among the series, oxadiazole **5** has the deepest HOMO creating a larger barrier for hole injection. Geometric isomers **1** and **2** have similar HOMO and LUMO levels. Substitution of CH_3 with the electron withdrawing $COOCH_3$ group stabilizes both the HOMO and LUMO by 0.3-0.5 eV. Despite their similar HOMO levels, the geometric isomers **3** and **4** have different LUMO levels suggesting different electron injection abilities. Accordingly, the calculated electron affinities (EA) (Table 6.10) for these two compounds differ by 0.7 eV. Oxadiazole **4** having the most negative EA (-1.32 eV) is thus the most electron accepting molecule in the series.

Table 6.9 B3LYP/6-31G* energies (in eV) of the frontier molecular orbitals in OXD derivatives **1**-**6**.

OXD	HOMO	LUMO	Δ(HOMO-LUMO)
1	-5.98	-1.51	4.47
2	-5.92	-1.48	4.44
3	-6.27	-1.86	4.41
4	-6.26	-2.06	4.20
5	-6.74	-2.00	4.74
6	-6.16	-1.67	4.49

Table 6.10 B3LYP/6-31G* calculated electron affinities (EA) in OXD derivatives **1**-**6**.

OXD	EA (eV)	OXD	EA (eV)
1	-0.19	**4**	-1.32
2	-0.17	**5**	-0.96
3	-0.59	**6**	-0.71

Figure 6.10 shows the wavefunctions of the frontier molecular orbitals in oxadiazole derivatives **1**-**6**. The HOMO and LUMO levels are delocalized over the entire molecule for all oxadiazoles (except for compound **6**). For the central ring, the HOMO is characterized by bonding orbitals between 3,4-nitrogen and 2,5-carbon whereas the LUMO is characterized by bonding between the 3,4-nitrogen atoms. In the case of compound **6**, the HOMO and LUMO levels are localized on different parts of the molecule. We note that, for this molecule with a non-coplanar biphenyl conformation (the angle between the two phenyl rings is around 124°), HOMO and HOMO-1 [LUMO and LUMO+1] lie close in energy (within 0.08 [0.15] eV of each other), and HOMO-1 [LUMO+1] is found to be localized on the other half of the molecule (see Figure 6.11).

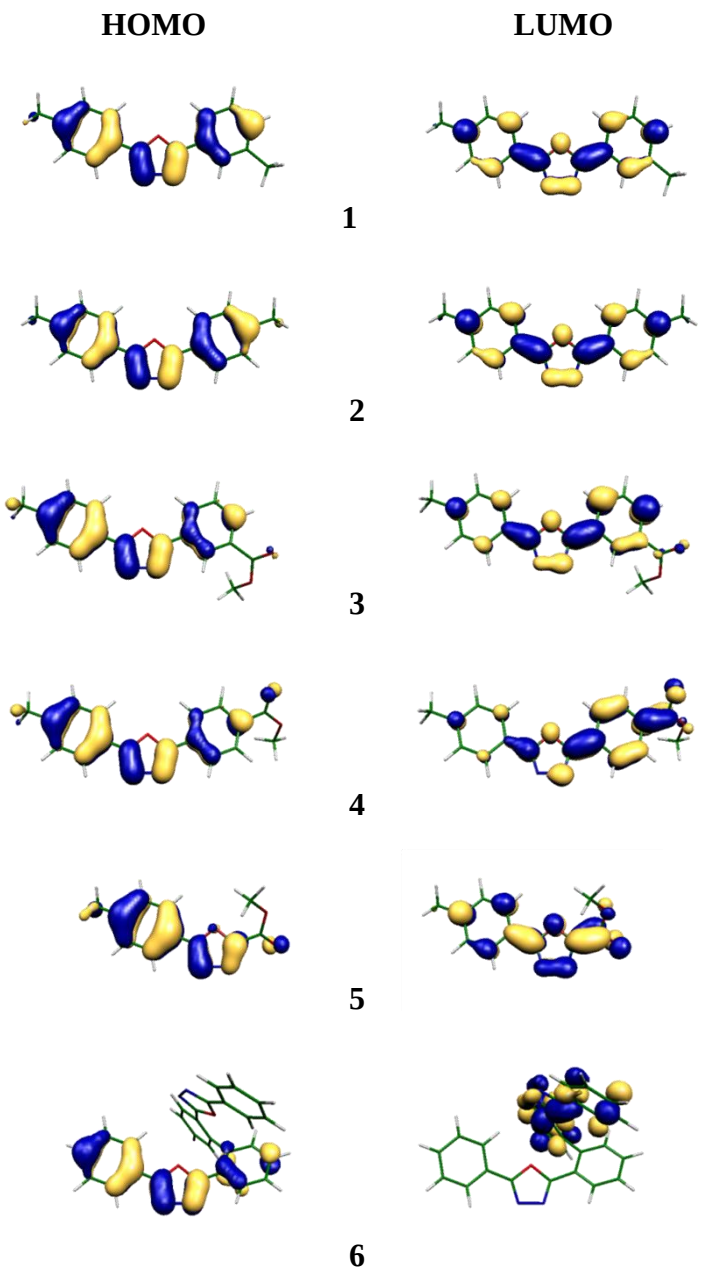

Figure 6.10 DFT/B3LYP wavefunctions of the frontier molecular orbitals in OXD derivatives **1**-**6**.

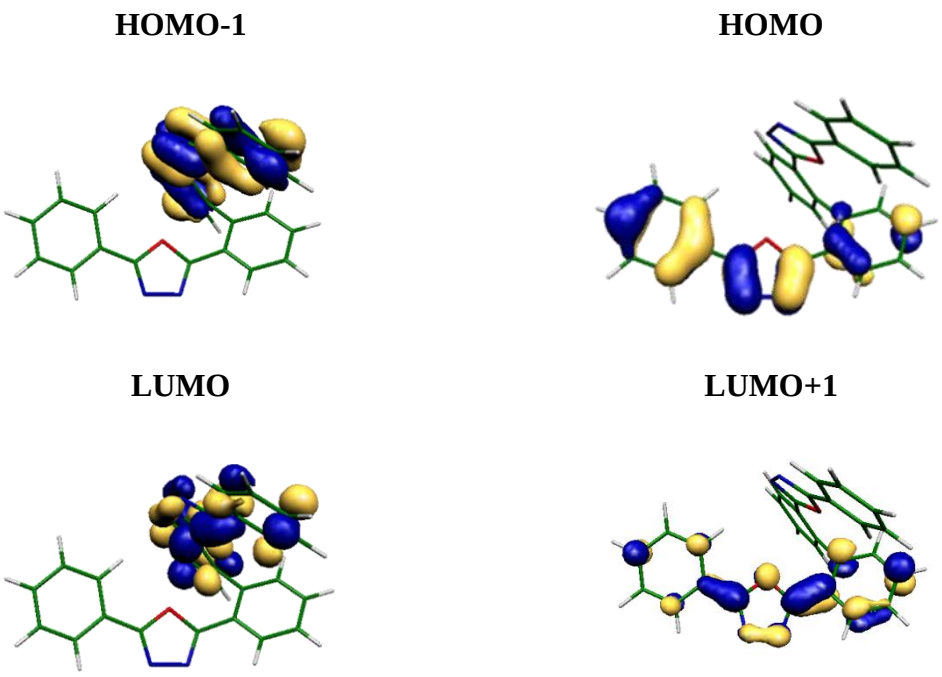

Figure 6.11 DFT/B3LYP wavefunctions of the molecular orbitals in compound **6**.

Singlet and Triplet Excited States of Oxadiazoles

The singlet and triplet excited-state energies of oxadiazole derivatives **1**-**6** are summarized in Table 6.11. The singlet excited states have energies in the range of 3.8-4.3 eV, in agreement with the absorption data found for oxadiazole-containing compounds.[229] Furthermore, the singlet excited states are characterized by HOMO to LUMO transitions. From the topology of the molecular orbitals shown in Figure 6.10, it is seen that this transition has a π-π* nature. However, in the case of OXD **6**, the singlet excited state is a charge-transfer state since HOMO and LUMO are localized on different parts of the molecule. Similarly, the charge-transfer character in the S_1 state is reported for related compounds.[229]

Table 6.11 TD-DFT/B3LYP calculated energies E (in eV) of the singlet (S_1) and triplet (T_1) excited states along with the singlet-triplet energy difference (ΔE_{ST}) of OXD derivatives **1**-**6**, based on the DFT-optimized S_0 geometries.

OXD	E (S_1)	E (T_1)	ΔE_{ST}
1	4.09	2.81	1.28
2	4.06	2.80	1.26
3	4.03	2.79	1.24
4	3.83	2.70	1.13
5	4.33	2.99	1.34
6	3.95	2.89	1.06

Although the position of the CH_3 substituent has almost no effect on the energetics of molecules **1** and **2**, the position of the $COOCH_3$ group changes the energies of the excited states to some extent. For instance, the singlet and triplet excited states of compound **4** are slightly red-shifted as compared to its geometric isomer **3** (see Table 6.11). Similar red-shifts are also observed in the experimental absorption and emission spectra of these compounds.[252]

The triplet excited states with energies in the range of 2.7-3.0 eV are characterized by HOMO to LUMO transitions for oxadiazoles **1**-**5**. For oxadiazole **6**, the HOMO and HOMO-1 lie very close in energy ($\Delta\varepsilon$ = 0.08 eV), and as a result the triplet state is found to be dominated by a transition from the HOMO-1 to the LUMO. From the topology of the molecular orbitals shown in Figure 6.11, it is seen that the HOMO-1 and LUMO are confined on the same half of the molecule. We note that half of compound **6** has nearly the same conjugation length as of compounds **1**-**4**. As a result, the triplet energies of these compounds are found to be very similar. Compound **5** with its smallest conjugation length in the series has the highest triplet energy.

TD-DFT calculations based on the ground-state geometry to obtain triplet energies do not take into account the geometry relaxation phenomena after

photoexcitation. Table 6.12 shows the DFT/B3LYP computed adiabatic, *i.e.*, between the relaxed S_0 and T_1 geometries, $S_0 \rightarrow T_1$ excitation energies in oxadiazole derivatives **1**-**6**. In this case, the triplet energies of OXDs **1**-**6** are found to be in the range of 2.5-2.8 eV. As a result, DFT calculations suggest that the OXD compounds **1**-**6** studied here can be appropriate hosts for green, red, and even light blue phosphorescent emitters. Indeed, OXD **6** has been reported to be a good electron-transport host for the green emitter $Ir(ppy)_3$ in PHOLED applications.[229]

Table 6.12 DFT/B3LYP calculated adiabatic $S_0 \rightarrow T_1$ energies (*E*) in OXDs **1**-**6**.

OXD	*E* (eV)	OXD	*E* (eV)
1	2.64	**4**	2.53
2	2.63	**5**	2.76
3	2.63	**6**	2.62

Hybrid Oxadiazole/Carbazole Compounds

Recently, bipolar hosts have attracted considerable interest in OLEDs, because they can induce balanced carrier injection and transport and, in addition, simplify device architectures.[233,234] However, there is a dilemma between the bipolar transporting properties and the band gap of the material, in the sense that electron-donating and electron-withdrawing moieties incorporated on bipolar molecules can lower the band gap of the material due to the intramolecular charge transfer. Low triplet energy of the host can cause reverse energy transfer from the guest back to the host leading to a decrease in device efficiency. To overcome this problem, it is common to break the π-conjugation between the electron-donating and electron-withdrawing moieties by introduction of steric groups[253-255] and/or *meta*-linkage[256,257] between the two moieties. Efficient blue (46 lm/W, 24%),[256] green (27.3 cd/A)[255] and orange (22 cd/A, 7.8%)[258] electrophosphorescence from such bipolar hosts has been reported.

As discussed above, carbazole derivatives are prominent as host materials because of their high triplet energy combined with good hole-transporting ability. Oxadiazole derivatives, on the other hand, are proven to be very effective in improving the injection and transport of electrons. Therefore, herein, we investigate a series of carbazole/oxadiazole hybrid molecules linked through the 9-position of the carbazole to a phenylene ring attached to the *ortho* position of the oxadiazole as bipolar host materials (Figure 6.12). This type of *ortho*-linked carbazole-oxadiazole hybrid host molecule is reported to reach a current efficiency of 77.9 cd/A for green and 13.6 cd/A for red electrophosphorescence.[233]

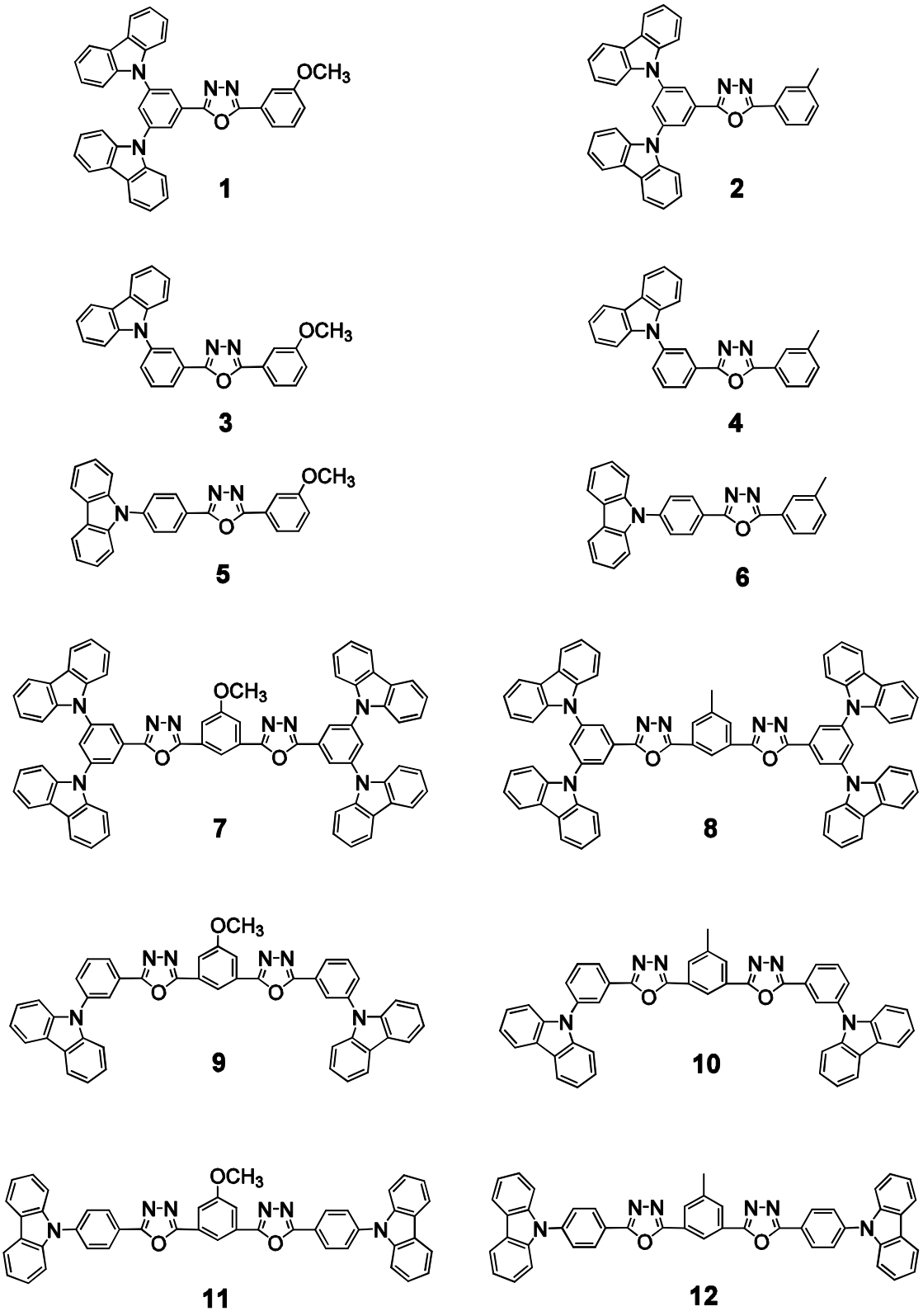

Figure 6.12 Chemical structures of the hybrid oxadiazole/carbazole compounds **1-12**.

Electronic Structure of Hybrid Oxadiazole/Carbazole Compounds

Table 6.13 summarizes the HOMO and LUMO energies of the hybrid oxadiazole/carbazole compounds **1-12**. As seen from the Table, substitution of OCH_3 with CH_3 has practically no effect on the HOMO and LUMO levels of these molecules. In addition, the HOMO levels stay almost identical (~5.5 eV) for all molecules in the series regardless of their molecular topology. On the contrary, the LUMO levels with energies in the range of 1.7-2.2 eV are more affected by the molecular architecture. The LUMOs of compounds **7-12** are lowered by 0.1-0.3 eV as compared to compounds **1-6**; this lowering can be explained by the increased π-delocalization seen in the LUMO of OXDs **7-12** (Figure 6.13). As we show below, the constant HOMO energies and slightly changing LUMO energies arise from the different localization patterns of the frontier molecular orbitals in these molecules.

Hybrid compounds **1-12** consist of both electron donor (carbazole) and acceptor (OXD) moieties, thus, well balanced carrier injection and transport could be expected. Indeed, hybrid oxadiazole/carbazole compounds have reduced HOMO energies (~5.5 eV) as compared to solely oxadiazole-containing compounds (≥6 eV) which may enable better hole injection in these compounds. In addition, the HOMO energies of the hybrid compounds are comparable to that of carbazole (~5.4 eV) further indicating their propensity for hole injection and transport. Hybrid oxadiazole/carbazole compounds also have deep LUMO levels, as was the case for oxadiazoles, suggesting favorable electron injection. Therefore, a good balance of carrier injection and transport can be anticipated with these hybrid materials.

Figure 6.13 shows the wavefunctions of the frontier molecular orbitals in compounds **1-12**. We see that hybrid oxadiazole/carbazole compounds show significant separation in the HOMO and LUMO distributions such that HOMOs and LUMOs are localized at the respective hole- and electron-transporting moieties (*i.e.*, HOMOs are localized on the carbazoles and LUMOs are localized on the oxadiazoles). This complete

separation of HOMO and LUMO to different parts of the molecules implies that the HOMO to LUMO transition in these molecules would have a strong charge-transfer character.

Table 6.13 B3LYP/6-31G* energies (in eV) of the frontier molecular orbitals in hybrid oxadiazole/carbazole (OXD/cbz) compounds **1-12**.

OXD/cbz	HOMO	LUMO	Δ(HOMO-LUMO)
1	-5.53	-1.92	3.61
2	-5.51	-1.89	3.62
3	-5.54	-1.78	3.76
4	-5.49	-1.75	3.74
5	-5.49	-1.77	3.72
6	-5.46	-1.74	3.72
7	-5.51	-2.16	3.35
8	-5.51	-2.16	3.35
9	-5.43	-2.05	3.38
10	-5.42	-2.05	3.37
11	-5.47	-2.02	3.45
12	-5.46	-2.02	3.44

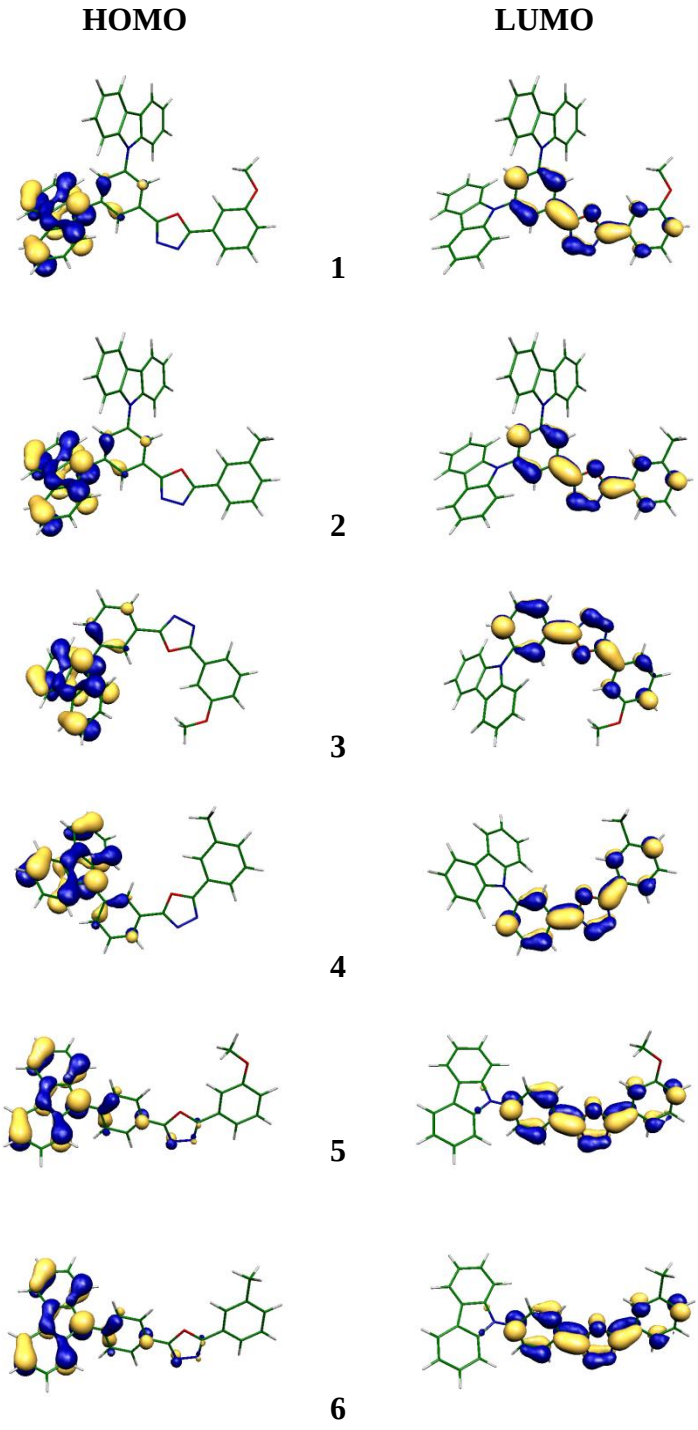

Figure 6.13 DFT/B3LYP wavefunctions of the frontier molecular orbitals in hybrid oxadiazole/carbazole compounds **1**-**12**.

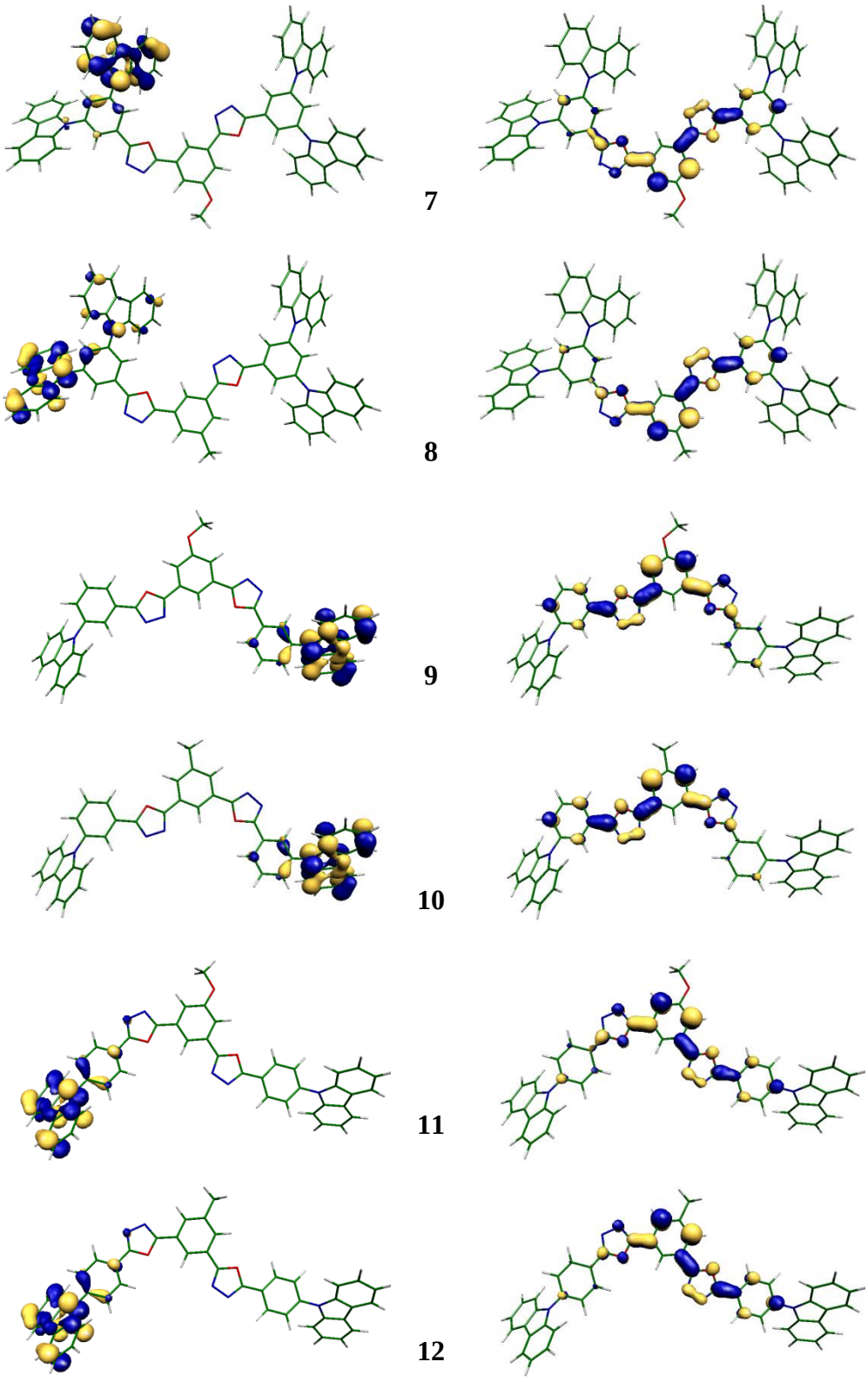

Figure 6.13 continued.

Singlet and Triplet Excited States of Hybrid Oxadiazole/Carbazole Compounds

The singlet and triplet excited states of hybrid oxadiazole/carbazole compounds **1-12** are summarized in Table 6.14. The low singlet energies (2.9-3.3 eV) are associated with charge-transfer type transitions from the HOMO located at the carbazole to the LUMO located at the oxadiazole. These energies are slightly lowered as compared to the triscarbazole derivatives discussed above (3.3-3.6 eV) which also exhibit CT singlet excited states.

The substitution of several carbazole units at different positions in oxadiazole exhibits little effect on the triplet energies. To understand this behavior, we investigated the structural changes upon relaxation into the T_1 state as well as the molecular orbitals contributing the most to the description of the lowest triplet state. We found that the largest structural changes upon $S_0 \rightarrow T_1$ transition take place on the central OXD moiety (see Figure 6.14). Furthermore, the analysis of the wavefunctions of the MOs showed that the lowest-triplet state in these hybrid compounds is predominantly oxadiazole in character (Figure 6.15). Consequently, all of these findings indicate that the electronic structure of oxadiazole/carbazole compounds in their triplet state is being dominated by the oxadiazole moiety.

Table 6.14 TD-DFT/B3LYP calculated energies E (in eV) of the singlet (S_1) and triplet (T_1) excited states along with the singlet-triplet energy difference (ΔE_{ST}) of hybrid oxadiazole/carbazole (OXD/cbz) compounds **1-12**.

OXD/cbz	E (S_1)	E (T_1)	ΔE_{ST}
1	3.10	2.71	0.39
2	3.11	2.75	0.36
3	3.25	2.74	0.51
4	3.24	2.78	0.46
5	3.26	2.65	0.61
6	3.27	2.67	0.60
7	2.91	2.67	0.24
8	2.92	2.67	0.25
9	3.02	2.70	0.32
10	3.02	2.69	0.33
11	3.10	2.59	0.51
12	3.11	2.59	0.52

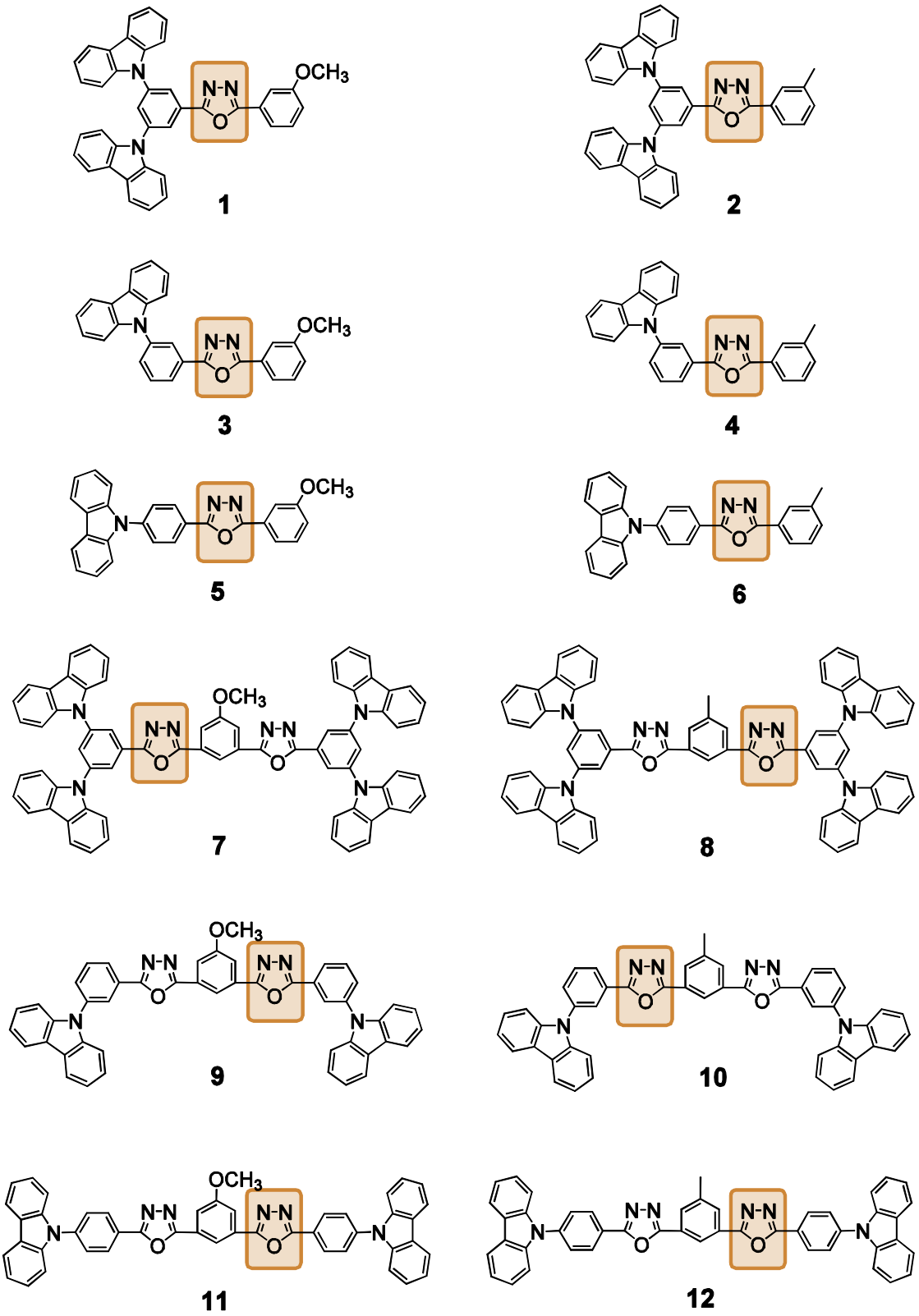

Figure 6.14 Locations of the largest geometrical changes (highlighted region) upon $S_0 \rightarrow T_1$ transition in hybrid oxadiazole/carbazole compounds **1-12**.

The TD-DFT/B3LYP calculated (vertical) triplet energies of the hybrid oxadiazole-carbazole compounds are in the range of 2.7-2.8 eV. These values are quite similar to the adiabatic T_1 energies calculated from the ΔSCF procedure (see Table 6.15). As a result, the triplet energies calculated by two methods differ only by 0.1 eV for this family of compounds. Therefore, on the basis of the TD-DFT and ΔSCF calculations, we conclude that these hybrid compounds can be effective host materials for green, red, and even light blue phosphorescent emitters.

Table 6.15 DFT/B3LYP calculated adiabatic $S_0 \rightarrow T_1$ energies (*E*) in hybrid oxadizole/carbazole (OXD/cbz) compounds **1-12**.

OXD/cbz	*E* (eV)	OXD/cbz	*E* (eV)
1	2.59	**7**	2.63
2	2.62	**8**	2.62
3	2.60	**9**	2.65
4	2.63	**10**	2.63
5	2.52	**11**	2.54
6	2.54	**12**	2.53

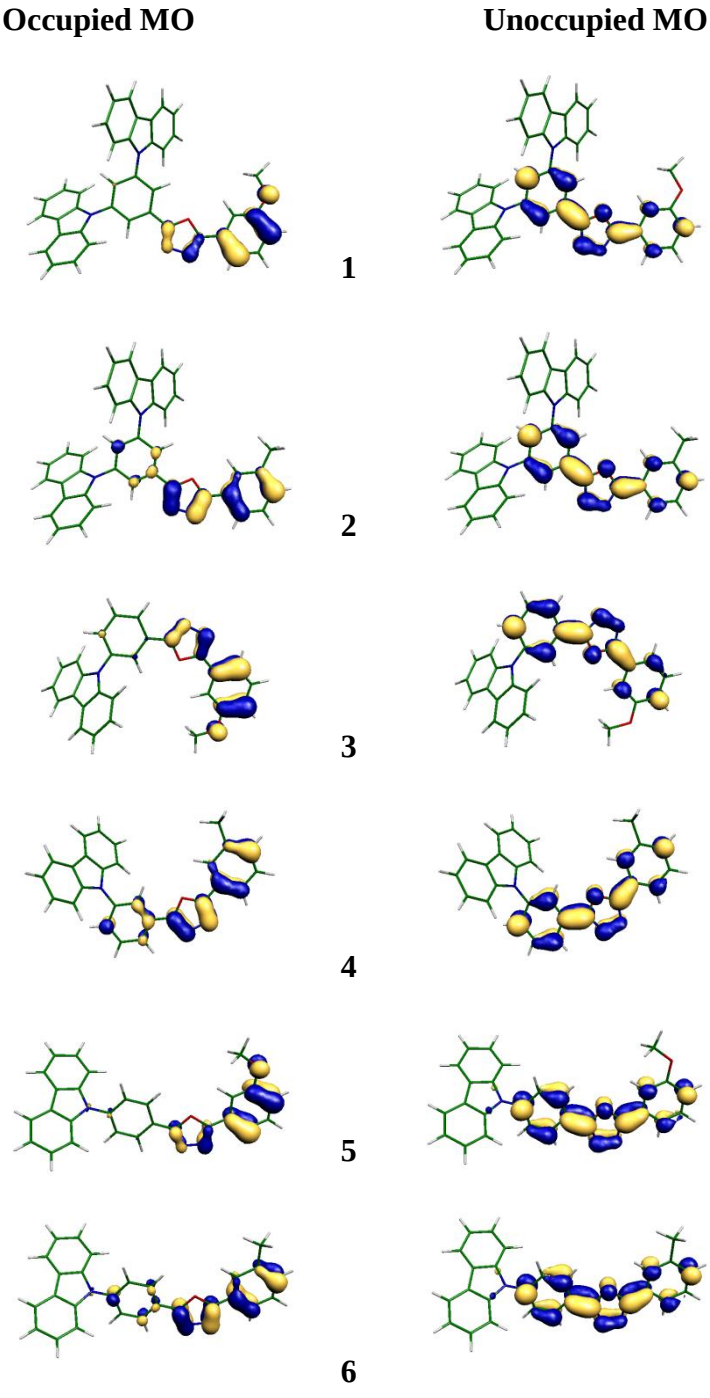

Figure 6.15 DFT/B3LYP wavefunctions of the molecular orbitals contributing the most to the description of the T_1 state in hybrid oxadiazole/carbazole compounds **1-12.**

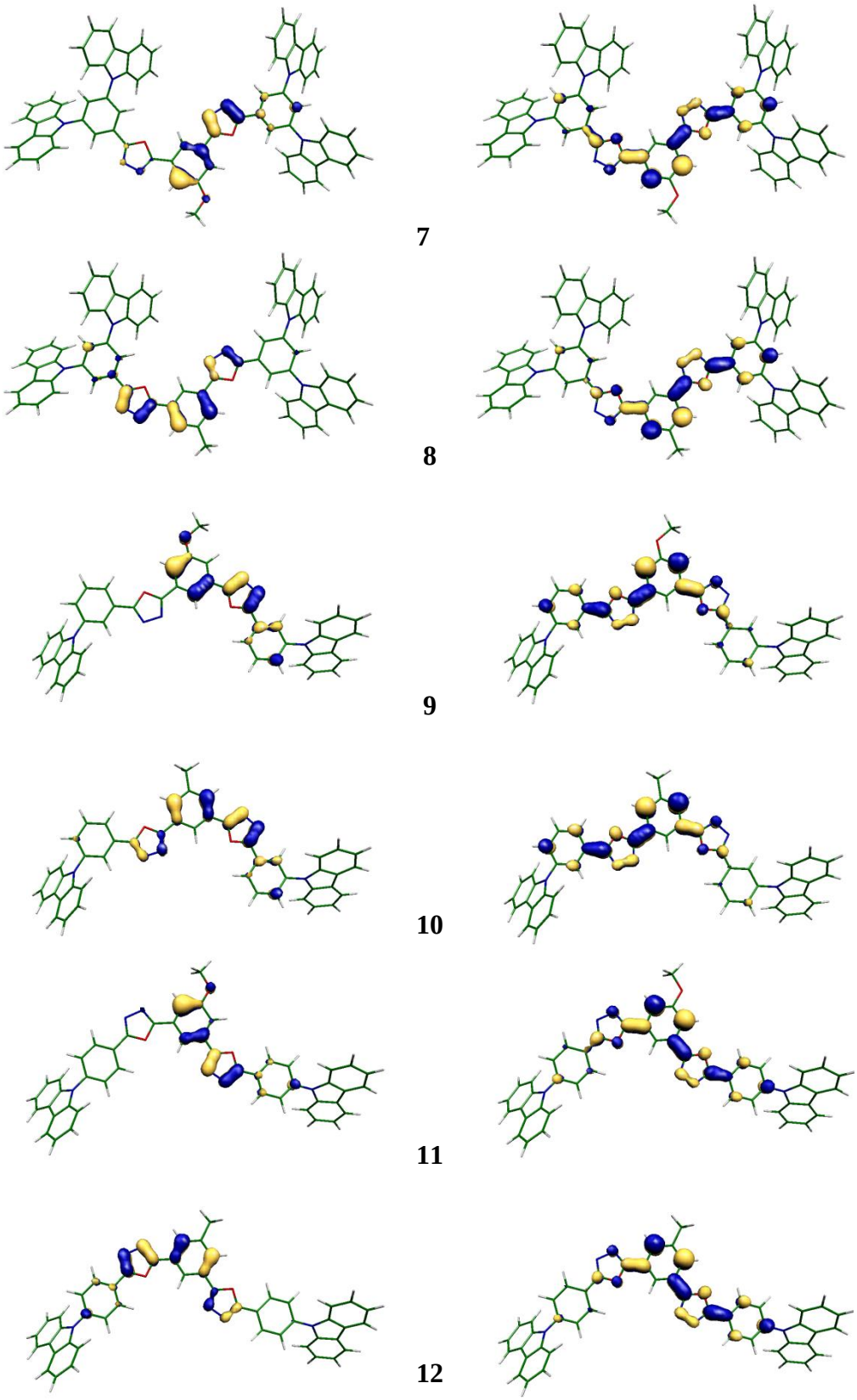

Figure 6.15 continued.

Organosilicon Compounds

As we already discussed, up to date, most suitable host materials for blue phosphorescence are mainly high triplet energy carbazole-based materials. The high triplet energy is achieved by limited π-conjugation of the central linkage containing either a short or a conformationally twisted core. More recently, host materials combining the characteristics of ultrahigh energy gap of arylsilanes and high triplet energy of 1,3-bis(9-carbazolyl)benzene (mCP) have been reported for highly efficient blue electrophosphorescence.[244] Due to the significant steric hindrance of the bulky silyl center, the promising performance of these novel host materials is attributed to their high triplet state energy and thin film stability. This observation triggers many possibilities in the molecular design of host materials which can combine the characteristics of different structural skeletons. This fact motivated us to study the electronic properties of organosilicon compounds shown in Figure 6.16 as potential wide energy gap host materials for blue electrophosphorescence applications. The bulky triphenylsilyl group is expected to block the electroactive sites of small molecules such as biphenyl and carbazole leading to high energy gaps. We note that, among the series, compounds **1**-**6** are arylsilane derivatives whereas compound **7** is a silole derivative.

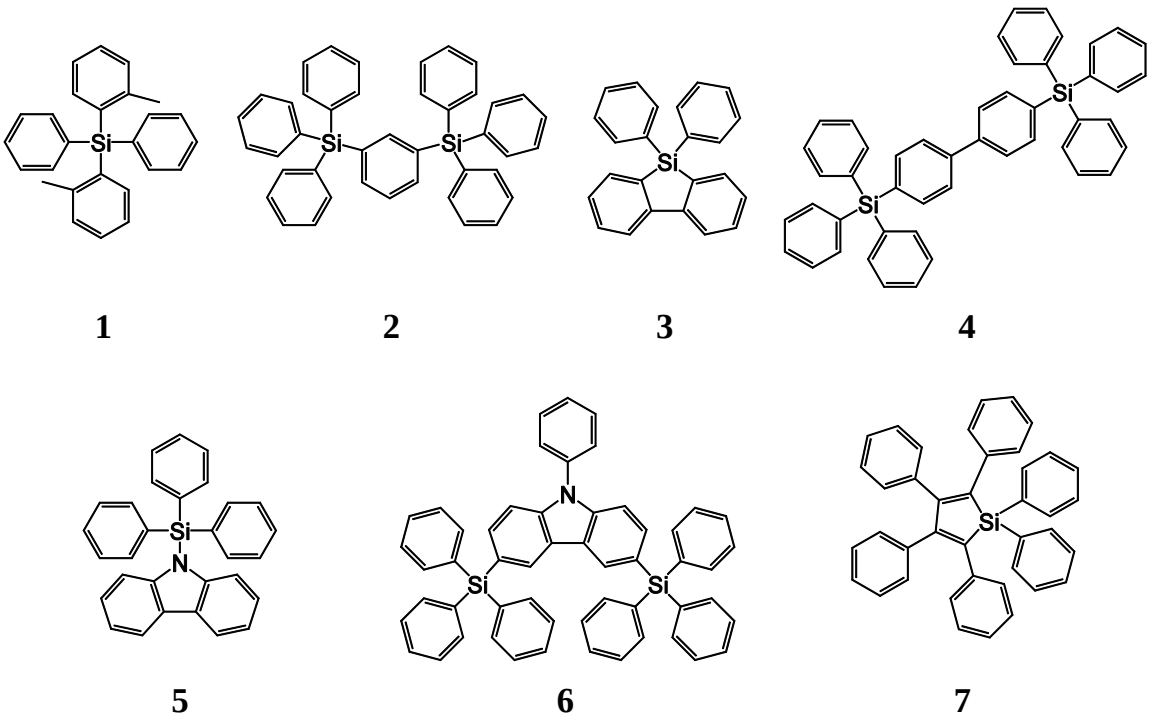

1 **2** **3** **4**

5 **6** **7**

Figure 6.16 Chemical structures of the organosilicon compounds **1**-**7** investigated here.

Electronic Structure of Organosilicon Compounds

Table 6.16 summarizes the HOMO and LUMO energies of the organosilicon compounds **1**-**7** studied here. Among the series, compounds **1** and **2** possess very deep HOMO and shallow LUMO levels giving rise to large HOMO-LUMO energy gaps (~5.9 eV). The large energy gaps are attributed to directly avoiding the phenyl-phenyl linkages by means of electronically isolating each phenyl ring in the structure. It is desirable for the ultrawide energy gap hosts (such as **1** and **2**) HOMO and LUMO energies to be large enough to lie below and above the same levels of the dopant, respectively. The guest energy levels are then nested between the HOMO-LUMO gap of the host, thereby eliminating the potential for exciplex formation between the dopant and host. Hence, the guest acts as the primary site for electron and hole conduction within the emissive layer as well as the trap site for excitons.

The HOMO energies of the rest of the compounds are higher than that of compounds **1** and **2**, presumably due to the presence of the phenyl-phenyl linkages (see Figure 6.17). Compounds **3** and **4** exhibit the HOMO/LUMO characteristics of the biphenyl linkage, whereas **5** and **6** show carbazole character. In the case of compound **6**, there is almost a complete separation of the HOMO and LUMO levels such that the HOMO is localized on the carbazole and the LUMO is localized on the triphenylsilyl group giving rise to a charge-transfer type HOMO to LUMO transition. Among them, compound **7** has the smallest HOMO-LUMO energy gap (~3.7 eV) due to its higher-lying HOMO and lower-lying LUMO levels. The different behavior of this compound arises from its silole nature (note that the rest of the compounds in the series are arylsilane derivatives with low HOMOs and large HOMO-LUMO gaps).

Table 6.16 B3LYP/6-31G* energies (in eV) of the frontier molecular orbitals in organosilicon compounds **1**-**7**.

Compound	HOMO	LUMO	Δ(HOMO-LUMO)
1	-6.36	-0.50	5.86
2	-6.52	-0.59	5.93
3	-5.82	-1.06	4.76
4	-6.03	-1.05	4.98
5	-5.36	-0.75	4.61
6	-5.41	-0.76	4.65
7	-5.30	-1.57	3.73

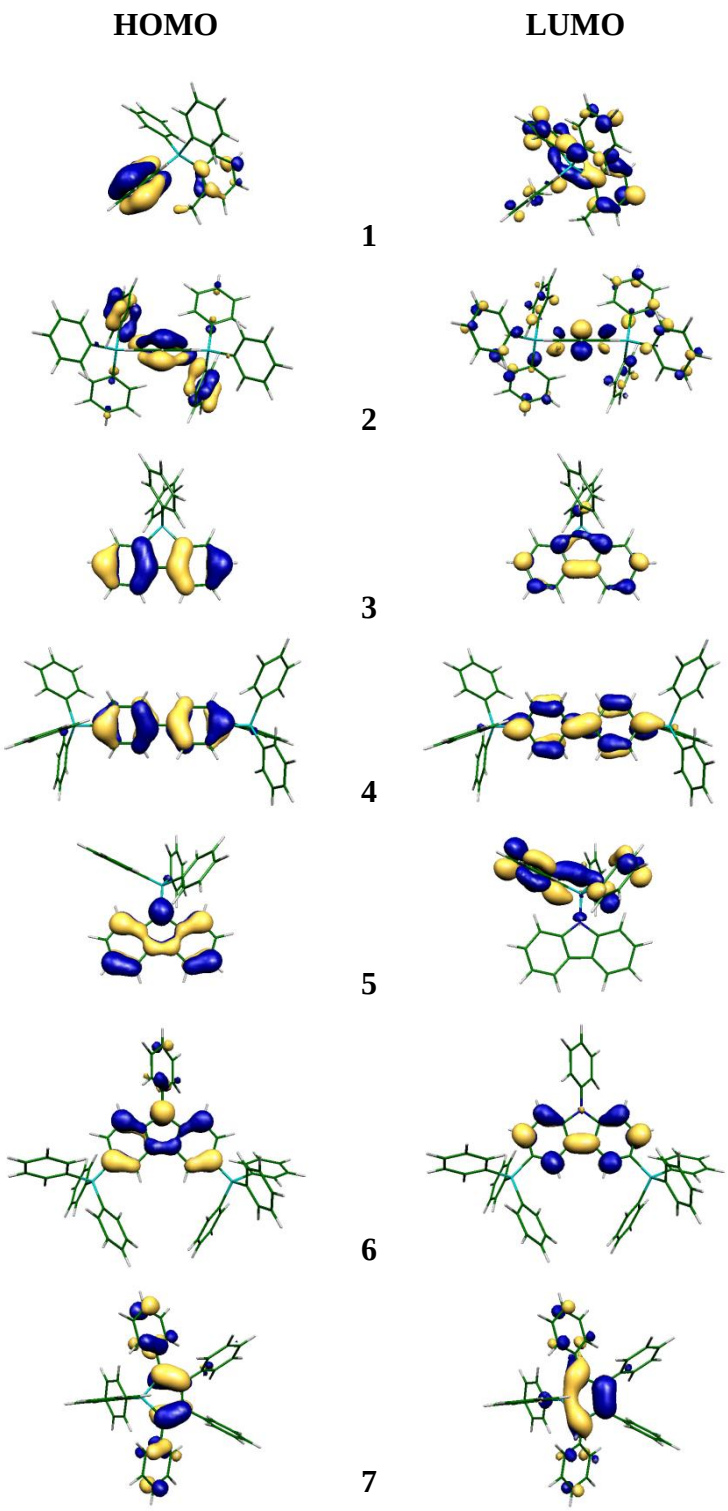

Figure 6.17 DFT/B3LYP wavefunctions of the frontier molecular orbitals in organosilicon compounds **1-7**.

Singlet and Triplet Excited States of Organosilicon Compounds

Table 6.17 summarizes the singlet and triplet excited state energies of the organosilicon compounds **1**-**7**. In addition to their large HOMO-LUMO gaps, compounds **1** and **2** have high singlet and triplet energies. Indeed, the triplet energies of these compounds (~3.6 eV) far exceed the triplet energies of most compounds investigated so far such as triscarbazoles (2.9-3.1 eV) and phosphine oxides (2.9-3.2 eV). The triplet energy of **4** is similar to that of biphenyl as a result of the localization of the triplet state on the biphenyl moiety (see Figure 6.18). For compounds **5** and **6**, TD-DFT/B3LYP estimates of the triplet energies are practically the same as for carbazole (E (T_1) = 3.19 eV), indicating that the triphenylsilyl substitution has simply no effect on the triplet state of these molecules. Indeed, as seen in Figure 6.18, the triplet states of molecules **5** and **6** are localized on the carbazole moieties without any contributions from triphenylsilyl substituents.

Table 6.17 TD-DFT/B3LYP calculated energies E (in eV) of the singlet (S_1) and triplet (T_1) excited states along with the singlet-triplet energy difference (ΔE_{ST}) of organosilicon compounds **1**-**7**.

	E (S_1)	E (T_1)	ΔE_{ST}
1	4.40	3.62	0.78
2	4.48	3.63	0.85
3	3.90	2.93	0.97
4	3.71	3.16	0.55
5	3.70	3.18	0.52
6	3.91	3.16	0.75
7	3.24	1.92	1.32

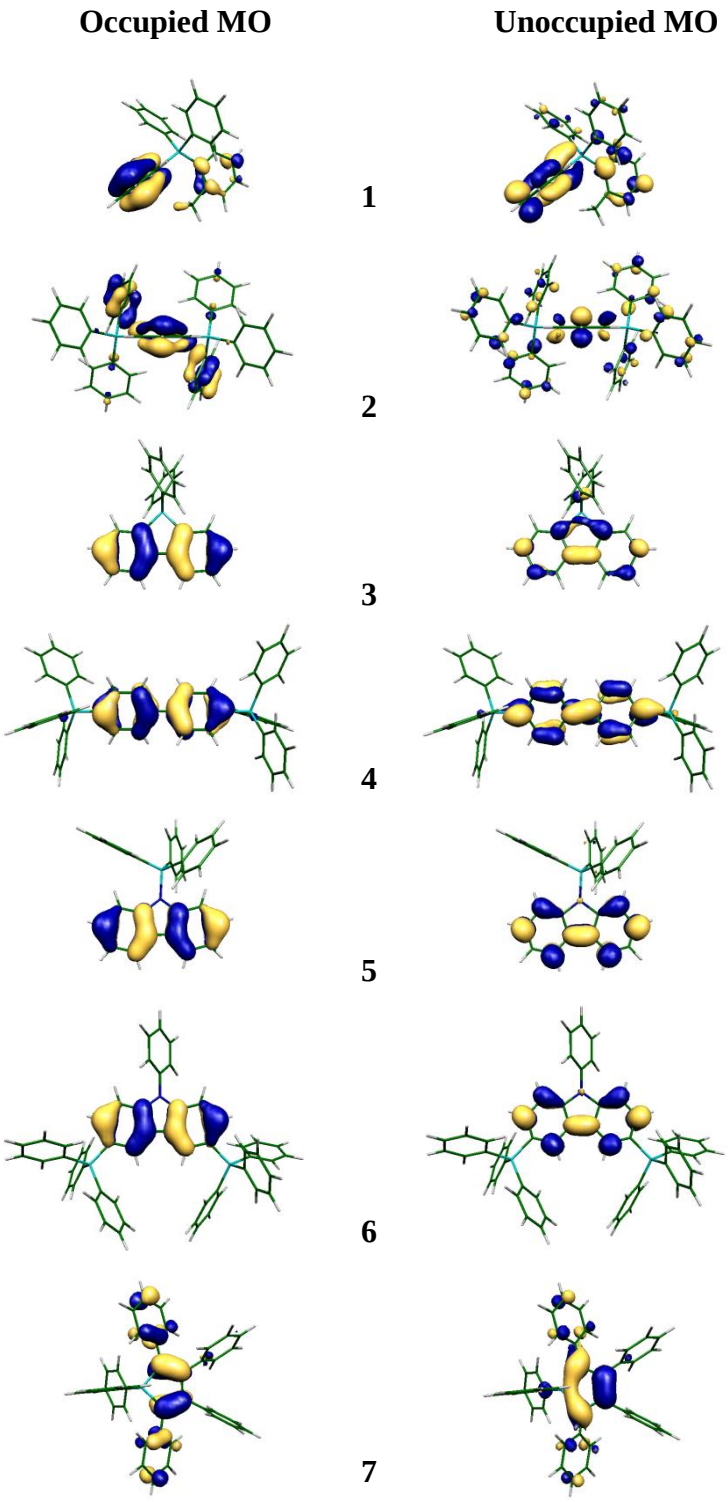

Figure 6.18 DFT/B3LYP wavefunctions of the molecular orbitals contributing the most to the description of the T_1 state in organosilicon compounds **1**-**7**.

Table 6.18 DFT/B3LYP calculated adiabatic $S_0 \rightarrow T_1$ energies ($E^{calc.}$) along with the available experimental triplet energies ($E^{exp.}$) in organosilicon compounds **1**-**7**.

Compound	$E^{calc.}$ (eV)	$E^{exp.}$ (eV)	Ref.
1	3.46	3.50[a]	259
2	3.61	3.50[a]	259
3	2.83		
4	2.91	2.76[a]	260
5	3.16		
6	3.17		
7	1.42		

[a]Estimated from the emission maxima of the phosphorescence spectra in 2-methyl-THF at 77 K.

The organosilicon compounds investigated here have also high adiabatic triplet energies (see Table 6.18), except for molecule **7** in which there occurs a large geometry relaxation energy. The large geometry relaxation upon $S_0 \rightarrow T_1$ transition lowers the triplet energy. Thus, a rigid structure with little geometric difference between S_0 and T_1 is desirable. Considering their high triplet energies (except for **7**), these molecules may function as effective host materials for blue phosphors. For instance, according to our calculations, the triplet energies of the arylsilanes studied here are higher than that of the prominent blue emitter FIrpic (E (T_1) = 2.7 eV).[199]

Conclusions

We have addressed the ground-state electronic structure as well as the singlet and triplet excited states of five classes of host materials (triscarbazoles, phosphine oxides, oxadiazoles, hybrid oxadiazole/carbazoles, and organosilicon compounds) by means of quantum-chemical calculations. Our key finding is that substitution of small molecules with phosphine oxides and carbazoles (as in the case of triscarbazoles) modifies HOMO/LUMO levels without much affecting the triplet energy. Interestingly, an

intuitive prediction of the HOMO/LUMO levels upon substitution in these molecules is not always possible due to the combination of stabilizing inductive and destabilizing MO effects. In the case of phosphine oxides, molecular orbitals are localized on the central units giving rise to localized singlet and triplet excitations. For triscarbazoles, differences in the localization pattern of the molecular orbitals suggest localized triplet states (*i.e.*, triplet exciton is localized on the central units) and charge transfer singlet states. Due to this localized nature of the triplet excitons, phosphine oxides and triscarbazoles maintain the high triplet energy of the small building blocks (monomers) to accommodate blue triplet emitters. Oxadiazoles exhibit deep HOMO/LUMO levels making them good candidates as hole-blocking/electron-accepting materials. In the case of hybrid oxadiazole/carbazole compounds, a dozen systems have been examined, and it is found that there is significant separation in the HOMO and LUMO distributions such that HOMOs and LUMOs are localized at the respective hole- and electron-transporting moieties (*i.e.*, HOMOs are localized on the carbazole and LUMOs are localized on the oxadiazole moities). This complete separation of the HOMO and LUMO to different parts of the molecules implies that the HOMO $\rightarrow$ LUMO transition becomes a typical charge transfer. The substitution of several carbazole units at different positions in oxadiazole exhibits little effect on the triplet energies, indicating that the electronic structure of hybrid oxadiazole/carbazole compounds in their triplet states are dominated by the oxadiazole moiety. The arylsilane derivatives, in general, are characterized by large HOMO-LUMO energy gaps, and high triplet energies among the five classes of host molecules studied, making them promising candidates as hosts for deep blue phosphors.

The TD-DFT/B3LYP estimates of the energy and nature of singlet and triplet excitations are usually found to be in line with the experimental observations. As a result, this computationally efficient theoretical approach can be used as a tool to screen

potentially interesting molecular systems as hosts for blue electrophosphorescence applications.

CHAPTER 7

TRIPLET EMITTERS FOR PHOSPHORESCENT OLEDs

Introduction

Utilization of organic transition metal complexes (such as Os^{II}, Ru^{II}, Re^{I}, Ir^{III}, and Pt^{II}) in organic light-emitting diodes (OLEDs) has gained much interest since the first report of Forrest and co-workers.[218] The strong spin-orbit coupling (SOC) of the heavy metal allows a very fast intersystem crossing (ISC) between the singlet and triplet excited states and allows the excitation to be stored in the lowest long-lived triplet state. Due to the participation of the triplet excitons in emission, in theory, internal quantum efficiencies as high as 100% can be achieved when OLED emissive layers are doped with phosphorescent emitters.[219] For full-color display applications, the realization of red, green, and blue (RGB) colors is necessary. The green emitting complex tris(2-phenylpyridine)iridium [$Ir(ppy)_3$] has been known for years,[261] and very high quantum efficiencies (greater than 80%) have been achieved when this complex is incorporated in devices.[18,262] Low energy gap red phosphors have been obtained successfully by extending the π-electron delocalization through the incorporation of highly conjugated groups into the ligand chromophore;[263] Adachi *et al.* have reported very high efficiency red emitting devices based on benzothienylpyridine ligands.[222] However, the realization of high-performance blue organic phosphorescence still remains a challenge owing to the difficulty of maintaining the necessary high energy gap as well as the high quantum yield and good stability for device applications.

The heteroleptic complex bis(4',6'-difluorophenylpyridinato)-iridium(III) picolinate (FIrpic) is considered, thus far, as the benchmark for blue phosphorescent materials. However, since FIrpic actually provides greenish-blue emission, there has been a great effort in academia and industry to develop saturated and highly efficient deep blue phosphors.[264-270] One strategy to shift the emission to the blue is to substitute picolinate

with other ancillary ligands such as triazolate, tetrazolate, bis(pyrazolyl)borate, diphosphine chelates, *tert*-butylcyanide, and *N*-heterocyclic carbene ligands.[268,270-272] For instance, the use of carbene ligands was successful in producing complexes that are claimed to emit 'true blue' light and even into the near UV. The luminescence quantum yields in these first generation complexes were, however, quite modest.[271]

Previous studies showed that phosphorescence in Ir complexes originate from the triplet ligand-centered (^{3}LC) π-π* and metal-to-ligand charge-transfer (^{3}MLCT) excited states. One important issue is the extent of mixture of LC and MLCT characters in the emissive triplet state. The admixture of these charge-transfer states and thus the nature of the lowest excited states depend strongly on the substitution pattern.[273] For instance, the LC/MLCT ratio can be modulated by grafting electroactive substituents that change the localization of the triplet excitons in heteroleptic complexes. The concept of emission color tuning by grafting electroactive substituents relies on the fact that the lowest excited state is often relatively well described as a HOMO to LUMO transition. Introduction of electroactive substituents at different positions of the ligands will, in general, change the HOMO-LUMO gap and, consequently the emission energy (the HOMO-LUMO gap here is the gap between the orbitals involved in the lowest energy electronic transition). Thus, tuning the emission wavelength throughout the entire visible spectrum relies on selective HOMO stabilization or LUMO destabilization. For example, according to DFT calculations performed on heteroleptic Ir complexes containing phenylpyrazole (ppz) and isoquinolinecarboxylic acid (iq) ligands, the HOMO and LUMO levels are localized on different ligands;[274] this localization pattern gives the possibility to modify the energies of the HOMO and LUMO levels independently, thus allowing for easier emission color control.

To design efficient blue phosphors, it is critical to understand the structure-photophysical property relationships. In this sense, quantum-chemical calculations offer great possibilities in elucidating the structural and electronic properties of both the

ground and excited states of transition metal complexes. Here, we present a detailed study of the electronic properties of a series of Ir(III)-based homoleptic (IrL_3) and heteroleptic (IrL_2L') complexes with changes in their ligand systems.

The homoleptic compounds given in Figure 7.1 comprise the ligands 2-phenylpyridine (ppy) and its fluorinated derivatives ($F_n$ppy, where n=2-4), 1-phenylpyrazole (ppz), and 1-phenyl-3-methylbenzimidazole (pmb). These compounds can serve as prototypical cyclometalated phosphors since they are well characterized both by theory and experiment. Iridium (III) complexes with ppy ligands emit green light; while, complexes carrying fluorinated phenylpyridines are reported to emit in the blue region.[262] Complexes utilizing pyrazolyl and imidazolyl type carbene ligands are promising as deep blue emitters.[271]

The homoleptic complexes exist as two stereoisomers, facial and meridional. The photophysical investigation of both stereoisomers sheds light on the differences in the nature of their low energy excited states, which are related to the different symmetries of facial and meridional configurations.

The heteroleptic FIrpic complex is considered as a common standard for "blue" phosphorescent materials. By analysis of the ground and lowest-lying excited state properties (such as orbital compositions and transition characters), we can explore the nature of absorption and emission properties of these complexes.

Our goal is to better understand the factors (*e.g.*, ligand isomerization, substitution, etc.) affecting the phosphorescence behavior. Acquiring such knowledge would allow us to predict the properties of light emission for a novel complex from its structural design.

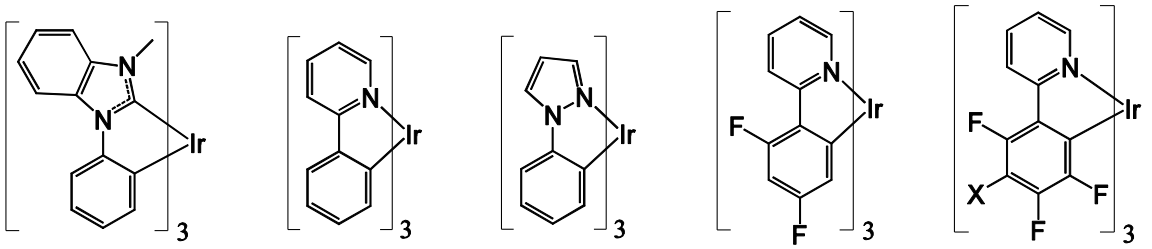

Figure 7.1 Chemical structures of the tris-cyclometalated Ir^{III} complexes. Abbreviations used throughout the text are given for each structure.

This Chapter is organized as follows: In the next section, the influence of ligand orientation (facial *vs*. meridional) on the geometries, frontier molecular orbitals, and excited-state properties such as excitation energies and phosphorescence lifetimes are presented. After that, the role of ligand tuning is introduced where special emphasis is put on the effect of fluorination and replacing pyridine with pyrazole and benzimidazole ligands on the emission and electrochemical properties of tris-cyclometaleted Ir complexes. Then, we turn to heteroleptic Ir complexes where the influence of electroactive substituents attached to cyclometalated and ancillary ligands is reviewed. The relations between the ligand chemical structure and nature of emission are pointed out. A theoretically designed isomer of the heteroleptic complex FIrpic is also considered in this part. In the last subsection, studies of the solvent impact on absorption and emission are given.

Effect of Ligand Orientation on Emission: Facial *versus* Meridional

Metal d^6 tris-complexes with asymmetric chelate ligands can have either a facial (*fac*) or a meridional (*mer*) configuration depending on the mutual disposition of the three monoanionic phenylpyridine ligands around the iridium ion (Figure 7.2). While there is no symmetry element present in the meridional configuration, the facial arrangement is characterized by the presence of a C_3 axis which makes the three phenylpyridine ligands

chemically equivalent. The *fac* isomers are well documented in the literature,[261,262,275,276] whereas the *mer* isomers have only recently been studied.[262,269]

Isolated samples of *mer*-Ir(C^N)$_3$ complexes can be thermally and photochemically converted to facial forms, indicating that the meridional isomers are kinetically favored products while the facial isomers, obtained at higher temperatures, are thermodynamically favored.[262] The lower thermodynamic stabilities of the meridional isomers are likely related to structural features of these complexes; that is, the meridional configuration places strongly *trans* influencing phenyl groups opposite each other, whereas all three phenyl groups are *cis* in the facial complexes. Tris-chelates with cyclometalating ligands such as 2-phenylpyridyl (ppy) have pronounced differences in the spectroscopic and photophysical properties between the facial and meridional isomers due to the marked disparity in the electronic and coordinating characteristics of the two types of coordinating ligand, that is, formally anionic phenyl and neutral pyridyl segments.[262] The meridional isomers are observed to be easier to oxidize, to exhibit broad, red-shifted emission, and to have lower quantum efficiencies than their facial counterparts.[262,271]

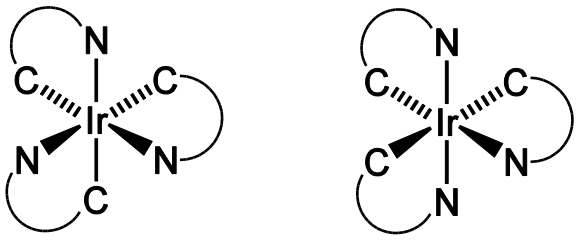

***fac*-Ir(*C*^*N*)$_3$** **_mer_-Ir(*C*^*N*)$_3$**

Figure 7.2 Illustration of the *fac vs*. *mer* orientation in tris-cyclometalated Ir^{III} complexes. All the phenyl rings are *cis* with respect to one another in the *fac* orientation; whereas, they are mutually *trans* in the *mer* configuration.

In the following subsections, we analyze the geometric, electronic, and excited-state properties (excitation energies, dipole moments, and phosphorescence lifetimes) of

facial *vs*. meridional Ir complexes in order to understand the relations between the ligand orientation and photophysical behavior of these compounds. The geometries are obtained at the DFT/(U)B3LYP level with the 6-31G basis set for ligands and LANL2DZ for iridium. Excitation energies are calculated using the TD-DFT method at the same level of theory.

Geometries

The results of the DFT/(U)B3LYP calculated Ir-C and Ir-N bond lengths in the singlet ground (S_0) and excited triplet (T_1) states of the facial and meridional isomers of $Ir(ppy)_3$ are given in Table 7.1. Since the facial isomer of $Ir(ppy)_3$ sits on a three-fold axis, this leads to identical ground-state Ir-C and Ir-N bond lengths of 2.036 and 2.167, respectively. Crystallographic analysis also reveals that *fac*-$Ir(ppy)_3$ has similar Ir-C (2.061 Å) and Ir-N (2.071) bond lengths,[277] although the calculated Ir-N distances show some deviation from the experimental value. The bond lengths in the meridional isomer differ markedly from those of the facial isomer. The Ir-C bond *trans* to a pyridyl group (Ir-C1 = 2.021 Å) and the Ir-N bond *trans* to the phenyl group (Ir-N3 = 2.191 Å) are nearly the same length as the Ir-C and Ir-N bonds of the facial isomer. The Ir-C bonds *trans* to phenyl groups (Ir-C2 = 2.094 Å and Ir-C3 = 2.110 Å) have lengths markedly longer than the Ir-C bonds of the facial isomer, consistent with the significant *trans* influence of phenyl groups on each other. In contrast, the Ir-N bonds of the mutually *trans* pyridyl groups in the meridional complex (Ir-N1 = 2.061 Å and Ir-N2 = 2.081 Å) are significantly shorter than Ir-N bonds of the facial isomer. This is consistent with the weaker *trans* influence of a pyridyl group relative to a phenyl ligand.[262] Likewise, the calculated Ir-C and Ir-N bond lengths in the triplet state of the *mer* isomer have similar length alternations as those observed in the ground state.

***fac*-Ir(ppy)$_3$** **mer-Ir(ppy)$_3$**

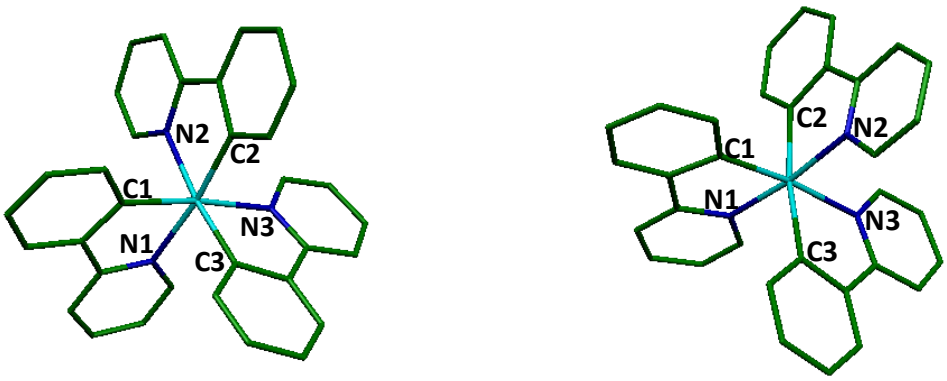

Table 7.1 Comparison of selected bond distances (Å) for *fac*-Ir(ppy)$_3$ and *mer*-Ir(ppy)$_3$ in the singlet ground state (S_0) and excited triplet state (T_1).

	S_0 state		**T_1 state**	
Bond	*fac*-Ir(ppy)$_3$	*mer*-Ir(ppy)$_3$	*fac*-Ir(ppy)$_3$	*mer*-Ir(ppy)$_3$
Ir-C1	2.036	2.021	2.027	1.992
Ir-C2	2.036	2.094	2.025	2.064
Ir-C3	2.036	2.110	2.027	2.113
Ir-N1	2.166	2.061	2.163	2.078
Ir-N2	2.167	2.081	2.161	2.070
Ir-N3	2.167	2.191	2.163	2.308

Frontier Molecular Orbitals

The DFT/B3LYP-calculated frontier orbital energies for *fac* and *mer* isomers of Ir(ppy)$_3$ and Ir(pmb)$_3$ are given in Table 7.2. Our results suggest that the HOMO energies of the meridional isomers are higher and the LUMO energies lower than those of the facial forms. As a result, the HOMO-LUMO gaps of *mer* isomers are decreased by about 0.2 eV as compared to *fac* counterparts. This explains the observed red-shifted emission in meridional compounds.[262,271] Furthermore, our results from DFT calculations, in accordance with electrochemical measurements,[262] indicate that it should be easier to both oxidize and reduce meridional Ir(ppy)$_3$ and Ir(pmb)$_3$ than would be the case for

facial analogues. Indeed, the oxidation potentials of *fac*- and *mer*-Ir(pmb)$_3$ are reported to be 0.48 and 0.31 V *vs*. Fc^+/Fc, respectively.[271]

Table 7.2 Energies (in eV) of the frontier molecular orbitals in facial and meridional isomers of the Ir complexes.

Molecule	HOMO	LUMO	Δ(HOMO-LUMO)
fac-Ir(ppy)$_3$	-4.80	-1.23	3.57
mer-Ir(ppy)$_3$	-4.68	-1.28	3.40
fac-Ir(pmb)$_3$	-4.86	-0.59	4.27
mer-Ir(pmb)$_3$	-4.75	-0.71	4.04

The HOMO and LUMO wavefunctions for the facial and meridional Ir(ppy)$_3$ and Ir(pmb)$_3$ complexes are shown in Figure 7.3. The HOMOs for both isomers of Ir(ppy)$_3$ consist of a mixture of phenyl-π and Ir-d orbitals. The LUMO – while predominantly phenylpyridine in character – is delocalized among the three ligands in the *fac* isomer as opposed to being localized on two ppy ligands in the *mer* isomer. Likewise, the HOMO of the facial isomer of Ir(pmb)$_3$ consists of metal and three pmb ligands, while the LUMO is delocalized among the three pmb ligands (mainly on the benzimidazolyl group). For the meridional complex, the HOMO is located largely on the metal and two pmb ligands (mostly on the phenyl portion) whereas the LUMO is primarily localized on the benzimidazolyl ring of one of the pmb ligands. Finally, on the basis of the orbital diagrams, the HOMO to LUMO transition in these complexes can be characterized as a metal-to-ligand charge-transfer (MLCT) with an admixture of ligand-centered (LC) and/or interligand π-π* transitions.

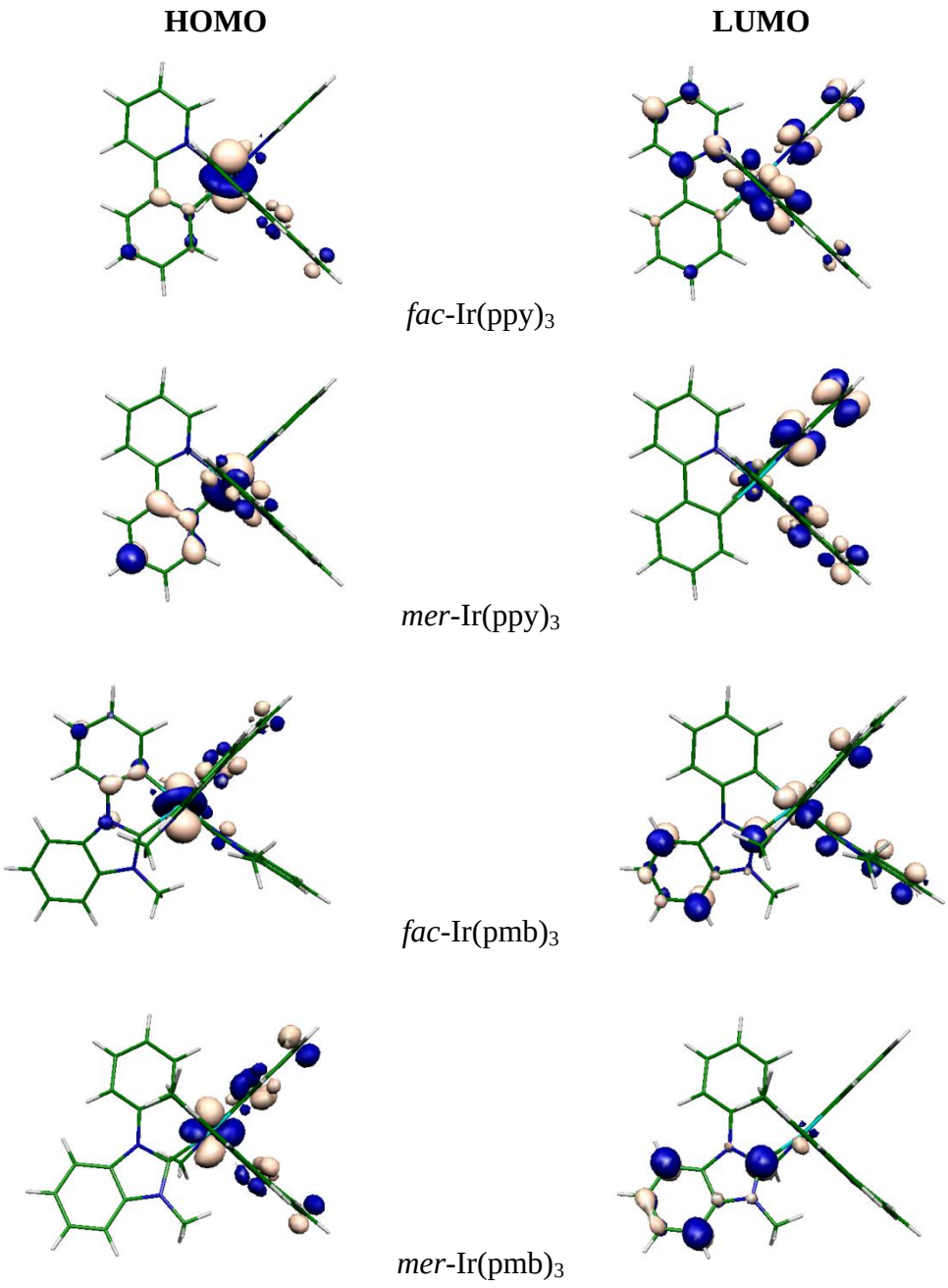

Figure 7.3 DFT/B3LYP wavefunctions of the frontier molecular orbitals in the facial and meridional isomers of Ir(ppy)$_3$ and Ir(pmb)$_3$ complexes.

Excitation Energies

The low-lying excited triplet and singlet states in the facial and meridional isomers of Ir(ppy)$_3$ and Ir(pmb)$_3$ are studied using the TD-DFT technique on the previously optimized ground-state (S_0) geometries. The vertical excitation energies for

the lowest three triplet and singlet states calculated at the optimized ground-state structure of $Ir(ppy)_3$ and $Ir(pmb)_3$ complexes are given in Tables 7.3 and 7.4, respectively. The nature of the orbitals involved in the dominant excitation process is also shown. The lowest triplet state T_1 in *fac*-$Ir(ppy)_3$ is calculated to lie at 2.59 eV, compared to 2.7 eV observed in absorption and 2.5 eV in emission.[261,276] The nearby triplet states (T_2 and T_3) appear extremely close in energy (within 0.01 eV) to T_1. All correspond to excitations from an electron in HOMO with significant d character to the lowest π^* orbitals of the ppy ligands. The corresponding singlet states are found to occur about 0.2 eV higher at 2.80 eV for S_1. In the case of *mer*-$Ir(ppy)_3$, the lowest excited states are no longer degenerate as a result of the broken C_3 symmetry at this configuration (recall that the bond distances between the Ir and the coordinating atoms in the meridional complex are no longer equal). For both facial and meridional complexes, all of the low-lying transitions are categorized as metal-to-ligand charge transfer (MLCT) transitions with an admixture of π-π^* ligand-centered (LC) and/or ligand-to-ligand charge transfer (LLCT) states. Likewise, the lowest-lying excited states in the facial isomer of the $Ir(pmb)_3$ have similar energies (due to the three-fold symmetry in this configuration). However, in the meridional complex, while T_1 and T_2 lie very close in energy, the next triplet state (T_3) is separated by ~0.04 eV from these two states. The corresponding singlet states are also well separated from each other.

Table 7.3 Excitation energies (*E*) and dominant orbital excitation from TD-DFT (S_0) calculations for facial and meridional isomers of $Ir(ppy)_3$.

	fac-$Ir(ppy)_3$		*mer*-$Ir(ppy)_3$	
Excited state	*E* (eV)	Excitation	*E* (eV)	Excitation
T_1	2.59	H → L	2.52	H → L+1
T_2	2.60	H → L+1	2.58	H → L+2
T_3	2.60	H → L+2	2.65	H → L
S_1	2.80	H → L	2.69	H → L
S_2	2.85	H → L+1	2.71	H → L+1
S_3	2.85	H → L+2	2.82	H → L+2

Table 7.4 Excitation energies (*E*) and dominant orbital excitation from TD-DFT (S_0) calculations for facial and meridional isomers of $Ir(pmb)_3$.

	fac-$Ir(pmb)_3$		*mer*-$Ir(pmb)_3$	
Excited state	*E* (eV)	Excitation	*E* (eV)	Excitation
T_1	3.32	H → L+1	3.25	H → L
T_2	3.32	H → L+2	3.26	H → L+1
T_3	3.32	H → L	3.30	H → L+2
S_1	3.57	H → L+1	3.37	H → L
S_2	3.58	H → L+2	3.46	H → L+1
S_3	3.58	H → L	3.55	H → L+2

It is important to point out at this stage that the degeneracy observed in the lowest-lying excited states of the metal complexes can lead to multiple emission phenomena, which results in the broadening of the emission spectrum. Our calculations suggest that the shape of the phosphorescence spectrum (broad or sharp) for the facial and meridional isomers should be dissimilar due to the differences in the positions of the

lowest-lying excited triplet states. In addition, the calculations confirm the red-shifted emission observed in meridional complexes with respect to their facial counterparts.

Dipole Moments

As we mentioned earlier, the excited states of Ir complexes result from an interplay of ^{3}MLCT and ^{3}LC transitions. Solvent affects the electronic mixing of these two states (^{3}MLCT and ^{3}LC). Furthermore, different stereoisomers (*fac* and *mer*) are expected to behave differently in solution due to their different geometry. To understand the photopysical properties of facial and meridional complexes in solution, we have used the finite-field (FF) technique outlined in Chapter 2 to evaluate the dipole moments of the lowest-lying triplet states in *fac*- and *mer*-Ir(ppy)$_3$.

Table 7.5 Energies of lowest-lying triplet states from TD-DFT (S_0) calculations and dipole moments (μ) obtained from the FF method for the facial and meridional isomers of Ir(ppy)$_3$.

Molecule	Excited State	Energy (eV)	μ (Debye)
fac-Ir(ppy)$_3$	T_1	2.59	2.04
	T_2	2.60	2.42
	T_3	2.60	2.11
mer-Ir(ppy)$_3$	T_1	2.52	4.85
	T_2	2.58	2.53
	T_3	2.65	7.73

Note: The FF method is based on the TD-DFT (S_0) calculations in the presence of an electric field. See Chapter 2 for its formulation.

Table 7.5 collects the energies and dipole moments of the lowest-lying triplet states in facial and meridional Ir(ppy)$_3$. In the case of the *fac* isomer, the lowest-lying triplet excited states are degenerate and their dipole moments are in close proximity to each other. The similarity in the polarity of the low-lying triplets in the facial isomer suggests the possibility of multiple emission in the presence of a solvent. On the contrary,

for *mer*-Ir(ppy)$_3$, the energetics and dipole moments of the lowest-lying triplet states are different from one another which weakens the chance of multiple emission in solution. However, it enhances the probability of reordering of triplet states in solvents of different polarity. If the ordering of the triplet states changes, then the T_1 state in solution could acquire a different nature than it would in vacuum. As a result, solvent effects in these complexes can be rather complicated and solvent may affect the nature of emission in several ways. These issues on solvent effects will be discussed further in the last subsection.

Phosphorescence Lifetimes

The phosphorescence matrix elements between the excited triplet state and singlet ground state, calculated from the residues of the quadratic response (QR) functions as implemented in the *DALTON* program,[120] are analyzed for facial and meridional isomers of Ir(ppy)$_3$. The phosphorescence radiative lifetime (τ^r_p) from the three sublevels of the lowest triplet state (corresponding to the three spin projections, $m_s = 0, \pm 1$) are calculated at the S_0 and T_1 optimized geometries (for details on the calculations, see Chapter 2).

Although it seems natural to calculate τ^r_p at the T_1 optimized geometry, since the final state is the ground state which determines the vibronic structure of the emission spectrum, it is also useful to consider the S_0-T_1 transition probability at the S_0 optimized geometry. The calculated phosphorescence radiative lifetimes for the three spin sublevels of the T_1 state (T^x, T^y, T^z) at the S_0 optimized geometry and at the first excited triplet state optimized geometry are presented in Table 7.6. The phosphorescence lifetimes for spin sublevels indicate substantial qualitative and quantitative differences for the two geometrical structures (S_0 and T_1) as well as for two isomers (*fac* and *mer*). For the facial isomer at the S_0 optimized geometry, emission from the T^x and T^y sublevels of the lowest triplet state provides x and y polarization with short radiative lifetimes. The T^z sublevel is almost dark ($\tau_z \approx 88$ μs). Thus, at thermal equilibrium (high temperature limit at 77 K)

the lowest triplet state will be depleted through emission from the T^x and T^y sublevels. At the T_1 optimized geometry, the T^y sublevel is more active in phosphorescence than the T^x and T^z substates, but the spin selectivity is not as high as before. In fact, the calculated τ value at the T_1 optimized geometry is in good agreement with the measured phosphorescence decay time for $Ir(ppy)_3$ in 2-methyltetrahydofuran at 298 K (1.9 and 0.15 μs for *fac* and *mer* isomers, respectively).[262]

Table 7.6 Radiative phosphorescence lifetimes for the three spin sublevels τ_α (μs) of the facial and meridional isomers of $Ir(ppy)_3$ complex calculated with HF/CIS/SDD-ECP/3-21G QR method.

	S_0					**T_1**				
	$\Delta E_{S\text{-}T}$	τ_x	τ_y	τ_z	τ	$\Delta E_{S\text{-}T}$	τ_x	τ_y	τ_z	τ
fac	2.59	0.41	0.64	87.9	0.75	2.40	5.65	0.61	6.10	1.51
mer	2.52	0.43	2.97	3.94	1.03	1.76	0.07	0.23	0.58	0.15

Note: τ (μs) is the radiative phosphorescence lifetime in the high-temperature limit. $\Delta E_{S\text{-}T}$ (eV) is the S_0-T_1 excitation energy. Calculations have been performed at the S_0 and T_1 optimized geometry.

As a result of our calculations, we expect significant differences in the phosphorescence behavior of facial and meridional isomers of $Ir(ppy)_3$: The T^y sublevel is more active in phosphorescence than the $T^{x,z}$ sublevels in the *fac* isomer, and T^x is more active than $T^{y,z}$ for the *mer* isomer as indicated by differences in their radiative lifetimes.

Role of Ligand Tuning on Emission

In this section, we investigate the effect of fluorination and replacing the pyridine with pyrazole and benzimidazole on the emission and electrochemical properties of tris-cyclometaleted Ir complexes. We found that fluorine substitution and replacement of pyridine by pyrazole and benzimidazole both leads to a widening of the HOMO-LUMO gap and results in blue-shifted emission.

Table 7.7 summarizes the frontier orbital energies of the meridional $Ir(ppy)_3$, fluorinated derivatives of $Ir(ppy)_3$, $Ir(ppz)_3$, and $Ir(pmb)_3$ complexes. The introduction of fluorine substituents to the phenyl ring of the 2-phenylpyridine ligand decreases both the HOMO and LUMO levels due to the inductive electron-withdrawing effect of fluorine. However, the lowering of the LUMO by fluorination is slightly less than that of the HOMO, resulting in a widening of the HOMO-LUMO gap and leading to an increase in excited-state energy. It is important to note that the HOMO-LUMO gap of the fluorinated phenylpyridines does not increase further upon increasing the number of fluorine atoms. For example, the introduction of the third and fourth fluorine atoms on the phenyl ring of the difluorosubstituted compound slightly decreases the HOMO-LUMO gap (see Table 7.7).

Table 7.7 Energies (in eV) of the frontier molecular orbitals in tris-cyclometalated Ir complexes.

	HOMO	LUMO	Δ(HOMO-LUMO)
mer-$Ir(ppy)_3$	-4.68	-1.28	3.40
*m*er-$Ir(F_2ppy)_3$	-5.52	-1.80	3.73
*m*er-$Ir(F_3ppy)_3$	-5.69	-2.03	3.66
*m*er-$Ir(F_4ppy)_3$	-5.94	-2.36	3.58
mer-$Ir(ppz)_3$	-4.80	-0.69	4.11
mer-$Ir(pmb)_3$	-4.75	-0.71	4.04

Ir complexes with ppy, ppz, and pmb as coordinating ligands all have similar HOMO energies. However, the LUMO energies of *mer*-$Ir(ppz)_3$ and *mer*-$Ir(pmb)_3$ are shifted to a considerably higher energy relative to that of *mer*-$Ir(ppy)_3$ (see Table 7.7). This can be attributed to the poor electron-accepting nature of pyrazole and benzimidazole as compared to pyridine.[271] As a result, the triplet energies of *mer*-$Ir(ppz)_3$ and *mer*-$Ir(pmb)_3$ are increased as compared to *mer*-$Ir(ppy)_3$ (see Table 7.8). Thus, it

becomes possible to observe efficient blue or near-UV phosphorescence at room temperature from Ir complexes that have cyclometalated *N*-pyrazolyl- or carbene-based ligands.

Table 7.8 Energy (E) of the lowest-triplet state (T_1) in tris-cyclometalated Ir complexes from TD-DFT (S_0) calculations along with the experimental data.

	$E^{calc.}$ (eV)	$E^{exp.}$ (eV)	Ref.
mer-Ir(ppy)$_3$	2.52	2.42	262
*m*er-Ir(F$_2$ppy)$_3$	2.78	2.57	262
*m*er-Ir(F$_3$ppy)$_3$	2.86	2.73	269
*m*er-Ir(F$_4$ppy)$_3$	2.81	2.63	269
mer-Ir(ppz)$_3$	3.06	2.90	262
mer-Ir(pmb)$_3$	3.25	3.26	271

Table 7.9 summarizes the selected bond distances for meridional Ir(ppz)$_3$ and Ir(pmb)$_3$. Comparison of the geometries indicates that the imidazolyl-carbene ligand has a stronger *trans* influence than pyrazolyl and, thus, imparts a greater ligand field strength. In *mer*-Ir(pmb)$_3$, the bond length of Ir-C$_{aryl}$ *trans* to benzimidazolyl (Ir-C2 = 2.099 Å) is greater than the length of the Ir-C$_{aryl}$ bond *trans* to the pyrazolyl group in *mer*-Ir(ppz)$_3$ (Ir-C3 = 2.031 Å), illustrating the stronger *trans* influence of the carbene ligand over that of pyrazolyl. The lengths of the mutually *trans* Ir-C$_{aryl}$ bond (Ir-C1 and Ir-C3, average (av) = 2.127 Å) in *mer*-Ir(pmb)$_3$ are slightly longer than those in *mer*-Ir(ppz)$_3$ (av = 2.075 Å), indicative of greater electron donation from the carbene ligand than from the pyrazolyl moiety. Comparison of the crystallographic structures of the facial and meridional isomers of Ir(pmb)$_3$ with the corresponding Ir(ppz)$_3$ isomers supports this view as well.[271] As a result, the structures of both isomers of Ir(pmb)$_3$ are consistent with a strong *trans* influence of a formally neutral carbene ligand. The bond-length differences suggest that the cyclometalated carbenes are stronger field ligands than their pyrazolyl or pyridyl

counterparts, and therefore, the Ir(C^C)$_3$ complexes have high energy ligand field states. This explains the highest triplet energy of Ir(pmb)$_3$ in the series observed by both theory and experiment.[271]

***mer*-Ir(ppz)$_3$** ***mer*-Ir(pmb)$_3$**

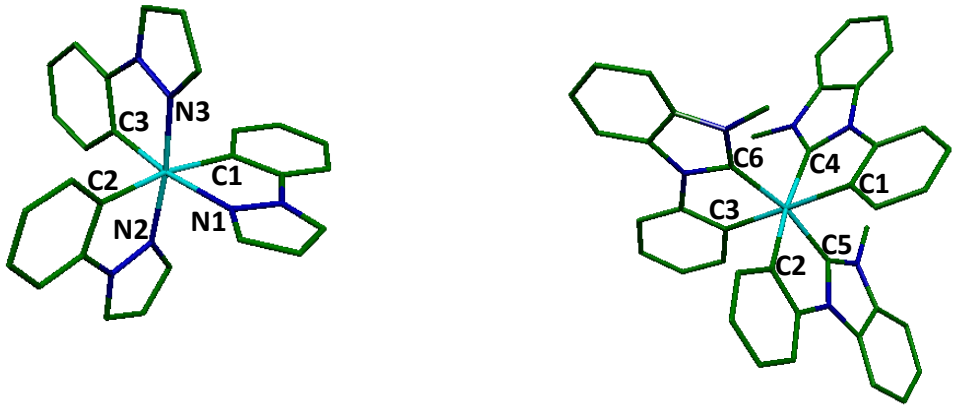

Table 7.9 Selected bond distances (Å) for meridional Ir(ppz)$_3$ and Ir(pmb)$_3$ along with the experimental data.[271]

	***mer*-Ir(ppz)$_3$**		***mer*-Ir(pmb)$_3$**	
Bond	Calc.	Exp.	Calc.	Exp.
Ir-N1	2.151	2.053		
Ir-N2	2.042	2.026		
Ir-N3	2.038	2.013		
Ir-C1	2.118	2.051	2.136	2.099
Ir-C2	2.105	2.057	2.099	2.078
Ir-C3	2.031	1.993	2.118	2.086
Ir-C4			2.067	2.043
Ir-C5			2.036	2.019
Ir-C6			2.046	2.032

Heteroleptic Complexes - FIrpic Derivatives

Iridium complexes bearing 2-phenylpyridine ligands have the advantage that their emission energy can be finely tuned from blue to red by functionalization of phenylpyridines with electron-withdrawing and electron-donating substituents or by replacement of one phenylpyridine with an ancillary ligand. For heteroleptic Ir^{III} complexes, the emission wavelength can be modified via structural changes of both cyclometalating and ancillary ligands. For example, our colleagues at Pusan National University in Korea reported that the photophysical properties of the commonly used blue emitter Ir^{III} bis(4,6-difluorophenylpyridinato)-picolinate (FIrpic) change depending on the electroactive R_1 and R_2 groups attached to the cyclometalated and ancillary ligands, respectively (see Figure 7.4).[278] The emission maximum, quantum yield, and shape of the phosphorescence spectrum (sharp or broad) vary as a function of the R_1 and R_2 substituents (see Table 7.10).

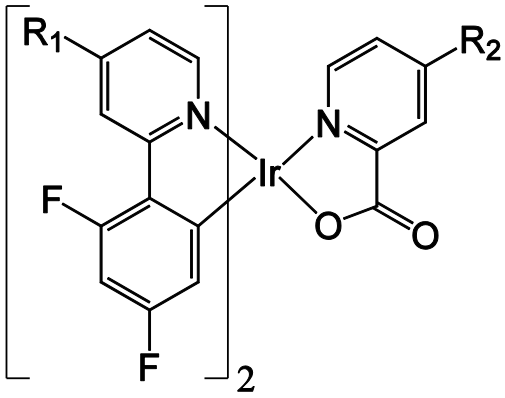

1:	$R_1 = H$;	$R_2 = CH_3$	**5:**	$R_1 = CH_3$;	$R_2 = OCH_3$
2:	$R_1 = H$;	$R_2 = CF_3$	**6:**	$R_1 = OCH_3$;	$R_2 = CH_3$
3:	$R_1 = CH_3$;	$R_2 = H$	**7:**	$R_1 = N(CH_3)_2$;	$R_2 = CH_3$
4:	$R_1 = CH_3$;	$R_2 = CH_3$	**8:**	$R_1 = N(CH_3)_2$;	$R_2 = CF_3$

Figure 7.4 General chemical structure of the Ir^{III} bis(4,6-difluorophenylpyridinato)-picolinate (FIrpic) as a function of electroactive R_1 and R_2 groups.

Table 7.10 Experimental emission data[278] for FIrpic derivatives **1**-**8** shown in Figure 7.4.

Complex	Quantum yield, Φ	λ_{max} (eV)	Peak shape
1	0.85	2.65	Sharp
2	0.26	2.22	Broad
3	0.44	2.42	Broad
4	0.23	2.68	Sharp w/ tail
5	0.69	2.67	Sharp
6	0.18	2.38	Broad
7	0.17	2.34	Broad
8	0.07	2.09	Broad

Experimental studies show that as opposed to homoleptic (IrL_3) complexes, where a different isomerism pattern (*fac* and *mer*) is seen, heteroleptic (IrL_2L') complexes are obtained as a single isomer by using a common intermediate (dichloro-bridged dimer) during synthesis.[279] This isomer is an octahedron with *cis*-C,C and *trans*-N,N orientations around the chelating agent.[270,272] On the other hand, Hay *et al.*[280] theoretically examined the alternate isomers in heteroleptic Ir complexes where the coordinating C atoms were *cis* to one another, and N atoms are either *cis* or *trans* to each other. It was concluded that these complexes show different phosphorescence behavior (such as emission wavelength and quantum efficiency) with respect to different types of isomerism. Here, we also considered two isomers of the FIrpic complex such that N atoms on the F_2ppy ligands are either *cis* or *trans* with respect to each other (see Figure 7.5). These isomers will be referred to as N-*cis* and N-*trans* throughout the text. The relative energies of the two isomers, based on the B3LYP energies of each structure, indicate that N-*cis* is +0.27 eV more energetic than the N-*trans* isomer.

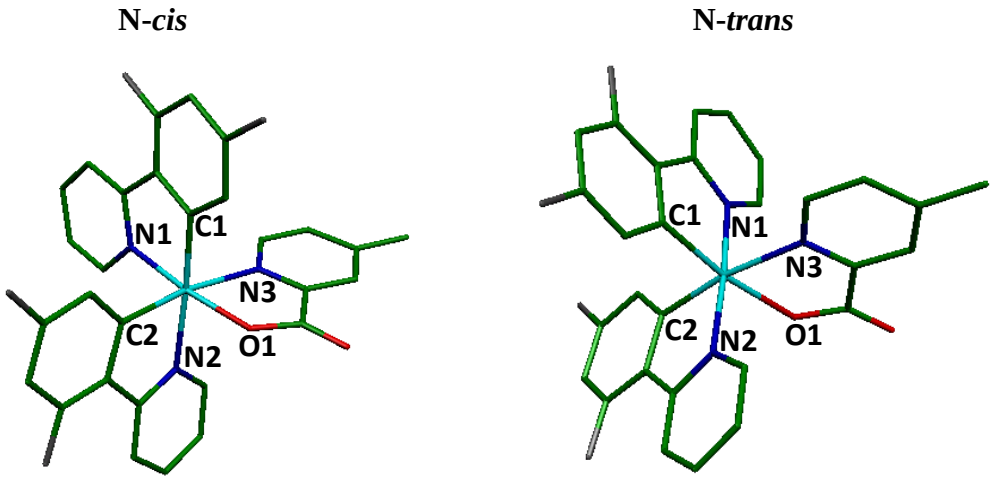

Figure 7.5 Two types of isomers discussed in the text: two N atoms in F_2ppy (labeled as N1 and N2) are at *cis* (on the left) or *trans* (on the right) positions with respect to each other.

In the following subsections, the geometric differences, ground-state frontier molecular orbitals, and excited-state properties of complexes **1**-**8** will be reviewed with an emphasis on the nature of triplet emission in N-*cis* and N-*trans* isomers. A brief introduction to solvent effects on absorption and emission is also given in the last part.

Geometries

To start with, we investigated the geometries of the singlet ground (S_0) and lowest excited triplet (T_1) states in N-*cis* and N-*trans* complexes **1**-**8**. All compounds are found to be distorted octahedrons around the central Ir atom. The critical bond distances between Ir and its coordinated atoms in ligands in both ground and excited triplet states of N-*cis* and N-*trans* compounds are listed in Tables 7.11 and 7.12, respectively. In the ground state, both isomers have Ir-C bond lengths between 2.014 and 2.030 Å, in agreement with typical Ir-C lengths of 2.00-2.02 Å.[262,270,281] In contrast, large deviations in the Ir-N bonds are found according to the ligand chelated at the counter position. For both isomers, bonds *trans* to C atoms are longer than bonds *trans* to N atoms due to the sigma donation of the carbons (*trans* effect) which is also observed in other Ir

complexes.[270] Similar bond lengths are also calculated for the unsubstituted FIrpic complex, *i.e.,* R_1 and R_2 = H (see Figure 7.4).

Upon $S_0 \rightarrow T_1$ transition, we found that the two isomers show different Ir-C bond length changes; one of the Ir-C bond length increases and the other one decreases for N-*cis* complexes, while both Ir-C bonds decrease for N-*trans* compounds. However, complexes **2** and **8** show some deviations from these trends, and, as we will show later in this discussion, these complexes usually behave in an opposite way as compared to the rest of the molecules in the series (recall that complexes **2** and **8** have electron withdrawing CF_3 groups on picolinate). With the exception of complexes **2** and **8**, the Ir-N bonds of the ppy ligand show similar behavior for both isomers: one of them decreases (Ir-N1) and the other one (Ir-N2) increases upon $S_0 \rightarrow T_1$ transition. We also observe analogous bond evolutions in the picolinate ligand for N-*cis* and N-*trans* isomers; while the Ir-N bond of the picolinate elongates, the Ir-O bond shortens upon relaxation into T_1. We note that for both isomers, the shortening of the Ir-O bond in the picolinate is significant (~0.14 Å) for complexes **2** and **8**; this will indeed result in larger geometry relaxation energies for these compounds (see subsequent section). One important result from the analysis of the geometries is that, with the exceptions of complexes **2** and **8,** all molecules show similar bond length changes upon $S_0 \rightarrow T_1$ transition within N-*cis* and N-*trans* compounds. As we show in the following subsections, the similarity in the geometrical changes upon excitation will be reflected in the calculated emission energies of these compounds.

Table 7.11 Critical bond lengths (in Å) between Ir and its coordinated atoms in the relaxed S_0 and T_1 gas-phase geometries for N-*cis* complexes **1**-**8** (see Figure 7.5 for atom numbering).

	S_0 state					
Complex	Ir-C1	Ir-N1	Ir-C2	Ir-N2	Ir-N3	Ir-O1
1	2.015	2.054	2.029	2.169	2.172	2.092
2	2.018	2.054	2.030	2.173	2.165	2.095
3	2.017	2.053	2.029	2.169	2.171	2.094
4	2.016	2.053	2.028	2.168	2.171	2.094
5	2.016	2.054	2.029	2.169	2.172	2.093
6	2.015	2.057	2.028	2.170	2.169	2.094
7	2.018	2.056	2.027	2.167	2.167	2.100
8	2.021	2.056	2.029	2.169	2.158	2.101
	T_1 state					
1	2.021	1.988	2.014	2.181	2.211	2.089
2	2.030	2.095	2.049	2.163	2.147	1.958
3	2.023	1.985	2.015	2.181	2.210	2.089
4	2.023	1.985	2.015	2.181	2.205	2.090
5	2.022	1.985	2.014	2.183	2.208	2.090
6	2.025	1.984	2.017	2.184	2.202	2.087
7	2.032	1.976	2.019	2.182	2.204	2.091
8	2.036	2.097	2.048	2.139	2.146	1.962

Table 7.12 Critical bond lengths (in Å) between Ir and its coordinated atoms in the relaxed S_0 and T_1 gas-phase geometries for N-*trans* complexes **1**-**8** (see Figure 7.5 for atom numbering).

	S_0 State					
Complex	Ir-C1	Ir-N1	Ir-C2	Ir-N2	Ir-N3	Ir-O1
1	2.015	2.056	2.021	2.071	2.185	2.180
2	2.015	2.059	2.020	2.072	2.184	2.183
3	2.016	2.057	2.021	2.071	2.182	2.180
4	2.014	2.057	2.021	2.070	2.183	2.180
5	2.014	2.056	2.021	2.071	2.186	2.179
6	2.015	2.059	2.021	2.073	2.179	2.178
7	2.012	2.059	2.020	2.074	2.182	2.184
8	2.013	2.060	2.021	2.075	2.174	2.192
	T_1 state					
1	1.987	2.043	2.009	2.086	2.228	2.162
2	2.026	2.071	2.035	2.080	2.177	2.048
3	1.988	2.042	2.010	2.083	2.227	2.165
4	1.988	2.042	2.009	2.084	2.225	2.165
5	1.988	2.042	2.009	2.085	2.228	2.162
6	1.988	2.043	2.011	2.084	2.221	2.164
7	1.983	2.050	2.009	2.083	2.225	2.170
8	2.032	2.083	2.039	2.055	2.168	2.048

Frontier Molecular Orbitals

The influence of a particular substituent on an aromatic system is usually discussed in terms of inductive and mesomeric effects. The mesomeric effect is related to the sharing of π-electrons between the aromatic core and the substituent. If the substituent is grafted at a position where a frontier molecular orbital has a node, its impact on this particular MO is weak. On the other hand, if there is a significant electron density at the

point of attachment, the interaction between the π-orbitals of the substituent and of the aromatic core is stronger.

The inductive effect is usually associated solely with the σ-electron system of the aromatic molecule. Electroactive groups that withdraw electron density by the inductive effect cause a lowering of the energies of the highest occupied and lowest unoccupied molecular orbitals. This can be explained qualitatively by the fact that electron acceptors withdraw some electron density from the ligands, thus reducing the repulsive Coulomb interaction among the electrons occupying the ligand-localized π-MOs and the electrons of the σ-system.

Here, we examined the impact of electroactive substituents R_1 and R_2 in complexes **1**-**8** by comparing the energies of the frontier orbitals with respect to that of the unsubstituted complex FIrpic (R_1 and R_2 = H). Although the mesomeric and inductive effects are largely local, each of these two contributions strongly affects the energy of the frontier orbitals and hence the electronic structure of the Ir complex. However, the task of quantifying and ranking these effects is not straightforward; though, it is possible to single out the most important effect in each complex.

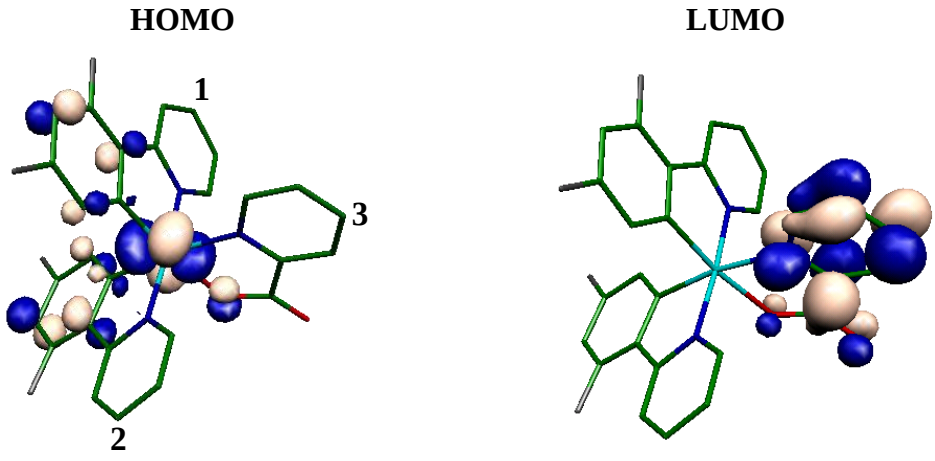

Figure 7.6 DFT/B3LYP wavefunctions of the frontier molecular orbitals in N-*trans* isomer of FIrpic (R_1 and R_2 = H) complex. Saturated H atoms are not shown for clarity purposes.

Figure 7.6 shows the wavefunctions of the frontier MOs in N-*trans* isomer of unsubstituted FIrpic (R_1 and R_2 = H) complex. We note that similar orbital pictures are also obtained for the N-*cis* isomer of this compound. For FIrpic, the HOMO is mostly localized on the difluorophenyl part of the two ppy ligands and has a large contribution arising from the 5d atomic orbitals of Ir, while the LUMO is exclusively localized on the picolinate ligand. The HOMO has nodes at positions 1 and 2 (see Figure 7.6 for labeling) where R_1 is attached, whereas the LUMO has large coefficients at position 3 which is the attachment position of the R_2 group. Therefore, the R_2 group is expected to influence the energy of the LUMO more than the energy of the HOMO.

Figure 7.7 shows the energies of the frontier molecular orbitals in N-*trans* isomers of R_1 and R_2 substituted Ir complexes **1**-**8** as well as the unsubstituted complex (FIrpic). It is seen that both frontier MOs of complex **2** (R_1 = H and R_2 = CF_3) are lowered with respect to the unsubstituted FIrpic due to the inductive electron withdrawing effect of the trifluoromethyl group attached to picolinate. Indeed, this compound has the deepest HOMO and LUMO levels in the series. In the case of complex **8** where R_1 = $N(CH_3)_2$ and R_2 = CF_3, the LUMO is significantly lowered (due to electron accepting CF_3), but the HOMO is slightly increased as opposed to complex **2**. This increase in the HOMO can be explained by the strong electron donating effect of the $N(CH_3)_2$ group. For instance, complex **7** (R_1 = $N(CH_3)_2$ and R_2 = CH_3) has the highest HOMO in the series due to the two electron donating groups attached to the phenylpyridine and picolinate ligands. The HOMOs and LUMOs of complexes **1** and **3**-**6** remain almost constant within the series because the electron donating effects of either the methyl or methoxy groups at positions 1, 2, and 3 do not have a significant influence on the frontier MOs. Among the series, complex **8** has the smallest HOMO-LUMO gap due to the two counteracting effects caused by the strong electron donating ($N(CH_3)_2$) and accepting (CF_3) groups attached to ppy and pic, respectively. Finally, we note that for N-*cis* isomers of complexes **1**-**8**, the variations in frontier orbitals are essentially the same as those of N-*trans* compounds.

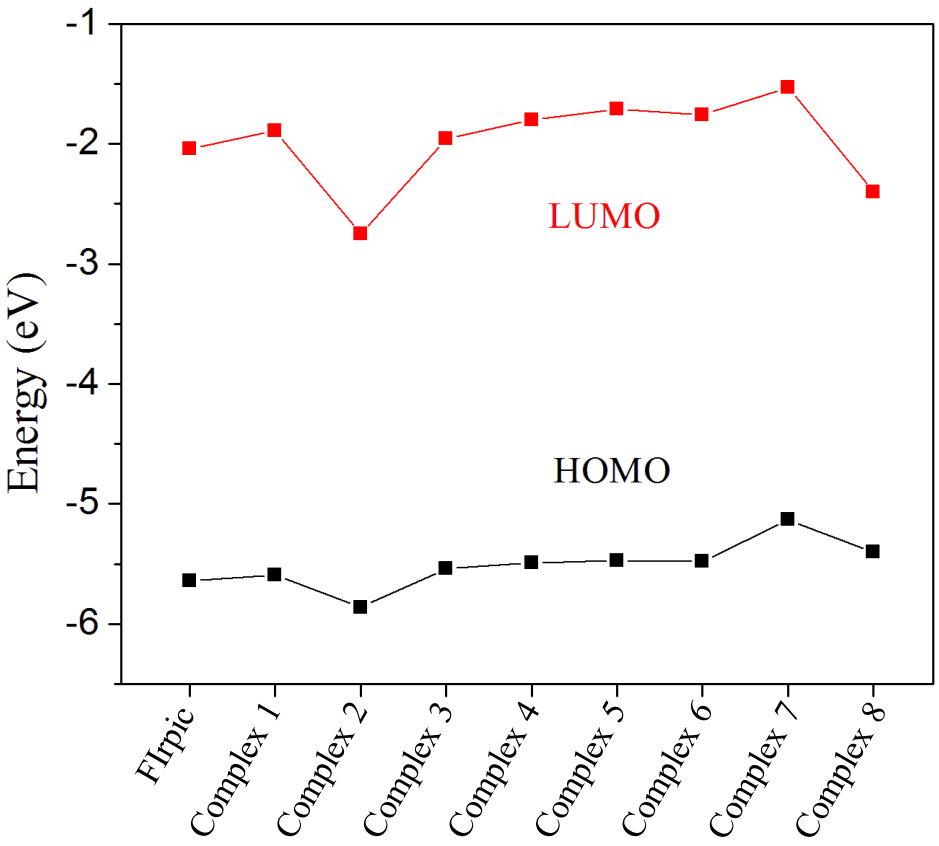

Figure 7.7 Energies of the frontier molecular orbitals in N-*trans* complexes **1**-**8** along with the energies for the unsubstituted complex FIrpic.

Lastly, it is important to emphasize that the HOMO-LUMO gaps (~3 eV) of complexes **2** and **8** substituted with the CF_3 group are significantly reduced as compared to the rest of the compounds in the series (~3.7 eV). The information on the HOMO-LUMO gaps is often used to estimate the energy of the excited states. On this basis, one should expect red-shifted emission for complexes **2** and **8**. Indeed, the excitation energies obtained from TD-DFT calculations predict significant red-shifts for these complexes (see subsequent section).

Excitation Energies

Time-dependent DFT calculations at optimized ground-state geometries (S_0) were employed to examine the low-lying triplet and singlet excited states of complexes **1**-**8**.

The results from TD-DFT (S_0) calculations for N-*cis* and N-*trans* isomers are shown in Tables 7.13 and 7.14, respectively. For each molecule, we give the vertical excitation energies for the lowest 4 triplet and singlet states together with the nature of the orbitals involved in the dominant excitation process. In some cases, other excitation processes are also involved for a particular state; for the sake of simplicity, we only show the dominant contribution in Tables 7.13 and 7.14. However, we note that contributions from other excitations can sometimes play an important role in the nature of the electronic excited states as discussed in the following parts.

From Tables 7.13 and 7.14, we see that in all complexes the S_1 state is characterized by a HOMO → LUMO transition regardless of the substituents (R_1 and R_2) or isomerization pattern (N-*cis vs*. N-*trans*). Since HOMOs in these complexes are largely localized on the metal and phenyl part of the phenylpyridine ligand and LUMOs are predominantly ligand based, the HOMO to LUMO transitions in these compounds have significant MLCT character mixed with interligand excitations. For the N-*cis* isomer of complex **1**, the LUMO+1 lies very close to LUMO ($\Delta\varepsilon$ = 0.05 eV) and shares the same character with the LUMO, *i.e.*, both LUMO and LUMO+1 are localized on the ppy and pic ligands (see Figure 7.8). This has a profound impact on the character of the excited states; in fact, the lowest singlet excited state S_1 corresponds to a HOMO → LUMO+1 transition in this compound with a mixing of HOMO → LUMO MLCT and interligand excitations.

In all complexes, the low-lying excited states are characterized by MLCT with an admixture of LC and/or LLCT transitions. For instance, Figure 7.9 shows the wavefunctions of the molecular orbitals involved in the transitions of N-*trans* complex **1**. The electron density of the HOMO is largely located on the metal and the phenyl part of the two phenylpyridine ligands with some contributions from the lone pairs of oxygen. The HOMO-1 and HOMO-2 are predominantly metal based. There is also significant contribution from oxygen atoms of picolinate to HOMO-1. The LUMO is largely located

on the picolinate, whereas LUMO+1 and LUMO+2 are mostly localized on one of the phenylpyridine ligands. There is also non-negligible contribution coming from the picolinate in LUMO+1. These features of the MOs indicate that the lowest transitions in this complex are ascribed to MLCT mixed with LC and/or LLCT excitations. The HOMO → LUMO transition represents MLCT and interligand charge transfer to picolinate.

Table 7.13 Excitation energies (*E*), oscillator strengths (*f*) and dominant orbital excitation obtained from TD-DFT (S_0) calculations for N-*cis* complexes **1**-**8**.

Complex	Excited states	*E* (eV)	*f*	Dominant excitation
1	T_1	2.68		H → L+1
	T_2	2.84		H-1→ L+1
	T_3	2.87		H → L+2
	T_4	2.95		H → L
	S_1	2.99	0.0111	H → L+1
	S_2	3.02	0.0050	H → L
	S_3	3.06	0.0044	H-1 → L
	S_4	3.17	0.0102	H → L+2
2	T_1	2.41		H → L
	T_2	2.43		H-1 → L
	S_1	2.51	0.0055	H → L
	T_3	2.63		H-2 → L
	T_4	2.72		H → L+1
	S_2	2.73	0.0045	H-2 → L
	S_3	2.85	0.0704	H-1 → L
	S_4	2.98	0.0120	H → L+1
3	T_1	2.71		H → L+1
	T_2	2.73		H-1 → L
	T_3	2.82		H → L
	T_4	2.90		H → L+2
	S_1	2.91	0.0035	H → L
	S_2	3.01	0.0128	H → L+1
	S_3	3.05	0.0072	H-2 → L
	S_4	3.07	0.0520	H-1 → L
4	T_1	2.70		H → L+1
	T_2	2.81		H-1 → L
	T_3	2.89		H → L+2
	T_4	2.92		H → L
	S_1	3.02	0.0048	H → L
	S_2	3.02	0.0119	H → L+1
	S_3	3.06	0.0101	H-1 → L+1

Table 7.13 (continued).

5	T_1	2.69		H → L
	T_2	2.89		H → L+2
	T_3	2.89		H-1 → L+1
	T_4	3.00		H-1 → L
	S_1	3.04	0.0114	H → L
	S_2	3.06	0.0042	H → L+1
	S_3	3.15	0.0038	H-1 → L
	S_4	3.20	0.0151	H → L+2
6	T_1	2.77		H → L+1
	T_2	2.79		H-1 → L
	T_3	2.90		H → L
	T_4	2.95		H → L+2
	S_1	3.00	0.0039	H → L
	S_2	3.08	0.0144	H → L+1
	S_3	3.11	0.0123	H-1 → L
	S_4	3.13	0.0126	H-1 → L+1
7	T_1	2.74		H-1 → L
	T_2	2.81		H → L
	S_1	2.87	0.0026	H → L
	T_3	2.89		H → L+1
	T_4	3.00		H-2 → L
	S_2	3.05	0.0069	H-1 → L
	S_3	3.07	0.0484	H-2 → L
	S_4	3.20	0.0438	H → L+1
8	T_1	2.26		H → L
	S_1	2.30	0.0029	H → L
	T_2	2.33		H-1 → L
	S_2	2.49	0.0036	H-1 → L
	T_3	2.50		H-2 → L
	S_3	2.73	0.0833	H-2 → L
	T_4	2.92		H → L+2
	S_4	2.96	0.0026	H → L+1

Table 7.14 Excitation energies (*E*), oscillator strengths (*f*) and dominant orbital excitation obtained from TD-DFT (S_0) calculations for N-*trans* complexes **1**-**8**.

Complex	Excited states	*E* (eV)	*f*	Dominant excitation
1	T_1	2.74		H → L+1
	T_2	2.80		H → L+2
	T_3	2.92		H → L
	T_4	2.94		H-1 → L
	S_1	2.98	0.0104	H → L
	S_2	2.99	0.0186	H → L+1
	S_3	3.04	0.0063	H → L+2
	S_4	3.11	0.0015	H-1 → L+1
2	T_1	2.35		H → L
	S_1	2.40	0.0020	H → L
	T_2	2.53		H-1 → L
	T_3	2.77		H → L+1
	S_2	2.78	0.0082	H-1 → L
	T_4	2.82		H → L+3
	S_3	2.89	0.0245	H → L+1
	S_4	2.93	0.0003	H-4 → L
3	T_1	2.78		H → L
	T_2	2.82		H → L+1
	S_1	2.85	0.0021	H → L
	T_3	2.85		H-1 → L
	T_4	2.85		H → L+2
	S_2	3.03	0.0338	H → L+1
	S_3	3.14	0.0085	H → L+2
	S_4	3.17	0.0116	H-1 → L
4	T_1	2.79		H → L+1
	T_2	2.84		H → L+2
	T_3	2.93		H-1 → L
	T_4	2.95		H → L
	S_1	2.97	0.0038	H → L
	S_2	3.02	0.0315	H → L+1
	S_3	3.14	0.0084	H → L+2
	S_4	3.16	0.0145	H-1 → L

Table 7.14 (continued).

5	T_1	2.78		H → L
	T_2	2.84		H → L+2
	T_3	3.00		H-1 → L+1
	S_1	3.01	0.0326	H → L
	T_4	3.06		H → L+1
	S_2	3.10	0.0024	H → L+1
	S_3	3.15	0.0082	H → L+2
	S_4	3.16	0.0011	H-1 → L
6	T_1	2.84		H → L+1
	T_2	2.90		H → L+2
	T_3	2.92		H-1 → L
	T_4	2.96		H → L
	S_1	2.99	0.0035	H → L
	S_2	3.10	0.0394	H → L+1
	S_3	3.19	0.0120	H → L+2
	S_4	3.20	0.0115	H-1 → L
7	T_1	2.80		H-1 → L
	T_2	2.83		H → L
	S_1	2.87	0.0024	H → L
	T_3	2.94		H → L+1
	T_4	3.01		H → L+3
	S_2	3.07	0.0099	H-1 → L
	S_3	3.17	0.0492	H → L+1
	S_4	3.20	0.0520	H-2 → L
8	T_1	2.27		H → L
	S_1	2.28	0.0020	H → L
	T_2	2.35		H-1 → L
	S_2	2.47	0.0046	H-1 → L
	T_3	2.60		H-2 → L
	S_3	2.84	0.0715	H-2 → L
	T_4	2.87		H-6 → L
	S_4	3.04	0.0027	H → L+1

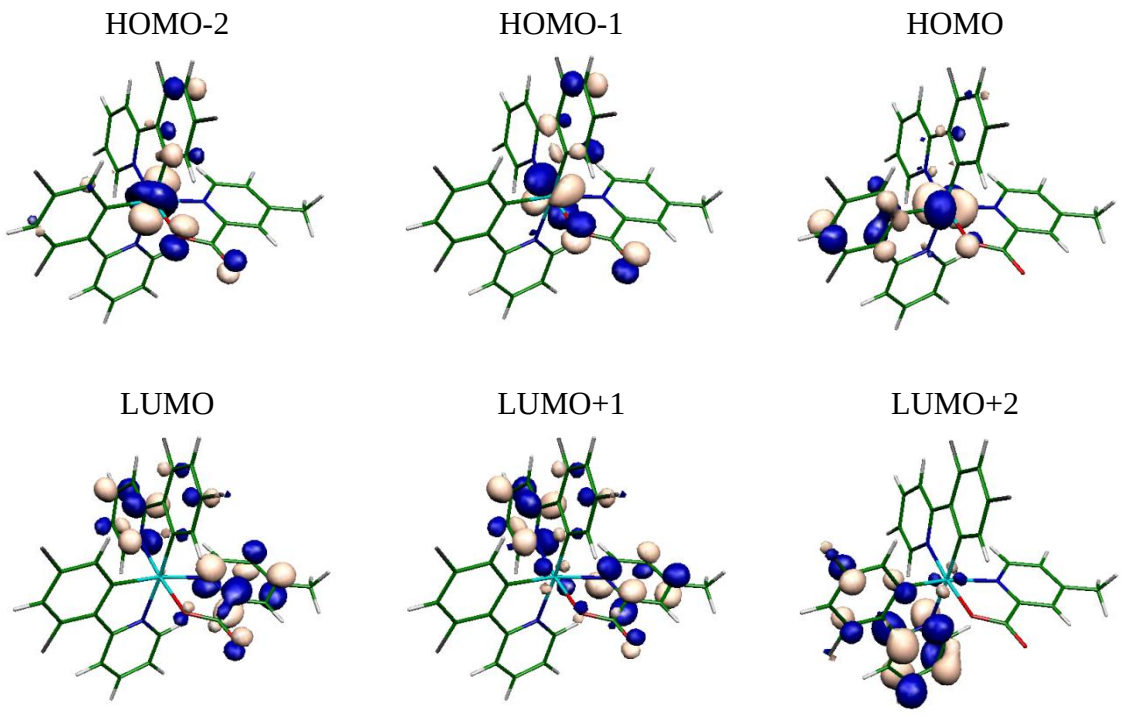

Figure 7.8 DFT/B3LYP wavefunctions of the ground-state molecular orbitals for the N-*cis* isomer of complex **1**. The HOMOs are largely confined on the Ir metal whereas the LUMOs are mainly localized on the ligands.

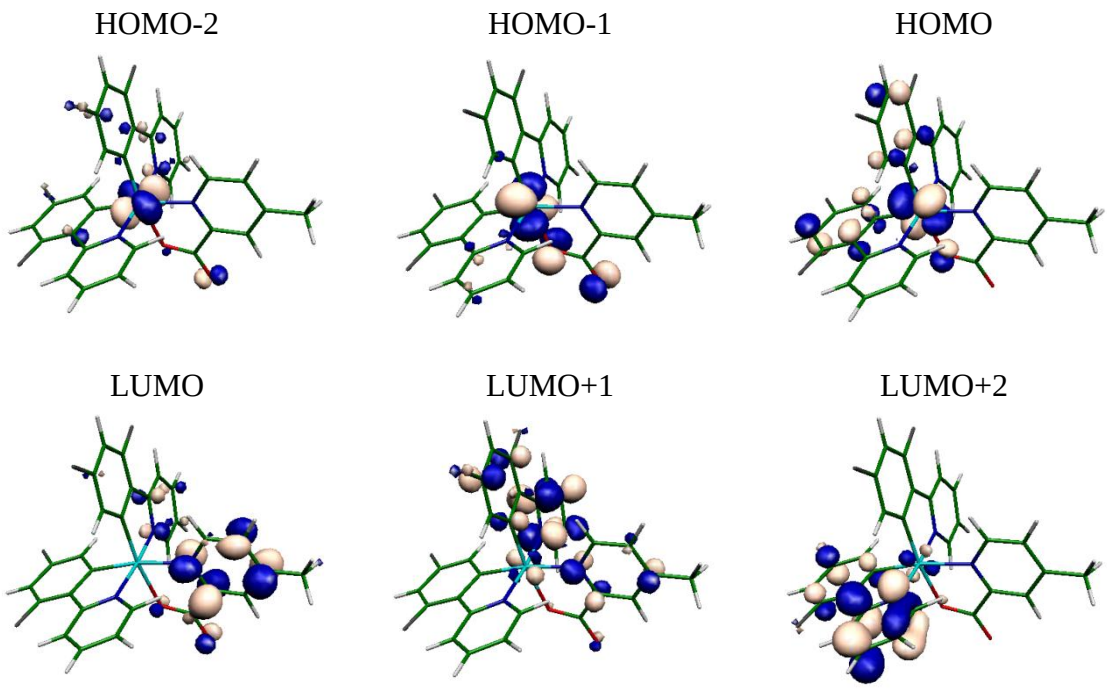

Figure 7.9 DFT/B3LYP wavefunctions of the ground-state molecular orbitals for the N-*trans* isomer of complex **1**. The HOMOs are largely confined on the Ir metal whereas the LUMOs are mainly localized on the ligands.

Nature of the Lowest Excited Triplet State

In addition to the previous TD-DFT studies of excited states, we have examined the lowest triplet state in Ir complexes by carrying out self-consistent unrestricted and restricted B3LYP calculations both at the optimized ground and triplet state geometries. Unrestricted single point calculations at the optimized ground-state geometry provide the energy of the T_1* point, whereas restricted calculations at the optimized triplet geometry provide the energy of the S_0* point illustrated in Figure 7.10. The energy calculation of these points gives an indication of the energy stabilization and overall geometry relaxation that occurs in the excited state in possible emission processes. Table 7.15 collects the SCF transition energies between the ground and excited triplet states for N-*cis* and N-*trans* complexes **1**-**8**. The calculated adiabatic T_1 energies $\Delta(S_0\text{-}T_1)$ are comparable to the TD-DFT excitation energies as the energies obtained by two methods are within 0.1 eV of each other. All molecules show almost the same degree of geometry

relaxation, $\Delta(S_0^*\text{-}S_0)$, upon emission which is consistent with the similar structural changes calculated for all molecules upon $S_0 \rightarrow T_1$ transition. The larger $\Delta(S_0^*\text{-}S_0)$ energy of both isomers of complexes **2** and **8** can be explained by the significant contraction of the Ir-O bond found in the T_1 state (see above the subsection on geometries). Owing to their large geometry relaxation, these compounds posses relatively low triplet energies as compared to the other molecules in the series.

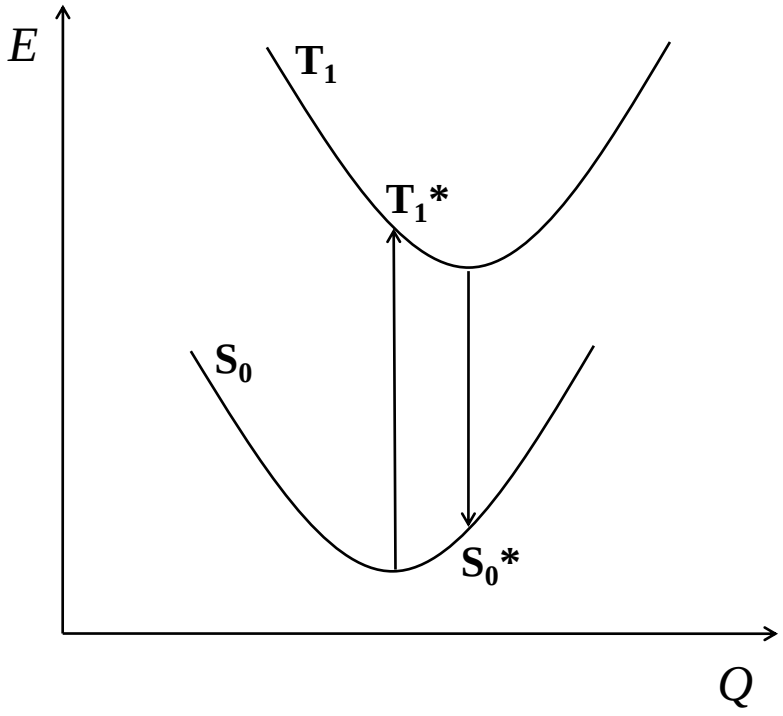

Figure 7.10 Illustration of the potential energy surfaces for the ground state (S_0) and lowest excited triplet state (T_1) of Ir complexes. Points T_1^* and S_0^* correspond the vertical transitions from optimized S_0 and T_1 states, respectively.

Table 7.15 SCF transition energies (in eV) between the ground (S_0) and lowest excited triplet (T_1) states for the N-*cis* and N-*trans* isomers of complexes **1**-**8** in their relaxed S_0 and T_1 gas-phase geometries. See Figure 7.10 for labeling.

	N-*cis*		
Complex	$\Delta(S_0\text{-}T_1)$	$\Delta(T_1\text{-}S_0^*)$	$\Delta(S_0^*\text{-}S_0)$
1	2.62	2.27	0.35
2	2.28	1.63	0.65
3	2.64	2.28	0.36
4	2.63	2.27	0.37
5	2.62	2.27	0.36
6	2.66	2.30	0.37
7	2.73	2.38	0.35
8	2.13	1.50	0.63
	N-*trans*		
1	2.69	2.43	0.26
2	2.37	1.72	0.65
3	2.70	2.44	0.27
4	2.70	2.43	0.27
5	2.69	2.42	0.26
6	2.74	2.46	0.28
7	2.83	2.54	0.29
8	2.21	1.57	0.64

The wavefunctions of the pair of MOs contributing the most to the description of the lowest excited triplet state together with the energies obtained from TD-DFT calculations at the optimized ground-state structures for N-*cis* and N-*trans* complexes **1**-**8** are presented in Tables 7.16 and 7.17, respectively. The highest occupied orbitals are predominately Ir(d) and phenylpyridine π orbitals (there is also a minor contribution from oxygen lone pair orbitals). The lowest virtual orbitals are mainly π^*-ligand in character. The nature of the lowest unoccupied orbitals contributing the most to the lowest triplet

state can be identified as phenylpyridine-localized, picolinate-localized, or a mixture of phenylpyridine and picolinate for the series of molecules **1**-**8**. As a result, the lowest triplet excited states of these molecules are characterized by MLCT mixed with interligand and/or intraligand excitations.

According to TD-DFT (S_0) calculations, the virtual orbital involved in the description of the lowest triplet excited state is usually localized on the same ligand for both isomers (N-*cis* and N-*trans*). However, compounds **3** and **7** do not follow these trends. In the N-*cis* isomers of these compounds, the unoccupied MO is localized on the phenylpyridine and picolinate ligands for complexes **3** and **7**, respectively (see Table 7.16). On the other hand, for the N-*trans* isomers, the localization pattern is exactly the other way round (*i.e.*, the unoccupied MO is localized on the picolinate and phenylpridine ligands of complexes **3** and **7**, respectively**,** see Table 7.17). Due to this inconsistency in localization pattern of the two isomers, we suspect that there might be other excitations contributing to the lowest triplet states of these molecules. For instance, a careful analysis of all the excitations involved in the lowest excited triplet state of the N-*trans* complex **3** reveals that there is also some contribution coming from the phenylpyridine-localized unoccupied MO in the T_1 state. Moreover, in some cases, higher-lying triplet states are found to lie very close in energy to the lowest triplet state. This might lead to an interchange in the ordering of the triplet states. Indeed, the interchange of the excited triplet states is observed in the case of triscarbazoles discussed in the previous chapter. For the N-*trans* isomer of complex **3**, the next triplet state (T_2) lies 0.04 eV above T_1, and the unoccupied MO contributing the most to this state is localized on the phenylpyridine ligand. As a result, both features seem to explain the opposite behavior observed in these compounds. This also points to the importance of analyzing all the lowest-lying excited states (T_n where n=1, 2, 3, etc.) and the nature of the excitations involved, rather than just focusing the dominant one in these states.

Table 7.16 DFT/B3LYP wavefunctions of the MOs contributing the most to the description of the lowest triplet excited states of N-*cis* complexes **1**-**8**.

Complex	*E* (eV)	Occupied MO	Unoccupied MO
1	2.68	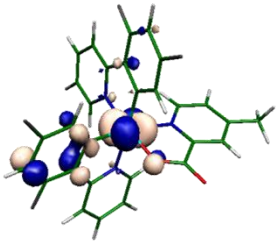	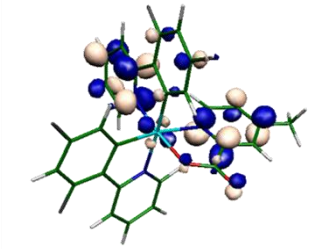
2	2.41	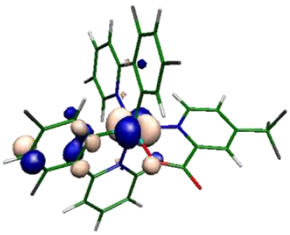	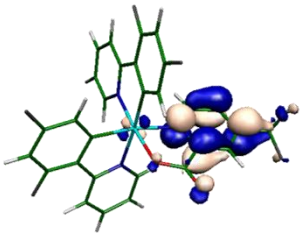
3	2.71	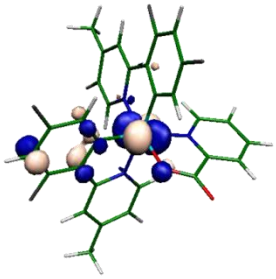	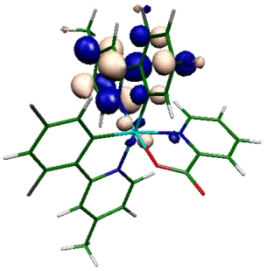
4	2.70	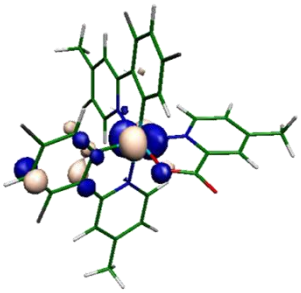	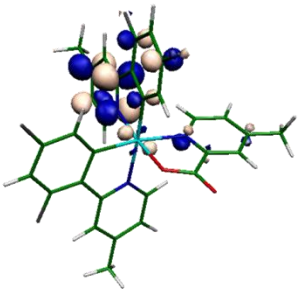
5	2.69	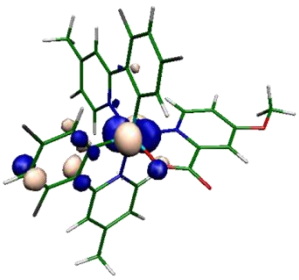	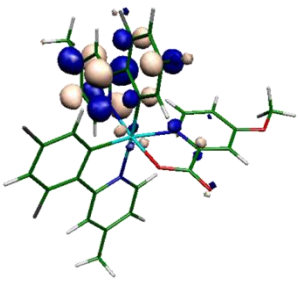

Table 7.16 (continued).

6	2.77	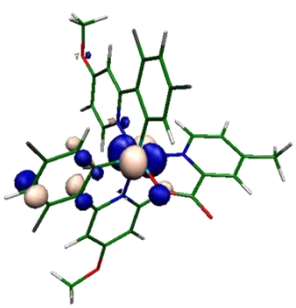	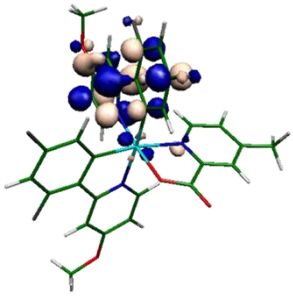
7	2.74	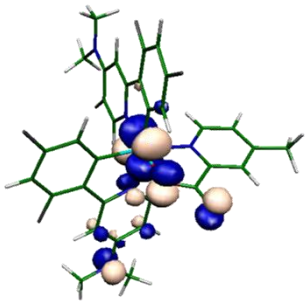	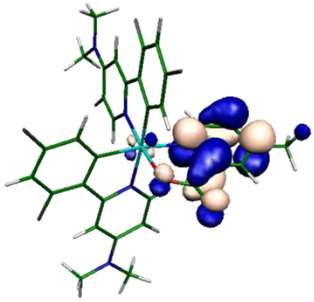
8	2.26	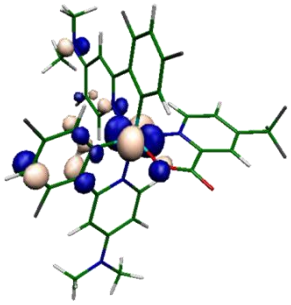	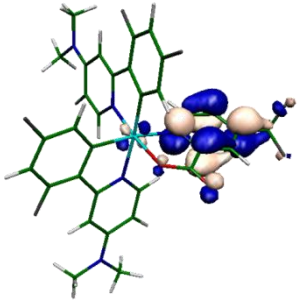

Note: Energy of the T_1 state is obtained from TD-DFT (S_0) calculations. DFT/B3LYP wavefunctions of the ground-state MOs are shown.

Table 7.17 DFT/B3LYP wavefunctions of the MOs contributing the most to the description of the lowest triplet excited states of N-*trans* complexes **1**-**8**.

Complex	*E* (eV)	Occupied MO	Unoccupied MO
1	2.74	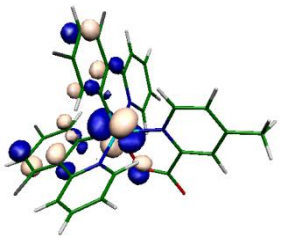	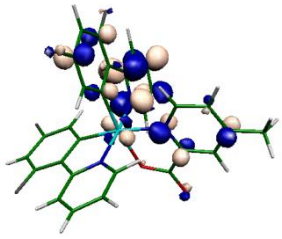
2	2.35	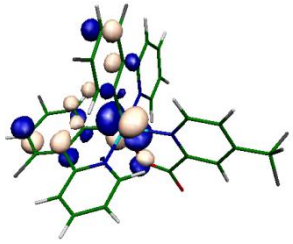	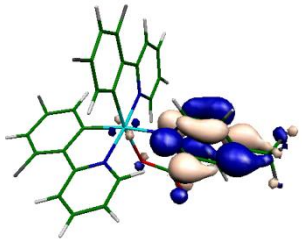
3	2.78	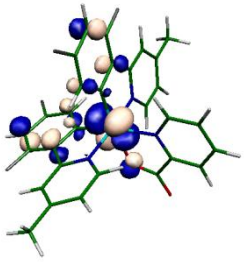	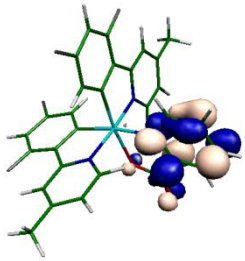
4	2.79	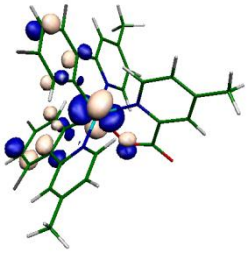	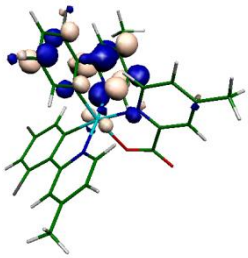
5	2.78	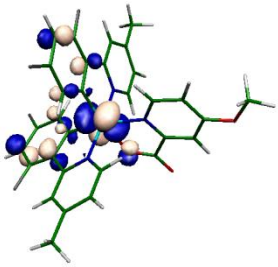	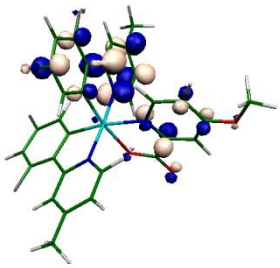

Table 7.17 (continued).

6	2.84	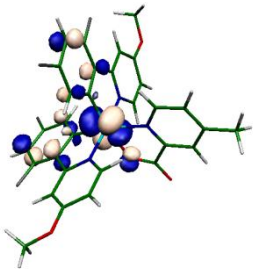	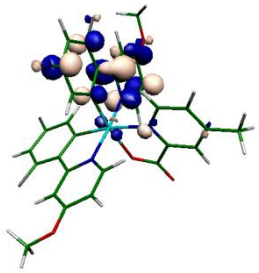
7	2.80	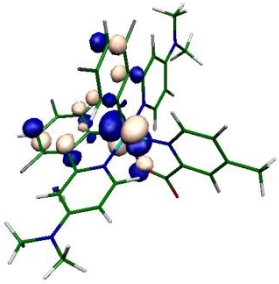	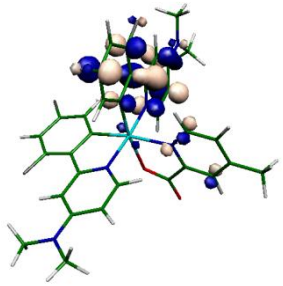
8	2.27	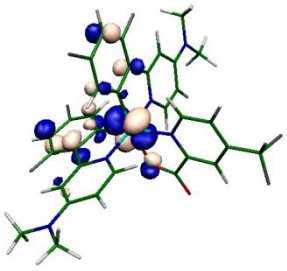	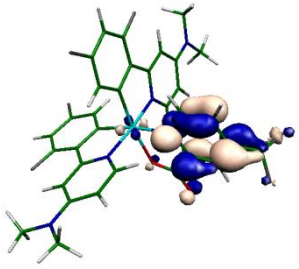

Note: Energy of the T_1 state is obtained from TD-DFT (S_0) calculations. DFT/B3LYP wavefunctions of the ground-state MOs are shown.

It is important to note at this stage that because of the high computational cost in getting the excited states, the emission properties are usually calculated based on the ground-state geometry,[273,280,282] assuming that the geometry does not change much between the ground and excited states. In this study, in addition to TD-DFT calculations at the optimized ground state (S_0), we also analyzed the transitions related to the excited state by means of TD-DFT method at the optimized triplet geometry (T_1). As we show next, TD-DFT treatment of vertical transitions at the optimized ground and excited states generally lead to similar orbital representations.

The energy of the lowest excited triplet state along with the wavefunctions of the pair of molecular orbitals contributing the most to the description of the T_1 state, as predicted by TD-DFT (T_1) calculations, are given in Tables 7.18 and 7.19 for N-*cis* and N-*trans* isomers of complexes **1**-**8,** respectively. Although TD-DFT (S_0) calculations gave some discrepancies in terms of MO localization between two isomers in a few cases (recall compounds **3** and **7**), the TD-DFT (T_1) treatment essentially leads to similar outcomes for all N-*cis* and N-*trans* complexes. The lowest triplet excited state is found to be dominated by a HOMO → LUMO transition for all compounds (both N-*cis* and N-*trans*). Similar to previous results, TD-DFT calculations at the T_1 optimized geometry resulted in HOMOs that are generally delocalized on the phenyl π orbitals of ppy with a large contribution from the d atomic orbital of Ir and also some contribution from the oxygen lone pair orbitals. The LUMOs are mostly localized on the phenylpyridine ligand for all complexes except for **2** and **8**. In these cases, the LUMOs are confined basically on the picolinate ligand. We note that the HOMOs of the N-*cis* isomers of complexes **2** and **8** do not have any contribution from the phenylpyridine ligands, rather they have large participations from the oxygen lone pairs in picolinate. As a result, the HOMO → LUMO transition in these compounds is characterized by MLCT to picolinate mixed with $n \rightarrow \pi^*$ intraligand (picolinate) excitations. For the rest of the N-*cis* compounds, the lowest excited triplet state is assigned as MLCT and interligand π(ppy) → π*(ppy) excitations with minor LC transitions. For the N-*trans* isomers, the lowest excited triplet state is usually ascribed to MLCT mixed with LC and interligand π(ppy) → π*(ppy) excitations. For complex **2**, the T_1 state includes MLCT and interligand π(ppy) → π*(pic) excitations, while for complex **8** the lowest triplet state is mainly MLCT in character.

As a result, the TD-DFT calculations both at the optimized ground-state and excited-state geometries suggest that the energy of the lowest excited triplet state stays almost identical for all complexes substituted with electron donating groups (complexes **1**

and **3**-**7**). On the other hand, the CF_3-substituted complexes **2** and **8** are significantly red-shifted, consistent with the experimental data (see Table 7.10). The similarity in the T_1 energies of complexes **1** and **3**-**7** parallels the comparable degree of bond-length changes (geometry relaxation effects) calculated for these compounds upon $S_0 \rightarrow T_1$ transition.

Table 7.18 TD-DFT (T_1) calculated energy and the wavefunctions of the pair of MOs involved in the description of the lowest triplet excited state in N-*cis* complexes **1**-**8**.

Complex	*E* (eV)	HOMO	LUMO
1	2.09	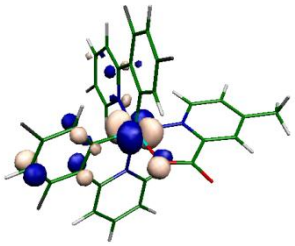	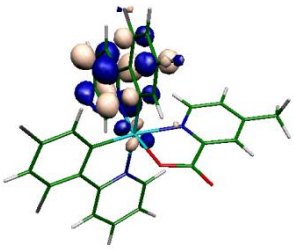
2	1.26	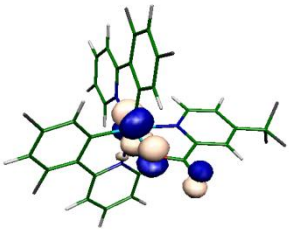	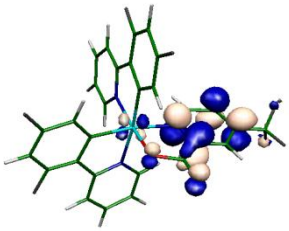
3	2.10	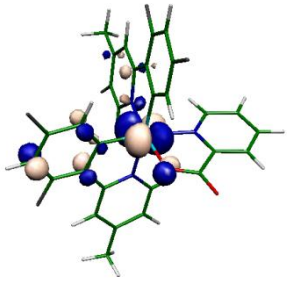	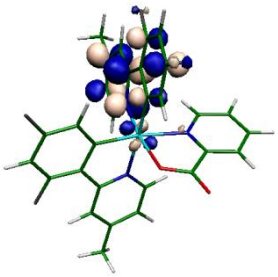
4	2.10	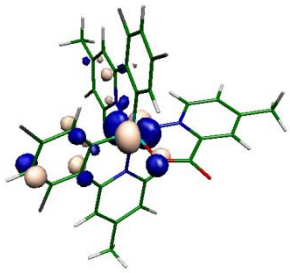	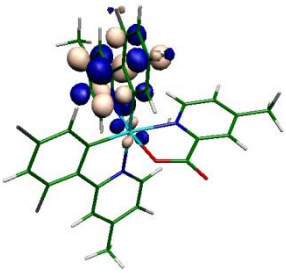
5	2.08	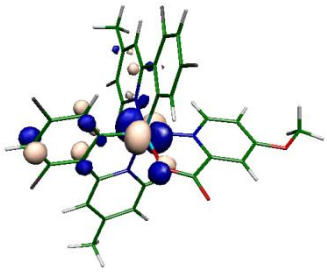	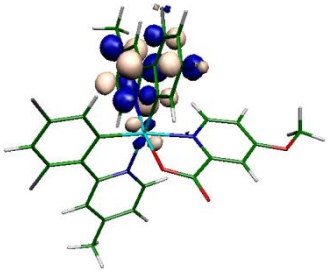

Table 7.18 (continued).

6	2.13	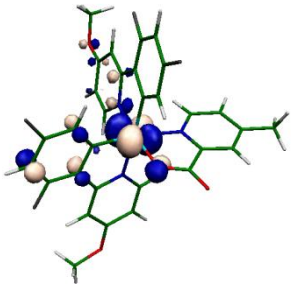	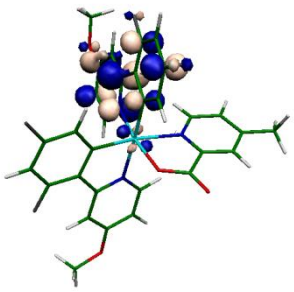
7	2.28	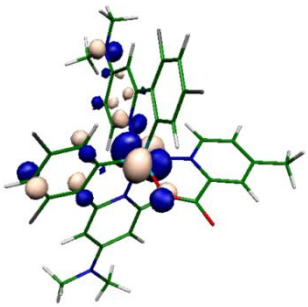	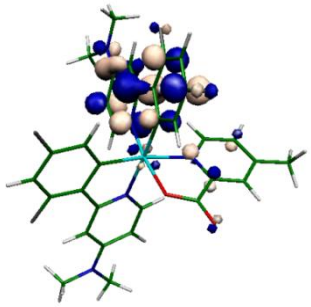
8	1.22	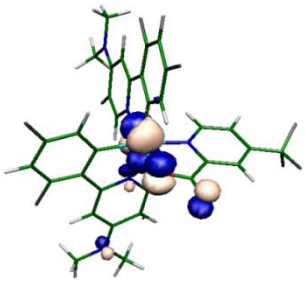	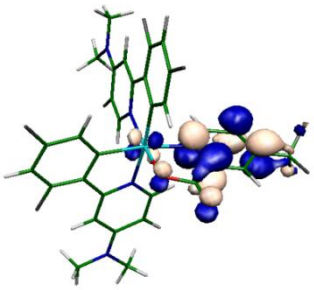

Note: The lowest triplet state is dominated by a HOMO → LUMO transition for all complexes, as given by TD-DFT calculations at the optimized T_1 geometry. The MOs are obtained from TD-DFT (T_1) closed-shell calculations.

Table 7.19 TD-DFT (T_1) calculated energy and the wavefunctions of the pair of MOs involved in the description of the lowest triplet excited state in N-*trans* complexes **1**-**8**.

Complex	*E* (eV)	HOMO	LUMO
1	2.27	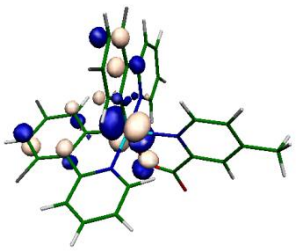	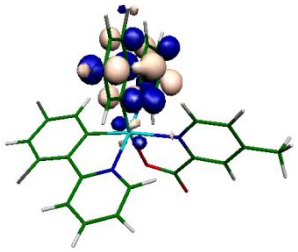
2	1.33	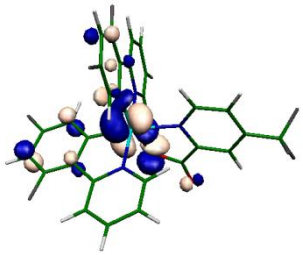	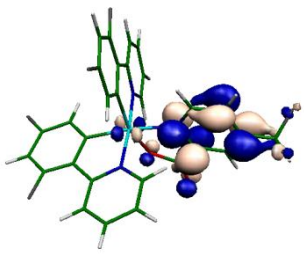
3	2.31	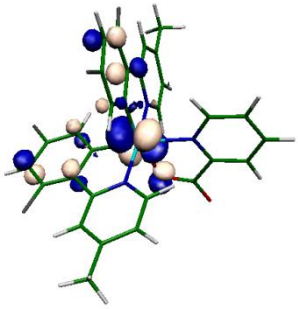	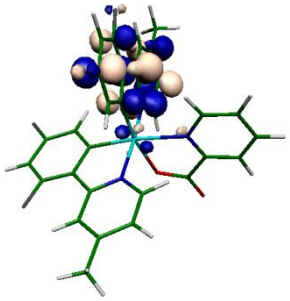
4	2.30	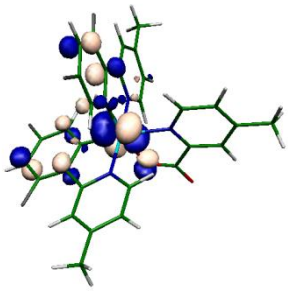	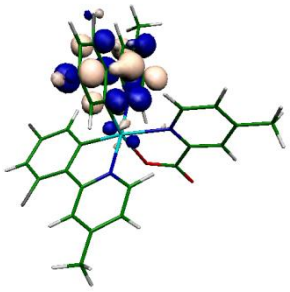
5	2.30	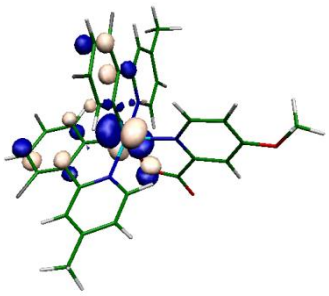	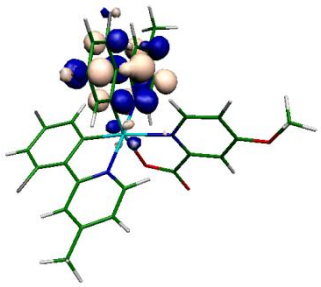

Table 7.19 (continued).

6	2.33	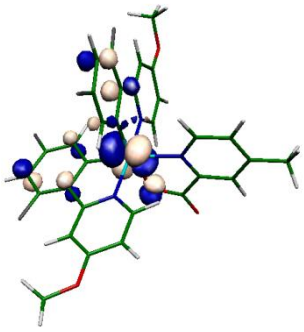	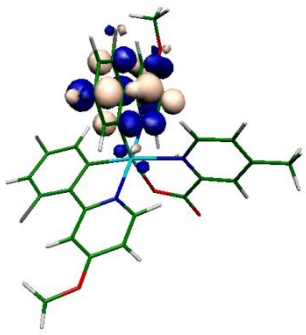
7	2.41	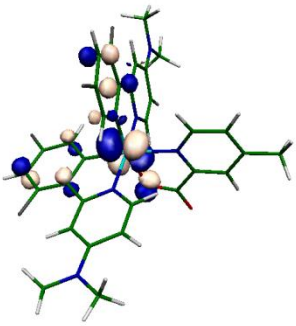	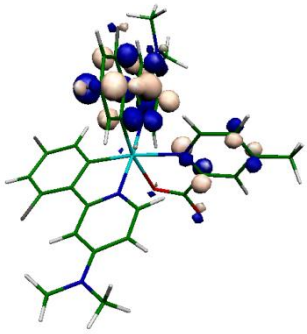
8	1.25	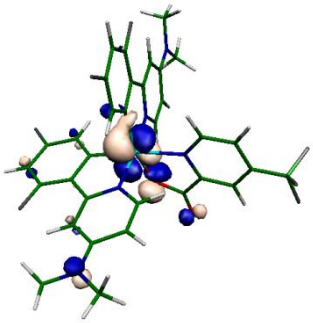	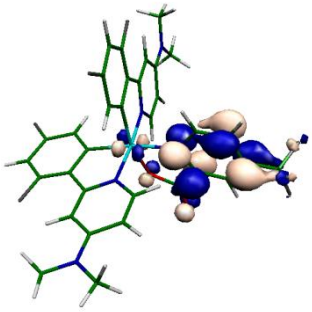

Note: The lowest triplet state is dominated by a HOMO → LUMO transition for all complexes, as given by TD-DFT calculations at the optimized T_1 geometry. The MOs are obtained from TD-DFT (T_1) closed-shell calculations.

The assignments of the lowest triplet excited state in Ir complexes are further supported by the calculations of the charge and spin distributions. Figures 7.11 and 7.12 collect the plots of the net Mulliken atomic charges Δq ($S_0 \rightarrow T_1$) transferred from (if positive: red) or to (if negative: blue) a particular atom of the complexes in the lowest triplet state with respect to the ground state charge distribution, as provided by DFT/B3LYP calculations. The charge distribution plots show that in all complexes charge is transferred from the Ir atom to the ligands. Interestingly, in all complexes

charge is predominantly transferred to phenylpyridine ligands, while for complexes **2** and **8** charge is mainly transferred to the CF_3-substituted picolinate. This is in agreement with the results of TD-DFT calculations; the strong electron withdrawing effect of the CF_3 group attached to picolinate results in the localization of the triplet state on this ligand (recall that there was a significant shortening of the Ir-O bond upon $S_0 \rightarrow T_1$ transition, further supporting the picolinate-localized triplet state of CF_3-substituted compounds). Moreover, the degree of MLCT in these complexes can be assessed from the magnitude of the charge transferred from the Ir atom or from the value of the spin density on Ir (see Table 7.20). For N-*trans* complexes, both the change in Mulliken charges Δq ($S_0 \rightarrow T_1$) and spin densities on Ir show that the picolinate-localized triplet excited states of complexes **2** and **8** exhibit the larger admixture of charge-transfer contributions. However, in the case of N-*cis* complexes, while spin densities on Ir indicate larger MLCT for complexes **2** and **8**, the Mulliken charges show less charge transfer for these complexes.

Table 7.20 Net Mulliken charge transferred from the Ir atom (Δq) upon $S_0 \rightarrow T_1$ transition and Mulliken atomic spin density on Ir in N-*cis* and N-*trans* complexes **1**-**8**.

	Mulliken charge		Mulliken spin density	
Complex	N-*cis*	N-*trans*	N-*cis*	N-*trans*
1	0.146	0.106	0.501	0.391
2	0.118	0.110	0.511	0.462
3	0.144	0.102	0.486	0.377
4	0.145	0.100	0.489	0.382
5	0.148	0.103	0.505	0.394
6	0.141	0.101	0.482	0.385
7	0.140	0.102	0.488	0.387
8	0.128	0.115	0.545	0.491

Note: Mulliken spin densities are calculated at the UB3LYP level. The schematics of the Δq ($S_0 \rightarrow T_1$) are shown in Figures 7.11 and 7.12 for N-*cis* and N-*trans* isomers, respectively.

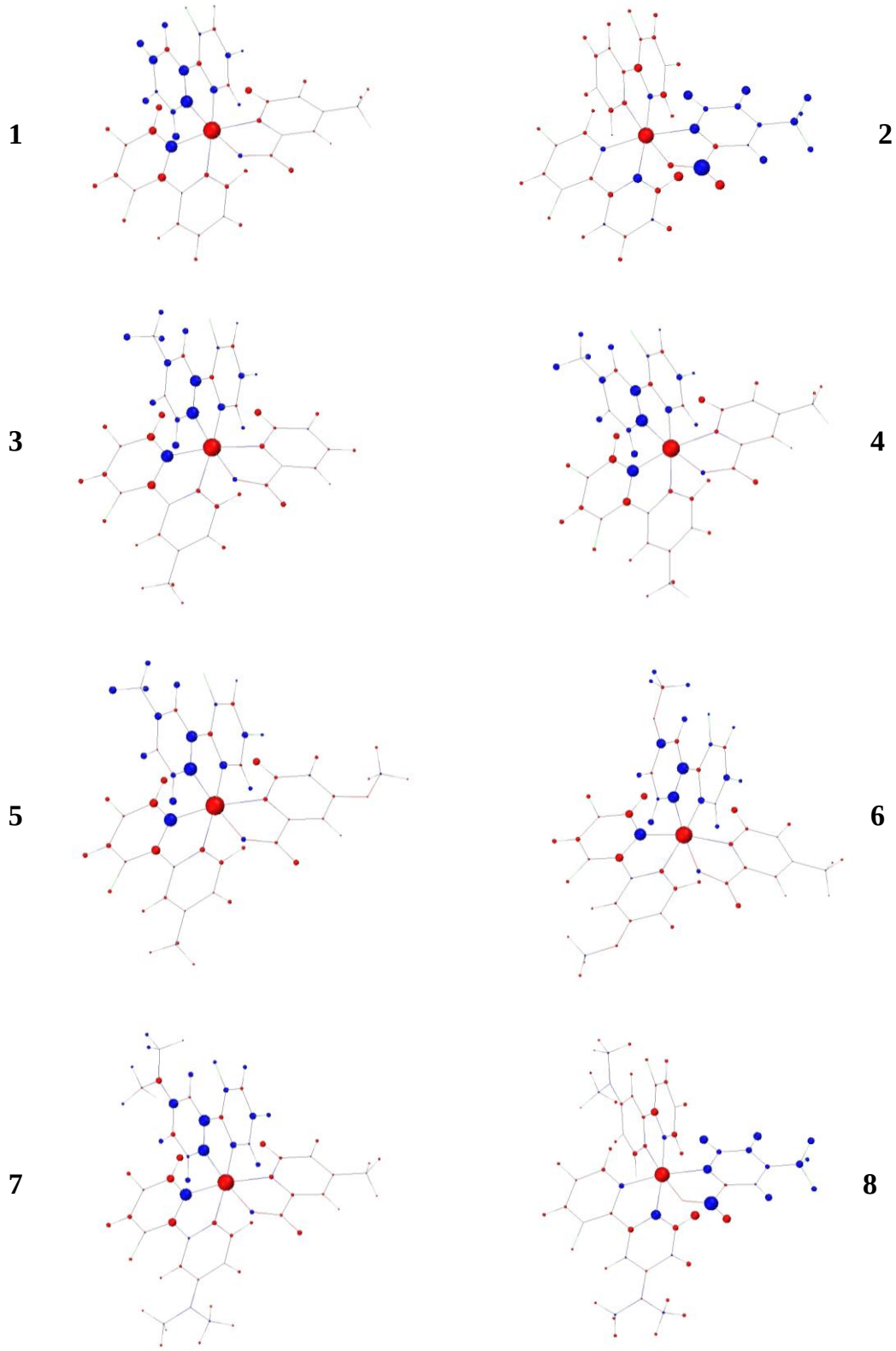

Figure 7.11 Plots of the change in the net Mulliken charge (Δq) upon $S_0 \rightarrow T_1$ transition in N-*cis* complexes **1**-**8**. Red and blue colors indicate positive and negative Δq, respectively.

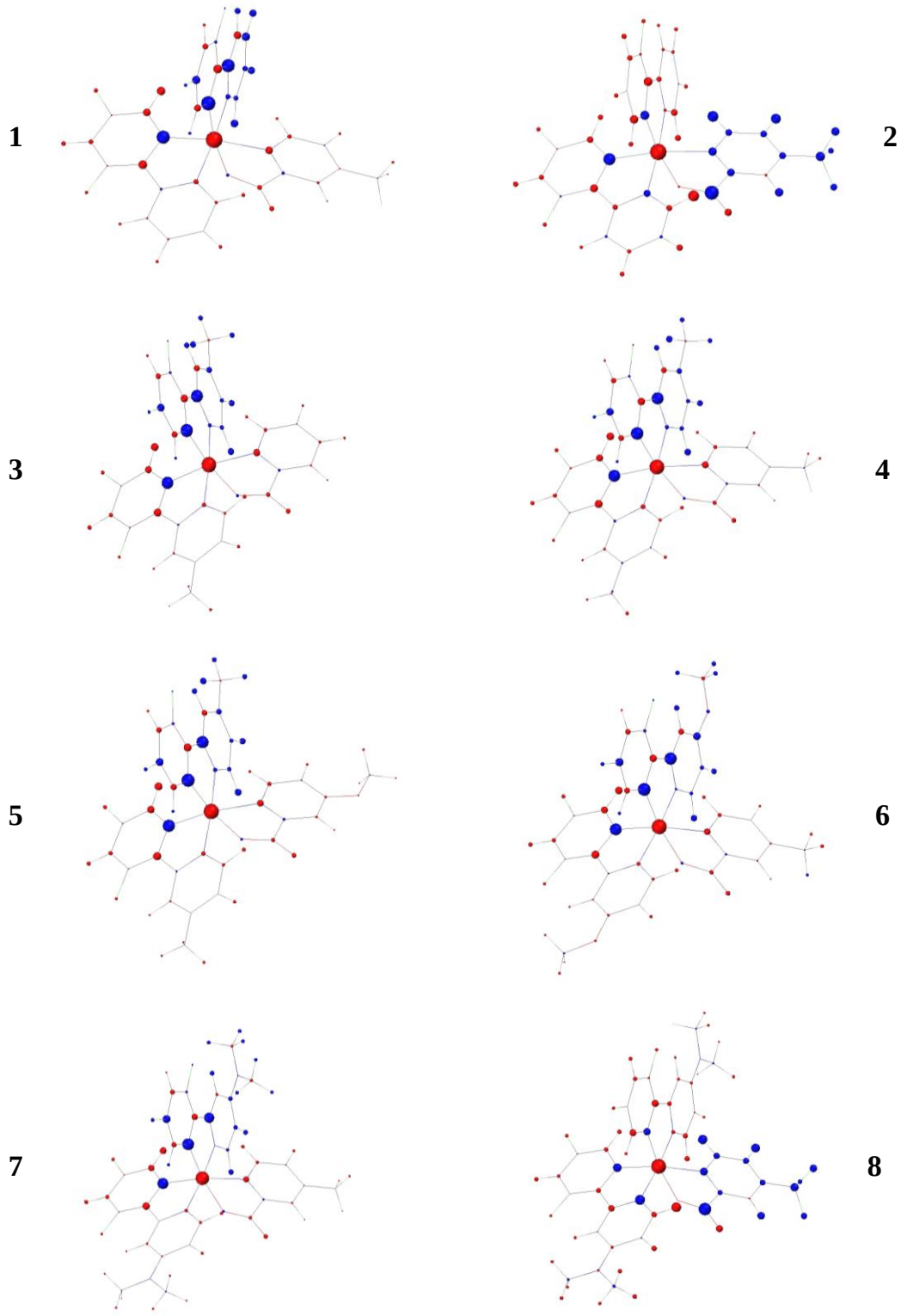

Figure 7.12 Plots of the change in the net Mulliken charge (Δq) upon $S_0 \rightarrow T_1$ transition in N-*trans* complexes **1**-**8**. Red and blue colors indicate positive and negative Δq, respectively.

Solvent Effects

Up to now, all the calculations were performed on isolated molecules ("in the gas phase"). In order to evaluate the solvent effects, the absorptions and emissions in the N-*cis* isomer of complex **1** are calculated by using a combined TD-DFT and PCM approach.[116,117] Table 7.21 shows the excitation energies as obtained from TD-DFT (S_0) for the N-*cis* isomer of complex **1** in a number of solvents. The transitions are slightly blue-shifted upon considering the solvent (E (S_1) = 2.99 and E (T_1) = 2.68 eV, in the gas phase). Photoexcitations estimated from the excited-state (T_1) geometry (Table 7.22) result in qualitative trends similar to those obtained from the ground-state (S_0) geometry. The excitation energies calculated from TD-DFT (T_1) technique are slightly blue-shifted with respect to their gas phase values of E (S_1) = 2.60 and E (T_1) = 2.09 eV.

The calculated excitation energies in complex **1** show little variations in solvents of different polarities (Tables 7.21 and 7.22). It is known that the substituents on the ligands affect the response of the emission spectra to different solvents (for instance, see Figure 7.13 for solution spectra of related Ir complexes).[283] Therefore, it would be important to obtain the experimental solvent study of complex **1** in order to test the reliability of our results. On the other hand, as Figure 7.13 shows, the emission spectra of analogous iridium-picolinate complexes display significant red-shifts (and broadening) in highly polar solvents such as methanol. However, our calculations with the combined TD-DFT and PCM approach give a little variation of excitation energies in solvents of various polarities. This suggests that the effect of solvatochromism on phosphorescence might be more complicated than predicted by the current methodology. The solvent model applied here neglects the solvent reorientation and therefore does not take into account possible structural reorganization of the Ir complex in solution. The presence of solvent may affect the extent of structural relaxation, ordering of the triplets, as well as the energy spacing between the lowest triplet states. The last case may lead to the

generation of quasi-degenerate low-lying triplets from which multiple photon emission becomes possible.

Table 7.21 Excitation energies, *E* (in eV), as obtained from TD-DFT (S_0) solution for N-*cis* isomer of complex **1**.

Solvent (Dielectric constant, ε)	*E* (S_1)	*E* (T_1)
Toluene (ε = 2.379)	3.09	2.73
Chloroform (ε = 4.9)	3.10	2.75
Acetone (ε = 20.7)	3.13	2.78
Methanol (ε = 32.63)	3.12	2.82
Acetonitrile (ε = 36.64)	3.15	2.76

Table 7.22 Excitation energies, *E* (in eV), as obtained from TD-DFT (T_1) solution for N-*cis* isomer of complex **1**.

Solvent (Dielectric constant, ε)	*E* (S_1)	*E* (T_1)
Toluene (ε = 2.379)	2.65	2.13
Chloroform (ε = 4.9)	2.69	2.16
Acetone (ε = 20.7)	2.73	2.19
Methanol (ε = 32.63)	2.75	2.21
Acetonitrile (ε = 36.64)	2.73	2.19

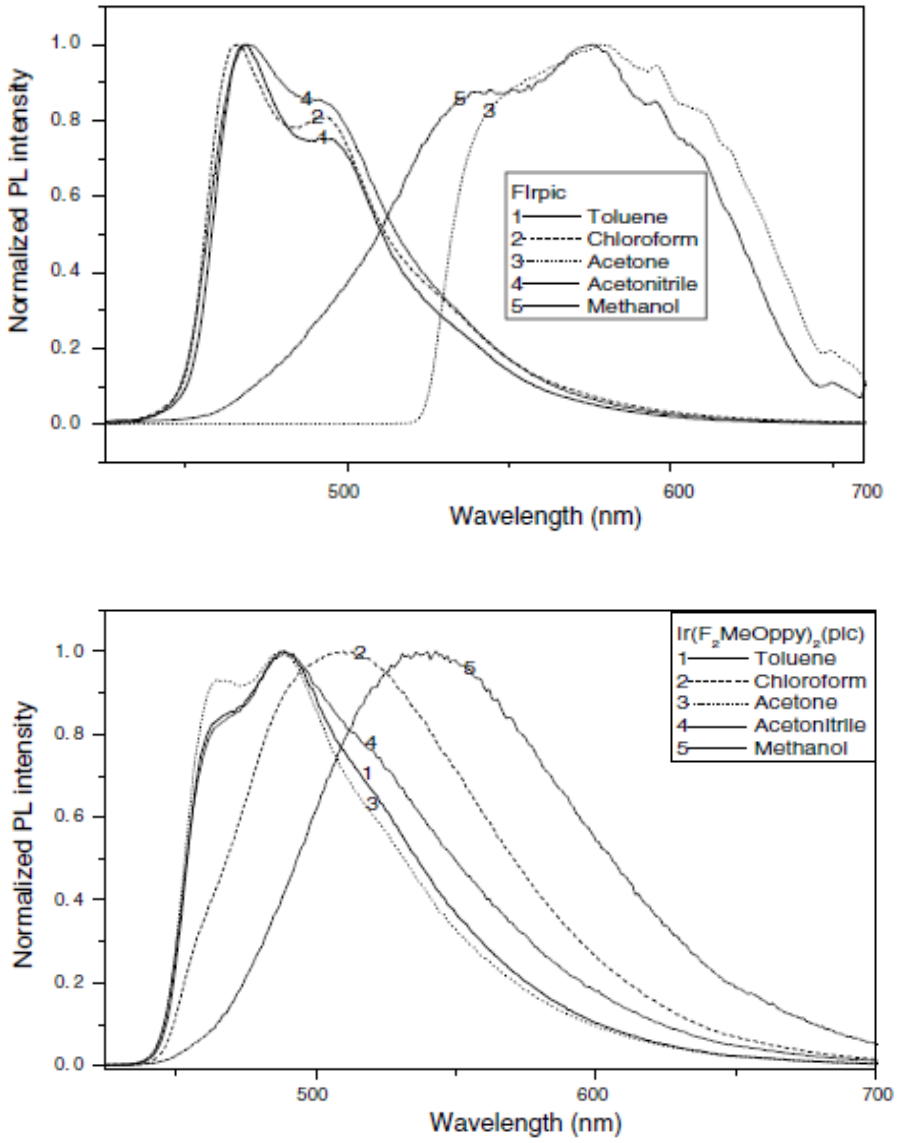

Figure 7.13 Solvent dependent emission spectra of FIrpic complexes. The top figure shows the solution emission spectra of unsubstituted FIrpic (R_1 = H and R_2 = H) and the bottom figure shows the emission spectra of the methoxy-substituted FIrpic (R_1 = OCH_3 and R_2 = H) complex in various solvents. Figure adapted from Ref. 283.

In order to understand the effect of solvent on the extent of structural relaxation, the T_1 state of complex **1** has been optimized "in solution" (ethanol) using the Onsager solvent model.[115] Table 7.23 summarizes the critical bond lengths between Ir and its coordinated atoms in gas-phase and solution. When the geometries in two media are compared, relatively small geometrical changes are observed. In solution, a slight shortening of the Ir-N bond in picolinate is found as compared to the gas-phase structure, whereas the rest of the bonds between Ir and its coordinated atoms remain almost unchanged. This finding weakens the possibility of large structural relaxation of the T_1 state in the presence of a solvent.

Table 7.23 Comparison of the selected bond lengths (Å) in the lowest triplet excited state of N-*cis* isomer of complex **1** in two media.

Medium	Ir-C1	Ir-N1	Ir-C2	Ir-N2	Ir-N3	Ir-O1
Gas	2.021	1.988	2.014	2.181	2.211	2.089
Solution	2.019	1.991	2.018	2.180	2.199	2.088

Note: The Onsager solvent model with ethanol is applied for optimization in solution.

The finite-field calculations of the dipole moments for the lowest-lying excited triplet states of complexes **1**-**8** indicate that the low-lying triplets differ in their static dipole moments (see Table 7.24). Furthermore, the ligand substitution (R_1 and R_2) affects the polarity of the triplet states as suggested by the diverse range of dipole moments. We also know that substitution of ligands changes the nature of the triplet states (such as MLCT, LLCT, LC, and MC transitions). As a result, the triplet states are expected to show different sensitivity towards solvents of different polarities. One possibility is that the ordering of the triplets may change in the presence of the solvent (due to marked differences in their dipole moments). If this happens, the triplet state could acquire a different nature in solution than it would in the gas phase.

There is also evidence from other metal compounds that the solvent molecule may replace one of the coordinating ligands,[284] when this is the case, one should expect a very

large structural relaxation in solution. As a result, the electronic structure of the lowest triplet state might not be necessarily related to a LC, LLCT, or MLCT transition with an original ligand participating anymore. However, this scenario is not explicitly taken into account in our calculations, and remains as a future work on this subject.

Table 7.24 Energies of lowest-lying triplet excited states from TD-DFT (S_0) calculations and dipole moments, μ, from finite-field method[a] for N-*cis* complexes **1**-**8**.

Complex	Energy (eV)	Dipole moment, μ (Debye)
1	T_1 = 2.68	μ_1 = 4.17
	T_2 = 2.84	μ_2 = 5.07
	T_3 = 2.87	μ_3 = 2.53
2	T_1 = 2.41	μ_1 = 10.25
	T_2 = 2.43	μ_2 = 8.30
	T_3 = 2.63	μ_3 = 10.28
3	T_1 = 2.71	μ_1 = 4.37
	T_2 = 2.73	μ_2 = 3.46
	T_3 = 2.82	μ_3 = 9.62
4	T_1 = 2.70	μ_1 = 3.85
	T_2 = 2.81	μ_2 = 7.10
	T_3 = 2.89	μ_3 = 2.95
5	T_1 = 2.69	μ_1 = 4.50
	T_2 = 2.89	μ_2 = 3.42
	T_3 = 2.89	μ_3 = 3.38
6	T_1 = 2.77	μ_1 = 3.84
	T_2 = 2.80	μ_2 = 4.13
	T_3 = 2.90	μ_3 = 7.92
7	T_1 = 2.74	μ_1 = 7.14
	T_2 = 2.81	μ_2 = 9.12
	T_3 = 2.89	μ_3 = 3.42
8	T_1 = 2.26	μ_1 = 10.85
	T_2 = 2.33	μ_2 = 8.24
	T_3 = 2.50	μ_3 = 9.80

[a]Finite-field method is based on the TD-DFT (S_0) calculations in the presence of an applied electric field. See Chapter 2 for more details.

Conclusions

To gain insight into the factors responsible for the emission color change and the different quantum yields, we performed DFT and TD-DFT calculations on the ground and excited states of Ir complexes, characterizing the excited-state geometries and including solvation effects on the calculation of the excited states. This computational procedure allowed us to provide a detailed assignment of the excited states involved in the absorption and emission processes and to rationalize the factors affecting the phosphorescent behavior in the investigated complexes.

The HOMO is confined on the metal-d and ppy-π orbitals, whereas the LUMO is in all cases a π* orbital localized on the ligand. The introduction of the strong electron withdrawing CF_3 group in the ancillary picolinate ligand leads to a remarkable drop of the LUMO level and corresponding changes in absorption and luminescence properties.

Our studies of the lowest triplet state in both isomers of FIrpic derivatives showed relatively small changes in geometry or energy (~0.3-0.4 eV). For complexes containing the CF_3 group on picolinate, larger geometry changes are observed upon relaxation into T_1 state, resulting in lower triplet energies for these compounds.

Our results indicated that the lowest excited states in these Ir complexes result from an interplay of MLCT, LLCT and/or LC transitions. Substituents significantly affect the mixing of these states. Our calculations also showed that there might be a competition between different types of MLCT transitions, where one state involves a π* orbital on the phenylpyridine ligand and another state involves a π* orbital on the picolinate ligand. The lowest excited triplet states of complexes **2** and **8** (where $R_2 = CF_3$) are characterized by MLCT to picolinate; for the rest of the compounds, the T_1 state is usually found to be dominated by MLCT to phenylpyridine.

The structure of the ligand affects the nature and polarity of the lowest triplet states and thus changes their response towards solvents of different polarity. The extent of structural relaxation is found to be similar in gas-phase and solution. However, there

exists a probability of reordering of triplets in solution as suggested by different static dipole moments of the low-lying excited triplet states.

In conclusion, designing a highly efficient blue phosphorescent emitter is a demanding task since the nature of the emissive state varies as a function of the substitution pattern. One strategy to shift the emission energy toward the blue region of the spectrum, on the basis of our calculations, may be functionalization of the phenylpyridine ligand by strong electron-donating groups. On the other hand, substitution of picolinate with strong electron-acceptors would shift the emission toward the red end of the spectrum. Further studies of spin-orbit coupling effects and specific interactions in solvent will give deeper insight for future development of blue phosphorescent emitters.

CHAPTER 8

CONCLUSIONS AND FUTURE WORK

The primary focus of this thesis was on two critical components of OLED operation: charge transport and light emission from excited state(s). Theoretical investigations of charge transport in organic materials have been often based on the "energy splitting in dimer" method and routinely assume that the transport parameters (site energies and transfer integrals) determined from monomer and dimer calculations can be reliably used to describe extended systems. The work presented in Chapter 3 demonstrated that this transferability can fail even in molecular crystals with weak van der Waals intermolecular interactions due to the substantial (but often ignored) impact of polarization effects, particularly on the site energies. We presented a straightforward method to compute transfer integrals directly, in terms of properly orthogonalized monomer orbitals. In Chapters 3 and 4, the charge-transport parameters of several organic crystals such as oligoacenes and derivatives were investigated in the framework of the methodology we contributed to develop. Following in Chapter 5, the geometric, electronic, and spectroscopic properties of the molecular organic materials presenting intramolecular charge transfer were addressed.

Another key issue in OLED research is the development of phosphorescent metal complexes showing all three primary colors for full-color displays. In this regard, Ir(III) complexes have received particular attention as they allow the fine tuning of emission color from blue/green to red by judicious modification of the coordinated ligands; however, there are fewer reports of blue emission from these species. To design efficient blue phosphorescent emitters for OLEDs, it is critical to understand the structure – photophysical property relationships. The host for blue phosphorescent emitters has to fulfill – besides the customary requirements known already from the use of fluorescent

emitters – the additional condition that the triplet energy of the host has to be higher than that of the guest. Thus, the design of suitable host materials is as important as that of phosphorescent emitters for the development of highly efficient OLEDs. Therefore, in the second half of this thesis, we concentrated on the theoretical analysis of host/guest systems for phosphorescent OLEDs. The work in Chapter 6 described the ground- and excited-state properties of several classes of host materials including carbazole and related compounds, phosphine oxides, oxadiazoles, hybrid oxadiazole/carbazole and organosilicon compounds with the aim of understanding their structure-property relations. The results demonstrated that the nature of the triplet excited states (localized *vs*. delocalized) depends strongly on the molecular topology and substituents. Localized excitations, *i.e.*, excited states confined within a small conjugated segment, resulted in host materials with high triplet energies. This strategy can be used to design high energy gap hosts suitable for blue phosphorescent OLEDs.

In the last chapter, we presented the impact of ligand chemical structure and orientation (facial *vs*. meridional) on the properties of the ground and lowest excited triplet states of iridium complexes. The work showed that the substitution on the ligands not only modulates the emission energy but also often changes the ordering of the lowest excited triplet states and hence their nature. The results of DFT and TD-DFT calculations on the ground and excited states of the Ir(III) complexes allowed us to characterize the nature of the excited states involved in the absorption and emission processes. The lowest triplet excited states are best characterized as MLCT mixed with LC and/or interligand excitations. The extent of mixing in these states strongly depends on the substituents. The strong influence of MLCT to the picolinate ligand in complexes substituted with strong electron-withdrawing groups on picolinate resulted in significant red shifts in emission. Thus, one strategy to design high energy blue emitters can be to avoid MLCT to picolinate, and instead to increase the extent of MLCT to phenylpyridine. This may be

achieved through functionalization of the picolinate ligand by strong electron-donating groups. This should be demonstrated in future studies.

The work on iridium complexes included preliminary studies on the consideration of spin-orbit coupling effects through the calculations of phosphorescence lifetimes in facial and meridional complexes of $Ir(ppy)_3$. However, there are still fundamental issues that require deeper understanding to gain control over molecular architecture and phosphorescence behavior of Ir complexes. These would include the details of phosphorescence parameters such as rates of intersystem crossing, transition moments, and zero-field splitting of the lowest triplet state, which may be the focus of further studies.

In addition, a detailed solvent study on the solution photoluminescence behavior of iridium complexes will be helpful in elucidating the role of solvent on the triplet emission phenomena. The current study suggested the reordering of the triplet states in the presence of solvent (due to the marked differences in their dipole moments). However, different solvents may affect phosphorescence in a different way. One scenario we have mentioned but not demonstrated in this study is the replacement of one of the coordinated ligands by solvent molecules. This possibility may be tested in future solvent studies. Furthermore, in Chapter 7, the solvent dependence of emission properties was demonstrated for one particular FIrpic compound. There is evidence from literature that the solution emission spectra of FIrpic complexes show variations with different substituents attached to the cyclometalated ligand.[283] Therefore, the present study should be completed for the rest of the compounds in the series in order to understand the role of different substitutents on the solution emission properties of Ir complexes.

It is our hope that further theoretical calculations including these additional considerations can help to understand the phosphorescence of known systems and at the same time provide a tool for building structure-property relationships that can be useful to synthesize efficient phosphorescent emitters.

REFERENCES

(1) Shirakawa, H. *Angewandte Chemie-International Edition* **2001**, *40*, 2575-2580.

(2) Chiang, C. K.; Fincher, C. R.; Park, Y. W.; Heeger, A. J.; Shirakawa, H.; Louis, E. J.; Gau, S. C.; Macdiarmid, A. G. *Physical Review Letters* **1977**, *39*, 1098-1101.

(3) Friend, R. H.; Gymer, R. W.; Holmes, A. B.; Burroughes, J. H.; Marks, R. N.; Taliani, C.; Bradley, D. D. C.; Dos Santos, D. A.; Bredas, J. L.; Logdlund, M.; Salaneck, W. R. *Nature* **1999**, *397*, 121-128.

(4) Sariciftci, N. S.; Smilowitz, L.; Heeger, A. J.; Wudl, F. *Science* **1992**, *258*, 1474-1476.

(5) Sirringhaus, H.; Brown, P. J.; Friend, R. H.; Nielsen, M. M.; Bechgaard, K.; Langeveld-Voss, B. M. W.; Spiering, A. J. H.; Janssen, R. A. J.; Meijer, E. W.; Herwig, P.; de Leeuw, D. M. *Nature* **1999**, *401*, 685-688.

(6) McQuade, D. T.; Pullen, A. E.; Swager, T. M. *Chemical Reviews* **2000**, *100*, 2537-2574.

(7) Pope, M.; Magnante, P.; Kallmann, H. P. *Journal of Chemical Physics* **1963**, *38*, 2042-2043.

(8) Tang, C. W.; Vanslyke, S. A. *Applied Physics Letters* **1987**, *51*, 913-915.

(9) Burroughes, J. H.; Bradley, D. D. C.; Brown, A. R.; Marks, R. N.; Mackay, K.; Friend, R. H.; Burns, P. L.; Holmes, A. B. *Nature* **1990**, *347*, 539-541.

(10) *http://pioneer.jp/corp/profile-e/history/*. Accessed on January 2009.

(11) *http://www.dpreview.com/news/0303/03030216kodakls633.asp*. Accessed on January 2009.

(12) *http://www.oled-info.com/samsungs-new-40-oled-tv-high-def-1920-x-1080*. Accessed on January 2009.

(13) *http://news.cnet.com/Sony-eyeing-OLED-TVs-for-2008/2100-1041_3-6148330.html*. Picture downloaded on January 05, 2009.

(14) *http://www.reuters.com/article/pressRelease/idUS235362+15-Jul-2008+BW20080715*. Accessed on January 2009.

(15) *http://www.polymervision.com/*. Picture downloaded on January 05, 2009.

(16) *http://www.research.philips.com/newscenter/pictures/ldm-lighting.html*. Picture downloaded on January 05, 2009.

(17) Baldo, M. A.; Thompson, M. E.; Forrest, S. R. *Nature* **2000**, *403*, 750-753.

(18) Adachi, C.; Baldo, M. A.; Forrest, S. R.; Thompson, M. E. *Applied Physics Letters* **2000**, *77*, 904-906.

(19) Shaheen, S. E.; Ginley, D. S.; Jabbour, G. E. *Mrs Bulletin* **2005**, *30*, 10-19.

(20) Becquerel, A. E. *Comptes Rendus* **1839**, *9*.

(21) Chapin, D. M.; Fuller, C. S.; Pearson, G. L. *Journal of Applied Physics* **1954**, *25*, 676-677.

(22) Bredas, J. L.; Beljonne, D.; Coropceanu, V.; Cornil, J. *Chemical Reviews* **2004**, *104*, 4971-5003.

(23) Forrest, S. R. *Mrs Bulletin* **2005**, *30*, 28-32.

(24) Pivrikas, A.; Sariciftci, N. S.; Juska, G.; Osterbacka, R. *Progress in Photovoltaics* **2007**, *15*, 677-696.

(25) *http://www.lios.at/Research/plastic/homecol.pdf*. Accessed on January 2009.

(26) Tsumura, A.; Koezuka, H.; Ando, T. *Applied Physics Letters* **1986**, *49*, 1210-1212.

(27) Podzorov, V.; Sysoev, S. E.; Loginova, E.; Pudalov, V. M.; Gershenson, M. E. *Applied Physics Letters* **2003**, *83*, 3504-3506.

(28) Sundar, V. C.; Zaumseil, J.; Podzorov, V.; Menard, E.; Willett, R. L.; Someya, T.; Gershenson, M. E.; Rogers, J. A. *Science* **2004**, *303*, 1644-1646.

(29) Endres, R. G.; Fong, C. Y.; Yang, L. H.; Witte, G.; Woll, C. *Computational Materials Science* **2004**, *29*, 362-370.

(30) Cornil, J.; Calbert, J. P.; Bredas, J. L. *Journal of the American Chemical Society* **2001**, *123*, 1250-1251.

(31) de Wijs, G. A.; Mattheus, C. C.; de Groot, R. A.; Palstra, T. T. M. *Synthetic Metals* **2003**, *139*, 109-114.

(32) Moon, H.; Zeis, R.; Borkent, E. J.; Besnard, C.; Lovinger, A. J.; Siegrist, T.; Kloc, C.; Bao, Z. N. *Journal of the American Chemical Society* **2004**, *126*, 15322-15323.

(33) Goldmann, C.; Haas, S.; Krellner, C.; Pernstich, K. P.; Gundlach, D. J.; Batlogg, B. *Journal of Applied Physics* **2004**, *96*, 2080-2086.

(34) Klauk, H.; Jackson, T. N. *Solid State Technology* **2000**, *43*, 63-76.

(35) da Silva, D. A.; Kim, E. G.; Bredas, J. L. *Advanced Materials* **2005**, *17*, 1072-1076.

(36) Podzorov, V.; Pudalov, V. M.; Gershenson, M. E. *Applied Physics Letters* **2003**, *82*, 1739-1741.

(37) Podzorov, V.; Menard, E.; Borissov, A.; Kiryukhin, V.; Rogers, J. A.; Gershenson, M. E. *Physical Review Letters* **2004**, *93*, 086602.

(38) Garnier, F.; Hajlaoui, R.; Yassar, A.; Srivastava, P. *Science* **1994**, *265*, 1684-1686.

(39) Senthilkumar, K.; Grozema, F. C.; Bickelhaupt, F. M.; Siebbeles, L. D. A. *Journal of Chemical Physics* **2003**, *119*, 9809-9817.

(40) van de Craats, A. M.; Warman, J. M.; Fechtenkotter, A.; Brand, J. D.; Harbison, M. A.; Mullen, K. *Advanced Materials* **1999**, *11*, 1469-1472.

(41) Jones, B. A.; Ahrens, M. J.; Yoon, M. H.; Facchetti, A.; Marks, T. J.; Wasielewski, M. R. *Angewandte Chemie-International Edition* **2004**, *43*, 6363-6366.

(42) Bao, Z.; Lovinger, A. J.; Dodabalapur, A. *Applied Physics Letters* **1996**, *69*, 3066-3068.

(43) Adam, D.; Schuhmacher, P.; Simmerer, J.; Haussling, L.; Siemensmeyer, K.; Etzbach, K. H.; Ringsdorf, H.; Haarer, D. *Nature* **1994**, *371*, 141-143.

(44) Cornil, J.; Lemaur, V.; Calbert, J. P.; Bredas, J. L. *Advanced Materials* **2002**, *14*, 726-729.

(45) Lemaur, V.; Da Silva Filho, D. A.; Coropceanu, V.; Lehmann, M.; Geerts, Y.; Piris, J.; Debije, M. G.; Van de Craats, A. M.; Senthilkumar, K.; Siebbeles, L. D. A.; Warman, J. M.; Bredas, J. L.; Cornil, J. *Journal of the American Chemical Society* **2004**, *126*, 3271-3279.

(46) Iino, H.; Hanna, J.; Haarer, D. *Physical Review B* **2005**, *72*, 193203.

(47) Bushby, R. J.; Lozman, O. R. *Current Opinion in Solid State & Materials Science* **2002**, *6*, 569-578.

(48) Baldo, M. A.; Adachi, C.; Forrest, S. R. *Physical Review B* **2000**, *62*, 10967-10977.

(49) Mas-Torrent, M.; Hadley, P.; Bromley, S. T.; Crivillers, N.; Veciana, J.; Rovira, C. *Applied Physics Letters* **2005**, *86*, 012110.

(50) S. Yoo, B. D., B. Kippelen *Applied Physics Letters* **2004**, *85*, 5427-5429.

(51) Anthopoulos, T. D.; Singh, B.; Marjanovic, N.; Sariciftci, N. S.; Ramil, A. M.; Sitter, H.; Colle, M.; de Leeuw, D. M. *Applied Physics Letters* **2006**, *89*, 213504/1-213504/3.

(52) Zhang, X. H.; Kippelen, B. *Journal of Applied Physics* **2008**, *104*, 104504/1-104504/6.

(53) Payne, M. M.; Parkin, S. R.; Anthony, J. E.; Kuo, C. C.; Jackson, T. N. *Journal of the American Chemical Society* **2005**, *127*, 4986-4987.

(54) Sheraw, C. D.; Jackson, T. N.; Eaton, D. L.; Anthony, J. E. *Advanced Materials* **2003**, *15*, 2009-2011.

(55) Anthony, J. E.; Eaton, D. L.; Parkin, S. R. *Organic Letters* **2002**, *4*, 15-18.

(56) Anthony, J. E.; Brooks, J. S.; Eaton, D. L.; Parkin, S. R. *Journal of the American Chemical Society* **2001**, *123*, 9482-9483.

(57) Payne, M. M.; Parkin, S. R.; Anthony, J. E. *Journal of the American Chemical Society* **2005**, *127*, 8028-8029.

(58) Payne, M. M.; Odom, S. A.; Parkin, S. R.; Anthony, J. E. *Organic Letters* **2004**, *6*, 3325-3328.

(59) Subramanian, S.; Park, S. K.; Parkin, S. R.; Podzorov, V.; Jackson, T. N.; Anthony, J. E. *Journal of the American Chemical Society* **2008**, *130*, 2706-2707.

(60) Meng, H.; Bendikov, M.; Mitchell, G.; Helgeson, R.; Wudl, F.; Bao, Z.; Siegrist, T.; Kloc, C.; Chen, C. H. *Advanced Materials* **2003**, *15*, 1090-1093.

(61) Chen, Z. H.; Muller, P.; Swager, T. M. *Organic Letters* **2006**, *8*, 273-276.

(62) Coropceanu, V.; Cornil, J.; da Silva, D. A.; Olivier, Y.; Silbey, R.; Bredas, J. L. *Chemical Reviews* **2007**, *107*, 926-952.

(63) Chen, T. A.; Wu, X. M.; Rieke, R. D. *Journal of the American Chemical Society* **1995**, *117*, 233-244.

(64) Yamada, K.; Okamoto, T.; Kudoh, K.; Wakamiya, A.; Yamaguchi, S.; Takeya, J. *Applied Physics Letters* **2007**, *90*, 072102.

(65) Sun, Y. M.; Ma, Y. W.; Liu, Y. Q.; Lin, Y. Y.; Wang, Z. Y.; Wang, Y.; Di, C. G.; Xiao, K.; Chen, X. M.; Qiu, W. F.; Zhang, B.; Yu, G.; Hu, W. P.; Zhu, D. B. *Advanced Functional Materials* **2006**, *16*, 426-432.

(66) Li, X. C.; Sirringhaus, H.; Garnier, F.; Holmes, A. B.; Moratti, S. C.; Feeder, N.; Clegg, W.; Teat, S. J.; Friend, R. H. *Journal of the American Chemical Society* **1998**, *120*, 2206-2207.

(67) Sirringhaus, H.; Kawase, T.; Friend, R. H.; Shimoda, T.; Inbasekaran, M.; Wu, W.; Woo, E. P. *Science* **2000**, *290*, 2123-2126.

(68) Leising, G.; Tasch, S.; Brandstatter, C.; Graupner, W.; Hampel, S.; List, E. J. W.; Meghdadi, F.; Zenz, C.; Schlichting, P.; Rohr, U.; Geerts, Y.; Scherf, U.; Mullen, K. *Synthetic Metals* **1997**, *91*, 41-47.

(69) Li, S. B.; Zhang, Y.; Niu, Q. L.; Zhao, L.; Fan, Q. L.; Peng, B.; Zhu, X. H.; Cao, Y.; Huang, W. *Acta Chimica Sinica* **2006**, *64*, 2509-2514.

(70) Yamamoto, H.; Wilkinson, J.; Long, J. P.; Bussman, K.; Christodoulides, J. A.; Kafafi, Z. H. *Nano Letters* **2005**, *5*, 2485-2488.

(71) Le, Y.; Umemoto, Y.; Okabe, M.; Kusunoki, T.; Nakayama, K. I.; Pu, Y. J.; Kido, J.; Tada, H.; Aso, Y. *Organic Letters* **2008**, *10*, 833-836.

(72) Facchetti, A.; Yoon, M. H.; Stern, C. L.; Hutchison, G. R.; Ratner, M. A.; Marks, T. J. *Journal of the American Chemical Society* **2004**, *126*, 13480-13501.

(73) Facchetti, A.; Yoon, M. H.; Stern, C. L.; Katz, H. E.; Marks, T. J. *Angewandte Chemie-International Edition* **2003**, *42*, 3900-3903.

(74) Yoon, M. H.; DiBenedetto, S. A.; Facchetti, A.; Marks, T. J. *Journal of the American Chemical Society* **2005**, *127*, 1348-1349.

(75) Chesterfield, R. J.; Newman, C. R.; Pappenfus, T. M.; Ewbank, P. C.; Haukaas, M. H.; Mann, K. R.; Miller, L. L.; Frisbie, C. D. *Advanced Materials* **2003**, *15*, 1278-1282.

(76) Cai, X. Y.; Burand, M. W.; Newman, C. R.; da Silva, D. A.; Pappenfus, T. M.; Bader, M. M.; Bredas, J. L.; Mann, K. R.; Frisbie, C. D. *Journal of Physical Chemistry B* **2006**, *110*, 14590-14597.

(77) Ichikawa, M.; Kawaguchi, T.; Kobayashi, K.; Miki, T.; Furukawa, K.; Koyama, T.; Taniguchi, Y. *Journal of Materials Chemistry* **2006**, *16*, 221-225.

(78) Liu, C. B.; Zhao, P.; Huang, W. *Central European Journal of Chemistry* **2007**, *5*, 303-315.

(79) Jansson, E.; Jha, P. C.; Agren, H. *Chemical Physics* **2006**, *330*, 166-171.

(80) Tamao, K.; Uchida, M.; Izumizawa, T.; Furukawa, K.; Yamaguchi, S. *Journal of the American Chemical Society* **1996**, *118*, 11974-11975.

(81) Adachi, C.; Tsutsui, T.; Saito, S. *Applied Physics Letters* **1990**, *56*, 799-801.

(82) Hughes, G.; Bryce, M. R. *Journal of Materials Chemistry* **2005**, *15*, 94-107.

(83) Cornil, J.; Bredas, J. L.; Zaumseil, J.; Sirringhaus, H. *Advanced Materials* **2007**, *19*, 1791-1799.

(84) Koh, S. E.; Risko, C.; da Silva, D. A.; Kwon, O.; Facchetti, A.; Bredas, J. L.; Marks, T. J.; Ratner, M. A. *Advanced Functional Materials* **2008**, *18*, 332-340.

(85) Bredas, J. L.; Calbert, J. P.; da Silva, D. A.; Cornil, J. *Proceedings of the National Academy of Sciences of the United States of America* **2002**, *99*, 5804-5809.

(86) Haddon, R. C.; Chi, X.; Itkis, M. E.; Anthony, J. E.; Eaton, D. L.; Siegrist, T.; Mattheus, C. C.; Palstra, T. T. M. *Journal of Physical Chemistry B* **2002**, *106*, 8288-8292.

(87) Lewis, F. D.; Kurth, T. L.; Delos Santos, G. B. *Journal of Physical Chemistry B* **2005**, *109*, 4893-4899.

(88) Troisi, A.; Orlandi, G. *Physical Review Letters* **2006**, *96*, 086601.

(89) Marcus, R. A. *Journal of Chemical Physics* **1956**, *24*, 966-978.

(90) Bixon, M.; Jortner, J. *Electron Transfer-from Isolated Molecules to Biomolecules, Pt 1* **1999**, *106*, 35-202.

(91) Atkins, P. W. *Physical Chemistry, 4th ed., Oxford University Press, Oxford 1990.*

(92) Perdew, J. P.; Chevary, J. A.; Vosko, S. H.; Jackson, K. A.; Pederson, M. R.; Singh, D. J.; Fiolhais, C. *Physical Review B* **1992**, *46*, 6671-6687.

(93) Velde, G. T.; Bickelhaupt, F. M.; Baerends, E. J.; Guerra, C. F.; Van Gisbergen, S. J. A.; Snijders, J. G.; Ziegler, T. *Journal of Computational Chemistry* **2001**, *22*, 931-967.

(94) Huang, J. S.; Kertesz, M. *Journal of Chemical Physics* **2005**, *122*, 12891-12898.

(95) Zerner, M. C.; Loew, G. H.; Kirchner, R. F.; Muellerwesterhoff, U. T. *Journal of the American Chemical Society* **1980**, *102*, 589-599.

(96) Becke, A. D. *Journal of Chemical Physics* **1993**, *98*, 5648-5652.

(97) M. J. Frisch, G. W. T., H. B. Schlegel, G. E. Scuseria,; M. A. Robb, J. R. C., V. G. Zakrzewski, J. A. Montgomery, Jr.,; R. E. Stratmann, J. C. B., S. Dapprich, J. M. Millam,; A. D. Daniels, K. N. K., M. C. Strain, O. Farkas, J. Tomasi,; V. Barone, M. C., R. Cammi, B. Mennucci, C. Pomelli, C. Adamo,; S. Clifford, J. O., G. A. Petersson, P. Y. Ayala, Q. Cui,; K. Morokuma, P. S., J. J. Dannenberg, D. K. Malick,; A. D. Rabuck, K. R., J. B. Foresman, J. Cioslowski,; J. V. Ortiz, A. G. B., B. B. Stefanov, G. Liu, A. Liashenko,; P. Piskorz, I. K., R. Gomperts, R. L. Martin, D. J. Fox,; T. Keith, M. A. A.-L., C. Y. Peng, A. Nanayakkara, M. Challacombe,; P. M. W. Gill, B. J., W. Chen, M. W. Wong, J. L. Andres,; C. Gonzalez, M. H.-G., E. S. Replogle, and J. A. Pople; Gaussian 98 (Revision A.11.1), Gaussian, Inc., Pittsburgh PA, 2001.

(98) M. J. Frisch, G. W. T., H. B. Schlegel, G. E. Scuseria,; M. A. Robb, J. R. C., J. A. Montgomery, Jr., T. Vreven,; K. N. Kudin, J. C. B., J. M. Millam, S. S. Iyengar, J. Tomasi,; V. Barone, B. M., M. Cossi, G. Scalmani, N. Rega,; G. A. Petersson, H. N., M. Hada, M. Ehara, K. Toyota,; R. Fukuda, J. H., M. Ishida, T. Nakajima, Y. Honda, O. Kitao,; H. Nakai, M. K., X. Li, J. E. Knox, H. P. Hratchian, J. B. Cross,; C. Adamo, J. J., R. Gomperts, R. E. Stratmann, O. Yazyev,; A. J. Austin, R. C., C. Pomelli, J. W. Ochterski, P. Y. Ayala,; K. Morokuma, G. A. V., P. Salvador, J. J. Dannenberg,; V. G. Zakrzewski, S. D., A. D. Daniels, M. C. Strain,; O. Farkas, D. K. M., A. D. Rabuck, K. Raghavachari,; J. B. Foresman, J. V. O., Q. Cui, A. G. Baboul, S. Clifford,; J. Cioslowski, B. B. S., G. Liu, A. Liashenko, P. Piskorz,; I. Komaromi, R. L. M., D. J. Fox, T. Keith, M. A. Al-Laham,; C. Y. Peng, A. N., M. Challacombe, P. M. W. Gill,; B. Johnson, W. C., M. W. Wong, C. Gonzalez, and J. A. Pople; Gaussian 03, Revision B.02, Gaussian, Inc., Pittsburgh PA, 2003.

(99) Sanchez-Carrera, R. S.; Coropceanu, V.; da Silva, D. A.; Friedlein, R.; Osikowicz, W.; Murdey, R.; Suess, C.; Salaneck, W. R.; Bredas, J. L. *Journal of Physical Chemistry B* **2006**, *110*, 18904-18911.

(100) Coropceanu, V.; Kwon, O.; Wex, B.; Kaafarani, B. R.; Gruhn, N. E.; Durivage, J. C.; Neckers, D. C.; Bredas, J. L. *Chemistry-a European Journal* **2006**, *12*, 2073-2080.

(101) Deleuze, M. S.; Claes, L.; Kryachko, E. S.; Francois, J. P. *Journal of Chemical Physics* **2003**, *119*, 3106-3119.

(102) Hay, P. J.; Wadt, W. R. *Journal of Chemical Physics* **1985**, *82*, 299-310.

(103) Becke, A. D. *Physical Review A* **1988**, *38*, 3098-3100.

(104) Perdew, J. P. *Physical Review B* **1986**, *33*, 8822-8824.

(105) van Lenthe, E.; Ehlers, A.; Baerends, E. J. *Journal of Chemical Physics* **1999**, *110*, 8943-8953.

(106) Vanlenthe, E.; Baerends, E. J.; Snijders, J. G. *Journal of Chemical Physics* **1993**, *99*, 4597-4610.

(107) Vanlenthe, E.; Baerends, E. J.; Snijders, J. G. *Journal of Chemical Physics* **1994**, *101*, 9783-9792.

(108) vanLenthe, E.; Snijders, J. G.; Baerends, E. J. *Journal of Chemical Physics* **1996**, *105*, 6505-6516.

(109) vanLenthe, E.; vanLeeuwen, R.; Baerends, E. J.; Snijders, J. G. *International Journal of Quantum Chemistry* **1996**, *57*, 281-293.

(110) Runge, E.; Gross, E. K. U. *Physical Review Letters* **1984**, *52*, 997-1000.

(111) Delbene, J. E.; Ditchfie.R; Pople, J. A. *Journal of Chemical Physics* **1971**, *55*, 2236-2241.

(112) Headgordon, M.; Rico, R. J.; Oumi, M.; Lee, T. J. *Chemical Physics Letters* **1994**, *219*, 21-29.

(113) Headgordon, M.; Grana, A. M.; Maurice, D.; White, C. A. *Journal of Physical Chemistry* **1995**, *99*, 14261-14270.

(114) J. Kong; C. A. White; A. I. Krylov; C. D. Sherrill; R. D. Adamson; T. R. Furlani; M. S. Lee; A. M. Lee; S. R. Gwaltney; T. R. Adams; C. Ochsenfeld; A. T. B. Gilbert; G. S. Kedziora; V. A. Rassolov; D. R. Maurice; N. Nair; Y. Shao; N. A. Besley; P. E. Maslen; J. P. Dombroski; H. Dachsel; W. M. Zhang; P. P. Korambath; J. Baker; E. F. C. Byrd; T. Van Voorhis; M. Oumi; S. Hirata; C. P. Hsu; N. Ishikawa; J. Florian; A. Warshel; B. G. Johnson; . M. W. Gill; M. Head-Gordon; Pople, J. A.; Q-Chem, Version 2.0, Q-Chem, Inc., Export, PA (2000).

(115) Onsager, L. *Journal of the American Chemical Society* **1936**, *58*, 1486-1493.

(116) Miertus, S.; Scrocco, E.; Tomasi, J. *Chemical Physics* **1981**, *55*, 117-129.

(117) Miertus, S.; Tomasi, J. *Chemical Physics* **1982**, *65*, 239-245.

(118) Liu, T.; Xia, B. H.; Zhou, X.; Zhang, H. X.; Pan, Q. J.; Gao, J. S. *Organometallics* **2007**, *26*, 143-149.

(119) Kamada, K.; Ueda, M.; Nagao, H.; Tawa, K.; Sugino, T.; Shmizu, Y.; Ohta, K. *Journal of Physical Chemistry A* **2000**, *104*, 4723-4734.

(120) DALTON; A molecular electronic structure program, Release 2.0 (2005), see http://www.kjemi.uio.no/software/dalton/dalton.html.

(121) Peierls, R. E. *Quantum Theory of Solids; Clarendon Press: Oxford*, 1955.

(122) Holstein, T. *Annals of Physics* **1959**, *8*, 325-342.

(123) Holstein, T. *Annals of Physics* **1959**, *8*, 343-389.

(124) Cheng, Y. C.; Silbey, R. J.; da Silva, D. A.; Calbert, J. P.; Cornil, J.; Bredas, J. L. *Journal of Chemical Physics* **2003**, *118*, 3764-3774.

(125) Kwon, O.; Coropceanu, V.; Gruhn, N. E.; Durivage, J. C.; Laquindanum, J. G.; Katz, H. E.; Cornil, J.; Bredas, J. L. *Journal of Chemical Physics* **2004**, *120*, 8186-8194.

(126) Hutchison, G. R.; Ratner, M. A.; Marks, T. J. *Journal of the American Chemical Society* **2005**, *127*, 16866-16881.

(127) Koopmans, T. *Physica* **1934**, *1*, 104-113.

(128) Wu, Q.; Voorhis, T. V. *The Journal of Chemical Physics* **2006**, *125*, 164105.

(129) Senthilkumar, K.; Grozema, F. C.; Guerra, C. F.; Bickelhaupt, F. M.; Lewis, F. D.; Berlin, Y. A.; Ratner, M. A.; Siebbeles, L. D. A. *Journal of the American Chemical Society* **2005**, *127*, 14894-14903.

(130) Löwdin, P. O. *Journal of Chemical Physics* **1950**, *18*, 365-375.

(131) Valeev, E. F.; Coropceanu, V.; da Silva, D. A.; Salman, S.; Bredas, J. L. *Journal of the American Chemical Society* **2006**, *128*, 9882-9886.

(132) Zhang, X. N.; Johnson, J. P.; Kampf, J. W.; Matzger, A. J. *Chemistry of Materials* **2006**, *18*, 3470-3476.

(133) San Miguel, L.; Porter, W. W.; Matzger, A. J. *Organic Letters* **2007**, *9*, 1005-1008.

(134) Pope, M.; Swenberg, C. E. *Electronic Processes in Organic Crystals and Polymers*; Oxford University Press: New York, 1999.

(135) Nelson, S. F.; Lin, Y. Y.; Gundlach, D. J.; Jackson, T. N. *Applied Physics Letters* **1998**, *72*, 1854-1856.

(136) Podzorov, V.; Menard, E.; Borissov, A.; Kiryukhin, V.; Rogers, J. A.; Gershenson, M. E. *Physical Review Letters* **2004**, *93*, -.

(137) Ponomarev, V. I.; Filipenko, O. S.; Atovmyan, L. O. *Kristallografiya* **1976**, *21*, 392-394.

(138) Brock, C. P.; Dunitz, J. *Acta Crystallographica Section B. Structural Science* **1990**, *46*, 795-806.

(139) Holmes, D.; Kumaraswamy, S.; Matzger, A. J.; Vollhardt, K. P. C. *Chemistry-a European Journal* **1999**, *5*, 3399-3412.

(140) Karl, N.; Marktanner, J. *Molecular Crystals and Liquid Crystals* **2001**, *355*, 149-173.

(141) Karl, N. *Journal of Crystal Growth* **1990**, *99*, 1009-1016.

(142) Troisi, A.; Orlandi, G. *Journal of Physical Chemistry B* **2005**, *109*, 1849-1856.

(143) Mattheus, C. C.; Dros, A. B.; Baas, J.; Oostergetel, G. T.; Meetsma, A.; de Boer, J. L.; Palstra, T. T. M. *Synthetic Metals* **2003**, *138*, 475-481.

(144) Campbell, R. B.; Trotter, J.; Robertson, J. M. *Acta Crystallographica* **1961**, *14*, 705-711.

(145) Fritz, S. E.; Martin, S. M.; Frisbie, C. D.; Ward, M. D.; Toney, M. F. *Journal of the American Chemical Society* **2004**, *126*, 4084-4085.

(146) Troisi, A.; Orlandi, G.; Anthony, J. E. *Chemistry of Materials* **2005**, *17*, 5024-5031.

(147) Siegrist, T.; Kloc, C.; Schon, J. H.; Batlogg, B.; Haddon, R. C.; Berg, S.; Thomas, G. A. *Angewandte Chemie-International Edition* **2001**, *40*, 1732-1736.

(148) Jurchescu, O. D.; Baas, J.; Palstra, T. T. M. *Applied Physics Letters* **2004**, *84*, 3061-3063.

(149) Yamada, M.; Ikemoto, I.; Kuroda, H. *Bulletin of the Chemical Society of Japan* **1988**, *61*, 1057-1062.

(150) Janzen, D. E.; Burand, M. W.; Ewbank, P. C.; Pappenfus, T. M.; Higuchi, H.; da Silva, D. A.; Young, V. G.; Bredas, J. L.; Mann, K. R. *Journal of the American Chemical Society* **2004**, *126*, 15295-15308.

(151) Babel, A.; Jenekhe, S. A. *Synthetic Metals* **2005**, *148*, 169-173.

(152) Tang, M. L.; Reichardt, A. D.; Miyaki, N.; Stoltenberg, R. M.; Bao, Z. *Journal of the American Chemical Society* **2008**, *130*, 6064-6065.

(153) Tannaci, J. F.; Noji, M.; Mcbee, J. L.; Tilley, T. D. *Journal of Organic Chemistry* **2008**, *73*, 7895-7900.

(154) Swartz, C. R.; Parkin, S. R.; Bullock, J. E.; Anthony, J. E.; Mayer, A. C.; Malliaras, G. G. *Organic Letters* **2005**, *7*, 3163-3166.

(155) Cho, D. M.; Parkin, S. R.; Watson, M. D. *Organic Letters* **2005**, *7*, 1067-1068.

(156) Sakamoto, Y.; Suzuki, T.; Kobayashi, M.; Gao, Y.; Fukai, Y.; Inoue, Y.; Sato, F.; Tokito, S. *Journal of the American Chemical Society* **2004**, *126*, 8138-8140.

(157) Sakamoto, Y.; Komatsu, S.; Suzuki, T. *Journal of the American Chemical Society* **2001**, *123*, 4643-4644.

(158) Meyer, E. A.; Castellano, R. K.; Diederich, F. *Angewandte Chemie-International Edition* **2003**, *42*, 1210-1250.

(159) Reichenbacher, K.; Suss, H. I.; Hulliger, J. *Chemical Society Reviews* **2005**, *34*, 22-30.

(160) Miao, Q.; Lefenfeld, M.; Nguyen, T. Q.; Siegrist, T.; Kloc, C.; Nuckolls, C. *Advanced Materials* **2005**, *17*, 407-412.

(161) Norton, J. E.; Brédas, J. L. *Journal of the American Chemical Society* **2008**, *130*, 12377-12384.

(162) Robertson, J.; Trotter, J.; Sinclair, V. C. *Acta Crystallographica* **1961**, *14*, 697-704.

(163) Delgado, M. C. R.; Pigg, K. R.; Filho, D. A. d. S.; Gruhn, N. E.; Sakamoto, Y.; Suzuki, T.; Osuna, R. M.; Casado, J.; Hernández, V.; Navarrete, J. T. L.; Nortinelli, N.; Cornil, J.; V. Coropceanu; Sánchez-Carrera, R. S.; Brédas, J.-L. *Journal of the American Chemical Society* **2009**, *131*, 1502-1512.

(164) Salman, S.; Delgado, M. C. R.; Coropceanu, V.; Brédas, J.-L. Submitted to *Chemistry of Materials*.

(165) Zhang, X. N.; Cote, A. P.; Matzger, A. J. *Journal of the American Chemical Society* **2005**, *127*, 10502-10503.

(166) Katz, H. E.; Bao, Z. *Journal of Physical Chemistry B* **2000**, *104*, 671-678.

(167) Laquindanum, J. G.; Katz, H. E.; Lovinger, A. J. *Journal of the American Chemical Society* **1998**, *120*, 664-672.

(168) Pappenfus, T. M.; Hermanson, B. J.; Helland, T. J.; Lee, G. G. W.; Drew, S. M.; Mann, K. R.; Mcgee, K. A.; Rasmussen, S. C. *Organic Letters* **2008**, *10*, 1553-1556.

(169) Ogawa, K.; Rasmussen, S. C. *Macromolecules* **2006**, *39*, 1771-1778.

(170) Radke, K. R.; Ogawa, K.; Rasmussen, S. C. *Organic Letters* **2005**, *7*, 5253-5256.

(171) Ogawa, K.; Rasmussen, S. C. *Journal of Organic Chemistry* **2003**, *68*, 2921-2928.

(172) Hutchison, G. R.; Ratner, M. A.; Marks, T. J. *Journal of the American Chemical Society* **2005**, *127*, 2339-2350.

(173) Kim, E. G.; Coropceanu, V.; Gruhn, N. E.; Sanchez-Carrera, R. S.; Snoeberger, R.; Matzger, A. J.; Bredas, J. L. *Journal of the American Chemical Society* **2007**, *129*, 13072-13081.

(174) Sato, N.; Mazaki, Y.; Kobayashi, K.; Kobayashi, T. *Journal of the Chemical Society-Perkin Transactions 2* **1992**, 765-770.

(175) Thompson, M. E.; Djurovich, P. E.; Barlow, S.; Marder, S. R.

(176) Barlow, S.; Marder, S. R. *Chemical Communications* **2000**, 1555-1562.

(177) Cauletti, C.; Green, J. C.; Kelly, M. R.; Powell, P.; Vantilborg, J.; Robbins, J.; Smart, J. *Journal of Electron Spectroscopy and Related Phenomena* **1980**, *19*, 327-353.

(178) Evans, S.; Green, M. L. H.; Orchard, A. F.; Jewitt, B.; Pygall, C. F. *Journal of the Chemical Society-Faraday Transactions Ii* **1972**, *68*, 1847-1865.

(179) Barlow, S.; Bunting, H. E.; Ringham, C.; Green, J. C.; Bublitz, G. U.; Boxer, S. G.; Perry, J. W.; Marder, S. R. *Journal of the American Chemical Society* **1999**, *121*, 3715-3723.

(180) Watanabe, M.; Motoyama, I.; Takayama, T. *Bulletin of the Chemical Society of Japan* **1996**, *69*, 2877-2884.

(181) Watanabe, M.; Motoyama, I.; Takayama, T. *Journal of Organometallic Chemistry* **1996**, *524*, 9-18.

(182) Barlow, S.; Henling, L. M.; Day, M. W.; Schaefer, W. P.; Green, J. C.; Hascall, T.; Marder, S. R. *Journal of the American Chemical Society* **2002**, *124*, 6285-6296.

(183) Laus, G.; Schottenberger, H.; Wurst, K.; Herber, R. H.; Griesser, U. *Journal of Physical Chemistry B* **2004**, *108*, 5082-5087.

(184) Wong, H.; Meyer-Friedrichsen, T.; Farrell, T.; Mecker, C.; Heck, J. *European Journal of Inorganic Chemistry* **2000**, 631-646.

(185) Krukonis, A. P.; Silverma.J; Yannoni, N. F. *Acta Crystallographica Section B-Structural Crystallography and Crystal Chemistry* **1972**, *B 28*, 987-990.

(186) Glaser, R.; Dendi, L. R.; Knotts, N.; Barnes, C. L. *Crystal Growth & Design* **2003**, *3*, 291-300.

(187) Sonoda, Y.; Kawanishi, Y.; Goto, M. *Acta Crystallographica Section E-Structure Reports Online* **2005**, *61*, O1200-O1202.

(188) Sonoda, Y.; Kawanishi, Y.; Goto, M. *Acta Crystallographica Section C-Crystal Structure Communications* **2003**, *59*, O311-O313.

(189) Zhong, J. C.; Munakata, M.; Kuroda-Sowa, T.; Maekawa, M.; Suenaga, Y.; Konaka, H. *Inorganica Chimica Acta* **2001**, *322*, 150-156.

(190) Hall, T.; Bachrach, S. M.; Spangler, C. W.; Sapochak, L. S.; Lin, C. T.; Guan, H. W.; Rogers, R. D. *Acta Crystallographica Section C-Crystal Structure Communications* **1989**, *45*, 1541-1543.

(191) Rabinovich, D.; Shakked, Z. *Acta Crystallographica Section B-Structural Science* **1975**, *B 31*, 819-825.

(192) Yuan, P.; Liu, S. H.; Xiong, W. C.; Yin, J.; Yu, G. A.; Sung, H. Y.; Williams, I. D.; Jia, G. C. *Organometallics* **2005**, *24*, 1452-1457.

(193) Togni, A.; Rihs, G. *Organometallics* **1993**, *12*, 3368-3372.

(194) Liu, J.; Castro, R.; Abboud, K. A.; Kaifer, A. E. *Journal of Organic Chemistry* **2000**, *65*, 6973-6977.

(195) Bourhill, G.; Bredas, J. L.; Cheng, L. T.; Marder, S. R.; Meyers, F.; Perry, J. W.; Tiemann, B. G. *Journal of the American Chemical Society* **1994**, *116*, 2619-2620.

(196) BlanchardDesce, M.; Alain, V.; Bedworth, P. V.; Marder, S. R.; Fort, A.; Runser, C.; Barzoukas, M.; Lebus, S.; Wortmann, R. *Chemistry-a European Journal* **1997**, *3*, 1091-1104.

(197) Kinnibrugh, T.; Salman, S.; Getmanenko, Y.; Coropceanu, V.; III, W. W. P.; Timofeeva, T. V.; Matzger, A. J.; Brédas, J.-L.; Marder, S. R.; Barlow, S. *Organometallics* **2009**, *28*, 1350-1357.

(198) Janowska, I.; Zakrzewski, J.; Nakatani, K.; Delaire, J. A.; Palusiak, M.; Walak, M.; Scholl, H. *Journal of Organometallic Chemistry* **2003**, *675*, 35-41.

(199) Salman, S.; Georgia Institute of Technology: Unpublished data.

(200) Alain, V.; Blanchard-Desce, M.; Chen, C.-T.; Marder, S. R.; Fort, A.; Barzoukas, M. *Synthetic Metals* **1996**, *81*, 133-136.

(201) Vosko, S. H.; Wilk, L.; Nusair, M. *Canadian Journal of Physics* **1980**, *58*, 1200-1211.

(202) Lee, C. T.; Yang, W. T.; Parr, R. G. *Physical Review B* **1988**, *37*, 785-789.

(203) Perdew, J. P.; Burke, K.; Ernzerhof, M. *Physical Review Letters* **1996**, *77*, 3865-3868.

(204) Perdew, J. P.; Burke, K.; Ernzerhof, M. *Physical Review Letters* **1997**, *78*, 1396-1396.

(205) Dreuw, A.; Weisman, J. L.; Head-Gordon, M. *Journal of Chemical Physics* **2003**, *119*, 2943-2946.

(206) Dreuw, A.; Head-Gordon, M. *Journal of the American Chemical Society* **2004**, *126*, 4007-4016.

(207) Dreuw, A.; Head-Gordon, M. *Chemical Reviews* **2005**, *105*, 4009-4037.

(208) Zhao, Y.; Truhlar, D. G. *Journal of Chemical Physics* **2006**, *125*, -.

(209) Zhao, Y.; Truhlar, D. G. *Journal of Chemical Theory and Computation* **2006**, *2*, 1009-1018.

(210) Zhao, Y.; Truhlar, D. G. *Journal of Chemical Theory and Computation* **2007**, *3*, 289-300.

(211) Foresman, J. B.; Headgordon, M.; Pople, J. A.; Frisch, M. J. *Journal of Physical Chemistry* **1992**, *96*, 135-149.

(212) Hirata, S.; Head-Gordon, M.; Bartlett, R. J. *Journal of Chemical Physics* **1999**, *111*, 10774-10786.

(213) Stanton, J. F.; Gauss, J.; Ishikawa, N.; Headgordon, M. *Journal of Chemical Physics* **1995**, *103*, 4160-4174.

(214) Szabo, A.; Ostlund, N. S. *Modern Quantum Chemistry*; Macmillan, New York, 1982.

(215) Hoh, G. L.; Kleinberg, J.; Mcewen, W. E. *Journal of the American Chemical Society* **1961**, *83*, 3949-3953.

(216) Robbins, J. L.; Edelstein, N.; Spencer, B.; Smart, J. C. *Journal of the American Chemical Society* **1982**, *104*, 1882-1893.

(217) Gassman, P. G.; Macomber, D. W.; Hershberger, J. W. *Organometallics* **1983**, *2*, 1470-1472.

(218) Baldo, M. A.; O'Brien, D. F.; You, Y.; Shoustikov, A.; Sibley, S.; Thompson, M. E.; Forrest, S. R. *Nature* **1998**, *395*, 151-154.

(219) Kawamura, Y.; Goushi, K.; Brooks, J.; Brown, J. J.; Sasabe, H.; Adachi, C. *Applied Physics Letters* **2005**, *86*, 071104.

(220) Holmes, R. J.; Forrest, S. R.; Tung, Y. J.; Kwong, R. C.; Brown, J. J.; Garon, S.; Thompson, M. E. *Applied Physics Letters* **2003**, *82*, 2422-2424.

(221) Tokito, S.; Iijima, T.; Suzuri, Y.; Kita, H.; Tsuzuki, T.; Sato, F. *Applied Physics Letters* **2003**, *83*, 569-571.

(222) Adachi, C.; Baldo, M. A.; Forrest, S. R.; Lamansky, S.; Thompson, M. E.; Kwong, R. C. *Applied Physics Letters* **2001**, *78*, 1622-1624.

(223) Brunner, K.; van Dijken, A.; Borner, H.; Bastiaansen, J. J. A. M.; Kiggen, N. M. M.; Langeveld, B. M. W. *Journal of the American Chemical Society* **2004**, *126*, 6035-6042.

(224) Shih, P. I.; Chiang, C. L.; Dixit, A. K.; Chen, C. K.; Yuan, M. C.; Lee, R. Y.; Chen, C. T.; Diau, E. W. G.; Shu, C. F. *Organic Letters* **2006**, *8*, 2799-2802.

(225) Tsai, M. H.; Hong, Y. H.; Chang, C. H.; Su, H. C.; Wu, C. C.; Matoliukstyte, A.; Simokaitiene, J.; Grigalevicius, S.; Grazulevicius, J. V.; Hsu, C. P. *Advanced Materials* **2007**, *19*, 862-866.

(226) Tsai, M. H.; Lin, H. W.; Su, H. C.; Ke, T. H.; Wu, C. C.; Fang, F. C.; Liao, Y. L.; Wong, K. T.; Wu, C. I. *Advanced Materials* **2006**, *18*, 1216-1220.

(227) Sapochak, L. S.; Padmaperuma, A. B.; Cai, X. Y.; Male, J. L.; Burrows, P. E. *Journal of Physical Chemistry C* **2008**, *112*, 7989-7996.

(228) Sapochak, L. S.; Padmaperuma, A. B.; Vecchi, P. A.; Qiao, H.; Burrows, P. E. *Organic Light-Emitting Devices and Materials - Proceedings of SPIE* **2006**, *6333*, 57-71.

(229) Leung, M. K.; Yang, C. C.; Lee, J. H.; Tsai, H. H.; Lin, C. F.; Huang, C. Y.; Su, Y. O.; Chiu, C. F. *Organic Letters* **2007**, *9*, 235-238.

(230) Lee, J. H.; Tsai, H. H.; Leung, M. K.; Yang, C. C.; Chao, C. C. *Applied Physics Letters* **2007**, *90*, 243501.

(231) Chen, S. Y.; Xu, X. J.; Liu, Y. Q.; Qiu, W. F.; Yu, G.; Sun, X. B.; Zhang, H. J.; Qi, T.; Lu, K.; Gao, X.; Liu, Y.; Zhu, D. B. *Journal of Materials Chemistry* **2007**, *17*, 3788-3795.

(232) Wang, C. S.; Jung, G. Y.; Batsanov, A. S.; Bryce, M. R.; Petty, M. C. *Journal of Materials Chemistry* **2002**, *12*, 173-180.

(233) Tao, Y.; Wang, Q.; Yang, C.; Wang, Q.; Zhang, Z.; Zou, T.; Qin, J.; Ma, D. *Angewandte Chemie International Edition* **2008**, *47*, 8104-8107.

(234) Tao, Y.; Wang, Q.; Shang, Y.; Yang, C.; Ao, L.; Qin, J.; Ma, D.; Shuai, Z. *Chemical Communications* **2009**, 77-79.

(235) Marsal, P.; Avilov, I.; da Silva, D. A.; Bredas, J. L.; Beljonne, D. *Chemical Physics Letters* **2004**, *392*, 521-528.

(236) Avilov, I.; Marsal, P.; Bredas, J. L.; Beljonne, D. *Advanced Materials* **2004**, *16*, 1624-1629.

(237) Vecchi, P. A.; Padmaperuma, A. B.; Qiao, H.; Sapochak, L. S.; Burrows, P. E. *Organic Letters* **2006**, *8*, 4211-4214.

(238) de Melo, J. S.; Pina, J.; Rodrigues, L. M.; Becker, R. S. *Journal of Photochemistry and Photobiology a-Chemistry* **2008**, *194*, 67-75.

(239) Wasserberg, D.; Dudek, S. P.; Meskers, S. C. J.; Janssen, R. A. J. *Chemical Physics Letters* **2005**, *411*, 273-277.

(240) Bonesi, S. M.; Erra-Balsells, R. *Journal of Luminescence* **2001**, *93*, 51-74.

(241) Terada, T.; Koyanagi, M.; Kanda, Y. *Bulletin of the Chemical Society of Japan* **1980**, *53*, 352-358.

(242) Padmaperuma, A. B.; Sapochak, L. S.; Burrows, P. E. *Chemistry of Materials* **2006**, *18*, 2389-2396.

(243) Bässler, H.; Arkhipov, V. I.; Emelianova, E. V.; Gerhard, A.; Hayer, A.; Im, C.; Rissler, J. *Synthetic Metals* **2003**, *135-136*, 377-382.

(244) Holmes, R. J.; D'Andrade, B. W.; Forrest, S. R.; Ren, X.; Li, J.; Thompson, M. E. *Applied Physics Letters* **2003**, *83*, 3818-3820.

(245) Burrows, P. E.; Padmaperuma, A. B.; Sapochak, L. S.; Djurovich, P.; Thompson, M. E. *Applied Physics Letters* **2006**, *88*, 183503.

(246) Sapochak, L. S.; Padmaperuma, A. B.; Vecchi, P. A.; Cai, X.; Burrows, P. E. *Organic Light-Emitting Devices and Materials - Proceedings of SPIE* **2007**, *6655*, 665506.

(247) D. Kim; S. Salman; V. Coropceanu; Brédas, J.-L. "Theoretical Study on the Phosphine Oxides as Host Materials for Blue Phosphors: Tuning HOMO and LUMO without influencing the triplet energy in small molecules", to be submitted.

(248) Wang, C. S.; Jung, G. Y.; Hua, Y. L.; Pearson, C.; Bryce, M. R.; Petty, M. C.; Batsanov, A. S.; Goeta, A. E.; Howard, J. A. K. *Chemistry of Materials* **2001**, *13*, 1167-1173.

(249) Tonzola, C. J.; Alam, M. M.; Bean, B. A.; Jenekhe, S. A. *Macromolecules* **2004**, *37*, 3554-3563.

(250) Inomata, H.; Goushi, K.; Masuko, T.; Konno, T.; Imai, T.; Sasabe, H.; Brown, J. J.; Adachi, C. *Chemistry of Materials* **2004**, *16*, 1285-1291.

(251) Oyston, S.; Wang, C. S.; Hughes, G.; Batsanov, A. S.; Perepichka, I. F.; Bryce, M. R.; Ahn, J. H.; Pearson, C.; Petty, M. C. *Journal of Materials Chemistry* **2005**, *15*, 194-203.

(252) Zang, Y.; Georgia Institute of Technology: Unpublished data.

(253) Ge, Z.; Hayakawa, T.; Ando, S.; Ueda, M.; Akiike, T.; Miyarnoto, H.; Kajita, T.; Kakimoto, M. A. *Chemistry of Materials* **2008**, *20*, 2532-2537.

(254) Lai, M. Y.; Chen, C. H.; Huang, W. S.; Lin, J. T.; Ke, T. H.; Chen, L. Y.; Tsai, M. H.; Wu, C. C. *Angewandte Chemie-International Edition* **2008**, *47*, 581-585.

(255) Ge, Z. Y.; Hayakawa, T.; Ando, S.; Ueda, M.; Akiike, T.; Miyamoto, H.; Kajita, T.; Kakimoto, M. A. *Advanced Functional Materials* **2008**, *18*, 584-590.

(256) Su, S. J.; Sasabe, H.; Takeda, T.; Kido, J. *Chemistry of Materials* **2008**, *20*, 1691-1693.

(257) Ge, Z. Y.; Hayakawa, T.; Ando, S.; Ueda, M.; Akiike, T.; Miyamoto, H.; Kajita, T.; Kakimoto, M. *Organic Letters* **2008**, *10*, 421-424.

(258) Lai, M.-Y.; Chen, C.-H.; Huang, W.-S.; Lin, J. T.; Ke, T.-H.; Chen, L.-Y.; Tsai, M.-H.; Wu, C.-C. *Angewandte Chemie* **2008**, *120*, 591-595.

(259) Ren, X. F.; Li, J.; Holmes, R. J.; Djurovich, P. I.; Forrest, S. R.; Thompson, M. E. *Chemistry of Materials* **2004**, *16*, 4743-4747.

(260) Lin, J. J.; Liao, W. S.; Huang, H. J.; Wu, F. I.; Cheng, C. H. *Advanced Functional Materials* **2008**, *18*, 485-491.

(261) Colombo, M. G.; Brunold, T. C.; Riedener, T.; Gudel, H. U.; Fortsch, M.; Burgi, H. B. *Inorganic Chemistry* **1994**, *33*, 545-550.

(262) Tamayo, A. B.; Alleyne, B. D.; Djurovich, P. I.; Lamansky, S.; Tsyba, I.; Ho, N. N.; Bau, R.; Thompson, M. E. *Journal of the American Chemical Society* **2003**, *125*, 7377-7387.

(263) Wu, F. I.; Su, H. J.; Shu, C. F.; Luo, L. Y.; Diau, W. G.; Cheng, C. H.; Duan, J. P.; Lee, G. H. *Journal of Materials Chemistry* **2005**, *15*, 1035-1042.

(264) Chen, L. Q.; You, H.; Yang, C. L.; Ma, D. G.; Qin, J. G. *Chemical Communications* **2007**, 1352-1354.

(265) Coppo, P.; Plummer, E. A.; De Cola, L. *Chemical Communications* **2004**, 1774-1775.

(266) Yang, C. H.; Li, S. W.; Chi, Y.; Cheng, Y. M.; Yeh, Y. S.; Chou, P. T.; Lee, G. H.; Wang, C. H.; Shu, C. F. *Inorganic Chemistry* **2005**, *44*, 7770-7780.

(267) You, Y.; Kim, S. H.; Jung, H. K.; Park, S. Y. *Macromolecules* **2006**, *39*, 349-356.

(268) Yang, C. H.; Cheng, Y. M.; Chi, Y.; Hsu, C. J.; Fang, F. C.; Wong, K. T.; Chou, P. T.; Chang, C. H.; Tsai, M. H.; Wu, C. C. *Angewandte Chemie-International Edition* **2007**, *46*, 2418-2421.

(269) Ragni, R.; Plummer, E. A.; Brunner, K.; Hofstraat, J. W.; Babudri, F.; Farinola, G. M.; Naso, F.; De Cola, L. *Journal of Materials Chemistry* **2006**, *16*, 1161-1170.

(270) Orselli, E.; Kottas, G. S.; Konradsson, A. E.; Coppo, P.; Frohlich, R.; Frtshlich, R.; De Cola, L.; van Dijken, A.; Buchel, M.; Borner, H. *Inorganic Chemistry* **2007**, *46*, 11082-11093.

(271) Sajoto, T.; Djurovich, P. I.; Tamayo, A.; Yousufuddin, M.; Bau, R.; Thompson, M. E.; Holmes, R. J.; Forrest, S. R. *Inorganic Chemistry* **2005**, *44*, 7992-8003.

(272) Li, J.; Djurovich, P. I.; Alleyne, B. D.; Yousufuddin, M.; Ho, N. N.; Thomas, J. C.; Peters, J. C.; Bau, R.; Thompson, M. E. *Inorganic Chemistry* **2005**, *44*, 1713-1727.

(273) Avilov, I.; Minoofar, P.; Cornil, J.; De Cola, L. *Journal of the American Chemical Society* **2007**, *129*, 8247-8258.

(274) Kwon, T. H.; Cho, H. S.; Kim, M. K.; Kim, J. W.; Kim, J. J.; Lee, K. H.; Park, S. J.; Shin, I. S.; Kim, H.; Shin, D. M.; Chung, Y. K.; Hong, J. I. *Organometallics* **2005**, *24*, 1578-1585.

(275) Dedeian, K.; Shi, J. M.; Shepherd, N.; Forsythe, E.; Morton, D. C. *Inorganic Chemistry* **2005**, *44*, 4445-4447.

(276) King, K. A.; Spellane, P. J.; Watts, R. J. *Journal of the American Chemical Society* **1985**, *107*, 1431-1432.

(277) Breu, J.; Stossel, P.; Schrader, S.; Starukhin, A.; Finkenzeller, W. J.; Yersin, H. *Chemistry of Materials* **2005**, *17*, 1745-1752.

(278) Yoon, U. C.; Hyun, M. H.; Choi, H. J.; Jing, Z. Unpublished data.

(279) Lamansky, S.; Djurovich, P.; Murphy, D.; Abdel-Razzaq, F.; Lee, H. E.; Adachi, C.; Burrows, P. E.; Forrest, S. R.; Thompson, M. E. *Journal of the American Chemical Society* **2001**, *123*, 4304-4312.

(280) Hay, P. J. *Journal of Physical Chemistry A* **2002**, *106*, 1634-1641.

(281) Lamansky, S.; Djurovich, P.; Murphy, D.; Abdel-Razzaq, F.; Kwong, R.; Tsyba, I.; Bortz, M.; Mui, B.; Bau, R.; Thompson, M. E. *Inorganic Chemistry* **2001**, *40*, 1704-1711.

(282) De Angelis, F.; Fantacci, S.; Evans, N.; Klein, C.; Zakeeruddin, S. M.; Moser, J. E.; Kalyanasundaram, K.; Bolink, H. J.; Gratzel, M.; Nazeeruddin, M. K. *Inorganic Chemistry* **2007**, *46*, 5989-6001.

(283) Laskar, I. R.; Hsu, S. F.; Chen, T. M. *Polyhedron* **2006**, *25*, 1167-1176.

(284) Vlcek, A.; Zalis, S. *Coordination Chemistry Reviews* **2007**, *251*, 258-287.

VITA

SEYHAN SALMAN

Seyhan SALMAN was born in Istanbul, Turkey. She attended schools in Izmir, Turkey, received a B.S. in Chemistry from Boğaziçi University, Istanbul, in 2002 and a M.S. in Chemistry from Boğaziçi University, Istanbul, in 2004 before coming to Georgia Tech to pursue a doctorate in Chemistry and Biochemistry.